Computational Fluid Dynamics for Nuclear Reactor Safety

CFD4NRS-9

Book of Abstracts

Draft Version

February 20-21, 2023

College Station, Texas, United States

Draft Version of the **Book of Abstracts**
CFD4NRS-9
OECD Nuclear Energy Agency (**NEA**) Workshop
February 20-21, 2023, College Station, United States of America.

General Chairs:

- Yassin Hassan, TAMU
- Raymond Furstenau, NRC

Organizing Committee Members

- Martina Adorni, NEA
- Emilio Baglietto, MIT
- Steve Bajorek, NRC
- Chris Boyd, NRC
- Kevin Fernández-Cosials, TAMU / UPM
- Philippe Freydier, EDF
- Stephan Kelm, IEK
- Elia Merzari, PSU
- Pierre Ruyer, IRSN
- Mingjun Wang, XJTU
- Ghani Zigh, NRC

Scientific Committee Members

- Satoshi Abe, NRA
- Henryk Anglart, KTH
- Emilio Baglietto, MIT
- Sofiane Benhamadouche, EDF
- Dominique Bestion, IND
- Ulrich Bieder, CEA
- Guillaume Bois, CEA
- Francesco Dauria, UNIPI
- Abdel Dehbi, PSI
- Milorad Dzodzo, Westinghouse
- Kevin Fernández-Cosials, TAMU / UPM
- Philippe Freydier, EDF
- Yassin Hassan, TAMU
- Thomas Hoehne, HZDR
- Richard Howard, EdF
- Yanping Huang, NPIC
- Brian Jackson, KAIROS
- Gonzalo Jimenez, UPM
- Joshua Kaizer, NRC
- Stephan Kelm, IEK
- Ed Komen, NRG
- Pavel Kudinov, KTH
- Jéróme M. Laviéville, EDF
- Dr. Dirk Lucas, HZDR
- Graham MacPherson, FNC
- Stéphane Mimouni, EDF
- Fabio Moretti, NEWCLEO
- Domenico Paladino, PSI
- Victor Petrov, ETH
- Maria-Giovanna Rodio, CEA
- Véronique Roig, IMFT
- Pierre Ruyer, IRSN
- Afaque Shams, KFUPM
- Jan-Patrice Simoneau, EDF
- Chris Stanek, LANL
- Gerhard Strydom, INL
- Wenxi Tian, XJTU
- Mingjun Wang, XJTU
- Jinbiao Xiong, SJTU

Schedule

Time	Monday, February 20		Tuesday, February 21	
	Room A	Room B	Room A	Room B
8:45 AM				
9:00 AM	**Openning Session**		**Keynote Speaker 3**	
9:30 AM	**Keynote Session 1**		**Panel Session 2**	
10:00 AM				
10:15 AM	**Break**		**Break**	
10:30 AM	**Technical Session 1 - Computational Methods**	**Technical Session 2 - Bubble Dynamics**	**Technical Session 7 - Fuel-fluid interactions**	**Technical Session 8 - Verification and Validation**
11:00 AM				
11:30 AM				
12:00 PM	**Lunch**		**Lunch**	
12:45 PM				
1:00 PM	**Panel Session 1**		**Keynote Session 2**	
1:30 PM				
2:00 PM	**Technical Session 3 - Aerosol and Fission Products Transport**	**Technical Session 4 - Two-phase Flow**	**Technical Session 9 - Verification and Validation I**	**Technical Session 10 - Severe Accidets**
2:30 PM				
3:00 PM				
3:30 PM	**Break**		**Break**	
3:45 PM	**Technical Session 5 - Numerical Studies**	**Technical Session - 6 Liquid Metals**	**Closing Ceremony**	
4:00 PM				
4:30 PM			**Lab Tour**	
5:00 PM				
5:30 PM				
5:45 PM			**Closing Reception**	
6:00 PM	**Reception**			
6:45 PM				
7:00 PM				

All CFD4NRS-9 Participants are entitled to participate in the Conference on Advanced Reactors Development (CARD-2023).

Technical Sessions Detailed Schedule

Technical Session 1 – Computational Methods. Feb 20, 10:30-12:00, Hagler Room.

Chair(s)

- Stephan Kelm (IEK)
- Chai Koren (EDF)

Presentations

1. Creating reproducible, scalable, portable and adaptable CFD validation workflows with snakemake.

   R. Lehnigk, D. Lucas, M. Rehm, F. Schlegel

2. From supercomputing simulations to engineering approaches: building a multiscale framework.

   Elia Merzari

3. High–low fidelity thermal hydraulic coupling using ai/machine learning algorithms.

   Wesley Williams, Vineet Kumar, Elvis Dominguez-Ontiveros

Not confirmed / Video Presentation

1. Development & validation of CORTAF-pt: a 3d thermal-hydraulic characteristic analysis code for plate-type fuel reactor core.

   Xitong Liu, Kai Liu, Mingjun Wang, Wenxi Tian, Suizheng Qiu, G. H. Su

2. Three-dimensional nuclear steam generator thermal-hydraulics analysis code staf—development and application.

   Zeng Chunjie, Wang Mingjun, Tian Wenxi, Qiu Suizheng, Su Guanghui

Technical Session 2 – Bubble Dynamics. Feb 20, 10:30-12:00, Room 1011B.

Chair(s)

- Emilio Baglietto (MIT)
- Igor Bolotnov (NCSU)

Presentations

1. CFD investigation on single bubble rising hydrodynamics and wall effect during pool scrubbing.

   Weiyi Yao, Marco Pellegrini, Ozdemir Erdal, Koji Okamoto.

2. Simulation of single ellipsoidal bubble dynamics for pool scrubbing.

   Yuria Okagaki, Kosuke Motegi, Satoshi Abe

3. Experimental data on bubble size distributions in horizontal annulus.

   Boštjan Zajec, Leon Cizelj, Boštjan Končar

4. Characterization of steam chugging by experimental and computational analyses.

   Marco Pellegrini, Nejdet Erkan, Shuichiro Miwa, Koji Okamoto

5. Interface-capturing flow boiling simulation with phasta: Progress, challenges, and path forward.

   Anna Iskhakova, Nam T. Dinh, Igor A. Bolotnov

Not confirmed / Video Presentation

1. Influence of gas-liquid surface tension on aerosol removal based on CFD method.

   Zhongkai Mei, Xu Cheng

2. Experimental study on bubble dynamics for wall boiling model through high-speed infrared thermometry.

   Song Ni, Kwun Ting Lau, Jiyun Zhao

Technical Session 3 – Aerosol and Fission Products Transport. Feb 20, 14:00-15:30, Hagler Room.

Chair(s)

- Shuichiro Miwa (UT)
- Afaque Shams (KFUPM)

Presentations

1. A CFD approach to simulation of particle deposition for nuclear power plant safety.

   Erdal Ozdemir, Marco Pellegrini, Avadhesh Kumar Sharma, Shuichiro Miwa, Shunichi Suzuki, Koji Okamoto.

2. Computational modeling and validation of a modified MARPLE cascade impactor.

   Vineet Kumar, Sasikumar Yadukrishnan, Rose Montgomery

3. Experimental investigation of bubble hydrodynamics in the globule regime inside a shallow pool.

   Nabil Ghendour, Detlef Suckow, Abdelouahab Dehbi, Michael Klauck

4. Simulation of noble metal particle growth and removal in the molten salt fast reactor.

   E.M.A. Frederix and E.M.J. Komen

Technical Session 4 – Two-phase Flow. Feb 20, 14:00-15:30, Room 1011B.

Chair(s)

- Tomasz Kwiatkowski (NCNR)
- Ed Komen (NRG)

Presentations

1. The morphology adaptive multifield solver openfoam-hybrid and its application to multiphase flow problems in nuclear safety.

   Benjamin Krull, Dirk Lucas, Richard Meller, Fabian Schlegel, Matej Tekavčič

2. Heated liquid film in vertical free fall air-water annular flow.

   Y. Rivera, c. Berna, y. Córdova, J.L. muñoz-cobo, A. Escrivá

3. Pre-test design of panda experiments with steam injection through a sparger pipe by effective heat and momentum models.

   Xicheng Wang, Dmitry Grishchenko, Pavel Kudinov

4. CFD investigation of two-phase flow pressure drop in helical tube steam generator for lwr based SMR application.

   Doh Hyeon Kim, Seunghwan Oh, Jeong Ik Lee

Not confirmed / Video Presentation

1. Implementation and assessment of new transition criteria for all regime two-phase flow simulations with neptune_CFD code.

   Lasseur théo, mimouni Stéphane

2. CFD simulation on the transient heat and mass transfer performance of a water-copper wicked heat pipe.

   Dali Yua,, Jian Liua,B, Chongju Hua

Technical Session 5 – Numerical Studies. Feb 20, 15:45-17:15, Hagler Room.

Chair(s)

- Sofiane Benhamadouche (EDF)
- Matej Tekavcic (JSI)

Presentations

1. CFD for natural circulation flows: numerical investigations with trioCFD for a pitchfork bifurcation in the framework of system scaling uncertainty quantification.

   Haifu Huang, , Jorge Perez, Nicolas Alpy, Marc Medale

2. Highly scalable meshless multi grid solver for simulation of 3d reactor vessel analysis.

   Seong Ju Do,Han Young Yoon

3. Assessment of the cupid code for multi-dimensional analysis of innovative small modular reactor.

   Yun-je Cho, Ji-Hyun Sohn, Seong-Jun Lee, Han-Young Yoon

4. Multiple flow regime CFD simulating generic pool boiling.

   T. Höhne, D. Lucas

5. CFD simulation for evaluating pressure drop and heat transfer correlations for pebble bed reactor.

   Muhammad Sohaib Malik, Jiaqi Chen and C.S. Brooks

Not confirmed/ Video Presentation

1. Numerical simulation of tritium behavior in tritium confinement system for china fusion engineering test reactor.

   Haixia Wang, Xuewei Fu, Jincheng Han, Wenhao Wu, Taosheng Li, Jie Yu

U.S.NRC United States Nuclear Regulatory Commission *Protecting People and the Environment*

Center for Advanced Small Modular and Micro Nuclear Reactors
Texas A&M Engineering Experiment Station

NEA NUCLEAR ENERGY AGENCY

Technical Session 6 – Liquid Metals. Feb 20, 15:45-17:15, Room 1011B.

Chair(s)

- Vineet Kumar (ONL)
- Milroad Dzodzo (WEC)

Presentations

1. Understanding the need for proper turbulent heat flux modelling for non-unity Prandtl number fluids

   Afaque Shams

2. Simulation of a partially blocked wire-wrapped fuel assembly using les with wall functions.

   Octavio Bovati and Yassin Hassan

3. Prediction of turbulent heat transfer in buoyancy-affected flow regime.

   Andrea Pucciarelli, Afaque Shams and Nicolad Forgione

4. Prediction of flow regime boundary and pressure drop for hexagonal wire-wrapped rod bundles using artificial neural networks.

   Hansol Kim and Yassin A. Hassan

Not confirmed/ Video Presentation

1. Numerical modelling of rotating flows with large free-surface deformation.

   S.D. Amar, A. Rashkovan, G. Ziskind

Technical Session 7 – Fuel Fluid Interactions. Feb 21, 10:30-12:00, Hagler Room.

Chair(s)

- Jan-patrice SIMONEAU (EDF)
- Pierre Ruyer (IRSN)

Presentations

1. Validation of fuel assembly CFD models using magnetic resonance velocimetry and turbulence measurements for 5x5 swirl type mixing vane configuration.

   Martin Bruschewski, Kristine John, Sven Grundmann, Markus Rehm, Hidajet Hadžić, Peter Pohl

2. Effect of baffle jetting on the heat transfer and fluid flow within rod assembly.

   Mohamed Ali, Ahmed Alkaabi, Yacine Addad, Imran Afgan

3. Use of computational fluid dynamics in westinghouse innovation projects.

   Michael E. Conner, Milorad Dzodzo, Emre Tatli, Yiban Xu, Paolo Ferroni, Jorge V. Carvajal

4. Perspectives on the use of wall-resolved large eddy simulation for flow induced vibrations.

   Sofiane Benhamadouche and Thomas Norddine

5. Utilization of 3d boron asymmetry information in nuclear reactor generated from CFD for 1d safety analysis.

   Seunghwan Oh, Doh Hyeon Kim, Jeong Ik Lee

Not confirmed/ Video Presentation

Technical Session 8 – Verification and Validation I. Feb 21, 10:30-12:00, Room 1011B.

Chair(s)

- Elia Mezari (PSU)
- Masaaki Tanaka (JAEA)

Presentations

1. Scaling analysis as a support of CFD best practices.

   Milorad B. Dzodzo

2. Novel measurements of fluctuating temperature in the solid pipe wall for validation of CFD of stratification and thermal fatigue in closed branch line flows.

   Howard Richard, Angele Kristian, Veber Pascal, Edh Nicolas, Olivier Braillard, Victor Petrov, Annalisa Maneira

3. A NEA/OECD benchmark experiment to evaluate CFD in branch line flows.

   Angele Kristian, Howard Richard, Veber Pascal, Edh Nicolas, Olivier Braillard, Victor Petrov, Annalisa Maneira

4. Wrong but not guilty: the Reynolds analogy and model error in CFD.

   Ralph Wiser, Emilio Baglietto

Not confirmed / Video Presentation

1. CFD validation: flomix-r rocom heterogeneous boron concentration transient – impact of model selection on results.

   Christophe Riga, Simon Verdebout and Pierre-Alexis Douxchamps

2. CFD analysis of complex mixing phenomena in dead-end lines.

   "C. Riga, D. Dourneau, and P-A. Douxchamps P. Planquart"

Technical Session 9 – Verification and Validation II. Feb 21, 14:00-15:30, Hagler Room.

Chair(s)

- Ronald Lehnigk (HZDR)
- Ryan Tunstall (Rolls Royce)

Presentations

1. Validation practices for plant thermal-hydraulic analyses with multi-level approach in arkadia-design for safe design of advanced nuclear reactors.

   Masaaki Tanaka, Takero Mori, Kazuo Yoshimura, Erina Hamase, Norihiro Doda, Kentaro Matsushita, Norihiro Kikuchi, Ryuji Yoshikawa, and Toshiki Ezure

1. Validation of multi-phase-CFD frameworks for natural circulation in advanced reactors.

   Brandon Aranda, Koroush Shirvan, Emilio Baglietto

2. Use of holisitc CFD model evaluation to demonstrate confidence in industry applications of CFD.

   Joe Hegarty, Sophie Brown, Heather Davies, Ryan Tunstall

3. Unstable flows: assessment of CFD for the prediction of temperature fluctuations.

   Jan-patrice SIMONEAU

Not confirmed/ Video Presentation

1. Large eddy simulations of fluid-structure interaction of two inline cylinders in a turbulent flow.

   Pierre-Emmanuel Angeli, Maria Adela Puscas

4. CFD validation of supercritical heat transfer with four averaging methods and joule heating effect.

   Kwun Ting Lau, Song Ni, Jiyun Zhao

Technical Session 10 – Severe Accident. Feb 21, 14:00-15:30, Room 1011B.

Chair(s)

- Marco Pellegrini (UT)
- Kevin Fernández-Cosials (TAMU/UPM)

Presentations

1. Using CFD for u-tube steam-generator vibrations.

   Vivaldi, D., Ruyer, P

2. CFD and LP code benchmark on passive autocatalytic recombiner operation under counter current flow conditions.

   Kevin Dieter (on behalf of) Martin Freitag, Eike w. Schmidt, Seongnyeon Lee, Jungjae Lee, Yongjin Cho, Alexandre Bleyer, Rupak Kumar Raman, Abdel Dehbi, Michele Andreani, Holger Nowack

3. Development of combustion models for non-homogeneous hydrogen-air mixtures.

   D. Dovizio, J. De Palma, E.M.J. Komen

4. Verification & validation of multi-physical behavior in high-temperature gas-cooled reactor.

   Avadhesh Kumar Sharmaa, Wataru Sagawaa, Yosuke Nishimurab, Koji Okamotoa,B

Not confirmed / Video Presentation

1. Simulation of hydrogen risk analysis during severe accident in a nuclear power plant using CFD code.

   Amponsah Joseph

5. Flow physics of single and two vibrating heated cylinders.

   Muhammad Ansab Ali, Imran Afgan, Yacine Addad,, Dominique Laurence

U.S.NRC
United States Nuclear Regulatory Commission
Protecting People and the Environment

Center for Advanced Small Modular and Micro Nuclear Reactors
Texas A&M Engineering Experiment Station

NEA
NUCLEAR ENERGY AGENCY

Technical Session 1

Computational Methods

Feb 20, 10:30-12:00, Room A.

Creating reproducible, scalable, portable and adaptable CFD validation workflows with Snakemake

R. Lehnigk[1], D. Lucas[1], M. Rehm[2], F. Schlegel[1]

[1]Helmholtz-Zentrum Dresden – Rossendorf e.V. (HZDR), Bautzner Landstr. 400, 01328 Dresden, Germany
[2]Framatome GmbH, Paul-Gossen-Straße 100, 91052 Erlangen, Germany

The modelling and simulation of nuclear reactors is increasingly carried out with open-source tools. To researchers, the most appealing benefits are the possibility to study and verify existing implementations and the freedom to add code for prototyping new concepts and models. Further, there is no direct dependency on a software manufacturer, which generally makes open-source codes a solid basis for collaboration. An important downside however is that the responsibility of controlling quality and reliability lies with the users. For actively developed code this is a continuous task and demands considerable resources which should be bundled.
In the area of Computational Fluid Dynamics, a well-established open-source solution is OpenFOAM. Its development follows agile principles with a strong focus on maintainability and usability. This increases the demands on users to keep their setups functional. Since 2020, HZDR is creating an IT environment that supports the centralized and continuous maintenance of OpenFOAM code and simulation setups developed by members of the German nuclear safety research community. The project focuses on work relevant for the reactor cooling system and is referred to as OpenFOAM_RCS. Both, an addon to the OpenFOAM release from The OpenFOAM Foundation and a dedicated repository for simulation setups are supplied. The basis for the project is the web-based software development environment GitLab provided by the Helmholtz Federated IT Services (HIFIS), which allows for a high degree of automation with the help of continuous integration and deployment pipelines. Part of the project is the creation of a validation workflow.
Validation workflows should, among other things: (1) allow for continuous and automated checks of the setup input syntax; (2) frequently validate the simulation results by comparison against reference solutions; (3) be able to evaluate the impact of model substitutions on the overall "goodness" of results; (4) automatically create self-contained reports; (5) be executable on different environments, i.e. be portable and scalable; (5) allow for easy integration of new setups, i.e. be adaptable; (6) enable design point studies; (7) be comprehensible, ideally be self-documenting; (8) follow well-defined standards.
All aforementioned requirements can be fulfilled with the popular and actively developed Python-based workflow management system Snakemake (Mölder et al., 2021), which was originally written for Bioinformatics workflows, but is far more versatile. In this work Snakemake is configured to embed all setups archived in OpenFOAM_RCS in a single workflow. Execution of simulation setups is controlled via so-called Snakefiles, which list inputs and outputs of a simulation, the required resources as well as the commands to run them. Within a top-level configuration file utilizing the easy to read markup language YAML, all setups to be incorporated in a workflow are listed. Once properly configured, users can run the workflow in four steps: (1) configuration, i.e. assembly of selected setups; (2) running the simulations; (3) post-processing the simulations; (4) creating HTML reports gathering all generated plots together with runtime statistics and provenance information. The third step can be executed on a workstation or a cluster. For the latter case, a top-level job organizes the workflow and automatically submits sub-jobs to the cluster.
The proposed framework provides the opportunity to reduce cost and effort for CFD validation and verification. It also is of great help for complex model development such as multi-phase CFD where a large range of test cases and test conditions is mandatory to judge the performance of a given model choice.

This work is carried out in the frame of a current research project funded by the German Federal Ministry for Environment, Nature Conservation, Nuclear Safety and Consumer Protection, project number 1501604.

Supported by:

Federal Ministry
for the Environment, Nature Conservation,
Nuclear Safety and Consumer Protection

based on a decision of
the German Bundestag

From Supercomputing Simulations to Engineering Approaches: Building a Multiscale Framework.

Elia Merzari, Pennsylvania State University

GPU-based supercomputing is enabling a significant advancement in Computational Fluid Dynamics (CFD) capabilities for nuclear reactors. In fact, pre-exascale GPU-based super-computers such as ORNL's Summit are allowing for the first time to perform full core CFD calculations with URANS and LES approaches. Key to this has been the development of NekRS, a novel GPU-oriented variant of Nek5000, an open source spectral element code in development at Argonne National Laboratory. NekRS delivers peak performance for key kernels on the GPUs, and good scaling performance even on GPU architectures. Recent performance measurements showed that NekRS, when running on GPUs, outperforms the CPUs by 40x.

In this manuscript, we focus on how these calculations are being used to improve the fidelity of more traditional approaches such as, but not limited to, porous media models for pebble beds. In fact, supercomputing simulation alone cannot impact design and safety analysis without a suitable multiscale framework. An ongoing IRP project led by Penn State is pursuing novel methods for scale bridging. We discuss details of the project and, in particular, we review some recent progress in the project centered on four industry driven challenge problems.

HIGH-LOW FIDELITY THERMAL HYDRAULIC COUPLING USING AI/MACHINE LEARNING ALGORITHMS

Wesley Williams*, Vineet Kumar, Elvis Dominguez-Ontiveros

Oak Ridge National Laboratory, 1 Bethel Valley Rd, Oak Ridge, TN 37831
williamswc@ornl.gov*

Extended Abstract

The primary goal of the US Department of Energy (DOE) office of Nuclear Energy Integrated Energy Systems (IES) program is to develop the tools and framework for coupling multi-scale and multi-physical thermal and electrical energy usage and storage systems. High- and low-fidelity (high–low) coupling is a key feature of multi-scale, multi-component systems and has been an important focus of research in the nuclear energy community for the past two decades. An essential feature of demonstrating the capability to couple high-fidelity and low-fidelity systems for real-time applications are surrogate/reduced order models (ROM). For the purposes of this study, surrogate models are essentially Blackbox models, typically developed using supervised Machine learning (ML) algorithms. The surrogate models can be used to mimic the response of high-fidelity models to represent large historical datasets, and coupled with more general low-fidelity system models distributed as Functional Mock-up Interface (FMI) or Functional Mock-up Units (FMU) modules. The example is demonstrated with Spallation Neutron Source (SNS) First Target Station flow loop data. The flow loop is a liquid mercury loop with a pump, piping, heat exchange, and internal heat generation in the target window. A high-fidelity representation of the helium injection in a CFD model of the target section is developed to provide a more accurate pressure drop and temperature change in the target window and bypass flow. The complex flow requires extensive simulation time; therefore, it can be best represented after conversion to a surrogate model. This surrogate model is coupled with the FMU-exported Modelica system model via a boundary transfer of information and run to convergence using a Picard iteration scheme[1].

A Modelica model of the liquid mercury flow loop built in Modelon Impact was utilized for this work. The flow loop has the general configuration of a mercury reservoir, a circulating pump, piping, the target surrogate location, and the return heat exchanger. A custom library of mercury properties were built for this model to capture thermophysical variation with temperature and pressure. The CFD model of the target section was built in STAR-CCM+ by extending a prior single-phase model to multiphase flow, to account for helium injection. Additionally a porous media-based approximation was used to model the bubbler region. The points of connection between the system and CFD models are the driver outlet temperature in two parallel trains, the driver pressure drops for each train, and the outlet temperature and pressure drop across the window section. Future work will explore the pathways to reading in the surrogate model as an FMU directly into Modelon Impact and/or reading an FMU into the CFD solver. Additionally, the current surrogate model which was developed using steady-state runs, can be easily extended for transient runs. This work elucidates some of the potential benefits and future needs of developing tools for high–low system coupling of energy systems.

References:

1. William Gurecky, Dane de Wet, Michael Scott Greenwood, Robert Salko Jr, and Dave Pointer. Coupling of CTF and TRANSFORM using the Functional Mockup Interface. Technical Report ORNL/TM-2020/1872, Oak Ridge National Lab.(ORNL), Oak Ridge, TN (United States), 2020.

Development & Validation of CorTAF-PT: a 3D Thermal-hydraulic Characteristic Analysis Code for Plate-type Fuel Reactor Core

Xitong Liu, Kai Liu, Mingjun Wang*, Wenxi Tian*, Suizheng Qiu, G. H. Su

State Key Laboratory of Multiphase Flow in Power Engineering, Department of Nuclear Science and Technology, Xi'an Jiaotong University, Xi'an, China

Email: wangmingjun@mail.xjtu.edu.cn; wxtian@mail.xjtu.edu.cn

Abstract: In this paper, coupled heat transfer model is established by combining correlativity of heat conduction in fuel plates as well as flow and heat transfer relation between rectangular coolant channels in allusion to plate-type reactor. Full scale three-dimensional thermal-hydraulic analysis method is proposed through integrating traditional sub-channel analysis concepts into CFD framework, where CorTAF-PT code is developed based on open-source platform OpenFOAM. Relevant international benchmark of rectangular narrow channels is selected for CorTAF-PT validation while three-dimensional numerical simulation of IAEA 10MW MTR under steady state is carried out additionally. Results indicate that CorTAF-PT is capable and reliable for thermal-hydraulic characteristics prediction of plate-type reactor core. This work provides reference value for correlational studies on three-dimensional thermal-hydraulic characteristics of plate-type fuel reactor core.

Keywords: plate-type fuel reactor; OpenFOAM; coupled heat transfer; CFD

1. Introduction

Reactor cores, as the primary component of nuclear energy transformation system, have multiplied into various types classified according to fuel structure [1, 2], coolant type [3], circulation pattern, etc. For instance, classic pressurized water reactors which have been frequently used in nuclear power plants; heavy water reactors represented by Canadian deuterium uranium reactor (CANDU) and molten salt reactors (MSR) [4, 5] which possess development prospects on account of inherent safety as well as prominent efficiency. Among multiple reactor types of different fuel structure, plate-type fuel reactor has been extensively utilized in various of small testing-reactors and integrated experimental reactors for its high power-density, deep burn-up and compact arrangement structure [6].

Therefore, thermal-hydraulic analysis of plate-type fuel reactor core is significant for reactor design, where various analysis methods have been established including simplest lumped parameter model, sub-channel analysis code, computational fluid dynamics (CFD) and burgeoning, interdisciplinary technology to predict multi-physical parameters of reactor system by machine learning [7] and artificial intelligence algorithm [8]. Lumped parameter method, as one of the most classic thermal analysis models, lays the foundation of subsequent development in heat transfer field, which simplifies macroscopic study object as single calculation node while degraded energy conservation relation is formulated. Aiming to improve the roughness of calculation results by lumped parameter model, sub-channel analysis method was proposed by dividing calculation cells along coolant channel while relative equations are dispersed axially. Tae-Hyun et al, predicted the critical heat flux (CHF) of tube-based bundle utilizing sub-channel analysis code [9], a CHF identification key is established over disparate bundle effect coefficients based on calculation results eventually. Coolant flow and heat transfer characteristics of 300MW pressurized water reactor (PWR) were studied using sub-channel analysis code SACOS [10], then parameter uncertainty influence was analyzed by Wilks' method and response surface method, illustrating potential of economic parameter prediction method by sub-channel analysis code.

Traditional sub-channel analysis code or lumped parameter method possess rapid computation speed through model simplification, resulting in conservative calculation results while fine details of flow and heat transfer process are unable to be captured; computational fluid dynamics (CFD), an elaborate numerical simulation method has developed in recent years which is capable of predicting three-dimensional thermal-hydraulic characteristics under various flowing condition in refined scale, but the high-resolution CFD simulation for entire reactor core requires enormous consumption of computing resource which can't be satisfied by present technology. In consequence, a comprehensive model realizing both high computation speed and calculation accuracy possesses realistic significance.

In this paper, taking inspiration from sub-channel analysis method, control volumes based on finite volume method are divided along central plane of adjacent fuel plates, corresponding relationship between coolant channel and computation cell is mapped with additional physical model introduced to solve heat transfer relation of fuel plates. Then three-dimensional thermal-hydraulic characteristics analysis code CorTAF-PT is developed based on open-source CFD platform OpenFOAM. Coupled

heat transfer model is proposed by combining correlativity of heat conduction and heat transfer. Relevant narrow rectangular channels benchmark is selected for code validation and three-dimensional numerical simulation of IAEA 10MW MTR under steady state is implemented from both core-scale and fuel-scale roundly.

2. Mathematical model

2.1 Coolant flow and heat transfer model

Based on the finite volume method, three-dimensional thermal-hydraulic analysis model is established in allusion to the geometric characteristics of plate-type fuel reactor core. The control volumes divided in this way are bounded by the middle plane of adjacent fuel plates thus containing both the fluid domain in the enclosed coolant channel and the solid domain consisting of fuel pellets and cladding on both sides. “Pin by pin” mapping pattern between actual calculational domain and control volume is utilized for strict correspondence from actual core structure to the control volume, aiming to achieve the requirements of high-fidelity numerical simulation technology. The pattern how control volumes are divided is shown in Figure 1.

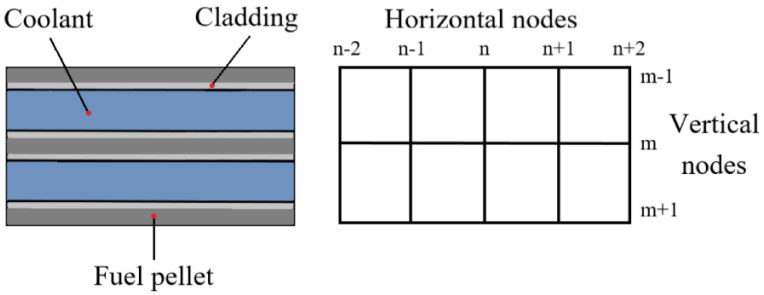

Fig. 1. Schematic diagram of control volumes divided among fuel plates

Considering the characteristics of control volumes divided similarly to sub-channel analysis method, the geometric parameters such as lateral area and volume need to be corrected when solving the coolant conservation equation, aiming to ensure the solution process to strictly correspond with the actual fluid region in rectangular narrow channel, correction methods for volume and lateral area of control volume are as follows:

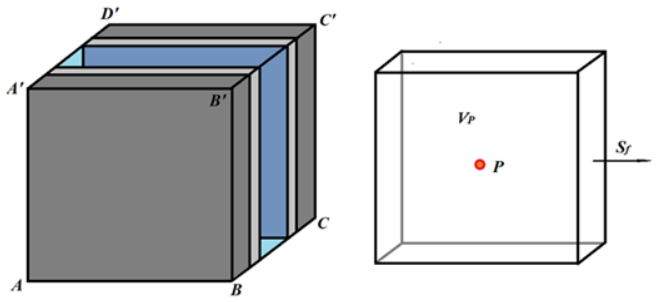

Fig. 2. Schematic diagram of geometric correction of control volume

$$V^{'} = V_0 - LD(Th_U + 2Th_c) \tag{1}$$

$$S_y^{'} = S_{y0} - L(Th_U + 2Th_c) \tag{2}$$

Where V_0 , $V^{'}$ are volume of divided coolant channel before and after geometric correction, L is length of control volume, D is width of control volume, Th_U is thickness of fuel pellet, Th_c is thickness of cladding, S_{y0} , $S_y^{'}$ are lateral area of control volume before and after correction.

Under the assumption of single-phase flow state of coolant over entire flow process, generalized transportation equation after discretization in control volume for physical quantity that obeys fluid transport theory satisfies following form:

$$\frac{\rho\phi^n - \rho\phi^{n-1}}{\Delta t}V_P' + \sum_f \overline{S}'_f \cdot \left(\rho\vec{u}\right)_f \phi_f^n = \sum_f \left(\rho\Gamma_\phi\right)\overline{S}'_f \cdot \left(\nabla\phi\right)_f^n + S_\phi V_P' \tag{3}$$

Where ρ is coolant density, ϕ is a particular physical quantity which obeys fluid transportation theory, Δt is time step, $\vec{u}$ is coolant velocity, Γ_ϕ is generalized diffusion coefficients, which can be specially substituted as dynamic viscosity μ in momentum equation, the superscript n represents current time step during discretization. Four physical terms are contained in aforementioned generalized transport equation, which are transient unsteady term, convective term, diffusion term and the source term respectively.

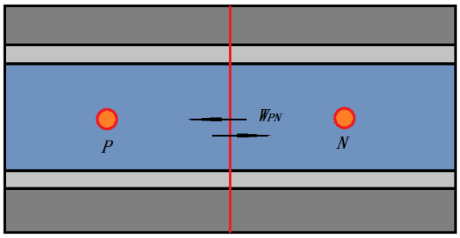

Fig. 3. Schematic diagram of turbulent mixing between coolant channels

On account of the existence of turbulent mixing between adjacent coolant computation cells, the physical quantities in control volume fluctuate randomly around the mean value and ultimately characterize as the exchange of momentum and energy between coolant channels [11], as shown in Fig. 3. In traditional CFD analysis, the deviation of the physical quantities in control volume caused by turbulent mixing is calculated by additional turbulent constitutive equations [12]; where k-ε and k-ω turbulent models are commonly selected for instance. Such treatment of solving the turbulent equations provides high computational accuracy therefore has been widely utilized, but meanwhile additional consumption of computational resource could be introduced inevitably, which is not conducive to improvement of computation efficiency. A similar approach to the sub-channel analysis method is adopted, the accessional transverse pulsating flow is directly calculated with related correlations. The exchange of momentum and energy caused by turbulent mixing for adjacent control volumes P and N can be described by following form:

$$\vec{M}'_{f,M} = -\beta \bar{G} \Delta x_{P,N} \left(\vec{u}_P - \vec{u}_N \right) \tag{4}$$

$$\vec{M}'_{f,E} = -\beta \bar{G} \Delta x_{P,N} \left(h_P - h_N \right) \tag{5}$$

Where $\vec{M}'_{f,M}$, $\vec{M}'_{f,E}$ are momentum and energy exchange caused by turbulent mixing between adjacent channels correspondingly, $\Delta x_{P,N}$ is the distance between geometric center of adjacent control volumes, h is the specific enthalpy of coolant, $\bar{G}$ is mass flow rate averaged by channel P and N , which can be obtained by weightily averaged:

$$\bar{G} = \frac{G_P D_P + G_N D_N}{D_P + D_N} \tag{6}$$

Where G is mass flow rate in each coolant channel, D is the length of control volume, subscript P, N represent adjacent control volumes for calculation, β is turbulent mixing

coefficient, which has been studied continuously by researchers worldwide. A precise experimental correlation applicable to rectangular channel proposed by Beus [13] is selected to calculate β:

$$\beta = 0.00175\frac{\sqrt{D_P D_N}}{D_P + D_N} Re^{-0.1} \tag{7}$$

Where *Re* is Reynolds number, a vital dimensionless criterion numeral to describe flow phenomenon:

$$Re = \frac{\rho \vec{u} L}{\mu} \tag{8}$$

Ultimately, coolant governing equations in control volumes considering geometric correction as well as turbulent mixing are reformed as follows, where mass, momentum and energy conservation relations are contained accordingly:

$$\frac{\partial \rho}{\partial t} + \nabla \cdot \left(\rho \vec{u}\right) = 0 \tag{9}$$

$$\frac{\partial \rho \vec{u}}{\partial t} + \nabla \cdot \left(\rho \vec{u}\vec{u}\right) = -\nabla p + \nabla \cdot \left(\mu \nabla \vec{u}\right) + \nabla \cdot \left(\vec{M}'_{f,M}\right) + \rho \vec{g} + \vec{S}_M \tag{10}$$

$$\frac{\partial \rho h}{\partial t} + \nabla \cdot \left(\rho \vec{u} h\right) = \nabla \cdot \left(\vec{q}\right) + \nabla \cdot \left(\vec{M}'_{f,E}\right) + S_E \tag{11}$$

Where p is absolute pressure of coolant, $\vec{g}$ stands for gravitational acceleration vector, $\vec{S}_M$ is momentum source term formed by frictional resistance during flowing while S_E is energy source term generated from fission heating released in fuel pellets. Aforementioned couple source terms can be processed as follows:

$$\vec{S}_M = \frac{f \rho \vec{u}^2 (D + Th_f)}{4 D Th_f} \tag{12}$$

Where Th_f is the thickness of coolant channel, f is single-phase frictional resistance coefficient which is calculated separately under laminar and turbulent flow. Recommended value by Shah-London [14] is selected when *Re* < 2300, otherwise for developed turbulent region, Kakac formula [14]is utilized for estimation, as shown in Table.1 and (13) respectively:

Table 1 Shah-London' s recommended value varied by aspect ratio α

α	1.0	0.8	0.6	0.4	0.2	1/10	1/20	1/50	0
f/*Re*	56.91	57.51	59.92	65.47	76.28	84.68	89.91	93.45	96.00

$$f=\begin{cases}\dfrac{96}{Re}(\text{Infinite slab assumption}) & Re<2300\\ 0.00128+\dfrac{0.1143}{Re^{0.311}} & Re\geq 2300\end{cases} \tag{13}$$

According to geometric characteristics of control volume divided, solid domain consisting of adjacent fuel pellets and claddings still remain in addition to original coolant region. Therefore, convective heat flux generated between fluid-solid interface is dispersed into certain control volume to obtain energy source term:

$$S_E=\frac{H(T_{cs}-T_f)}{Th_f} \tag{14}$$

Where T_{cs} and T_f are temperature of cladding and coolant at fluid-solid interface, H stands for convective heat transfer coefficient, which can be estimated by Dittus-Boelter formula [15]:

$$H=0.023Re^{0.8}Pr^{0.4}\frac{\lambda}{De} \tag{15}$$

Where Pr is Prandtl number, λ is thermal conductivity of coolant, De represents equivalent hydraulic diameter of rectangular channel.

2.2 Fuel plates heat transfer model

Distinguish from traditional CFD analysis method, additional heat transfer model of fuel plates is established considering both radial thermal conduction and thermal contact conduction. Unidimensional nodes are configurated transversely centering from symmetric plane of fuel plate as shown in Fig.4.

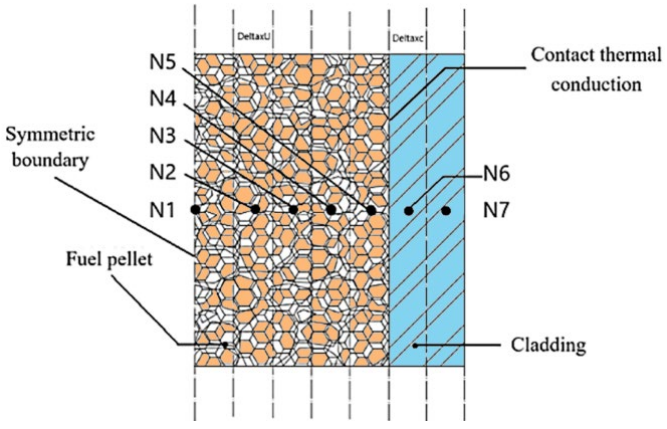

Fig. 4. Schematic diagram of nodes settling in fuel plate

Thereinto, assumption is made that N calculation nodes are placed in fuel pellet

while cladding contains rest two nodes. Unidimensional energy conservation equation for node *i* is discretized as follows:

$$\rho_i C_{p_i} \Delta x_i \frac{\partial T_i}{\partial t} = q_{i-1,i} + q_{i+1,i} + Q_i \Delta x_i \tag{16}$$

The physical significance of this equation represents: for each calculation node, temperature variation per unit time equals to heat flux conducted from front and back as well as energy source released by fuel. Where subscript *i*, *i*+1, *i*-1 stand for one particular node as well as nodes in and after it respectively in solid region, C_p is specific heat capacity under constant pressure, Δx is the distance between adjacent calculation nodes, t is time step, Q is volumetric heat release rate, q is surface heat flux, which can be obtained by Fourier heat equation applying to rectangular plate:

$$q_{i-1,i} = \frac{\lambda_{i-1} + \lambda_i}{2(x_i - x_{i-1})}\left(T_{i-1} - T_i\right) \tag{17}$$

$$q_{i+1,i} = \frac{\lambda_{i-1} + \lambda_i}{2(x_{i+1} - x_i)}\left(T_{i+1} - T_i\right) \tag{18}$$

For several special nodes which are positioned to central plane of fuel plate, interface between pellet and cladding as well as external surface of cladding, according boundary conditions are established correspondingly:

1) Central plane of fuel plate is defined as symmetry boundary, thus adiabatic condition is adopted for the energy conservation equation at node1: $q_{0,1} = 0$;

2) Thermal contact conduction between fuel pellet and cladding is considered in plate-type reactor core, which is distinguished from commonly-used gap conductance model in traditional fuel rods of pressurized water reactor (PWR), heat flux when *i*=*N*-1 can be calculated as follows [16]:

$$q_{i,i-1} = \psi \cdot \frac{2\lambda_U \lambda_c}{\lambda_U + \lambda_c} \cdot \frac{P_i(T_i - T_{i-1})}{\Theta[(\delta_U{}^2 + \delta_c{}^2)/2]^{1/2}} \tag{19}$$

Where ψ is constant with scale, which values as 10 here defined by geometric characteristics of fuel plates, λ_U, λ_c are thermal conductivities of fuel pellet and cladding respectively, P_i is contact pressure, Θ is Meyer hardness, δ_U, δ_c are surface

roughness of fuel pellet and cladding correspondingly.

3) Directly contact with coolant, convective heat flux is selected as Neumann boundary condition for external surface of cladding: $q_{N+1,N} = H\left(T_f - T_N\right)$.

2.3 Coupled heat transfer model

For the established coolant flow and heat transfer relation as well as fuel plates heat conduction model, coupled heat transfer model is proposed with cladding-coolant intersection as coupling zone, which is implemented as following steps with flow chart listed in Fig. 5.

Firstly, initialize coolant flow field and temperature field in global computational domain, retrieve the values of physical parameters at the corresponding temperature and obtain the coolant flow field at present moment by solving the coolant conservation equation considering additional momentum, energy source term and turbulent mixing effect. Then the parameters of coolant flow field are substituted into the Dittus-Boelter correlation to calculate surface convective heat transfer coefficient H on the external surface of cladding. Furthermore, newly-obtained convective heat transfer coefficient H is introduced to solve the heat transfer equation of fuel plates as boundary condition to calculate temperature distribution of fuel pellet and cladding.

After that, utilize the obtained convective heat flux calculated by H as additional energy source term in energy conservation equation of coolant, therefore flow field and temperature field of coolant for next time step can be calculated. Ultimately, return to first step for iterative solution of coolant conservation equations with updated coolant physical parameters under new time step, eventually three-dimensional distribution of thermal-hydraulic parameters for entire reactor core can be acquired after convergence.

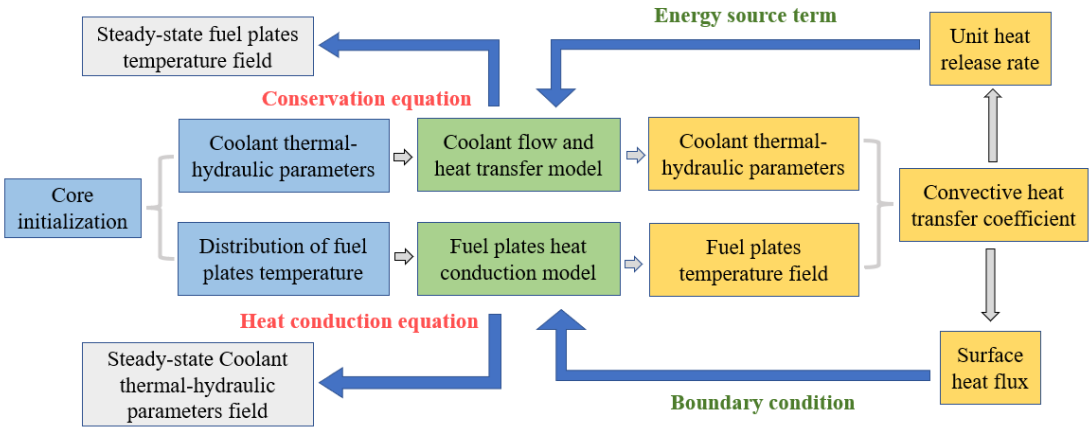

Fig. 5. The solution process of coupled heat transfer model

3. Experimental Validation & steady-state simulation

3.1 Narrow rectangular channel experiment

The narrow rectangular channel experiment is conducted by Key Laboratory of Nuclear Safety and Simulation Technology of Harbin Engineering University in 2011[17], where friction and heat transfer characteristics in narrow rectangular channel are investigated under isothermal and non-isothermal condition respectively. Exclusive heat transfer and flow resistance correlations were obtained by nine groups of experiments, the operating pressure values 0.8 MPa, the size of test section embedded with a couple of stainless-steel sheets is 1100 long with cross section of 40mm*2mm. Experimental loop with test section zoomed is shown in Fig.6.

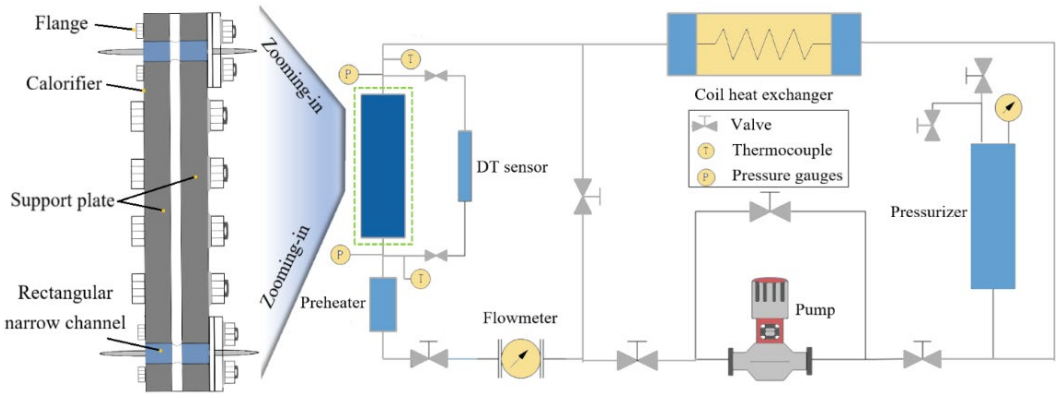

Fig. 6. Experimental loop with test section zoomed of narrow rectangular channel experiment [17]

In isothermal experiment, inlet coolant temperature was fixed at 40℃ while introducing specific heat flux on the lower wall to realize uniform coolant temperature during full flow process; in non-isothermal experiment, inlet coolant temperature was selected as 30 and 50℃ additionally while outlet temperature increased 20, 32, 42, 53, 60 and 74℃ separately under various wall heat flux. Distribution regularity of single-phase friction coefficient, Nusselt number and total axial temperature rise at different Reynolds numbers are simulated and compared with experimental result as shown in Fig. 7.

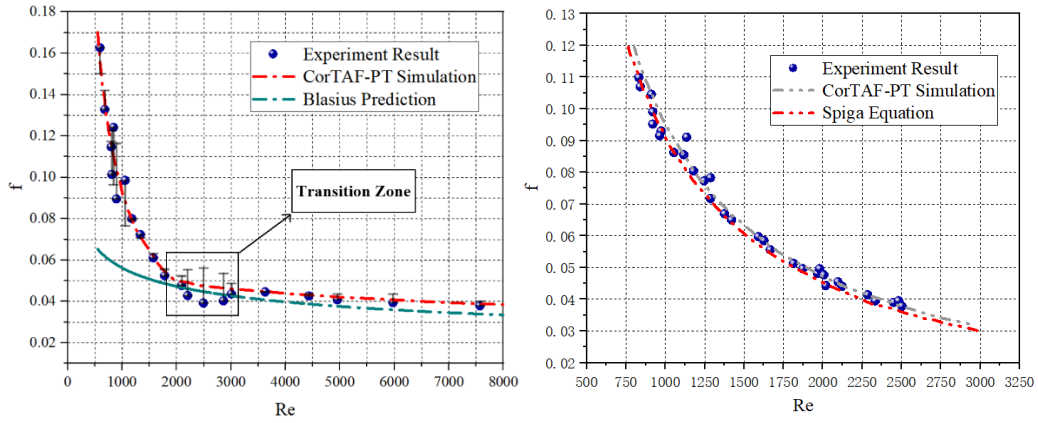

(a) Friction coefficient distribution in isothermal experiment

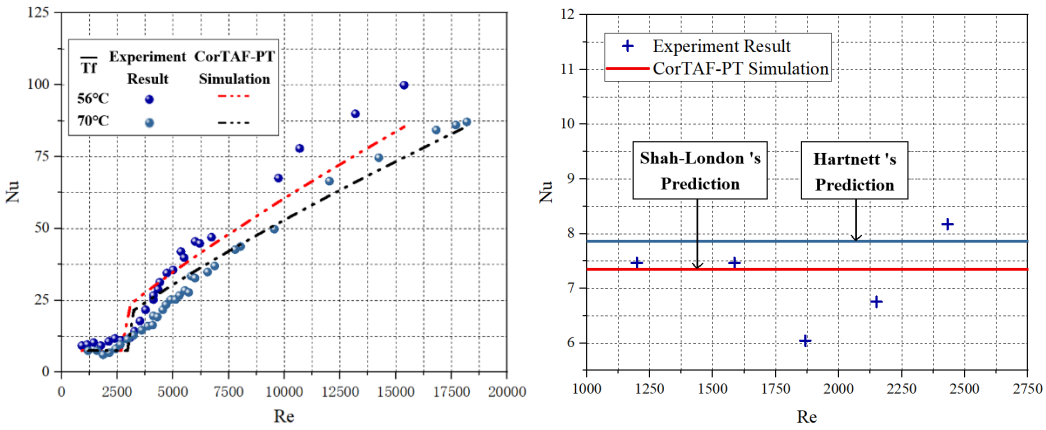

(b) Nusselt number distribution in heat transfer experiment

Fig.7. Calculation result of narrow rectangular channel experiment

In both Fig.7 (a) and (b), Reynolds numbers are divided into two ranges: laminar zone and full flow zone consisting of additional transition zone as well as fully-developed turbulent region. For friction coefficient distribution in isothermal experiment, single-phase friction coefficient sharply decreases when $0 < Re < 2500$ while slightly rises during transition zone. Widely-used Blasius equation is selected for comparison in fully-developed turbulent flow zone while correlation carried out by Spiga and Morini [18] is given in laminar region:

$$\lambda = \frac{96}{Re}\left(1 - 1.3553\alpha + 1.9467\alpha^2 - 1.7012\alpha^3 + 0.9564\alpha^4 - 0.2537\alpha^5\right) \qquad (20)$$

In non-isothermal experiment, distribution of Nusselt number represents ability of heat transfer, which also obeys different regularity during distinguishing flow zone where constant value is usually selected for Nusselt number prediction under laminar flow. As shown in Fig.7, calculation result of CorTAF-PT is substantially accordant

with the experimental values, comparing with correlations proposed by Blasius, Spiga and Hartnett [19] , CorTAF-PT reveals satisfactory accuracy in calculating friction factor and Nusselt number, indicating that CorTAF-PT is capable of predicting thermal-hydraulic characteristics in narrow rectangular channels.

3.2 Steady-state simulation of IAEA 10MW MTR

IAEA 10MW MTR is cooled by light water, fueled by 20% enriched dispersion uranium compacted with aluminum cladding while vertical natural circulation is adopted for coolant [20]. 21 standard fuel assemblies consisting of 23 fuel plates and 4 control fuel assemblies consisting of 17 fuel plates and 4 neutron absorbers are closely arranged in the middle of reactor core, surrounding by graphite and water gap to absorb and moderate neutrons. Schematic diagram of core structure and computational grids are shown in Fig.8.

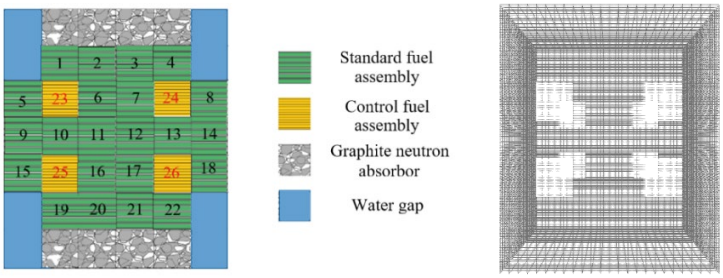

Fig.8. Structure and computational grids of IAEA 10MW MTR

In order to ensure the accuracy of the numerical calculation while maximizing the saving of computing resources, four sets of computational grids with axial layers of 10, 20, 40 and 60 are selected for the steady-state calculation of reactor core separately; Tout and Pout, the outlet temperature and outlet pressure are selected as the observation parameters for grid independence analysis as shown in Fig.9, relative error gradually stabilizes after 40 layers of axial grid for which subsequent simulation under steady state is selected ultimately.

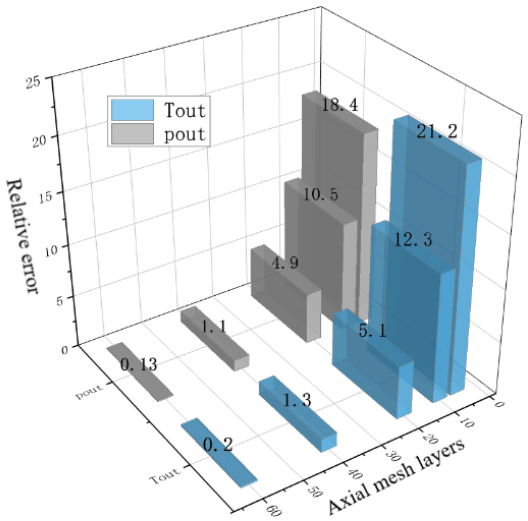

Fig.9. Grid independence analysis

Based on design parameters provided in Table 2, corresponding boundary conditions are confirmed for calculation. To obtain the full-scale temperature distribution of reactor core, vertical sections are demarcated along y=0.4m, x=0.12m, x=0.228m and x=0.336m with control fuel assemblies displayed particularly; in addition, to visually demonstrate the temperature distribution along the coolant flow direction within the core, the equivalent surfaces are divided along y=0.09m, 0.18m, 0.27m, 0.36m, 0.45m and 0.54m, the global distribution of temperature-related parameters obtained is shown in Fig.10:

Table 2: Design parameters of IAEA 10MW MTR

Parameter	Value
Thermal conductivity of fuel ($W \cdot cm^{-1} \cdot K^{-1}$)	0.5
Fuel density ($g \cdot cm^{-3}$)	4.45
Thermal conductivity of cladding ($W \cdot cm^{-1} \cdot K^{-1}$)	1.8
Cladding density ($g \cdot cm^{-3}$)	2.7
Power peak factor	1.2
Operation pressure (bar)	1.7
Inlet temperature (K)	311.15

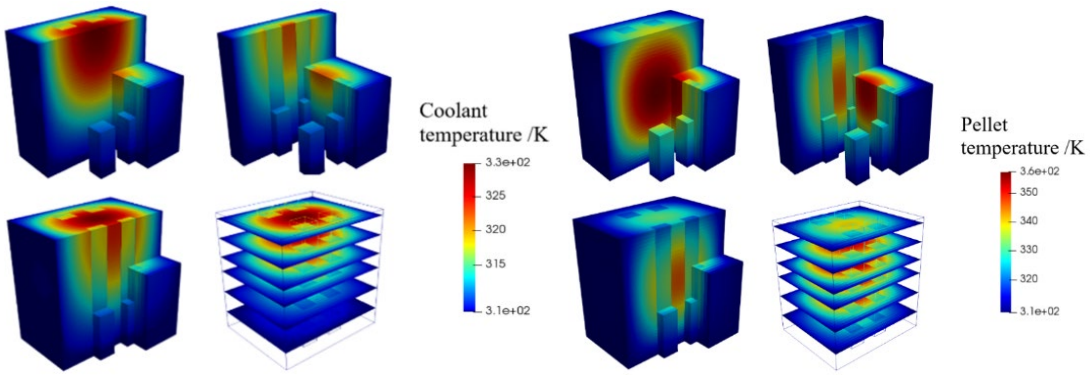

Fig.10. Temperature field distribution under steady-state calculation

As coolant flows along vertical direction, its temperature gradually increases and tends to decrease from the middle to both sides in any horizontal section while reaching the peak temperature at outlet. In addition, obvious temperature saltation at the interface between control fuel assembly and standard fuel assembly can be observed while the temperature of fuel pellet gradually decreases along the circumference with peak value at central core, which is mainly influenced by the thermodynamic dynamic equilibrium process of fuel plates consisting of fission heating in pellets and convective heat transfer by coolant. The detailed numerical analysis results of the core temperature field are presented by curves in following:

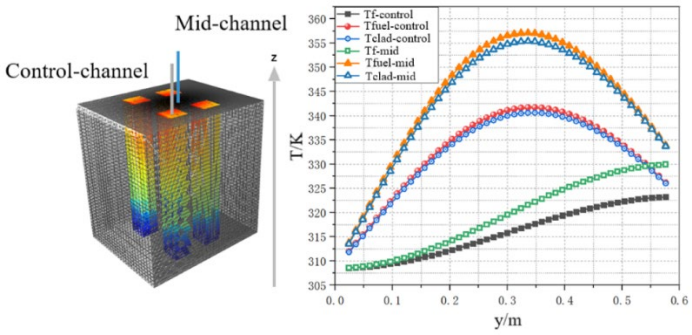

Fig.11. Axial temperature distribution along middle channel and control channel

To capture regularities of temperature distribution in different assemblies, middle channel and control channel which vertically passes across central assembly and control fuel assembly respectively are selected for observation in Fig.11. Along the flowing direction, coolant temperature characterizes an "S"-shaped growth curve with slope first increases then decreases; which is reasoned by convective heat flux linear to parabolic distribution of cladding temperature; outlet coolant temperature in middle channel and control channel are 329.87K and 322.76K respectively. For fuel pellet and cladding,

similar cosine distribution is appeared due to the spatial distribution of power density while maximum temperatures are 341.73K and 340.63K separately.

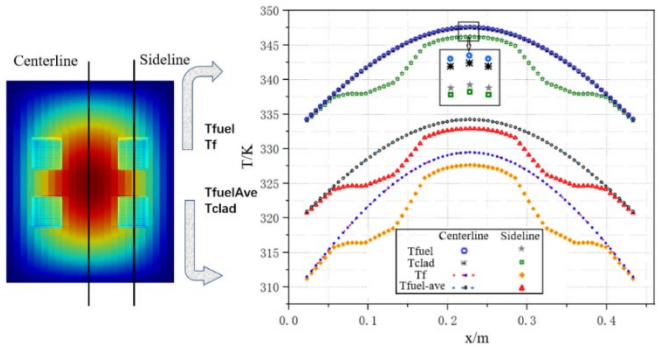

(a) Longitudinal temperature distribution

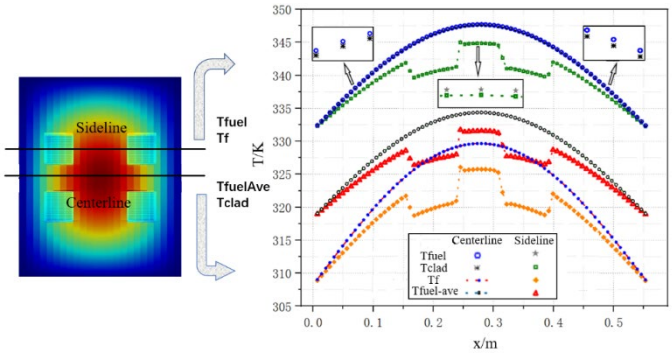

(b) Transverse temperature distribution

Fig.12. Outlet temperature distribution along centerline and sideline

Fig.12 provides temperature distribution including fuel pellet, cladding, coolant and volume-averaged temperature on outlet section along different directions and observation lines; cosine distribution is shown for each temperature value on center line while the side lines passing through control fuel assembly show various degrees of depression transversely and longitudinally; the temperature change is smoother along longitudinal direction which is reasoned by significant thermal conduction resistance between adjacent fuel assemblies along transverse direction.

Except for macroscopic-scale simulation of core temperature field, elaborate distribution of temperature field in fuel plates and coolant channels can be implemented as well by CorTAF-PT for sophisticated capture of flow-heat transfer details. Specifically, three adjacent fuel plates in 10^{th} standard fuel assembly are selected for observation as shown in Fig.13:

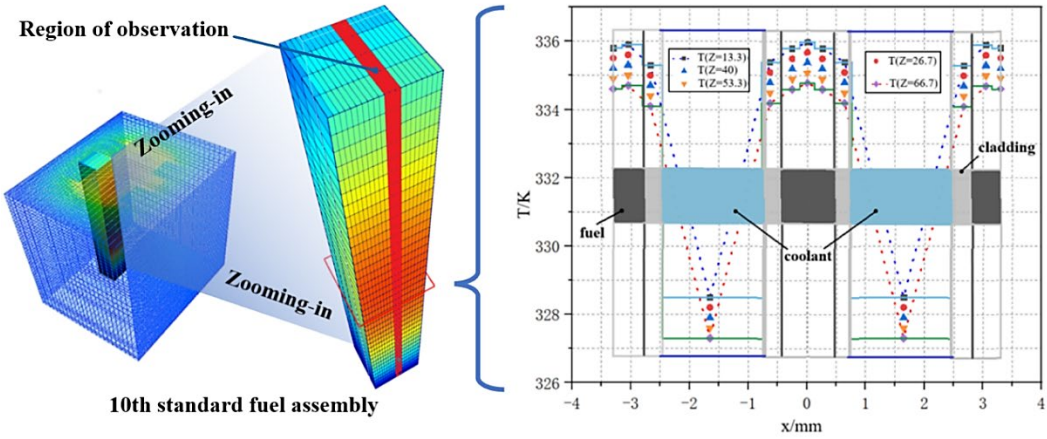

Fig.13. Temperature distribution of three adjacent fuel plates in 10th standard fuel assembly

Varying from one-dimensional calculation results by traditional sub-channel code, high-resolution multiscale distribution of thermal-hydraulic parameters is attainable with CorTAF-PT as shown in Fig.13, where calculation results are given on sections of z=13.3mm, 26.7mm, 40mm, 53.3mm and 66.7mm respectively. In addition, result comparison between experimental value provided by IAEA and simulation using CorTAF-PT is given in Table 3, calculation of key parameters is in satisfactory agreement with experimental result, indicating that code developed can satisfactorily predict thermal-hydraulic characteristics of plate-type fuel reactor core.

Table 3 Result comparison in steady-state calculation

Parameter	Absolute error	Relative error
Outlet temperature of coolant (K)	0.62	1.1%
Maximum temperature of claddings (K)	1.97	2.31%
Maximum temperature of pellets (K)	1.51	1.77%
Axial pressure drop (Pa)	165.5	4.86%

4. Conclusion

In order to satisfy the demand of advanced numerical simulation of plate-type fuel reactor core with both high resolution as well as economic computation efficiency, special analysis model is established combining sub-channel analysis code and CFD method. Coupled heat transfer model is established by combining correlativity of heat conduction in fuel plates as well as flow and heat transfer relation between rectangular

coolant channels in allusion to plate-type reactor. Then three-dimensional thermal-hydraulic characteristics analysis code CorTAF-PT is developed based on open-source CFD platform OpenFOAM, relevant narrow rectangular channels benchmark is selected for code validation, three-dimensional numerical simulation of IAEA 10MW MTR under steady state is implemented from both core-scale and fuel-scale roundly. Calculation results of experimental validation and MTR simulation are generally accordant with verification value, indicting that CorTAF-PT is capable of predicting three-dimensional thermal-hydraulic characteristics of plate-type fuel reactor core.

This work provides more possibility in advanced requirement for future high-fidelity numerical simulation of nuclear reactors, for further expectation, transient simulation under typical accidents as well as multi-physics coupling model will be implemented sequentially on CorTAF-PT.

Acknowledgement

This research has been supported by the CNNC Science Fund for Talented Young Scholars.

References

[1] Mohamed N.M.A., Design of a PWR for long cycle and direct recycling of spent fuel, Nuclear Engineering and Design, 295 (2015) 559-566.
[2] Yapıcı H., Ipek O., Neutronic performance of coupled hybrid blanket fueled with ThO2 and UO2, Energy Conversion and Management, 44 (2003) 1853-1873.
[3] Bae J.H., Son D.G., Kim K.H., Kang J.Y., Song Y.M., Kim S.H., Jeong J.Y., Numerical simulation of CS28-1 experiment by using CANDU severe accident analysis code, CAISER, Annals of Nuclear Energy, 150 (2021) 107820.
[4] Guerrieri C., Cammi A., Luzzi L., An approach to the MSR dynamics and stability analysis, Progress in Nuclear Energy, 67 (2013) 56-73.
[5] Zhang D., Qiu S., Su G., Development of a safety analysis code for molten salt reactors, Nuclear Engineering and Design, 239 (2009) 2778-2785.
[6] Khan S.U.-D., Peng M., Li L., Khan S.U.-D., Modification and validation of THEATRe code for the plate type fuel nuclear reactor, Annals of Nuclear Energy, 53 (2013) 519-528.
[7] Kitcher E.D., Osborn J.M., Chirayath S.S., Characterization of plutonium for nuclear forensics using machine learning techniques, Annals of Nuclear Energy, 170 (2022) 108987.
[8] Nakhabov A., Kolesov V., Soglaev P., Prediction of a reactivity margin for partial refueling of nuclear reactor using artificial neural networks, Procedia Computer Science, 169 (2020) 310-313.
[9] Chun T.-H., Hwang D.-H., Baek W.P., Chang S.H., Assessment of a tube-based bundle CHF prediction method using a subchannel code, Annals of Nuclear Energy, 25 (1998) 1159-1168.

[10] Wang M., Qiu S., Su G., Tian W., Preliminary study of parameter uncertainty influence on Pressurized Water Reactor core design, Progress in Nuclear Energy, 68 (2013) 200-209.
[11] Zhao H., Gu H., Liu M., Xiao Y., Numerical investigation of transverse flow and turbulent mixing in a helical cruciform fuel bundle, Annals of Nuclear Energy, 169 (2022) 108944.
[12] Esmaeili M., Afshari A., Jaberi F.A., Turbulent mixing in non-isothermal jet in crossflow, International Journal of Heat and Mass Transfer, 89 (2015) 1239-1257.
[13] Rogers J.T., Rosehart R.G., MIXING BY TURBULENT INTERCHANGE IN FUEL BUNDLES. CORRELATIONS AND INFLUENCES, ASME Pap, (1972).
[14] Tatchell D.G., Handbook of single-phase convective heat transfer: Sadik Kakaç, Ramesh K. Shah and Win Aung (editors) Wiley, New York, 1987, International Journal of Heat and Mass Transfer, 32 (1989) 408.
[15] Dittus F.W., Boelter L.M.K., Heat transfer in automobile radiators of the tubular type, International Communications in Heat and Mass Transfer, 12 (1985) 3-22.
[16] V M.C., Thermal contact conductance, Springer-Verlag, (1996).
[17] Wang C., Gao P., Tan S., Wang Z., Xu C., Experimental study of friction and heat transfer characteristics in narrow rectangular channel, Nuclear Engineering and Design, 250 (2012) 646-655.
[18] Spiga M., Morino G.L., A symmetric solution for velocity profile in laminar flow through rectangular ducts, International Communications in Heat and Mass Transfer, 21 (1994) 469-475.
[19] Hartnett J.P., Kostic M., Heat Transfer to Newtonian and Non-Newtonian Fluids in Rectangular Ducts, in: Hartnett J.P., Irvine T.F. (Eds.) Advances in Heat Transfer, Elsevier, 1989, pp. 247-356.
[20] Al-Yahia O.S., Albati M.A., Park J., Chae H., Jo D., Transient thermal hydraulic analysis of the IAEA 10MW MTR reactor during Loss of Flow Accident to investigate the flow inversion, Annals of Nuclear Energy, 62 (2013) 144-152.

Three-dimensional Nuclear Steam Generator Thermal-hydraulics Analysis Code STAF—Development and Application

ZENG Chunjie, WANG Mingjun, TIAN Wenxi, QIU Suizheng, SU Guanghui
(School of Nuclear Science and Technology, Xi'an Jiaotong University, Xi'an 710049, China)

Abstract: To ensure the safe operation of the steam generator (SG) in the nuclear power system is of great importance. A number of three-dimensional thermal-hydraulic SG analysis codes have been developed which used for SG thermal safety analysis and design reference. In order to develop a domestic advanced SG analysis code, the NuTHeL of Xi'an Jiaotong University developed the three-dimensional SG thermal-hydraulic analysis code—STAF based on the drift flux model and porous media. The initial program version was STAF1.0, which was characterized by simplifying the U-tube bundles of primary side into a one-dimensional flow, and thermal coupling with the secondary side (three-dimensional porous media model) was realized. The election of heat transfer model, resistance model, turbulence model and drift flux model has also been discussed. Combined with the FRIGG experiment data, the thermal-hydraulic calculation accuracy of STAF is better than the ATHOS code. For simulating the three-dimensional flow of U-tube bundles on primary side, the refined modeling combined with the porous media has been adopted in the STAF-CT (STAF2.0). The mesh of bundles on secondary side and primary side was overlapped, which was used for full three-dimensional thermal coupling between the primary and secondary sides. STAF-CT characterized by full three-dimensional thermal coupling between the primary and secondary side, which could obtain more reliable distribution of thermal-hydraulic parameters compared with STAF1.0. The above two SG codes are both developed based on commercial CFD platform (ANSYS). In order to avoid the copyright restrictions, STAF3.0 version abandoned the commercial CFD platform, developed on the open source CFD platform OpenFOAM instead. The OpenFOAM does not possess all the physical models that STAF needed, extra models have been developed and implanted into OpenFOAM, all the functions of old versions (STAF-CT) were also retained and the computing results have been tested well. To take full advantage of the multi-core processor, the parallel function was also upgraded, which effectively improves the computing efficiency compared with serial computing. Finally, typical applications of the STAF series have been introduced, such as SG thermal-hydraulic analysis, enhanced heat transfer with axial economizer, tube plugging conditions, ^{16}N migration in secondary side of the SG, corrosion deposits on tubes and marine conditions. The STAF series of programs have a wide range of functions and applications, and can provide important reference for the development of the SG three-dimensional thermal-hydraulic analysis program for advanced nuclear power systems, as well as provide tools to support new generation steam generator design optimization and safety analysis.

Key words: steam generator; porous media; STAF series; CFD

U.S.NRC
United States Nuclear Regulatory Commission
Protecting People and the Environment

Center for Advanced Small Modular and Micro Nuclear Reactors
Texas A&M Engineering Experiment Station

NEA
NUCLEAR ENERGY AGENCY

Technical Session 2

Bubble Dynamics

Feb 20, 10:30-12:00, Room B.

CFD INVESTIGATION ON SINGLE BUBBLE RISING HYDRODYNAMICS AND WALL EFFECT DURING POOL SCRUBBING

Weiyi YAO[1], Marco PELLEGRINI[1], Ozdemir ERDAL[1], Koji OKAMOTO[1,2]

1. Department of Nuclear Engineering and Management, Graduate School of Engineering, the University of Tokyo
2. Nuclear Professional School, School of Engineering, the University of Tokyo

Extended Abstract

Pool scrubbing plays a vital role in the aerosol removal during decommissioning of the Fukushima Daiichi Nuclear Power Plant. The radioactive particles with gas are injected into the pool and are retained by the water during the bubble rising process. The hydrodynamic behavior of the bubble affects particle removal mechanism directly and thus appropriate understanding of bubble rising hydrodynamics and decontamination mechanism is necessary. Pool scrubbing was investigated by numerous experimental and numerical studies and, as a result, some models and codes were developed. In these severe accident analysis codes, many empirical formulas and assumptions of the bubble hydrodynamics are applied which are crucial to the evaluation of the particle removal efficiency and thus the source term to the environment during the hypothetical severe accident (SA).

The pool scrubbing model in integrated SA code MELCOR is based on SPARC-90. The bubbles in the swarm are assumed to be oblate spheroids of a constant, stable size. The bubble rising velocity is assumed to remain constant with a given value depending on the particle size. The decontamination factor reflecting the removal efficiency of aerosol particles is related to the internal velocities of the particles in the bubble. The deformation, deceleration by the liquid and the wall are not considered in the MELCOR code. It is necessary to understand the realistic bubble behavior and modify the models based on the analysis of the bubble hydrodynamics.

The objective of the present work is to explore the single bubble hydrodynamic behavior at pool scrubbing conditions and the wall effect on it in detail by the VOF method. The geometric and dynamic characteristics of one single rising oil/air bubble are tracked by STAR-CCM+. The initial bubble size was firstly set the same as that in Fujiwara's PIV experiment and the material of the bubble was set as oil. The aspect ratio, rise velocity and interfacial velocity between oil and water were tracked. It was found that the aspect ratio of the bubble changed with increasing height which indicated the large deformation of the bubble. The rising velocity was not constant and oscillated around the mean value, which increased slightly with the bubble rising. The local interface velocity varied with the deformation of the bubble and was compared with PIV data and MELCOR results. By contrast, the recirculation of the oil and the trend of the interface velocity were comparable to the experimental data and the results estimated by the equation in SPARC-90. Then the material of the bubble was switched to air to expand the hydrodynamics characteristics and compare with the SA code result. Additionally, the wall effect

on the single rising bubble was also studied. The pool size was set close to the bubble size. The result showed when the pool size is small or the bubble moves nearby the wall, the shape of the bubble will be affected and the bubble rising velocity could be decelerated due to the presence of the wall. The results indicate that the change of the bubble shape and rising velocity during the rising process inside the pool with/without the wall effect will cause the difference in the decontamination factor estimated.

Key words: Pool scrubbing, hydrodynamics, aerosols, two-phase flow, MELCOR, SPARC-90

SIMULATION OF SINGLE ELLIPSOIDAL BUBBLE DYNAMICS FOR POOL SCRUBBING

Yuria Okagaki[1], Kosuke Motegi[1], Satoshi Abe[2]

[1]Japan Atomic Energy Agency, 2-4 Shirakata, Tokai-mura, Naka-gun, Ibaraki 319-1195, Japan
[2]Nuclear Regulation Authority, 1-9-9, Roppongi, Minato-ku, Tokyo 106-8450, Japan

Extended Abstract

Pool scrubbing is an important filtering process that prevents radioactive aerosols from entering the environment in the event of severe accidents in a nuclear reactor. In this process of transporting aerosol particles using bubbles, bubble hydrodynamics plays a crucial role in modeling pool scrubbing and significantly affects particle removal in a bubble. The pool scrubbing code based on Lumped Parameter (LP) approach includes the particle removal model, and its hydrodynamic parameters are determined based on simple assumptions. Our future research strategy is to apply the three-dimensional (3D) Computer Fluid Dynamics (CFD) approach to understand the detailed bubble internal flow effect for aerosol particle transportation, which is difficult to be assessed experimentally. This study focused on the flow behavior within a single buoyant rising elliptical bubble in a quiescent liquid. Based on previous studies, a solver based on the Simple Coupled Volume Of Fluid with Level Set (S-CLSVOF) method was applied for OpenFOAM to capture the gas-liquid interface. Simulations were performed for an initial bubble diameter of 4 mm in full 3D geometry models in addition to quarter symmetry (quarter structure with symmetry boundaries) 3D geometry models. This is because the bubble rise behavior becomes unstable for bubble diameters larger than 4 mm and the bubble wake loses its axisymmetry, as is well known. We revealed the difference in the simulation results between the quarter symmetry and full 3D geometry models in this study. Moreover, the Adaptive Mesh Refinement (AMR) method was applied to investigate the accuracy of the calculation with limited computational resources, and the results were compared with those obtained with equally spaced fine meshes. As a result, the terminal velocities of the rising bubbles close to the empirical correlations were obtained in the AMR mesh regardless of the geometry model. The bubble motion with zig-zag and spiral was indicated in the full 3D geometry model. The bubble shapes were asymmetrical due to the zig-zag motion with the loss of axisymmetry of the bubble wake. The zig-zag motion in the quarter-symmetric 3D geometry model appeared qualitatively as oscillations. Still, the terminal velocity was larger than the full 3D geometry because it was without the zig-zag motion in the full 3D geometry. Regardless of geometry, a toroidal vortex was confirmed within the elliptical bubbles in both geometry models, as shown in previous experimental studies. It is assumed that aerosol particles move from the center of the bubble toward the interface and that more aerosol particles are collected at the area with the largest interfacial curvature. However, the internal flow in the bubble was affected by the bubble wake causing the zig-zag motion, and fine mesh, which subdivided the entire bubble, predicted the bubble instability more accurately. Therefore, to accurately predict the internal flow, it was not sufficient to subdivide the inside of the bubble with the AMR mesh in full 3D geometry, and it was necessary to subdivide the mesh of the bubble inside and the bubble wake side. The terminal velocity might approach closest to the empirical correlations by subdividing the bubble inside and bubble wake side meshes. The knowledge obtained is expected to play an important role in developing and evaluating the constitutive equations in the stand-alone pool scrubbing code.

INFLUENCE OF GAS-LIQUID SURFACE TENSION ON AEROSOL REMOVAL BASED ON CFD METHOD

Zhongkai Mei, Xu Cheng

Institute for Applied Thermofluidics (IATF), Karlsruhe Institute of Technology (KIT)
Kaiserstrasse 12, 76131, Karlsruhe, Germany
mei@kit.edu, xu.cheng@kit.edu

Extended Abstract

As severe accidents in nuclear power plants happen, radioactive materials may be released into the containment owing to the core damage. As a promising method to remove radioactive particles, pool scrubbing has been especially paid attention to in previous studies. Given that the global removal capacity of the liquid pool is highly affected by the local mass transfer inside swarm bubbles, it is paramount to investigate the particle transport process inside each bubble individually. The present work focuses on the case of a single bubble rising in water with the process of internal particle transport. The numerical method employed in this work is the combination of the Volume of Fluid (VOF) method and the Lagrangian Particle Tracking (LPT) method. The VOF method is used to resolve the evolution of gas and liquid phases, whereas the LPT method is applied to track the temporal particle motion inside the bubble. Since the particle size in this work is of micron scale, the one-way coupling is adopted. Furthermore, the present work considers the effect of particle interfacial behavior on local mass transfer and thus develops a new interfacial penetration model coupling with the VOF-LPT method. The interfacial penetration model differentiates the particle interfacial behavior as submergence and no-submergence in simulation, which is based on the particle Weber number. The results indicated that with the increase in the surface tension coefficients, although the variation in the probability of particle-interface encounter is slight, the particle can hit the bubble surface with an increased normal impact velocity, which is beneficial to particle removal on one side. On the other side, the increase in surface tension coefficients contributes to the increase in surface tension force on the particles and consequently, impedes the particle penetrating through the gas-liquid interface. The influences from both aspects result in a nonlinear dependency of the decontamination factor versus gas-liquid surface tension coefficients. Furthermore, the change in surface tension coefficients affects the particle removal distribution inside the bubble. With increasing surface tension coefficients, the portion of particles removed on the bubble bottom surface is increased, which implies that the particles deviating from the internal gas streamline to hit the side interface are difficult to achieve decontamination in the context of high surface tension coefficients. In general, the present numerical model is proved to be feasible to simulate the local particle removal process inside a single bubble, which could provide the fundamental perspectives of aerosol removal information via the bubble scrubbing system.

EXPERIMENTAL STUDY ON BUBBLE DYNAMICS FOR WALL BOILING MODEL THROUGH HIGH-SPEED INFRARED THERMOMETRY

Song Ni, Kwun Ting Lau, Jiyun Zhao

Department of Mechanical Engineering, City University of Hong Kong, Hong Kong SAR

Extended abstract

The wall boiling model, which is actually a complex system and consists of many sub-models related to bubble dynamics, plays a vital role in accurately simulating the boiling phenomenon with CFD codes. In recent years, as the modeling becomes more detailed, more bubble behavior has been considered, and more sub-models have been introduced. However, due to the lack of the ability to measure the temperature near the bubbles with high resolution in the early years, some of the assumptions of temperature distribution and heat transfer proposed in these sub-models lack validation. Fortunately, recent advances in high-speed infrared thermometry allow researchers to measure the temperature of the regions where bubbles form, which helps them better understand heat transfer mechanisms and then make improvements on the wall boiling model.

In this article, a series of pool nucleate boiling experiments using high-speed infrared thermometry were carried out, and a thin titanium foil served as the heater. The thickness of the foil is so thin (8 micrometers) that it is reasonable to ignore the temperature difference between its two slides. So, the temperature of the heater surface where nucleate boiling happens can be recorded from its opposite side (contact with air) with a very fast sampling rate (1500 Hz) which is high enough to monitor the trend within a bubble period. An elaborate image processing code is designed to process a bulk of infrared temperature data. The code can identify the presence and location of active nucleation sites and each bubble period of each nucleation site. The applicability of this code has been validated using infrared temperature data from other researchers.

The temperature and heat flux distributions on the heater surface are present, and both show continuous unimodal normal distribution. This means that with the increase of wall heat flux, all temperatures related to bubble dynamics increase synchronously, and it is inappropriate to set a certain temperature-related parameter as a constant during bubble dynamic modeling. Meanwhile, the continuous distribution of heat flux indicates that the ranges of heat flux corresponding to evaporation and convection are not distinctly separated but overlap. Some widely used bubble dynamics parameters, such as active nucleation site density, bubble frequency and bubble waiting period, on conditions with different heat flux and wall temperatures, have been extracted from infrared temperature images by the code. Besides, the temperatures at the moment of the bubble-formation starts and ends, which receive little attention in other's research, are also collected. Every parameter related to bubble dynamics under different thermal conditions is discussed in this article. By processing a bulk of data, we found that these parameters related to bubble dynamics have a huge amount of randomness, which can't be solely ascribed to measurement uncertainty. Boiling is inherently chaotic and

exhibits randomness. The traditional tool for quantifying these parameters related to bubble dynamics is mostly fitting correlations that can only calculate the average value but can't give the degree of randomness. Similarly, using a few experimental data points to validate a correlation introduces errors because each data point is sampled with inherent randomness. In this article, we aim to quantify this randomness and look for factors that influence its magnitude. This paper is expected to help researchers improving the wall boiling model have a clearer understanding of the thermal characteristics and bubble behavior during boiling, thereby avoiding unreasonable temperature and heat transfer assumptions.

EXPERIMENTAL DATA ON BUBBLE SIZE DISTRIBUTIONS IN HORIZONTAL ANNULUS

Boštjan Zajec, Leon Cizelj, Boštjan Končar

Reactor Engineering Division, Jožef Stefan Institute, Jamova cesta 39, 1000, Ljubljana, Slovenia

Extended Abstract

Computational modelling of two-phase flows is challenging for the lack of complete equations describing bubble formation, coalescence, breakup and other phenomena related to phase boundaries. For development of new models and for validation of simulations, experimental data is of crucial importance. Besides heat transfer and pressure drop predictions, bubble size, bubble departure frequency and void fraction distribution are also important quantities to consider in bubble population balance modelling. Bubble diameters and void fractions were traditionally reported as integral or time-averaged values at certain locations, with little or no information on the distribution of bubble sizes. With the advancement of high-speed imaging techniques and analysis methods with concurrent increase in computational power, the interest for detailed analysis of these quantities has increased. Such data is especially for development of bubble multigroup models. While several authors report, there are limited data in annular geometry and even less in horizontal orientation.

In our paper, measurements on uniquely designed temperature-controlled test section for investigation of boiling flow are presented. The test section is designed as a double-pipe heat exchanger with the inner pipe with a diameter of 12 mm and the outer borosilicate glass tube with inner diameter of 24 mm, enabling flow visualization. Refrigerant R245fa is used as boiling fluid in the annulus while hot water flows through the inner pipe to boil the refrigerant. The inner pipe is fitted with a finned structure which enhances heat transfer and enables temperature and local heat flux measurements in the streamwise direction. For the visualization of the flow high-speed camera is used with a macro lens and high-powered LED lighting to enable sufficiently large depth of focus and short exposition times. Image analysis is used to determine bubble size distributions in both axial and radial directions in the test section.

Boiling flow was investigated at constant heating water conditions, similar to conditions present in real-world operation of heat exchangers. Refrigerant mass flux was increased from 150 kg/m^{2}s to 750 kg/m^{2}s and changes in bubble size distributions and heat flux were observed. The results show that in such horizontally positioned test section, bubble size distributions change significantly while heat flux changes only moderately between 22 kW/m^2 and 31 kW/m^2. The bubble size distributions shift from bimodal (two-peaked) distribution at low mass fluxes to single peaked Rayleigh distributions at higher mass fluxes. Additionally, variance (i.e. the width) of distributions is reducing with increasing refrigerant mass flux. Acquired flow images were then divided into sub-frames, to quantify void distribution transformation in the radial and axial direction. We observed that in the stream-wise direction, the total amount void is shifting from smaller to larger bubbles. Despite stream-wise changes in distributions, the general shape of the distributions remains the same. From and any single sub-frame distributions it can be distinguished which of the two flow patterns is behind it. Uncertainty of distributions was determined by a Monte-Carlo method by artificially applying noise to bubble sizes determined from flow images and vary for different flow rates and different parts of distribution. In general, the uncertainty is the largest for larger sized bubbles due to their lower numbers and their bigger impact on the total void in the test section.

Characterization of Steam Chugging by Experimental and Computational Analyses

Marco Pellegrini[a], Nejdet Erkan[b], Shuichiro Miwa[a], Koji Okamoto[a]

[a]Nuclear Professional School, The University of Tokyo, 2-22 Shirakata, Tokai-mura, Ibaraki, 319-1188, Japan

[b]Fusion Technology Facility, United Kingdom Atomic Energy Authority (UKAEA), Advanced Manufacturing Park, Rotherham, S60 5FX, UK

Extended Abstract

Direct Contact Condensation (DCC) is a simple and convenient method to condense steam into a water pool. Despite its design simplicity DCC can generate peculiar phenomena which might be difficult to control in an industrial environment. An example of a complex but fascinating behavior at low mass fluxes and low pool temperature is the so-called *chugging phenomenon*, which is characterized by the implosion of the generated steam bubble at the nozzle outlet.

Chugging has been studied in the past experimentally with high-speed camera to identify the regimes of condensation providing qualitative explanations [1]. An attempt to explain the process of chugging in more detail was done with image processing to evaluate the instability occurring at the interface and measuring the volume reduction [2][3]. The authors concluded that even though an instability at the interface is the main contributor of the bubble implosion, such instability does not behave as a Rayleigh-Taylor instability because the volume reduces with decreasing speed, i.e. negative acceleration. However, the results of the authors extract the volume from a single camera hence their estimation contains a large uncertainty that might exceed the level of accuracy which is required for their instability analysis. More recently Pellegrini et al. [4] have modelled chugging in CFD through Eulerian-Eulerian approach of a large pipe including a Rayleigh-Taylor instability model of the interface between steam and water achieving better results than any past attempt to simulate chugging by CFD. Nevertheless, their approach is heavily modelled and hard to be used to explain the implosion physics. In the current work the authors attempt to study the chugging dynamics experimentally by use of PIV to confirm the nature of the instability. In addition, the high-resolution Volume of Fluid (VOF) approach is employed to extract information of the bubble implosion which are hard to be measured in the experiment.

The PIV is performed in a two-dimensional small-scale facility [5] where particles covered with emitting dyes (Rhodamine B and Rhodamine 6G) are dispersed in the water. A green laser (wavelength 532 nm) with continuous light is used and a sharp cut filter on the camera at wavelength 560 nm allows to cut out all the reflections created by the bubble and the pipe. The post-processing data allow to study the speed of the bubble implosion analyzing the velocity vectors and not the simple and inaccurate bubble shape. In addition the vertical jet created because of the implosion can be extracted averaging across a number of implosions. The vertical jet appears to have non-dimensional spreading behavior as a regular single phase flow jet.

Confirmation of the characteristics of the steam bubble implosion during chugging can be done also by high level CFD computations. Hence, CFD simulations using VOF in STAR-CCM+ [6] are performed recreating the geometry of the same two-dimensional facility presented above. The better the accuracy requested from the VOF method, the higher the level of refinement is necessary. As the interface keeps

changing location, the generation of a large refinement over the whole volume where the bubble interface is expected to move would result in an excessively expensive simulation. In this simulation the adaptive mesh strategy is used with a four level of refinement to refine the mesh in advance towards the direction of the interface movement and limit the mass imbalance that might occur at every refinement. The CFD-VOF results show the ability to recreate a qualitative continuous chugging implosion with the same dynamic of the PIV experiments. The velocity created during the bubble implosion is of the same order of magnitude compared to the experiments. The CFD model itself, is basically model free from the point of view of physics, if we neglect the turbulence model which has a minor effect in the simulation. Hence a sensitivity analysis is performed on the numerical models related to High Resolution Interface Capturing (HRCI) scheme and the adaptive mesh parameters which are the primary players in the simulation. The results show that the sharper the interface the more realistic results are obtained in comparison with the experimental data.

References:

[1] G. Gregu, M. Takahashi, M. Pellegrini, R. Mereu, Experimental study on steam chugging phenomenon in a vertical sparger, Int. J. of Multiphase Flow, Vol. 88, (2017)

[2] I. Ueno, Y. Hattori, R, Hosoya, Condensation and Collapse of Vapor Bubbles Injected in Subcooled Pool, Microgravity Sci. Technol. Vol. 23 (2011)

[3] I. Ueno, J. Ando, Y. Koiwa, et al. Interfacial instability of a condensing vapor bubble in a subcooled liquid. Eur. Phys. J. Spec. Top. Vol. 224, (2015).

[4] M. Pellegrini, M. Naitoh, C. Josey, E. Baglietto, Modeling of Rayleigh-Taylor instability for steam direct contact condensation, NURETH-2015, Vol. 4 (2015)

[5] B. Jo, N. Erkan, S. Takahashi, et al. Thermal stratification in a scaled-down suppression pool of the Fukushima Daiichi nuclear power plants, Nuc. Eng. and Design, Vol. 305, (2016).

[6] STAR-CCM+, User Guide, Siemens, (2020)

INTERFACE-CAPTURING FLOW BOILING SIMULATION WITH PHASTA: PROGRESS, CHALLENGES, AND PATH FORWARD

Anna Iskhakova, Nam T. Dinh, Igor A. Bolotnov

Department of Nuclear Engineering, North Carolina State University, Raleigh, NC, USA

Extended Abstract

Flow boiling is an efficient heat transfer mechanism used in industrial thermal applications including in nuclear power plants. Extensive experimental, theoretical and computational studies on physics that govern flow boiling fluid dynamics and heat transfer conducted over the past century have created a comprehensive knowledge and database. However, predicting flow boiling behavior in new settings (fluids, system conditions, geometries, surfaces) remains elusive due to the inherently stochastic nature of the boiling process and multiple parameters that greatly influence heat transfer rate (e.g., contact angle, surface imperfections, etc.). Over a couple of years, a small contribution to the flow boiling process understanding has been made using PHASTA code. PHASTA is a highly parallel, finite-element code that solves compressible and incompressible Navier-Stokes and energy equations in 3D. Additionally, the level-set method is used in tandem with fluid flow and heat transfer equations to capture the interface dynamics and interfacial interactions. Previous studies showed that PHASTA is capable of modeling turbulent bubbly flow, adiabatic flow regime transitions, pool boiling and flow boiling in simple channels.

Recently, PHASTA capabilities have been extended to flow boiling simulations in heat-exchanger's complex-geometry channels. For this purpose, refinements were made in the code to ensure robust modeling of level-set function interactions with multiple walls and accurate contact angle modeling in subsequent bubble generation processes. PHASTA flow boiling capabilities have been assessed against data from TAMU's flow boiling experiments with a single nucleation site in a rectangular vertical channel. Parametric contact angle and nucleation cavity studies have been performed to evaluate their influence on bubble dynamics. Obtained bubble statistics (bubble departure diameter and departure frequency) agree well with experimental data for the smallest nucleation cavity considered. Although this cavity size is enlarged (order of 100 μm) compared to real cavity sizes (order of μm), bubble characteristics and dynamics predicted by direct numerical simulation (DNS) with interface-tracking method (ITM) are representative. Subsequently, PHASTA is used to perform numerical studies of flow boiling in a heat-exchanger channel with offset fins. Notably, several nucleation sites were seeded in the simulation domain. Contact angle and bulk superheat sensitivity studies are conducted for each of channel configurations, bubble statistics and heat transfer coefficient data are collected. Substantial heat transfer enhancement is found near channel walls due to bubbles' presence. Such physical processes as bubble sliding along channels' walls (that causes boundary layer disturbance), liquid replacement rate in a nucleation cavity is analyzed that has potential to inform high-efficiency heat exchanger design.

Although DNS with ITM have become computationally affordable for relatively short transients in small parts of heat exchangers, DNS methods are not practical for use in design analysis and optimization to inform engineering-scale applications. Within the PHASTA technology, the path forward considered is to perform machine learning (ML) guided coarse grid (CG) simulations for real-size heat exchangers. The main source of error in CG two-phase simulations is discretization error and, thereby, inaccurate interface representation. The CG correction workflow is proposed that allows to use ML-predicted level-set field in CG simulations. In this workflow a couple of advanced ML algorithms are explored: super resolution and Fourier neural operator (FNO). Super resolution technic uses multiple convolutional layers to predict output values on a finer mesh using CG input data. FNO allows to predict a solution of a PDE given initial and boundary conditions. The general idea is to integrate this workflow with CG PHASTA simulations with prior ML algorithms training on high-fidelity (HF) PHASTA data. Preliminary results conducted with FNO to predict HF level-set field are encouraging and future work will be focused on overall workflow implementation.

U.S.NRC
United States Nuclear Regulatory Commission
Protecting People and the Environment

Center for Advanced Small Modular and Micro Nuclear Reactors
Texas A&M Engineering Experiment Station

NEA
NUCLEAR ENERGY AGENCY

Technical Session 3

Aerosol and Fission Products Transport.

Feb 20, 14:00-15:30, Room A.

A CFD Approach to Simulation of Particle Deposition for Nuclear Power Plant Safety

Erdal Ozdemir[a], Marco Pellegrini[b], Avadhesh Kumar Sharma[a], Shuichiro Miwa[a], Shunichi Suzuki[b], Koji Okamoto[a]

[a]*Nuclear Professional School, The University of Tokyo, 2-22 Shirakata, Tokai-mura, Ibaraki, 319-1188, Japan*

[b]*Department of Nuclear Engineering and Management, The University of Tokyo, 7-3-1 Hongo, Bunkyo-ku, Tokyo, Japan*

Extended Abstract

The deposition and resuspension of radioactive particles in the primary circuit of a nuclear power plant are the principal factors that impact the release of radioactive elements (fission products, activated structural components) into the containment during severe accident conditions. Thus, accurate modeling of deposition and resuspension of radioactive particles is crucial for estimating release of radioactive elements. In this study, we aim to combine different models developed for simulating particle deposition such as drag force, turbulent dissipation and thermophoresis with the capability of a commercial CFD code STAR-CCM+.

The drag force is the main retarding force for the particles. In this study, the Schiller-Neumann correlation which is suitable for spherical solid particles is used. It is formulated as [1]:

$$C_d \begin{cases} \dfrac{24}{\mathrm{Re}_p}\left(1+0.15\,\mathrm{Re}_p^{0.687}\right) & \mathrm{Re}_p \le 10^3 \\ 0.44 & \mathrm{Re}_p > 10^3 \end{cases} \qquad (1)$$

In a turbulent flow, a particle encounters a randomly variable velocity field to which it responds based on its inertia. This behavior is described using a stochastic technique that incorporates the particle's instantaneous velocity fluctuations. The effect of turbulence on the particles can be included by using the eddy lifetime model of Gosman and Ioannides [2]. As it crosses a turbulent flow field, a particle is expected to transit through a series of turbulent eddies. An eddy is a local perturbation in the Reynolds-averaged velocity field. The particle remains in the eddy until either the eddy time-scale is exceeded, or the separation between the particle and the eddy exceeds the length scale of the eddy. In practice, an eddy transit time serves in place of the latter [3]. The particle experiences an instantaneous fluid velocity in each eddy, which is given by:

$$v = \bar{v} + v' \qquad (2)$$

where $\bar{v}$ is the local Reynods-averaged velocity and v' is the eddy velocity fluctuation, unique to each particle. The latter is a normal (Gaussian) deviate with zero mean value and a standard deviation that comes from the eddy velocity scale

$$u_e = \frac{l_t}{\tau_l}\sqrt{\frac{2}{3}} \qquad (3)$$

The turbulence model provides the length and timescales of the turbulence, l_t and τ_t. For example, their ration $\sqrt{k}$ with a k-ε or k-ω turbulence model. The eddy time-scale measures the maximum interval over

which a single realization of v' remains valid (the lifetime of the eddy). It can be related to the diffusion of a passive scalar according to the underlying turbulence model giving:

$$\tau_e = \frac{2\mu_t}{\rho u_e^2} \qquad (4)$$

Small particles can experience a force that acts in the opposite direction as the temperature gradient due to a process known as thermophoresis. As a result, particles inside hot gas will be drawn to relatively cold walls. The effect of thermophoresis on particle deposition can be substantial therefore in this study the thermophoretic force acting on the particles considered using thermophoretic force by Talbot et al.[4] who review the various approaches and propose an interpolating scheme based on Brock's formula[5].

$$F_T = -\pi\mu\nu R\frac{\nabla T}{T}\alpha_T\left(K_n\right) \qquad (5)$$

$$\alpha_T\left(K_n\right) = \frac{k_g / k_p + C_t K_n}{\left(1+3C_m K_n\right)\left(1+2k_g / k_p + 2C_t K_n\right)} \qquad (6)$$

where $\alpha_T\left(K_n\right)$ is a thermophoretic correction factor, while k_g and k_p are the thermal conductivities of the gas and the particle, respectively.

The proposed CFD model was validated against experimental data from an extensive experimental programme undertaken at ISPRA, known as STORM (Simplified Tests on Resuspension Mechanisms) [6]. The STORM tests was conducted in scope of the International Standard Problem No. 40 exercise which was devoted to deposition and resuspension of aerosols in pipes. The exercise was divided in two parts: the deposition phase mostly by thermophoresis and eddy impaction, and the resuspension phase under a stepwise increasing gas flow. The experimental conditions in STORM tests were selected following a detailed examination of number of severe accident calculations for full plants[6]. By validating CFD model with test data of STORM experiments, it can be applied full scale containment conditions as well as can be used to estimate possible dispersion of radioactive materials during the removal of debris such as in Fukushima Daiichi Nuclear Power Plants. Even though the physical processes incorporate in current CFD model based on experimental observations there is a need to improve the current model further to enhance the source term prediction for nuclear power plant safety.

References:

[1] Schiller, L., and Naumann, A. 1933. "Uber die grundlegenden Berechnungen bei der Schwerkraftaufbereitung", VDI Zeits, 77(12), pp. 318 – 320.

[2] Gosman, A.D., and Ioannides, E. 1983. "Aspects of computer simulation of liquid-fueled combustors", AIAA, J. Energy, 7(6), pp. 482–490.

[3] SIEMENS, STAR-CCM+ Version 15.04 User Guide, 2020

[4] L.Talbot, R.K. Chen, R.W. Schefer and D.R. Willis, J.Fluid Mech. 101 (1980) 737

[5] J.R. Brock, J. Colloid Interface Sci. 61 (1977) 77.

[6] De Los Reyes, Alfredo Castelo, Areia Capitao, Joaquim, & De Santi, Giovanni (1999). International Standard Problem 40 - Aerosol Deposition and Resuspension Final Comparison Report (NEA-CSNI-R--1999-4). Nuclear Energy Agency of the OECD (NEA)

STATUS AND FIRST APPLICATION OF CONTAINMENTFOAM

Kelm S[1], Liu X[1], George A[1,4], G. Vijaya Kumar[1,2], Cammiade L.M[1,3], Ji R[1,4], Yassin K[1], Schumacher D[1], Druska C[1], Kuhr A[1], Lopez L S[6]

[1]Forschungszentrum Juelich GmbH, Institute of Energy and Climate Research, Juelich, Germany
[2]Indian Institute of Technology Madras, Department of Applied Mechanics, Chennai, India,
[3]RWTH Aachen University, Institute for Heat and Mass Transfer, Aachen, Germany
[4]Karlsruhe Institute of Technology, Institute of Applied Thermofluidics, Karlsruhe, Germany
[5]Universität der Bundeswehr München, Institute for Numerical Methods in Aerospace Engineering, Munich, Germany
[6]Universidad Politécnica de Madrid, ETSI Industriales, Madrid, Spain

Extended Abstract

The severe reactor accident at Fukushima Daiichi confirmed the need to understand the flow and transport processes inside the containment and connected buildings in more detail to design and evaluate efficient (passive) safety concepts. At Forschungszentrum Jülich, the *containmentFOAM* CFD package, a tailored open-source solver and model library based on OpenFOAM®, is developed. Its model library is designed to be well balanced in terms of accuracy and numerical efficiency to enable R&D related to technical-scale accidental containment atmosphere mixing processes, pressurization, aerosol transport and assessment of passive safety systems.

The paper aims to recap the development and V&V status of *containmentFOAM*, outline a current application, and summarize the lessons-learned so far along with technical-scale containment CFD analysis. For this purpose, the experience gained during a recent re-assessment of the ISP-37 'VANAM M3 Multi-Compartment Aerosol Depletion Test with Hygroscopic Aerosol Material' in the Battelle Model Containment ($V \sim 626\ m^3$) is discussed. While the simulation results demonstrate the practical applicability of the CFD approach to technical-scale analysis of accident transients, they also revealed that a large part of the total computation time is spent for resolving localized, short term high momentum releases. Thus, different strategies are currently explored to model them more efficient on technical scale, e.g., by using volumetric source terms. Furthermore, a strategy is developed enable initializing a CFD analysis, in particular structure temperature fields, using (coarse) experimental data or system code results.

Concluding, the future directions, in particular with respect to an extension of the package to a volume-of-fluid (VOF) formulation and model development for iPWR-SMR applications are outlined.

Computational modeling and validation of a modified Marple cascade impactor

Vineet Kumar[1], Yadukrishnan Sasikumar[2], Rose Montgomery[1]
[1]Oak Ridge National Laboratory, One Bethel Valley Rd, Oak Ridge, TN 37831
[2]Purdue University, 610 Purdue Mall, West Lafayette, IN, 47907

Abstract

Oak Ridge National Laboratory (ORNL) is investigating respirable aerosol fractions from failed high-burnup (HBU) commercial spent nuclear fuel (SNF) rods. The work aims to characterize the source term of radioactive aerosols that could result from mechanical failure of fuel rods during storage and/or transportation. The experiment involves capturing and characterizing aerosols from a four-point bending experiment of fueled rod segments at ORNL's Irradiated Fuels Examination Laboratory. Keeping in mind the goals and restrictions of the planned experiments, a Marple cascade impactor (Series 290) with the ability to collect particles up to aerodynamic equivalent diameters of ~15 µm was tested for feasibility. The commercially available Marple cascade impactor design was modified for the experiment: the cascade inlet was replaced with a 3D-printed inlet nozzle. Collection efficiency curves were then generated with the modified impactor, and the cascade's performance was tested using ISO dust capture experiments followed by scanning electron microscope analysis of the collection and computational modeling. The current work highlights the performance testing and experimental characterization of this modified Marple impactor for SNF aerosol collection. The experimental and CFD obtained stage cut-off values are observed to be in disagreement and future work is proposed to address the inconsistencies. The data presented in the paper is also different from the original Marple impactor, pointing towards the sensitivity of the design modification.

Introduction

Consequence assessments that involve estimating and modeling the release of contamination in the event of a cladding breach during handling and storage of spent nuclear fuel (SNF) are being conducted. As part of this, experimental studies are being conducted at Oak Ridge National Laboratory (ORNL) to mechanically fail SNF rods and characterize the aerosolized particles that are dispersed in such scenarios [1]. The parameters of interest include the respirable fraction of particles, including those particles having a mean aerodynamic diameter of <10 mm, which is termed as the minimum particle size that can be inhaled and has the potential to reach human lungs [2]. Four-point bending tests to failure are conducted using commercial SNF rods and the dust-type and respirable-sized particulate released is captured by sampling the air around the test specimen. Inertial impactors are used for this experiment to efficiently sample the air in the collection box.

A candidate for the impactor setup is the commercially available Marple impactor. The commercially available Marple impactor has eight stages with cut points of 21.3 µm, 14.8 µm, 9.8 µm ,6 µm, 3.5 µm, 1.55 µm, 0.93 µm and 0.52 µm Aerodynamic Diameter (AED), specified at a flow rate of 2.1 LPM (Figure 1) [3]. Although the cut points are ideal in terms of the SNF aerosol collection experiment, the Marple impactor comes with a large opening inlet (Figure 2), which needed to be modified to connect and sample aerosols for the experimental rig at ORNL [1]. A custom inlet (Figure 3) was designed and 3D printed to replace the original inlet shown in Figure 2. However, this modification meant that there would be a change in the impactor's air flow rate and flow path, requiring re-validation of the impactor's performance. Validation of the Marple's performance and collection efficiency was performed in two steps: computationally, using computational fluid dynamics (CFD), and experimentally, using International Organization for Standardization (ISO) test dust capture and microscopic characterization. Experimental evaluations of inertial impactors involve obtaining stage-wise collection efficiency curves using monodisperse or polydisperse powders and post-experiment particle characterization using particle sizers, microscopy analysis, or spectroscopy analysis [4-7].

Figure 1: Disassembled Marple impactor (with the original inlet) with respective cut-off values for each stage.

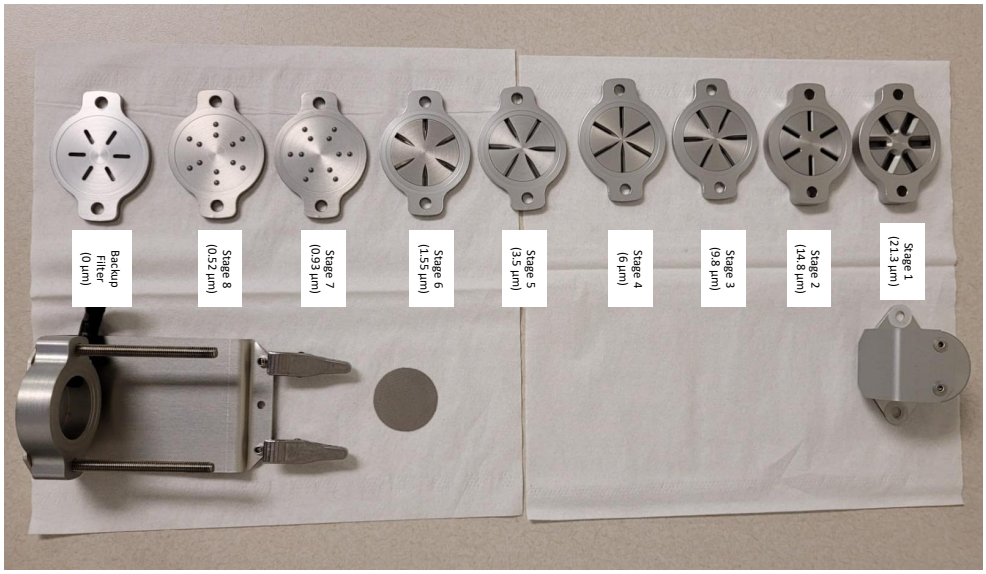

Figure 2: Inlet nozzle of the purchased Marple Impactor.

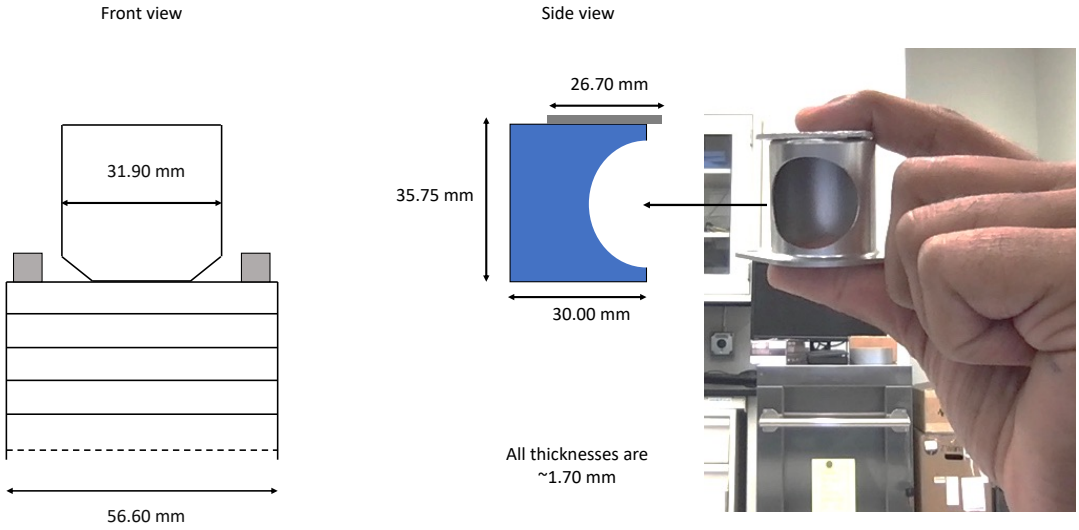

Figure 3: Designed inlet that was 3D printed for modifying the Marple Impactor.

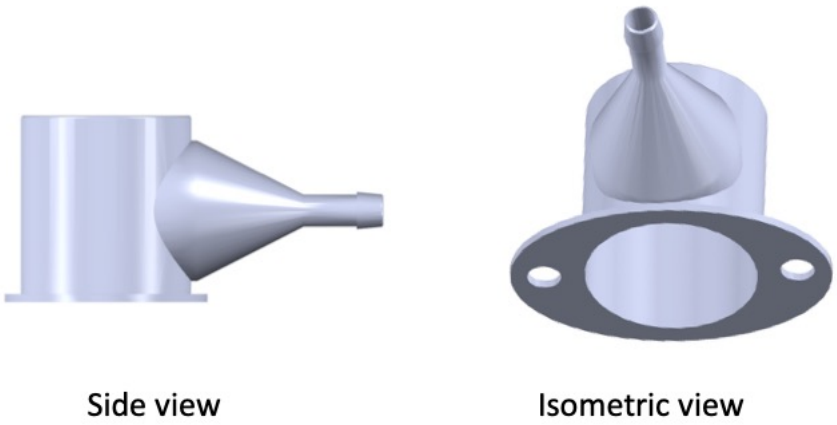

There has been an increasing focus on using CFD to evaluate the performance of cascade impactors, especially to better understand the internal flow dynamics that impact particle collection. However, most of these studies have focused on the Anderson Cascade Impactor (ACI), including scaling studies for high flow rates (28.3 LPM) [8], (28.3 & 60 LPM) [9]. The three studies ([5], [8-9]) did not simulate all the ACI stages at once because of high computational costs; therefore, they employed a stage-by-stage iterative procedure. In the vast majority of studies in the literature, the flow distribution is solved using a Eulerian approach, while a Lagrangian particle-based approach is employed to solve for particle deposition. Ohsaki et al. [10] investigated the particle motions and deposition behavior of the eight-stage AN-200 cascade impactor to evaluate the performance of dry powder inhalations using the discrete element method (DEM) as one of the approaches to model particle dynamics. The authors observed that the coupled DEM model yielded good predictions in comparison to experimental data, as it accounts for particle–particle and particle–wall collisions. In summary, no studies have analyzed the performance of the Marple impactor, nor cascade impactors in general, for the flow rates in the range of interest (2-8 LPM) for the current application.

This study focuses on the performance evaluation of the Marple cascade impactor with a modified inlet configuration to collect larger-size aerosolized UO_2 particles. The objectives of this study is threefold: (1) to experimentally characterize the performance of a Marple cascade impactor–based aerosol collection capability with a modified impactor inlet configuration, using ISO dust particles as a surrogate, (2) to model the flow distribution and particle deposition characteristics of the Marple cascade impactor with the modified inlet using the commercial CFD solver STAR-CCM+, and (3) to compare particle distribution statistics obtained using the CFD model with experimental data.

Experimental setup and design verification tests

A commercially available ISO 12103-1 A1 Ultrafine dust mixture was used to test the modified Marple impactor. The ISO dust mixture is a polydisperse mixture consisting of several compounds, including SiO_2, Al_2O_3, CaO_2, and MgO_2. The cascade was run on a setup (Figure 4) resembling the main experiment rig inside the hot cell. A manual powder dispenser was used for puffing the dust into the collection enclosure while the modified Marple impactor was sampling the enclosure. The Marple stage collector surfaces were lined with sticky carbon tapes to be imaged after collection.

Figure 4: ISO dust experimental validation test setup of the modified Marple impactor inside a fume hood.

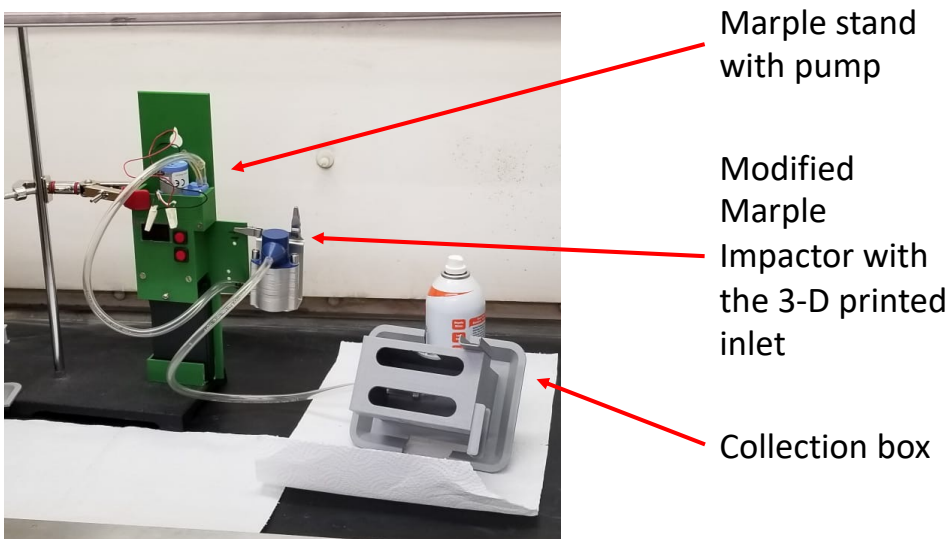

Scanning electron microscopy (SEM) was used to analyze the ISO dust collections and perform a particle size distribution of each of the Marple stages. Once the stage collections were imaged, the images were pre-processed using FIJI [11] and analyzed using MATLAB. Several methods were adopted for processing the image and ensuring that all particles were counted as separate and in full, despite being stacked up or different in contrast. The first step was to run a Trainable Weka Segmentation plugin on ImageJ to capture, identify, and outline individual particles [12]. The plugin was trained to identify the substrate and the ISO dust as separate classes, and the machine learning algorithm was run multiple times until all particles were distinguishable (Figure 5). Each image was then manually converted to a binary pixel image using ImageJ thresholding. Furthermore, binary and noise reduction operations were performed to fill holes and de-speckle, respectively. The image was then imported into MATLAB for counting using a generic particle counting script. The script also included an opening and closing morphology to ensure complete geometries for particle counting. The 'region props'

function was used on the images to obtain the mean pixel intensity, area, perimeter, centroid, and diameter of all particles. The last operation involved converting the pixel values from 'region props' into micrometers using the scaling factor employed in FIJI.

Figure 5: (a) Weka Segmentation classifiers (background and particles) used to train the machine learning model and (b) output from WEKA segmentation where all particles have been detecte

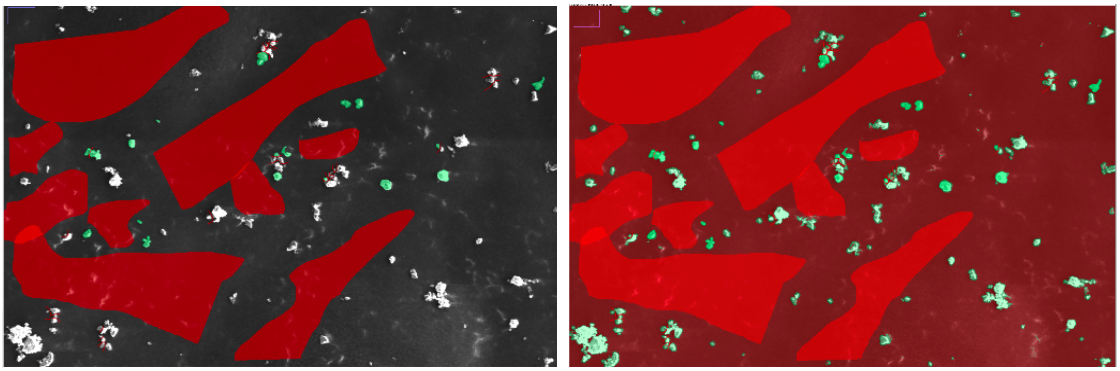

(a) **(b)**

Computational Fluid Dynamics Modeling

The flow distribution and particle deposition on the eight-stage (modified) Marple cascade impactor was investigated using the commercial CFD code, STAR-CCM+. STAR-CCM+ (Version 2021.1 Build 16.02.008) from Siemens is an American Society of Mechanical Engineers (ASME) Nuclear Quality Assurance (NQA-1)–compliant CFD solver [13]. The computational geometry consists of the modified inlet configuration (discussed in the previous section), followed by the eight stages of the Marple impactor, at the end of which is located the outlet pipe. Stage F—which is located after the eighth stage and performs the function of trapping particles that are not collected in the preceding stages—was not simulated in the computational model. The reason for ignoring stage F is that the focus of this study is on particle collection in the eight stages. Moreover, it was observed that only a few particles were found beyond stage 8 in the simulation, and no particles were observed from SEM imaging of stage F.

The CAD model of the impactor geometry was not readily available and therefore had to be recreated. As the stage pressure drop is very sensitive to the orifice dimensions, therefore additional geometry verification was performed using microscopy measurements. A side cross-section view (with respect to the impactor) of the meshed computational model is shown in Figure 6, with the inlet boundary colored in red. The eight stages can be distinguished in Figure 6 by the staggered arrangement of their orifices. In any given stage, particles are collected on the surface of the succeeding stage (i.e., perforated collector substrate in the actual system). The polyhedral mesher in STAR-CCM+ was used to mesh the complex geometry with a base size of 0.25 mm and a minimum surface size of 0. 025 mm (~0.1x of smallest dimension). Volumetric refinement was used in and around the orifice region of the final stage. The mesh convergence process involved monitoring the predicted system pressure drop in the flow simulations until negligible changes (less than 1%) were observed therein for successively refined meshes. The final mesh used for all the simulations consisted of ~4.98 million cells.

Figure 6: Slice through the computational grid on the symmetry (x = 0) plane.

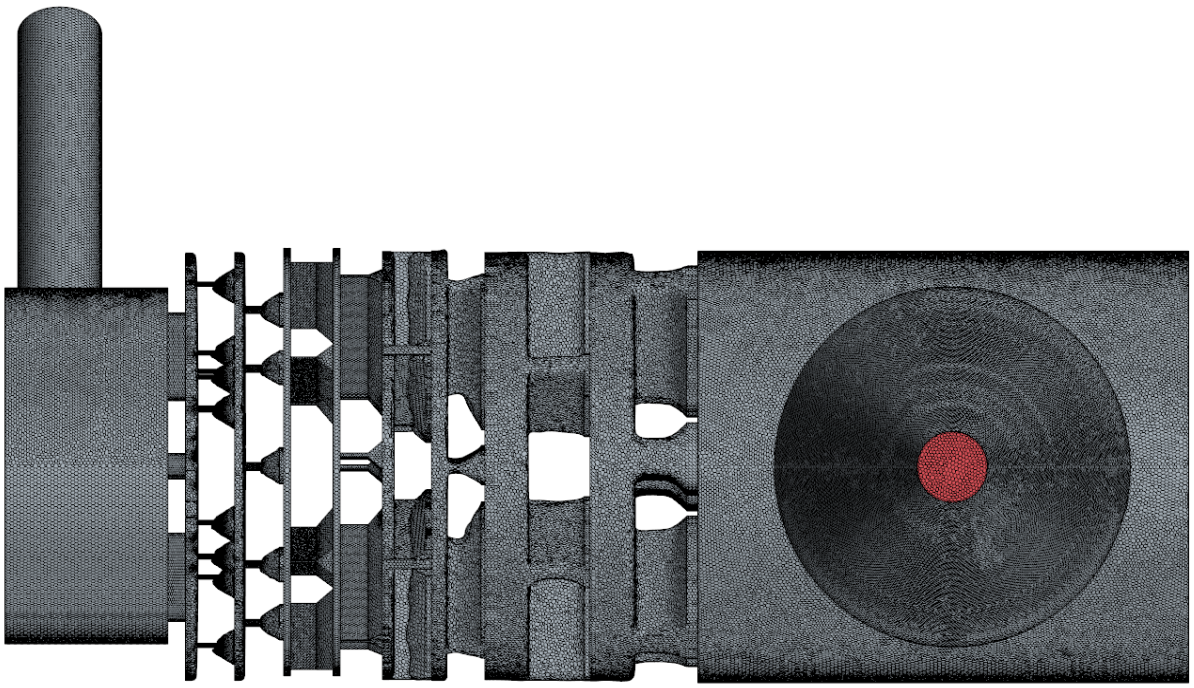

For the flow simulations, laminar flow was assumed; the coupled solver was used to solve for the continuity and momentum equations with second-order numerics, and the energy equation was not solved for. Air with constant material properties was used at atmospheric system pressure, assuming incompressible flow. The assumption of laminar flow was based on both a low inlet Reynolds number as well as low-stage (orifice) Reynolds numbers (within ~1000), at the manufacturer-recommended mass flow rate of 2.1 standard liters per minute (SLPM). Given that the flow was laminar, the mesh requirements were largely dictated by adequate mesh resolution to capture the bulk flow around the orifice region. A velocity inlet was imposed at the inlet boundary (based on ~2.1 SLPM) with the outlet boundary condition imposed at the outlet. The no-slip boundary condition was used for all the wall surfaces. The CFD simulations were run on high-performance computing (HPC) resources hosted by ORNL's Nuclear Energy and Fuel Cycle Division on 64 processors with a total runtime of ~ 1 day for the steady-state simulations, and a runtime of ~3 days for the Lagrangian particle simulations (~2.5s).

Results and Discussion

The streamline plot of the flow distribution colored by velocity magnitude is shown in Figure 7. The modification to the inlet configuration results in recirculating flow after impingement on the impactor inlet domain. Given the short distance for the flow to recover, there is considerable non-uniformity in the flow as it enters the first stage of this modified impactor. However, the flow becomes uniform further downstream. Given that the first two stages tend to filter out the bigger particles, the non-uniformity might not be a considerable factor in affecting the overall collection dynamics of the impactor. All the pressure drop and flow acceleration occurs as the flow enters the orifice. This can be observed in the pressure drop Isosurface plot shown in Figure 8 across an eighth stage orifice, where the majority of the pressure drop occurs at the entrance to the orifice. Additionally, the mean velocities in the 8^{th} stage orifices (as well as 7^{th} stage orifices) are higher in comparison to the rest of the domain. The stage and overall pressure drop comparison between the simulation and air pressure drop tests is

given in Table 1. Whereas the measurement uncertainty is included in the table for experimental data, the simulation uncertainty was not determined. From both the experimental data and simulation prediction, it can be observed that the stage pressure drop is significant only for the final two stages, with most of the pressure drop occurring in the final stage. There is a significant over-prediction in the simulation pressure drop in comparison to data for the last stage. A possible cause is the marginal differences in the orifice geometry between the actual system and the reconstructed CAD geometry; this discrepancy can be easily shown using a sensitivity analysis, which would be considered in a future study.

Figure 7: Streamline plot of the flow distribution through the eight-stage modified Marple cascade impactor colored by velocity magnitude (2.1 SLPM).

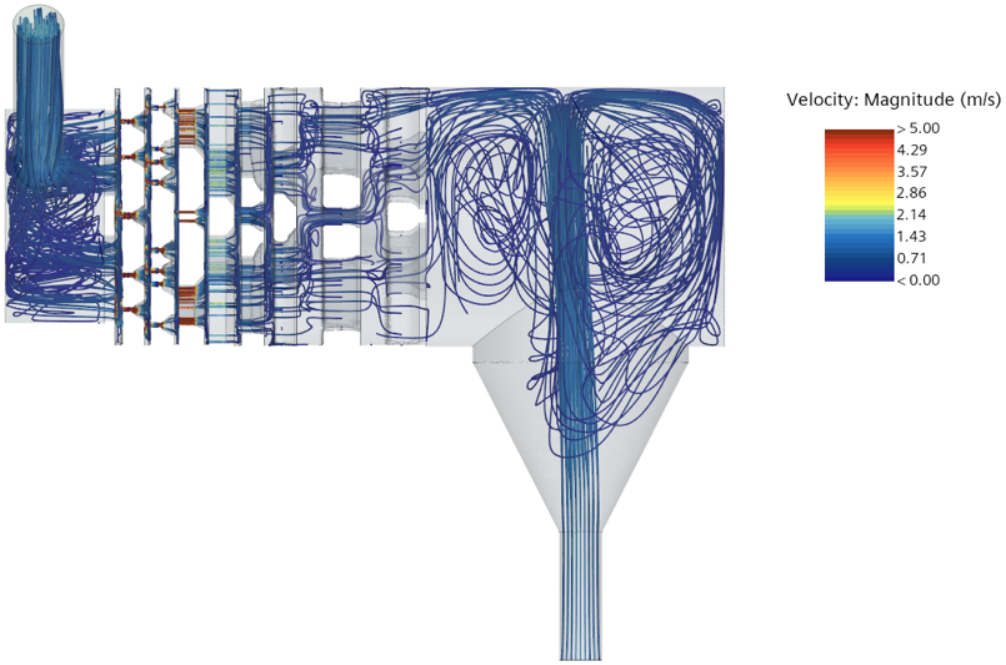

Figure 8: Pressure drop cross-section plot across an orifice in the eighth stage of the modified Marple cascade impactor.

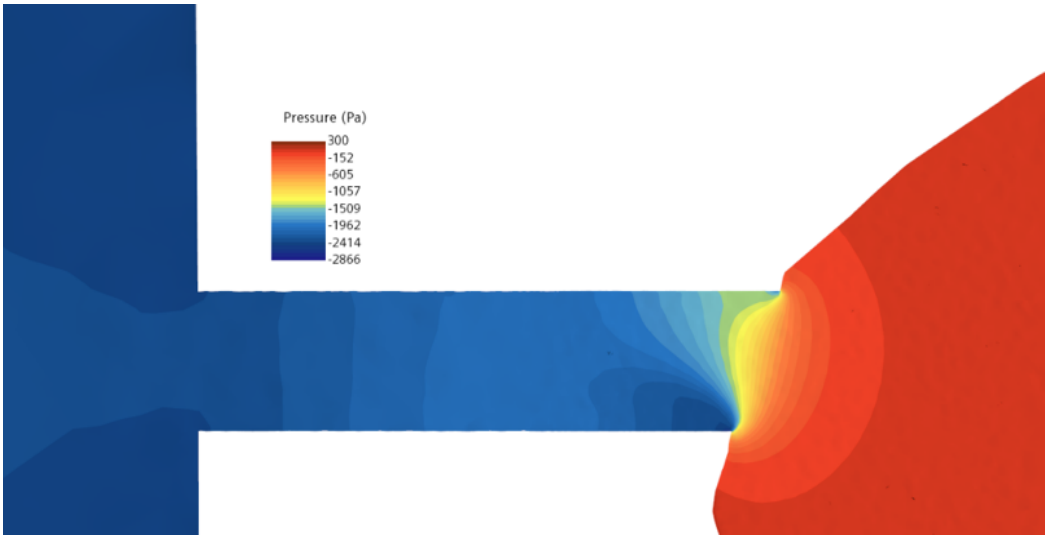

Table 1: Pressure drop comparison between experimental data and CFD for the eight-stage modified Marple impactor for 2.1 SLPM.

Location	ΔP (Exp.) (Pa)	ΔP (CFD) (Pa)
Full Stack	2316 ± 30	2694
Stage 1	0	0
Stage 2	0	0
Stage 3	0	1
Stage 4	0	2
Stage 5	0	18
Stage 6	87 ± 30	120
Stage 7	375 ± 30	327
Stage 8	1708 ± 30	2226

The Lagrangian solver was used to simulate particle deposition in the modified impactor with the standard list of surface forces and the gravity body force. One way coupling was assumed between the flow solver and the Lagrangian solver. This assumption was separately tested using the two-way coupling approach and insignificant differences were observed in the results between the two approaches. Solid UO_2 particles (ρ=10,970 kg/m^3) were injected in the inlet boundary assuming a log normal distribution with an assumed physical mean diameter of 3 µm and a range of [0.1, 10] µm. The inlet range is an estimation of the particles which enter the impactor after the rod fracture. A total of ~5.89E5 particles were injected over ~0.2 s. The total particle count was deemed to be sufficient as converged statistics were obtained for the input particle distribution. A timestep of 1E-4 s was used for the second-order implicit transient solver. The sticky boundary condition was imposed on all the collector surfaces. The collected particles in stage 1 (10× actual size) and stage 7 (100× actual size) are shown in Figures 9(a) and (b), and the particle size distribution plots are given in Figures 10(a) and (b). Stage 1 collects particles of various sizes, whereas stage 7 has a sharper diameter distribution. The collection efficiency curves are shown for stage 1 and stage 7 in Figures 11(a) and (b). These curves are cumulative distribution functions calculated from (fitted) probability density functions of the particle size distributions. The comparison of the stage cut points from the CFD results (d_{50} from collection curves) with the analytical correlation [14] and manufacturer data are shown in Figure 12. The d_{50} obtained from CFD is consistently higher than d_{50}s from analytical and manufacturer data, which could be due to the inlet modification in the current work.

Figure 9: CFD-predicted particle collection (scaled physical particle sizes) on (a) Stage 1 (b) Stage 7.

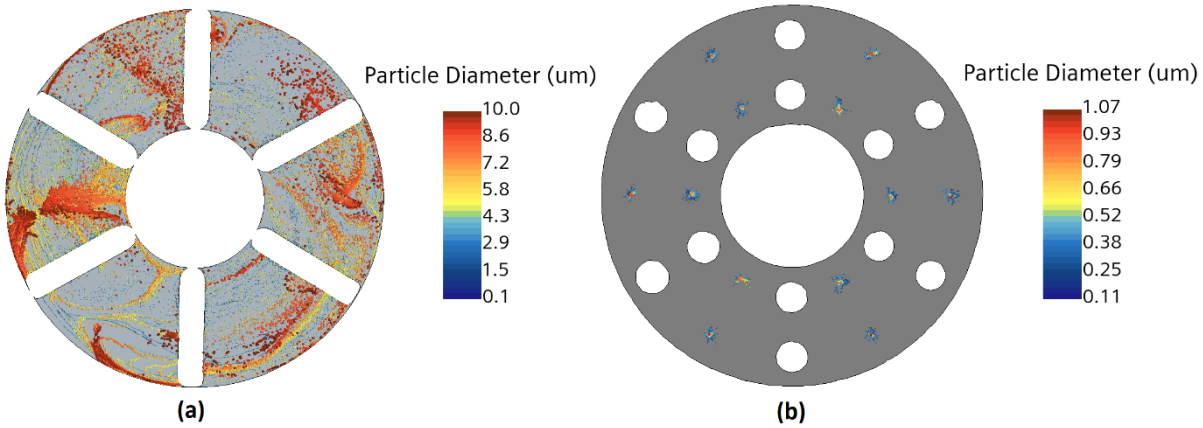

Figure 10: CFD-predicted particle physical diameter frequency distribution for (a) Stage 1 (b) Stage 7.

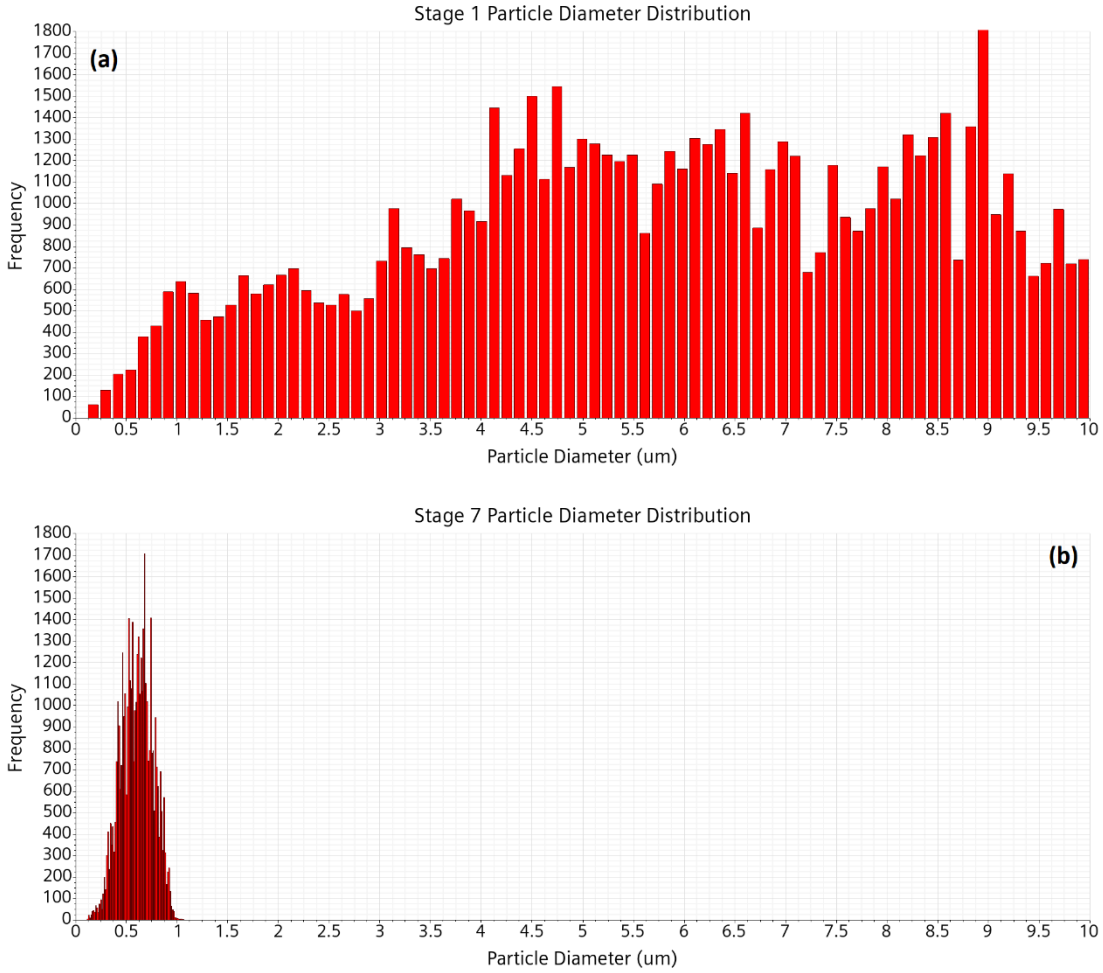

Figure 11: Collection Efficiency curves (AED) obtained by CFD with the stage cut-off shown in red for (a) Stage 1 (b) Stage 7.

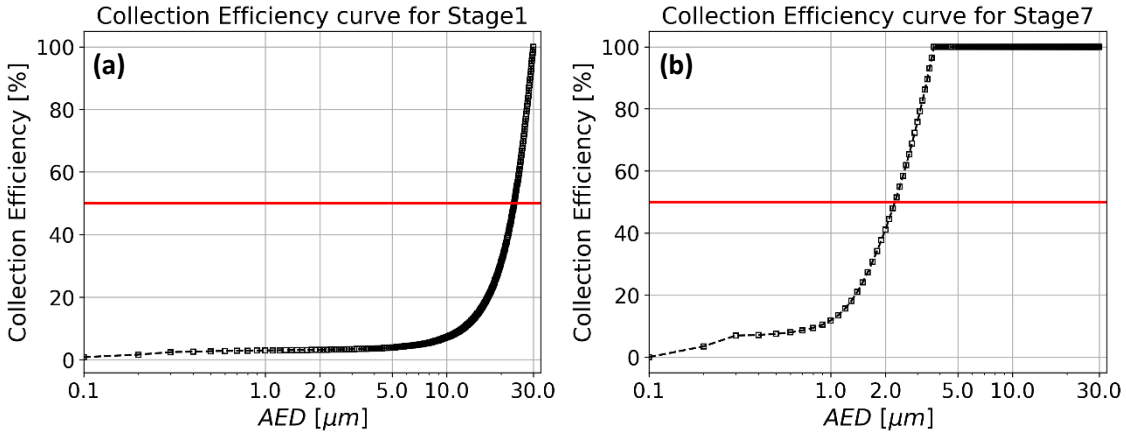

Figure 12: Comparison of stage cut points (AED) obtained by CFD, manufacturer data [9], and analytical correlation [14].

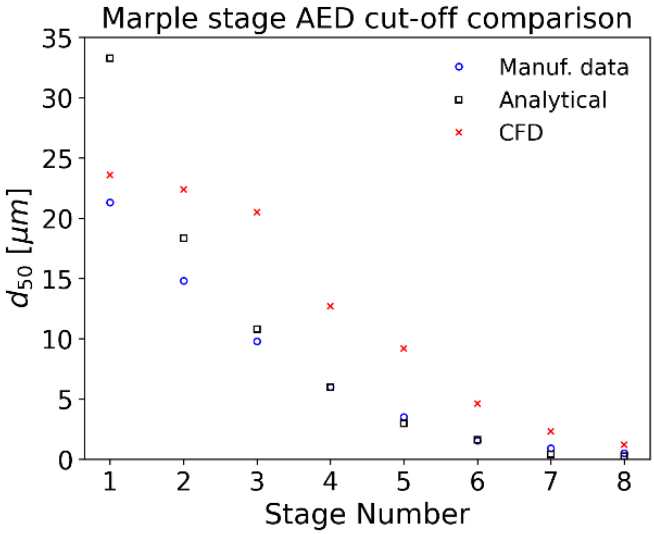

The experimentally obtained and CFD-predicted cut points at 50% collection efficiency for the modified Marple impactor are presented in Table 2, along with the manufacturer determined cut points of the original Marple impactor. The cut-off values are seen to decrease in the lower stages. As seen from the table, the values obtained are higher from the rated cut-off values for both the experimental results and the CFD predictions, with the exception of experimental results from Stage 1. Stage 1 is assumed to simply act as a prefilter to collect large debris from the inlet and the variations can be understood to be a result of the non-uniformity in the flow as it enters the impactor due to the modification (Figure 7). The experimentally determined cut-off values for all stages except Stage 2 are seen to be lower than the CFD predictions. The reason behind the differences could be due to the large uncertainties in the ISO dust particle size distribution [1]. The higher experimental value in Stage 2 can be attributed to the agglomerations in the collected particles that were counted as bigger blobs due to limitations in image processing and counting procedures—both of which are being addressed under the future work scope. From the CFD perspective, DEM would be considered for Lagrangian modeling as it accounts for particle-particle interactions, as well as more physical particle-wall interactions.

Table 2: Cut-off points predicted by experimental image processing and the CFD model of the modified Marple impactor.

Location	$d_{50,Exp}$ (µm)	$d_{50,CFD}$ (µm)	$d_{50,Manuf}$ (µm)
Stage 1	7.3	23.6	21.30
Stage 2	29.8	22.4	14.80
Stage 3	14.3	20.5	9.80
Stage 4	11.3	12.7	6.00
Stage 5	6.8	9.2	3.50
Stage 6	3.8	4.6	1.55
Stage 7	1.8	2.3	0.93
Stage 8	0.8	1.2	0.52

Conclusions

The performance of the Marple cascade impactor with a modified inlet configuration was evaluated to sample a range of respirable aerosolized UO_2 particles using surrogate SNF aerosol particles. For the purposes of a preliminary evaluation study, ISO dust particles with a similar AED range were used as a surrogate for radioactive UO_2 particles. Simultaneously, a CFD model of the Marple impactor was also constructed using STAR-CCM+ to study the flow distribution and the particle deposition characteristics with the modified inlet. The CFD model predicted a non-uniform flow distribution—especially for the first stage because of the modified inlet configuration. The CFD model also predicted stage 1 to collect a range of particle sizes as well as trapping the majority of the larger particle sizes, as expected. The results obtained from image processing of the ISO dust particles from the collection substrates were compared with simulation predictions as well as manufacturer data. Although the D50 cut points decreased in the experimentally determined cut-off diameters and the CFD predictions, there are differences between the two approaches. This difference can be understood as a consequence of the choice of dust used in the experiments and the agglomeration tendencies of ISO dust that was not modelled in the CFD approach. Future work will look into alternate design changes (including different inlet configurations) and addressing the disagreement between the experimental and CFD results by using monodisperse dust for experiments and charged particle simulations (to model agglomerations) for CFD. The post-processing difficulties of the verification experiments related to identifying layered particles will be addressed by using advanced image processing techniques while also looking at the DEM model to improve CFD predictions.

References

[1] Montgomery, R., *et al*., *Sister Rod Destructive Examinations (FY20) Appendix I: SNF Aerosols Released During Rod Fracture*, ORNL, doi: 10.2172/1864438, March (2022).

[2] NUREG-2125, Spent Fuel Transportation Risk Assessment, Final Report, 2014, pp. E21-22.

[3] M. I. Operator's Manual, "Marple Style Personal Cascade Impactors 290 Series Operators Manual." (2003) .

[4] Nöel, A., *et al.*, "Assessment of the contribution of electron microscopy to nanoparticle characterization sampled with two cascade impactors", *J. Occup. Environ. Hyg*., vol. 10, no. 3, pp. 155–172, doi: 10.1080/15459624.2012.760391, March (2013).

[5] Dechraksa, J., *et al.,* "Deposition Pattern of Polydisperse Dry Powders in Andersen Cascade Impactor - Aerodynamic Assessment for Inhalation Experimentally and In Silico", *Turkish J. Pharm. Sci.*, vol. 17, no. 1, p. 20, doi: 10.4274/TJPS.GALENOS.2018.15870 (2020).

[6] Marple, V. A., *et al.,* "A Microorifice Uniform Deposit Impactor (MOUDI): Description, Calibration, and Use", *Aerosol since and Technology*, vol. 14, no. 4, pp. 434–436, doi: 10.1080/02786829108959504 (1990).

[7] Demokritou, P., *et al.*, "Development and Laboratory Performance Evaluation of a Personal Cascade Impactor", *Journal of the Air & Waste Management Association*, vol. 52, no. 10, pp. 1230–1237, doi: 10.1080/10473289.2002.10470855 (2011).

[8] Vinchurkar, S., *et al.*, "CFD simulations of the Andersen cascade impactor: Model development and effects of aerosol charge", *J. Aerosol Sci*., vol. 40, no. 9, pp. 807–822, doi: 10.1016/J.JAEROSCI.2009.05.005 (2009).

[9] Flynn, S. J., *et al.*, "Computational fluid dynamics (CFD) investigation of the gas–solid flow

and performance of Andersen cascade impactor", *Powder Technol*., vol. 285, pp. 128–137, doi: 10.1016/J.POWTEC.2015.03.039 (2015).

[10] Ohsaki, S., *et al.*, "Numerical Simulation of Particle Motions in Cascade Impactor and Human Respiratory System", MATEC Web Conf., vol. 333, p. 02013, doi: 10.1051/MATECCONF/202133302013 (2021).

[11] Schindelin, J., *et al.*, "Fiji: an open-source platform for biological-image analysis," Nat. Methods 2012 97, vol. 9, no. 7, pp. 676–682, doi: 10.1038/nmeth.2019 (2012).

[12] Arganda-Carreras, I., *et al.*, "Trainable Weka Segmentation: a machine learning tool for microscopy pixel classification", *Bioinformatics*, vol. 33, no. 15, pp. 2424–2426, doi: 10.1093/BIOINFORMATICS/BTX180 (2017).

[13] SIEMENS, "STAR-CCM+ Simcenter Documentation", (2021).

[14] Hinds, W., "Aerosol Technology Properties, Behavior, and Measurement of Airborne Particles Second Edition", (2012).

EXPERIMENTAL INVESTIGATION OF BUBBLE HYDRODYNAMICS IN THE GLOBULE REGIME INSIDE A SHALLOW POOL

Nabil GHENDOUR[1], Detlef SUCKOW[1], Abdelouahab DEHBI[1], Michael KLAUCK[2]

[1] Paul Scherrer Institute, Villigen, Switzerland
[2] Forschungszentrum Jülich GmbH, Germany

Extended Abstract:

To prevent the release of radioactive Fission Products (FP) from the degraded fuel following severe accidents, nuclear reactors have been designed and equipped with different barriers and safety systems. The wet Filtered Containment Venting System (FCVS) is widely used as the last protection stage to avoid overpressure failure of the containment in case of reactor pressure vessel (RPV) failure. This system consists of a vessel filled with water, in which the contaminated gas is injected to decrease atmospheric pressure in the containment. By bubbling the contaminated gas in the water pool, a large fraction of radioactive FP can be scrubbed. Analyzing the release, transport, and retention of these FP inside the pool is a fundamental step toward evaluating the efficiency of the FCVS. Current models to predict FP particle removal rates in pools are as empirical as uncertain. However, a more rigorous treatment is now possible via Computational Fluid Dynamics (CFD) which has recently become a mature tool for slow momentum two-phase flows.

Since the transport of particle removal depends on bubble hydrodynamics, this work aims to provide a comprehensive database on submerged nozzle experiments in a shallow pool in order to enhance hydrodynamics and particle removal models used in 1D pool scrubbing codes. The focus is on two-phase flow bubble hydrodynamics near the injector region, where most of the aerosol mass is removed. The experiments are performed in the large-scale TRISTAN facility, which has a 50×50 cm cross-section and height of 6 m. The facility is equipped with a High-Speed Camera (HSC) and two large Wire Mesh Sensors (WMS) of 128×128 wires. The nozzle used has a diameter of 10 mm and is submerged 300 mm below the water surface. The mass flow rate of the injected Nitrogen ranges from 1 to 10 l_n/min. Fifty (50) tests in total were performed for the HSC experiments and WMS experiments at three different distances from the nozzle tip (40, 100, and 200 mm).

The HSC images show that the flow is in the aperiodic globule regime, and is characterized by intensive globule coalescence and break-up. These phenomena are enhanced when the flow rate increases. For instance, at a flow rate of 10 l_n/min, a coalescence of more than two globules at the injection region is observed. The images show also the significant effect of the wake on the bubbles' behavior and globule formation. The local time-averaged Gas Void Fraction (GVF) is calculated from the HSC images. It is found that the GVF is higher (GVF≈1) in the injection region due to the quick succession of globules formation. The globule detachment frequency becomes independent of gas flow rate when the latter exceeds 5 l_n/min. However, the size and velocity of the detached globule are still proportional to the flow rate.

The analysis of WMS data reveals a similar trend for the GVF distribution compared to the values obtained from HSC images. The effect of the flow rate on the GVF distribution is also investigated. It is observed that an increase in the flow rate yields a growth of the void and a rise in its maximum value. The profile of the time-averaged velocity along horizontal lines shows the highest values at the center. Velocities reach up to 1.2 m/s for a flow rate of 10 l_n/min.

The next phase of our work involves aerosol retention experiments under the same test conditions as the hydrodynamics tests using the large-scale SAAB test facility at Forschungszentrum Jülich, Germany. Finally, we will conduct CFD validation simulations against collected data using our in-house code PSI-BOIL and Ansys FLUENT™.

Simulation of noble metal particle growth and removal in the molten salt fast reactor

Edo Frederix[1], **Ed Komen**[1]
[1]Nuclear Research and Consultancy Group (NRG),
Westerduinweg 3, 1755 LE, Petten,
the Netherlands

Abstract

In the Molten Salt Fast Reactor (MSFR), fuel is dissolved in a liquid salt, causing the formation and decay of fission products, such as noble metals, inside the salt. Noble metals have very low solubility and do not dissolve in the salt. They are known to agglomerate into particles which, in turn, diffuse, drift or sediment to interfaces such as walls, free surfaces and bubbles, where they deposit. Leveraging this in the MSFR, online or offline helium bubbling is foreseen to act as a means to extract noble metal particles from the salt. This can potentially limit strong deposition of particles onto walls (i.e., plating), preventing dangerous decay heat hotspots in the heat exchangers or other primary circuit components. In this paper, we investigate the efficiency of particle removal by helium bubbles in the MSFR using CFD modelling. Theoretical estimates of equilibrium particle size distributions are used as initial condition. CFD calculations are performed in a simplified MSFR geometry. Bubble expansion, turbulent bubble coalescence and turbulent break-up are accounted for using the poly-disperse LogMoM model [1], embedded in the two-fluid framework in OpenFOAM. The CFD analyses presented in this paper, in conjunction with the developed theory of noble metal particle formation, growth and capture, will help in the understanding and optimization of the fuel cycle in the MSFR or any other molten salt reactor design. The precise knowledge of how noble metal particle populations in the salt can be controlled, and how plating of noble metal particles onto primary circuit reactor components can be reduced, contributes to safe molten salt reactor operation.

Introduction

In the Molten Salt Fast Reactor (MSFR) [2], fuel is dissolved in a liquid salt, causing the formation and decay of fission products inside the salt. Some of these fission products are salt seekers and dissolve in the salt by forming stable bonds with fluorine. Other products, being noble gases and noble metals, have very low solubility and do not dissolve in the salt [3]. Noble metal atoms are known to agglomerate into particles which, in turn, diffuse, drift or sediment to interfaces such as walls, free surfaces and bubbles, where they deposit. Leveraging this in the MSFR, online or offline helium bubbling is foreseen to act as a means to extract noble metal particles from the salt [4]. This can potentially limit plating, preventing dangerous decay heat hot spots in the heat exchangers or other primary circuit components. However, currently the knowledge on the quantitative behavior of noble metal particles in the MSFR is unknown from both an experimental as well as modeling point of view.

The mechanics of noble metal particle flotation in the MSFR, as it is currently understood, involves a complex interplay of noble metal atom formation by fission and decay, particle growth by coagulation, and particle capture by interfaces driven by Brownian diffusion, sedimentation or interception. Particle capture efficiency depends strongly on particle size. Small particles, having a diameter in the range of the nanometer scale, tend to diffusive more efficiently towards bubbles due to Brownian motion [5]. Larger particles, in the range of the micrometer scale and beyond, tend to sediment or drift due to inertial effects towards bubbles more efficiently [6]. The balance of this interplay of physics determines key integral properties of the system such as equilibrium particle size and noble metal atom cycle time, the latter being an import input parameter to salt inventory calculations.

In this paper, we investigate the efficiency of particle removal by helium bubbles in the MSFR using CFD modelling. At steady-state operation, an estimate of the noble metal particle population can be calculated using homogeneous theory [7], incorporating particle formation, growth and removal. However, this theory depends on the behavior of helium bubbles in the MSFR, in terms of mean void fractions and bubble sizes. Preliminary CFD calculations are performed in a simplified MSFR geometry, in order to compute the mean bubble void fraction and size as a function of superficial inlet velocity and inlet size. Bubble expansion, turbulent bubble coalescence and turbulent break-up are accounted for using the poly-disperse LogMoM model [1], embedded in the two-fluid framework in OpenFOAM. A large number of CFD simulations spanning the input parameter space produce a correlation between superficial bubble inlet velocity on one hand, and the mean bubble void fraction and mean particle size on the other. In turn, this correlation is used to calculate the equilibrium noble metal particle size distribution residing in the reactor at steady-state conditions, from homogeneous theory. Finally, these size distributions are used as initial condition for transient CFD simulations, incorporating both diffusional and hydrodynamic flotation. From the decay rate of noble metal mass in the system, cycle times may be inferred.

The CFD analysis presented in this paper, in conjunction with the developed theory of noble metal particle formation, growth and capture, will help in the understanding and optimization of the fuel cycle in the MSFR or any other molten salt reactor design. The precise knowledge of how noble metal particle populations in the salt can be controlled, and how plating of noble metal particles onto primary circuit reactor components can be reduced, contributes to safe molten salt reactor operation.

Three-phase flotation model

The problem of noble metal particle flotation is essentially governed by the interaction of three phases: gas bubbles, liquid molten salt and solid noble metal particles. To model this three-phase system, a combination of numerical methods is made. This is described in [8]. Here, we briefly recollect the main features of the three-phase flotation model.

Conservation equations for mass, momentum, energy and particles

For the gas−liquid mixture, the two-fluid model is adopted. The two-fluid model, retaining a full coupling between both phases, is needed because compressibility of bubbles may play an important role in the fluid mechanics of an MSR design as a whole [9] and because the coupling between salt and gas will be strong as a result of high void fractions. The behavior of noble metal particles, on the other hand, is modeled using a passive Eulerian approach that is one-way coupled to the gas−liquid mixture. This is a reasonable simplification because the volume fraction of particles in the reactor is expected to be extremely small making the salt and bubbles relatively unaware of the presence of particles, thus requiring no explicit coupling between particles on one hand and the gas–liquid mixture on the other.

Starting with the two-fluid model [10], we identify the liquid salt phase ℓ and the gas phase g, which have a local volume fraction α, velocity $\mathbf{u}$ and mass density ρ. For $k \in (\ell,g)$, we have an equation for the conservation of mass, i.e.,

$$\frac{\partial \rho_k \alpha_k}{\partial t} + \nabla \cdot (\rho_k \alpha_k \mathbf{u}_k) = \Lambda_k, \tag{1}$$

with interfacial mass transfer term Λ_k which is zero for helium bubbles in salt. Next, we have an equation for the conservation of momentum, i.e.,

$$\frac{\partial \rho_k \alpha_k \mathbf{u}_k}{\partial t} + \nabla \cdot (\rho_k \alpha_k \mathbf{u}_k \mathbf{u}_k) = -\alpha_k \nabla p + \nabla \cdot \left[\alpha_k (\mathbf{T}_k + \mathbf{T}_k^t\right] + \rho_k \alpha_k \mathbf{g} + \mathbf{M}_i, \tag{2}$$

with phase k viscous and turbulent stress tensors $\mathbf{T}_k$ and $\mathbf{T}_k^t$, respectively, mixture pressure p, gravitational acceleration $\mathbf{g}$ and phase k interfacial momentum transfer term $\mathbf{M}_k$ which also satisfies $\mathbf{M}_\ell = \mathbf{M}_g$. Finally, the phase k energy conservation equation is given by

$$\frac{\partial \rho_k \alpha_k e_k}{\partial t} + \nabla \cdot (\alpha_k \rho_k e_k \mathbf{u}_k) = -\nabla \cdot \left[\alpha_k (\mathbf{q}_k + \mathbf{q}_l^t\right] + \nabla \cdot (\alpha_k \boldsymbol{\tau}_k \cdot \mathbf{u}_k) + \rho_k \alpha_k \mathbf{g} \cdot \mathbf{u}_k + E_k, \tag{3}$$

with phase k internal energy e_k, laminar and turbulent heat fluxes $\mathbf{q}_k$ and $\mathbf{q}_k{}^t$, total stress tensor $\boldsymbol{\tau}_k = -p_k\mathbf{I}_k + \mathbf{T}_k$ and interfacial energy transfer term E_k which, just like the interfacial mass and momentum transfer terms, satisfies $E_\ell = -E_g$. The system (1–3) is closed by the selection of a suitable equation of state, constitutive relations for the viscous stress tensor and heat flux, a turbulence model for the turbulent stress and turbulent heat flux and appropriate models for the interfacial mass, momentum and energy transfer terms. The selection of these models will be discussed later on. For more details on the two-fluid model, the reader is referred to Ishii & Hibiki [10] or Drew & Passman [11].

Noble metal particles are modeled in a poly-disperse way, meaning that the full size distribution of particles is considered. We distinguish between a ‘free’ particle population $n_f(d)$ of which member particles are suspended in the salt and are free to diffuse or sediment, and a ‘captured’ particle population $n_c(d)$ of which member particles are attached to a bubble and move along with that bubble. Here, d is

the particle diameter. We use a simple sectional discretization of the particle size domain, so that both distributions are represented by a finite collection of Dirac delta functions, each of which describing the concentration of particles at a distinct and fixed particle diameter d_i. More precisely, if we let $n_j(d)$ be a population with $j \in (f,c)$ defined in such a way that $n_j(d)\mathrm{d}d$ gives the total number of type j particles per unit volume in the size range $[d, d + \mathrm{d}d]$, then it is approximated by

$$n_j(d) = \sum_i N_{i,j}\delta(d_i - d), \tag{4}$$

with $N_{i,j}$ the number concentration of type j particles having size d_i. Conversely, if we integrate $n_j(d)$ over a section defined by, for example, the range $[(d_{i\text{-}1} + d_i)/2, (d_i + d_{i+1})/2]$, then we obtain $N_{i,j}$. Such an integration can be applied to the population balance equation modeling the dynamics of the complete population (e.g., see [12−14]), and results in

$$\frac{\partial N_{i,j}}{\partial t} + \nabla \cdot (\mathbf{v}_{i,j} N_{i,j}) = \nabla \cdot (D_{i,j} \nabla N_{i,j}) + S_{i,j}, \tag{5}$$

with particle velocity $\mathbf{v}_{i,j}$, particle diffusivity $D_{i,j}$ and source term $S_{i,j}$, all three for type j particles in section i. The velocity of free particles must be modeled by taking into account their inertia, drag imposed by salt, gravity and other forces exerted onto the particles. Moreover, the free particle velocity is a function of particle size. A simple algebraic 'local equilibrium' model for the particle velocity can be used, incorporating inertia, Stokes drag and gravity, see [8]. It is given by

$$\mathbf{v}_{i,f} = \mathbf{u}_\ell + [(1 - \rho_\ell/\rho_p)\mathbf{g} - \mathrm{d}\mathbf{u}_\ell/\mathrm{d}t)]\,\tau_p, \tag{6}$$

with particle mass density ρ_p and Stokes relaxation time τ_p. This model is suitable only for very low particle Reynolds numbers, an assumption which is expected to hold because particles will not exceed the micron scale. The free particle diffusivity can be modeled using the Stokes-Einstein relation. Captured particles move with the gas phase, meaning that $\mathbf{v}_{i,c} = \mathbf{u}_g$ and $D_{i,c} = 0$ for all i. Finally, the source term $S_{i,j}$ accounts for the transfer of particles between the free and the captured populations, through flotation. Additionally, it can also account for new particle formation due to precursor decay or fission, loss due to decay, or changes in the population due to particle coagulation. However, in this work these contributions are ignored, as we will only consider the removal rates of particles from an initial population that is at an equilibrium as predicted by homogeneous theory. Returning to the process of particle transfer by flotation, the source term for free particles can be modeled as [6]

$$S_{i,f} = -(H_i P_{\mathrm{col},i} P_{\mathrm{ad},i} P_{\mathrm{stab},i} + D_i) N_{i,f} N_b, \tag{7}$$

with H_i the hydrodynamic flotation rate, D_i the diffusive flotation rate, N_b the number concentration of bubbles and $P_{\mathrm{col},i}$, $P_{\mathrm{ad},i}$ and $P_{\mathrm{stab},i}$ the efficiencies of collision, adhesion and stabilization, which will be explained momentarily. The hydrodynamic flotation part of (7) represents 'classical' flotation by means of particle inertia and sedimentation leading to interception, which is relevant for relatively large particles with sizes just below the micro scale and beyond. The diffusive flotation part is not as commonly considered in flotation theory, and is relevant mostly for relatively small particles with sizes around the micro scale and below (for example, see [5]). The source term for captured particles is simply given by $S_{i,c} = -S_{i,f}$. Next, we will shortly discuss the models for hydrodynamic and diffusional flotation.

Hydrodynamic and diffusional flotation theory

Starting from classical hydrodynamic flotation theory, if we consider a spherical bubble then the rate at which it would collect particles if those particles were not to change trajectory is given by [6]

$$H_i = \frac{\pi}{4}(d_b + d_i)^2 |\mathbf{v}_{i,f} - \mathbf{u}_g|. \tag{8}$$

with bubble diameter d_b, which is simply the frontal area of interception of the bubble multiplied by the relative velocity magnitude. This would be the ideal rate of flotation. In practice, particles will be pushed away by the salt flow around the bubble, reducing the number of particles in the path of the bubble that will collide with it. To account for this, the collision efficiency P_{col} is introduced. Subsequently, when particles collide with a bubble, they may not necessarily attach to the bubble. The fraction of particles colliding with the bubble and attaching to it is usually smaller than unity, and is modeled by $P_{\text{ad},i}$. Finally, attached particles can form a bond with the bubble that is not stable and may be shed by the bubble again. This is accounted for by the efficiency of stabilization, $P_{\text{stab},i}$. All these three efficiencies are subject to a vast amount of flotation research, e.g., see Nguyen & Schulze [6]. Here, we use the model of Yoon & Luttrell [15] for P_{col} and $P_{\text{ad},i}$. This model is applicable to finite non-zero Reynolds number flow around the bubbles. Moreover, we assume that the efficiency of stabilization, $P_{\text{stab},i}$, is unity as a result of the low solubility of noble metals in salt. Thus, we have

$$P_{\text{col},i} = \frac{3}{2}\left(1 + \frac{8\text{Re}_b^{0.72}}{45}\right)\frac{d_i^2}{d_b^2}, \tag{9}$$

$$P_{\text{ad},i} = \sin^2\left[2\ \arctan\left\{\exp\left(-P_{\text{col},i}\Gamma_i\frac{d_b}{d_i}\right)\right\}\right] \qquad \text{and} \tag{10}$$

$$P_{\text{stab},i} = 1 \tag{11}$$

with bubble Reynolds number Re_b and the non-dimensional coefficient Γ_i given by

$$\Gamma_i = \frac{2|\mathbf{u}_g - \mathbf{u}_\ell|\tau_i}{d_i + d_b}, \tag{12}$$

with induction time τ_i. The induction time is essentially a parameter that embodies the complex interplay of microscopic forces acting on the bubble interface, salt and particle leading to adhesion of particles. From the experiments of Dai et al. [16] we have $t_{\text{ind},i} = Ad_i^B$ with $A = 0.05$ and $B = 0.6$.

The diffusional flotation part of (7) is represented by the flotation rate D_i. Following what was done in [7], it is given by

$$D_i = \pi \text{Sh}_i d_b \mathcal{D}_i, \tag{13}$$

with Sherwood number Sh_i and particle diffusivity $\mathcal{D}_i$. The diffusivity is given by the Stokes-Einstein relation, i.e.,

$$\mathcal{D}_i = \frac{k_B T}{3\pi\mu_\ell d_i} \tag{14}$$

with Boltzmann's constant k_B, temperature T and salt dynamic viscosity μ_ℓ. The Sherwood number is modeled using the Ranz-Marshall relation [17], given by

$$\mathrm{Sh}_i = 2.0 + 0.6\sqrt{\mathrm{Re}_b}\sqrt[3]{\mathrm{Sc}_i}, \tag{15}$$

with Sc_i the Schmidt number given by $\mathrm{Sc}_i = \nu_\ell / \mathcal{D}_i$ where ν_ℓ is the salt kinematic viscosity. The Ranz-Marshall model was originally developed for evaporating drops, but also holds validity for colloidal mass transfer in light of the diffusive nature of the transfer process. Moreover, in the MSRE it was observed that noble metals migrate according to the simplest form of mass transfer theory [3,18,19], which gives further credence to the validity of this analogy.

Log-normal method of moments for bubbles

Bubbles are injected into the bottom of the reactor vessel at a certain size. Depending on that size, their number and local turbulent conditions, they will undergo coalescence or break-up. Moreover, with decreasing pressures higher up in the vessel, they will expand. Therefore, the evolution of the bubble population subject to these effects must be modeled. For this, we use the Log-normal Method of Moments (LogMoM), developed in [1,20]. The method assumes that the bubble size distribution has a log-normal shape. The log-normal function has three degrees of freedom: its width, height and offset. The function is closed by the solution of three independent moment transport equations (number, interfacial area and volume concentrations) which are obtained from the bubble population balance equation, by integration. The integration of the coalescence and break-up terms is done using Gauss quadrature, which makes the approach very versatile and able to deal with complicated break-up and coalescence kernels. Special attention is paid to the consistent integration of the break-up term, assuring a source term that is always non-negative. From the solution of the three moment equations, LogMoM produces the full bubble size distribution from which the Sauter mean diameter can be calculated. In turn, the Sauter mean diameter is fed to all closure models that require information of the size of bubbles, such as the drag model for bubbles or the hydrodynamic and diffusional flotation rates.

This, then, completes the short description of the main features of the mathematical three-phase model. We now continue with the description of the simulation setup for particle flotation in the MSFR.

Simulation setup of particle flotation in the MSFR

The model as discussed above is implemented in OpenFOAM-9. The two-fluid model is solved using the standard multiphaseEulerFoam solver of OpenFOAM. A separate library called flotationFoam is developed for the modeling of the free and captured particle populations. This library can be dynamically linked against the standard multiphaseEulerFoam solver of OpenFOAM, therewith avoiding any modification of standard OpenFOAM code. In this Section, we describe the simulation setup of particle flotation in the MSFR, using OpenFOAM.

Simplified geometry of the MSFR

The MSFR is envisioned to be a cylindrical vessel in which molten salt is circulated by means of both natural convection and forced convection. Previously, within the EVOL project, studies have been performed on the specific design of the vessel in order to promote mixing and reduce temperature peaking, see for example [21]. This led to a complex design with a curved core cavity shape and a number of radial channels in which a heat exchanger and pump are placed, cooling the salt and re-injecting it again at the bottom of the vessel. The proper simulation of this geometry requires a full three-dimensional mesh of at least one periodic slice of the domain. Instead, here a simplified axisymmetric

geometry is considered, that was also used by Caruggi et al. [22] to study gaseous fission product removal rates. Because of the axial symmetry, it is sufficient that only a two-dimensional wedge of the full geometry is simulated. This two-dimensional wedge is shown in Figure 1. A wedge angle of 5° is chosen, conform OpenFOAM's recommendation for wedge geometry simulations. The domain consists of a vessel cavity (shaded by stripes in Figure 1), which is connected to a pump and heat exchanger region (shaded by blue and red). The dimensions of the geometry are indicated in Figure 1, where it is noted that the inlet and outlet of the heat exchanger and pump channel are equal in height and width. Bubbles are injected from the bottom, and the salt-bubble mixture is allowed to expand into an expansion tank as indicated. Bubbles and captured particles attached to them are removed from the salt mixture once they reach the region shaded in green, such that no bubbles or captured particles are recirculated. The heat exchanger is modeled by a sink term that brings the temperature back to the desired inlet temperature. The effect of the pump is represented by a momentum source that establishes the desired flow rate of salt. The inlet mass flow rate of bubbles is controlled by specification of the inlet velocity $\mathbf{u}_g$ at a constant void fraction of 10%. Boundary conditions are the standard ones for wall bounded flow. At the outlet the pressure is fixed at atmospheric pressure and a zero-gradient condition is applied for the salt and bubble velocity. Conversely, on the inlet both velocities are set while pressure is zero-gradient.

Figure 1: Simplified two-dimensional wedge representation of the MSFR with pump region (red), heat exchanger region (blue and red) and bubble and captured particle remover (green, red and blue). Divisions between mesh blocks are indicated by the thin red lines. The reactor cavity is shaded by the diagonal grey lines.

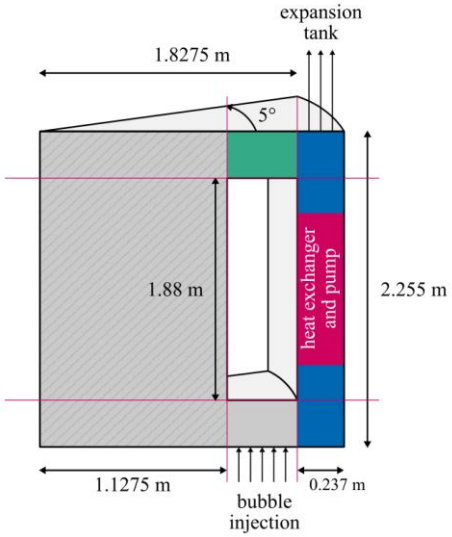

The mesh is constructed using OpenFOAM's blockMesh tool, from the eight blocks that result from the division of the mesh as marked by the thin red lines in Figure 1. Each block is mapped by hexahedral cells in such a way that the mesh density is equal, or very close to, 64 cells/m per spatial direction. In the radial direction, from axis to the outer wall of the heat exchanger and pump, blocks have 72, 44 and 15 cells, respectively. In the axial direction, from bottom to top, blocks have 12, 120 and 12 cells, respectively. This gives a total of 13.584 cells, which is very moderate and allows for long calculations with limited computational effort.

Figure 2: Prompt and decay heat source as obtained from the steady-state results of Caruggi et al. [22].

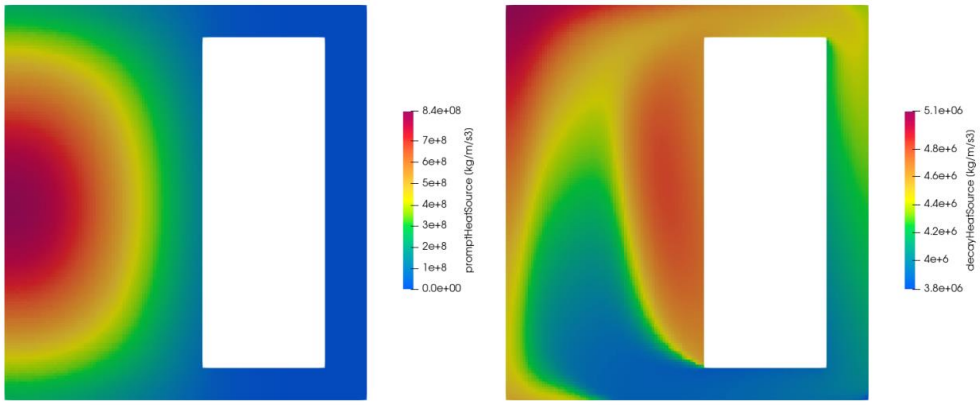

Selection of physical models

For the gas phase, the turbulent closure terms are set to zero, i.e., a 'laminar' turbulence model in OpenFOAM is selected. For the salt phase the turbulent closure terms are calculated using the k-epsilon model. Because the mesh is not wall resolving, standard OpenFOAM wall models are used for k and epsilon.

The gas phase is constituted by helium, which is assumed to behave as a compressible ideal gas. Its mole weight is set to 4 g/mol and its viscosity to $4.6913 \cdot 10^{-5}$ kg/m/s. The mass density of the salt is set to a constant value of 4215 kg/m^3, which corresponds to its mass density at 1000 K. This is expected to be close to the mean temperature of the reactor inventory. The constant salt density leads to a lack of natural circulation in the system, possibly affecting the flow pattern in the vessel. Also viscosity is set to a constant value, being 0.01 kg/m/s.

The two-fluid model's interfacial mass, momentum and energy transfer terms are closed as follows:

- It is assumed that no mass transfer occurs between helium bubbles and salt, meaning that helium does not condense onto the salt and salt does not evaporate into the bubbles.
- Heat transfer between bubbles and salt is based on the Ranz-Marshall correlation (15) (where Sh becomes Nu, i.e., the Nusselt number) as given above. Preliminary simulations showed that the heat transfer between salt and gas is so quick that virtually anywhere the temperature difference between salt and gas is very small, within tenths of Kelvin. Thus, the choice of heat transfer model between the two phases is not important.
- For the momentum transfer between salt and bubbles, we use the Schiller-Naumann model [23] for drag, virtual mass force with a standard coefficient of 0.5, the turbulent dispersion model of Lopez de Bertodano et al. [24] and a wall-damped lift model of Tomiyama et al. [25]. Where needed, bubbles are assumed to be perfectly spherical.

The LogMoM model requires the selection of a break-up kernel and a coalescence kernel. For break-up we use the model of Luo & Svendsen [26] with σ = 0.07197, 5 Gauss-Hermite quadrature points and 5 Gauss-Legendre quadrature points. For the coalescence kernel we use the one of Prince & Blanch [27] including both turbulent and buoyant coalescence, and with 5 Gauss-Hermite quadrature points. As

closing moments in LogMoM we use the zeroth (number), second (interfacial area) and third (volume) moments.

As outlined above, the particle phase is modeled using a sectional representation of the free and captured particle populations. For each distribution we use 16 sections, that logarithmically map the diameter space in such a way that the first section is located at 1 Å and the last section at 1 μm, thus spanning four diameter decades each with four sections. For the particle velocity a 'local equilibrium' model is used. Particle diffusivity is given by the Stokes-Einstein model. The modeling of hydrodynamic and diffusional flotation rates and efficiencies is as discussed above.

Unlike Caruggi et al. [22], no full multi-physics simulation is performed in the sense that the neutronics part of the problem is completely ignored. Instead, steady-state 'prompt' and 'decay' power fields were obtained from [22], to model the heat deposition inside the salt. These two fields are shown in Figure 2.

Numerical setup

Time-accurate simulations are performed with an adaptive time step controlled by a Courant-Friedrich-Lewy (CFL) limit of 0.5. The pressure-velocity system is solved in a segregated way using OpenFOAM's standard PIMPLE algorithm, with two outer iterations and three inner ones. In the first two inner iterations, the pressure equation is solved such that the residual has decreased by two decades. In the final inner iteration, the pressure equation is solved to an absolute tolerance level of 10^{-5}. The preconditioned conjugate gradient solver is used for the pressure equation. All other equations are solved using OpenFOAM's 'smoothSolver', all to an absolute tolerance level of 10^{-5}. No under- or over-relaxation is applied, so that simulation results are, in principle, time-accurate (although we mostly look at steady-state solutions of the salt-gas mixture).

Time derivatives are discretized using a mix of forward and backward Euler schemes, where the backward scheme is preferred in favor of the forward scheme if terms can be taken implicitly with respect to the main solution variable, for stability. The convective terms in the momentum and energy equation are discretized using OpenFOAM's standard 'limitedLinear' scheme. The convective terms in the k and epsilon equations are discretized using the first order upwind scheme, for stability. All other convective terms, including that of the void fraction, the zeroth and second moment of the bubble size distribution and the sectional free and captured particle concentrations, are discretized using the Van Leer scheme [28]. Laplacians, face interpolations and surface-normal gradients are all calculated using linear schemes without any non-orthogonality corrections because the computational grid is fully orthogonal.

Figure 3: Steady state solution for the axial velocity (top left), radial velocity (top right), salt temperature (bottom left) and pressure (bottom right), calculated for φ = 10 g/s and d_{in} = 1 mm.

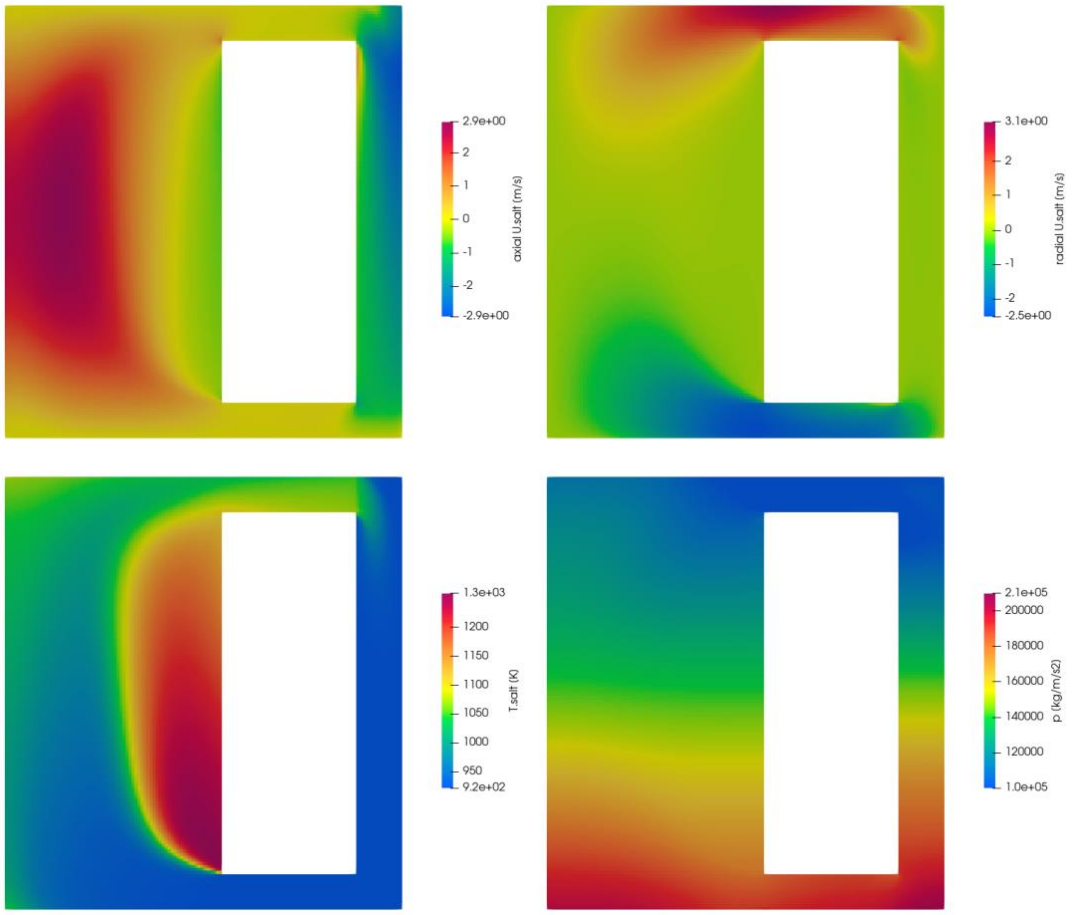

Simulation results and analysis

The goal of performing flotation simulations in the MSFR is to compute the cycle time of noble metals in the reactor, as a function of operational conditions. The key parameter to control noble metal content in the reactor is the mass flow rate φ of helium bubbles. One could envision the inlet bubble size as a secondary parameter. However, we will later show that the inlet bubble size has negligible influence on the mean particle size inside the reactor vessel, because the bubble size distribution rapidly adjusts to a mean bubble size that depends solely on the interplay of void fraction, coalescence and break-up but not on bubble size history. Thus, the only parameter to the problem is the helium mass flow rate.

In principle, we should perform transient simulations of particle formation, particle growth by coagulation and particle removal by bubbles. However, in [7] it was shown that the establishment of particle size distribution equilibria can, as a function of a single parameter Π (being the ratio between growth and removal time scale), take extremely long, even up to years for small values of Π. Such long operation times are infeasible for full transient CFD simulations. Moreover, in order to model particle growth a numerical method to solve the coagulation equation (e.g., see [29]) should be implemented, which is currently not done. Thus, the following alternative simulation strategy is adopted:

1. The main idea is to start from equilibrium size distributions that follow from theory, and to compute cycle times from the decay of such initial particle size distributions by bubble removal, without production or growth of new particles. As shown in [7], the equilibrium size distribution depends on parameter Π. In turn, Π depends on the interfacial area concentration of bubbles which is not known a priori and is a function of the helium mass flow rate. Thus, we must first compute the dependence of Π, averaged over the reactor vessel volume, on the mass flow rate φ, using our CFD model.
2. Once this dependence is known, an initial equilibrium size distribution of free particles can be calculated for any mass flow rate φ from theory [7]. Starting from such an initial condition, the rate of decay of total noble metal particle inventory as a function of time gives an estimate of the cycle time of noble metals in the MSFR. This cycle time can be compared with the theoretical one, in order to establish an interpretation of the role that both spatial inhomogeneity and hydrodynamic flotation play—physics that were neglected by the theory.

In this Section, we will discuss the simulation results of these two steps.

Figure 4: Steady state solution for the void fraction (top left), Sauter mean bubble diameter (top right), salt turbulent kinetic energy (bottom left) and salt turbulent viscosity (bottom right), calculated for φ = 10 g/s and d_{in} = 1 mm.

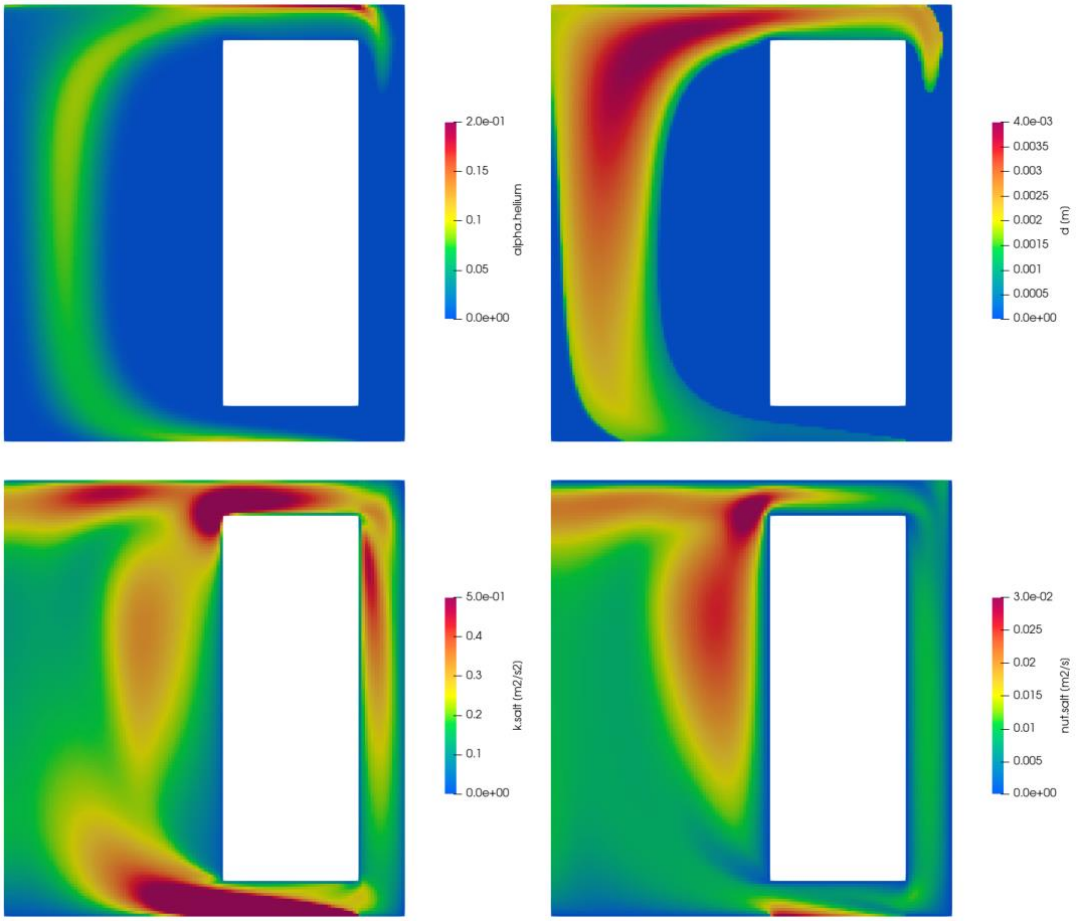

Figure 5: Reactor cavity volume-averaged void fraction and Sauter mean bubble diameter calculated for a range of mass flow rates and three inlet Sauter mean bubble diameters.

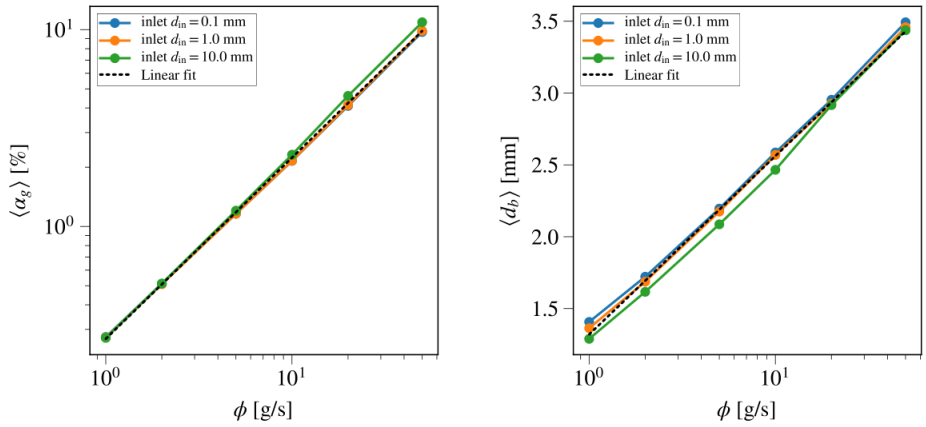

Preliminary simulations without noble metal particles

We perform preliminary simulations of the complex bubble-salt flow in the two-dimensional simplified representation of the MSFR geometry. For a range of inlet bubble diameters d_{in} and helium mass flow rates φ (defined in terms of the full geometry, not the wedge geometry), the steady-state vessel volume-average void fraction and bubble Sauter mean diameter are calculated. Note that the volume flow rate of helium depends on the pressure, which is the result of the static pressure of salt which is held at atmospheric pressure at the outlet to the expansion tank, see Figure 1. This leads to a pressure of roughly 2 bars at the inlet, although the exact value depends on the gas holdup in the vessel.

Figure 3 and 4 show the steady state solution variables at t = 100 s calculated using a helium mass flow rate of 10 g/s and an inlet Sauter mean bubble diameter of 1 mm. The calculation of the Sauter mean bubble diameter is not very accurate (nor very relevant) in low void fraction regions. Its value is set to zero in areas with void fractions below 0.1%. It can be observed from the temperature plot that the heat exchanger reduces the salt temperature back to an inlet temperature of approximately 920 K. Also the removal of bubbles is seen to be effective, so that no re-circulation of bubbles is established. The bubble diameter is seen to grow, which is the result of isothermal expansion due to reduced pressures. Moreover, the bubble size distribution is modified by the interplay of break-up and coalescence, which, in turn, depends on salt turbulence. The salt turbulence, expressed by the turbulent kinetic energy and turbulent viscosity fields, is seen to be highly non-uniform in the reactor vessel as a result of its geometry. The CFD model is capable of capturing these spatial effects, and the influence of the change of the bubble size distribution on the flotation efficiency, which will be discussed below.

From the simulations results we can calculate a volume-average void fraction and Sauter mean diameter in the reactor cavity. We define these two quantities as

$$\langle \alpha_g \rangle = \frac{1}{V_{\text{cav}}} \int_{V_{\text{cav}}} \alpha_g \mathrm{d}\mathbf{x} \qquad \text{and} \qquad \langle d_b \rangle = \frac{1}{\langle \alpha_g \rangle V_{\text{cav}}} \int_{V_{\text{cav}}} \alpha_g d_b \mathrm{d}\mathbf{x} \tag{16}$$

where V_{cav} is the reactor cavity volume as indicated in Figure 1. Figure 5 shows the two volume-averaged quantities, calculated at steady state for a range of helium mass flow rates and three inlet Sauter mean

bubble diameters. Clearly, both quantities are quite independent of the choice of inlet diameter, suggesting that break-up and coalescence re-organize bubbles sufficiently quickly so that the inlet diameter has no significant influence on the volume-average result. On the other hand, both the volume-averaged void fraction and bubble diameter are seen to change noticeably with increasing helium mass flow rate. This is a trivial result for the void fraction, however, for the bubble diameter it is less obvious, as it results from a complex interplay of the coalescence and break-up kernels depending on non-uniform void fraction and turbulence. The effect of coalescence and break-up can generally be understood by the observation that a larger concentration of bubbles increases the likelihood of coalescence and thus size.

Also shown in Figure 5 is a linear fit on both quantities, each averaged over the three inlet diameters. These linear fits give a correlation between helium mass flow rate and mean vessel void fraction on one hand, and helium mass flow rate and mean vessel bubble diameter on the other. In turn, these two quantities can be fed into the definition of parameter Π, yielding the vessel volume-average parameter

$$\langle \Pi \rangle = \frac{3\mathrm{Sh}}{\pi b} \frac{\langle \alpha_g \rangle}{\langle d_b \rangle^2} \sqrt{\frac{K}{F}}, \tag{17}$$

with initial noble metal particle diameter b, coagulation constant K and noble metal particle production rate F, see [7]. The Sherwood number is, through the Ranz-Marshall relation (15), a function of bubble Reynolds number, for which a correlation is given in [7] as function of the bubble diameter, and the particle Schmidt number which is estimated in [7] too. Using the resulting Sherwood number function along with the fits shown in Figure 5 for $\langle \alpha_g \rangle$ and $\langle d_b \rangle$ and the values of b, F and K (also given in [7]), gives the vessel volume-averaged parameter $\langle \Pi \rangle$ which is shown in Figure 6 as a function of helium mass flow rate. A linear fit in the double logarithmic space as displayed in Figure 6 yields

$$\langle \Pi \rangle = 0.512 \phi^{0.700}. \tag{18}$$

This function, then, is used as the sole input to the model presented in [7] that predicts the equilibrium noble metal size distribution. In turn, the outcome of that model which, through $\langle \Pi \rangle$, has become a function of φ, is used as the initial condition for the free particle population for the flotation CFD calculations presented next.

Figure 6: The reactor vessel volume-average parameter ⟨Π⟩ as function of the helium mass flow rate for the simplified two-dimensional geometry of the MSFR.

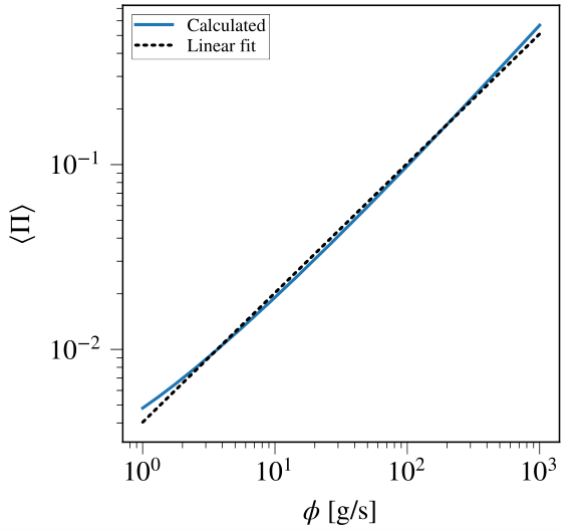

Noble metal particle flotation simulations

From the model presented in [7] and the function for ⟨Π⟩ (18) the initial free particle population $n_f(d)$ at time t = 0 can be constructed. For large values of ⟨Π⟩ at high helium mass flow rates, the initial free particle population will have predominantly small particles while for small values of ⟨Π⟩ at low helium mass flow rates the initial free particle population will have predominantly much larger particles. Thus, when we increase the helium mass flow rate, we automatically decrease the initial mean noble metal particle sizes because at high helium mass flow rates the equilibrium particle size distribution predicted by theory will not grow significantly as a result of more effective flotation.

Next, we calculate the initial sectional concentrations using

$$N_{i,f} = \int_{y_i}^{y_{i+1}} n_f(d)\mathrm{d}d, \tag{19}$$

with y_i the lower integration limit of section i and y_{i+1} the upper integration limit of section i. These limits are set midway between the two adjacent representative sectional sizes in logarithmic space, i.e., $y_i = \sqrt{(d_{i-1}d_i)}$ with the exception of y_1 and y_{n+1} which are set to zero and infinity, respectively.

Figure 7: Total noble metal mass inventory in the reactor scaled by its initial amount as a function of time for eight values of the helium mass flow rate (left) and the corresponding cycle times (right).

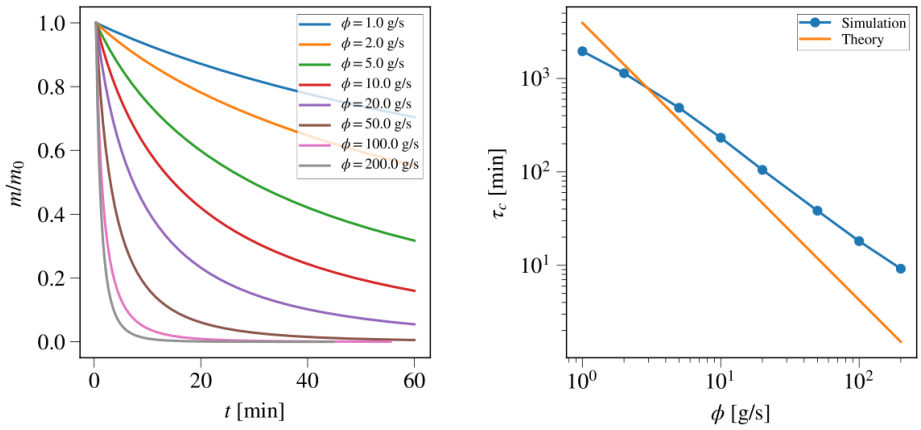

Starting from a fully developed steady-state solution in terms of the salt-helium mixture, we initialize the appropriate equilibrium free noble metal particle population and simulate the transfer of that free particle population to the captured particle population by means of flotation. We recall that the removal rate of particles as predicted by the CFD simulation may differ from the theory because of spatial inhomogeneity, but also because the CFD simulation incorporates hydrodynamic flotation. Thus, the initial free particle population is only an estimate and does not necessarily reflect exact steady-state conditions subject to the CFD model. Simulations are performed over the course of one hour, in order to establish significant particle removal for all considered mass flow rates. Figure 7 (left) shows the total noble metal mass inventory m in the reactor, scaled by its initial value, as a function of time, for eight values of the helium mass flow rate. The mass inventory is calculated as the third moment of the free particle size distribution, i.e.,

$$m = \frac{\rho_p \pi}{6} \int_0^\infty d^3 n_f(d) \mathrm{d}d \approx \frac{\rho_p \pi}{6} \sum_i d_i^3 N_{i,f} \tag{20}$$

It is clearly observed in Figure 7 (left) that low mass flow rates lead to slow particle removal while for higher mass flow rates the removal becomes progressively more efficient, as a result of the presence of more interfacial area. We may quantify the rate of removal by calculating the cycle time τ_c that generates the best match between the numerical data and an exponential decay function given by

$$\frac{m}{m_0} = \exp\left(-\frac{t}{\tau_c}\right). \tag{21}$$

Since our simulation time is 1 h, we can thus calculate the cycle time as $\tau_c = -1/\log(m_{1\mathrm{h}}/m_0)$ in units of hours, where $m_{1\mathrm{h}}$ is the total noble metal mass inventory after 1 h of simulated time. The cycle times that result from this definition are shown in Figure 7 (right) for a range of helium mass flow rates. Also shown is the theoretical prediction. From this plot, we can draw three conclusions:

- For high helium mass flow rates the initial particle population contains only small particles that are not susceptible to hydrodynamic flotation and only to diffusional flotation, the latter upon

which the theoretical prediction is exclusively based. Thus, at high flow rates the difference between theory and numerical prediction are related to the diffusion term and not to the hydrodynamic flotation term. We observe that the numerically calculated cycle time is almost a decade larger than the theoretical one at the highest flow rate shown, which is significant. One reason for this is that the parameter $\langle \Pi \rangle$ is based on the reactor vessel cavity only, while free particles can also enter the pump and heat exchanger volume which comprises a significant amount of volume (due to radial expansion of the geometry) but where no bubbles are present giving free particles more chance to avoid removal. Also, as can be seen in Figure 4, bubbles are concentrated locally in an upward plume. Particles in that plume are removed efficiently, but particles outside it largely avoid removal until they diffuse into the plume. This diffusional processes is slow, particularly for large particles which hold most mass. Moreover, mean bubble size is seen to be strongly varying in space too, changing the local flotation characteristics with respect to the vessel volume averaged one.

- We also observe in Figure 7 that the slope of the cycle time curve is slightly steeper in the theoretical line, even at large mass flow rates. This can be explained by the fact that in the theory the particle Sherwood number is assumed to be independent of particle size while in reality it carries a weak dependence ($\sim d^{-1/3}$). This dependence is considered in the CFD simulation, but is ignored in theory, resulting in a slightly steeper slope in the theoretical cycle time prediction.
- At lower helium mass flow rates the difference in cycle time prediction decreases, and at some point changes sign; for small flow rates the cycle time becomes smaller than the theoretical one. This can be attributed to the modeling of hydrodynamic flotation and the enhancement in removal rates it results in for large particles. Such large particles are only present for low helium mass flow rate runs, because for low mass flow rates the initial noble metal particle size distribution contains significantly larger particles.

The results above are ‘integral’ quantities in the sense that we considered the decay rate of the total noble metal mass inventory. Instead, we can also look at the decay rate of the sixteen individual free particle sections, for the set of eight simulated mass flow rates giving 128 data points. Moreover, from each such point a corresponding ‘partial’ cycle time can be computed in the same way as before, but now based on the fraction of free particles in section i, $N_{i,f}(1\text{h})/N_{i,f}(0)$, giving the partial cycle time as a function of both helium mass flow rate and noble metal particle size. This, then, is shown in Figure 8. It can be seen that at constant helium mass flow rate, the cycle time increases monotonically until particle sizes of about 500 nm as a result of decreased Brownian diffusivity. Above roughly 500 nm, hydrodynamic flotation is seen to become more effective, decreasing the cycle time in turn. We note, however, that the net cycle time of noble metal mass inventory is an integral over all sizes weighted by the free particle population. This is what is discussed above and presented in Figure 7, and represents the main finding of this work.

Figure 8: Partial cycle time as a function of both helium mass flow rate and noble metal particle size.

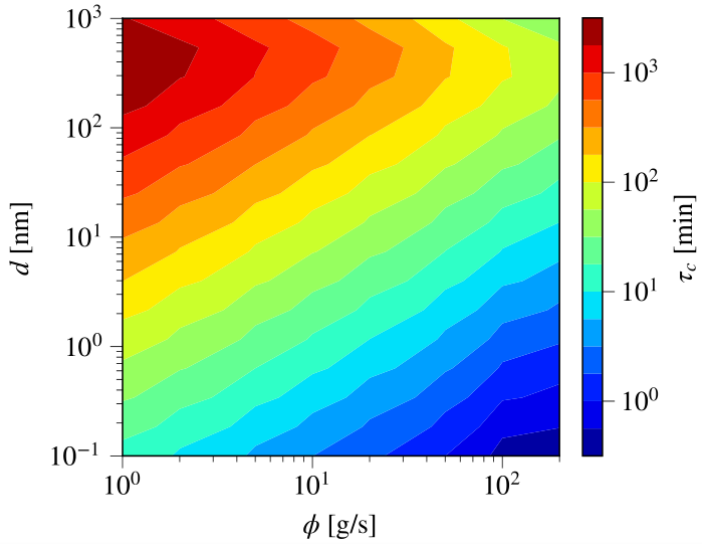

Conclusions

This work has investigated the hydrodynamic and diffusional flotation of noble metal particles in an MSR, by CFD simulation of a simplified reactor geometry. Theory shows that at low bubble flow rates it takes very long to establish equilibrium particle distributions, which is not feasible to be simulated by CFD. Instead, we imposed approximate equilibrium size distributions that were calculated by theory as initial condition, and simulated the removal of member particles of that initial size distribution in time. Based on the decay rate of noble metal mass, a cycle time was calculated for a range of bubble mass flow rates. It was shown that simulated cycle times are almost an order of magnitude larger at very high bubble flow rates as compared to theory, suggesting that inhomogeneity of the reactor, which is not accounted for in the theory, plays an important role. Several reasons for this were discussed. Most importantly, the plume of bubbles and the bubble sizes contained within are very non-uniform and are expected to change flotation characteristics significantly. From this we can conclude that it is important to simulate an accurate representation of the real MSFR geometry and that a two-dimensional simplified geometry may not be sufficient for the calculation of accurate removal rates. Moreover, it was observed that the slope of the cycle time curve was slightly steeper in the simulations, attributed to the fact that the size dependence of the Sherwood number is ignored in the theory.

Finally, we concluded that at low bubble flow rates the initial particle distribution (predominantly containing large particles) was subject to hydrodynamic flotation too, reducing the cycle time as compared to the theory which only includes diffusional flotation. However, large particles can only arise in the MSR after very long steady-state operational times, which may be unrealistic.

Funding

This project has received funding from the Euratom research and training program 2019–2023, under grant agreement No. 847527.

Data

The data that support the findings of this study are openly available in Zenodo at https://doi.org/10.5281/zenodo.7628854.

Disclaimer

The content of this paper does not reflect the official opinion of the European Union. Responsibility for the information and/or views expressed therein lies entirely with the authors.

References

[1] V. Habiyaremye, E.M.J. Komen, J.G.M. Kuerten, and E.M.A. Frederix. Modeling of bubble coalescence and break-up using the log-normal method of moments. Chemical Engineering Science, page 117577, 2022.

[2] E. Merle-Lucotte, D. Heuer, M. Allibert, M. Brovchenko, N. Capellan, and V. Ghetta. Launching the thorium fuel cycle with the molten salt fast reactor. In Proceedings of ICAPP, volume 2, 2011.

[3] R.J. Kedl. Migration of a class of fission products (noble metals) in the molten-salt reactor experiment. Technical report, Oak Ridge National Lab., Tenn.(USA), 1972.

[4] S. Delpech, E. Merle-Lucotte, D. Heuer, M. Allibert, V. Ghetta, C. Le-Brun, X. Doligez, and G. Picard. Reactor physic and reprocessing scheme for innovative molten salt reactor system. Journal of Fluorine Chemistry, 130(1):11–17, 2009.

[5] N. Mishchuk, J. Ralston, and D. Fornasiero. The analytical model of nanoparticle recovery by microflotation. Advances in Colloid and Interface Science, 179:114–122, 2012.

[6] A.V. Nguyen and H.J. Schulze. Colloidal Science of Flotation, volume 118. CRC Press, 2003.

[7] E.M.A. Frederix. Estimates of noble metal particle growth in a molten salt reactor. Colloids and Surfaces A: Physicochemical and Engineering Aspects, page 130167, 2022.

[8] E.M.A. Frederix. Helium bubbling literature review, model development and model application. Technical report, NRG, 2018.

[9] E. Cervi, S. Lorenzi, A. Cammi, and L. Luzzi. An Euler-Euler multiphysics solver for the analysis of the helium bubbling system in the MSFR. In 26th International Conference Nuclear Energy for New Europe, 2017.

[10] M. Ishii and T. Hibiki. Thermo-fluid dynamics of two-phase flow. Springer Science &Business Media, 2010.

[11] D.A. Drew and S.L. Passman. Theory of multicomponent fluids, volume 135. Springer Science & Business Media, 2006.

[12] S.K. Friedlander. Smoke, dust and haze: Fundamentals of aerosol behavior. 1977.

[13] D.L. Marchisio and R.O. Fox. Computational models for polydisperse particulate and multiphase systems. Cambridge University Press, 2013.

[14] D. Ramkrishna. Population balances theory and applications to particulate systems in engineering. 2000.

[15] R.H. Yoon and G.H. Luttrell. The effect of bubble size on fine particle flotation. Mineral Procesing and Extractive Metallurgy Review, 5(1-4):101–122, 1989.

[16] Z. Dai, D. Fornasiero, and J. Ralston. Particle–bubble attachment in mineral flotation. Journal of colloid and interface science, 217(1):70–76, 1999.

[17] W.E. Ranz and W.R. Marshall. Evaporation from drops. Chemical Engineering Progress, 48(3):141–146, 1952.

[18] M.W. Rosenthal, R.B. Briggs, and P.R. Kasten. Molten-salt reactor program semiannual progress report for period ending February 28, 1969. Technical report, Oak Ridge National Lab.(ORNL), Oak Ridge, TN (United States), 1969.

[19] E.L. Compere, S.S. Kirslis, E.G. Bohlmann, F.F. Blankenship, and W.R. Grimes. Fission product behavior in the molten salt reactor experiment. Technical report, Oak Ridge National Lab.(ORNL), Oak Ridge, TN (United States), 1975.

[20] E.M.A. Frederix, T.L.W. Cox, J.G.M. Kuerten, and E.M.J. Komen. Poly-dispersed modeling of bubbly flow using the log-normal size distribution. Chemical Engineering Science, 201:237–246, 2019.

[21] H. Rouch, O. Geoffroy, P. Rubiolo, A. Laureau, M. Brovchenko, D. Heuer, and E. Merle-Lucotte. Preliminary thermal–hydraulic core design of the molten salt fast reactor (MSFR). Annals of Nuclear Energy, 64:449–456, 2014.

[22] F. Caruggi, A. Cammi, E. Cervi, A. Di Ronco, and S. Lorenzi. Multiphysics modelling of gaseous fission products in the molten salt fast reactor. Nuclear Engineering and Design, 392:111762, 2022.

[23] R. Clift, J.R. Grace, and M.E. Weber. Bubbles, drops, and particles. Courier Corporation, 2005.

[24] M. Lopez de Bertodano, R.T. Lahey, and O.C. Jones. Phase distribution in bubbly two-phase flow in vertical ducts. International Journal of Multiphase Flow, 20(5):805–818, 1994.

[25] A. Tomiyama, H. Tamai, I. Zun, and S. Hosokawa. Transverse migration of single bubbles in simple shear flows. Chemical Engineering Science, 57(11):1849–1858, 2002.

[26] H. Luo and H.F. Svendsen. Theoretical model for drop and bubble breakup in turbulent dispersions. AIChE Journal, 42(5):1225–1233, 1996.

[27] M.J. Prince and H.W. Blanch. Bubble coalescence and break-up in air-sparged bubble columns. AIChE journal, 36(10):1485–1499, 1990.

[28] B. Van Leer. Towards the ultimate conservative difference scheme. V. A second-order sequel to Godunov's method. Journal of Computational Physics, 32(1):101–136, 1979.

[29] S. Kumar and D. Ramkrishna. On the solution of population balance equations by discretization–I. A fixed pivot technique. Chemical Engineering Science, 51(8):1311–1332, 1996.

[30] E.M.A. Frederix. Dataset for CFD4NRS-9 conference paper "Simulation of noble metal particle growth and removal in the molten salt fast reactor". https://doi.org/10.5281/zenodo.7628854.

U.S.NRC
United States Nuclear Regulatory Commission
Protecting People and the Environment

Center for Advanced Small Modular and Micro Nuclear Reactors
Texas A&M Engineering Experiment Station

NEA
NUCLEAR ENERGY AGENCY

Technical Session 4

Two-phase Flow

Feb 20, 14:00-15:30, Room B.

THE MORPHOLOGY ADAPTIVE MULTIFIELD SOLVER OPENFOAM-HYBRID AND ITS APPLICATION TO MULTIPHASE FLOW PROBLEMS IN NUCLEAR SAFETY

B. Krull[1], D. Lucas[1], R. Meller[1], F. Schlegel[1], M. Tekavčič[2]

[1]*Helmholtz-Zentrum Dresden – Rossendorf e.V. (HZDR), Bautzner Landstr. 400, 01328 Dresden, Germany*
[2]*Jožef Stefan Institute, Jamova cesta 39, 1000 Ljubljana, Slovenia*

Extended Abstract

A typical feature of nuclear safety facilities are multiphase flows with coexisting morphologies, i.e. with phases which occur both in a continuous form (such as in a stratified flow) and in a disperse form (bubbles or droplets). Established simulation methods are usually suitable for either resolved structures (e.g., Volume-of-Fluid) or dispersed structures (e.g., Euler-Euler). We propose a morphology adaptive multifield two-fluid model, which is able to handle both disperse and resolved interfacial structures coexisting in a common computational domain, covered by a unified set of equations. This requires (A) a careful selection of closure models. On the continuous side, the interfacial drag formulation of Štrubelj and Tiselj (Int J Numer Methods Eng, 2011, 85, 575-590) is used to describe large interfacial structures in a volume-of-fluid-like manner. For the dispersed structures, the HZDR baseline model is applied. Meller et al. (Int J for Numer Method Fluid, 2021, 93, 748-773) and Tekavčič et al. (Nucl Eng Des, 379, 111223) presented several test cases to prove that the numerical consistent coexistence of different morphologies is ensured. The interaction of the morphologies is only controlled by the aforementioned closure models without being disturbed by numerical effects. A second requirement is (B) a reliable transition between continuous and disperse states, depending on the size of the structures and the degree of spatial resolution. This is subject of the current work. A prerequisite for reliable transitions is the stable coverage of intermediate situations, where bubbles are either over- or under-resolved for Euler-Euler or Volume-of-Fluid (Fig. 1). An adaptive interfacial drag model and a filtering technique are applied for stable and robust handling of the transition regions. Two morphology transfer models are established, allowing large resolved structures to disintegrate into small unresolved fluid particles and, vice versa, the accumulation of disperse fluid particles to continuous large-scale structures. This is applied to generic verification and validation test cases, representing typical sub-problems relevant in safety facilities. The model is applied to a cyclic separator (Fig. 2), which can only be simulated with methods allowing the transition from a disperse to a continuous morphology. This is particularly challenging because the gas core must exhibit a stable behavior in the highly rotating flow while gas and liquid are moving in opposite directions along the rotational axis.

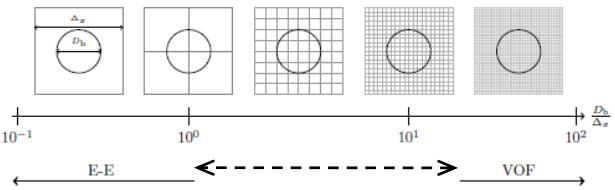

Figure 1: Optimal numerical method to compute an interfacial structure of a certain dimension depending on the number of available cells

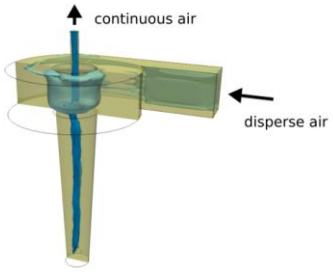

Figure 2: Cyclic separator allowing the removal of bubbles by accumulating them in a continuous gas core

IMPLEMENTATION AND ASSESMENT OF NEW TRANSITION CRITERIA FOR ALL REGIME TWO-PHASE FLOW SIMULATIONS WITH NEPTUNE_CFD CODE.

Lasseur Théo, Mimouni Stéphane

EDF R&D Division, 6 Quai Watier 78400, Chatou, France

Extended Abstract

Two-phase flows include a vast diversity of different patterns that frequently involve a large range of space and time scales. For instance, plug and slug flow are composed of a continuous liquid phase carrying small, dispersed bubbles along larger deformable pack of vapor. Due to this intrinsic behaviour, accurate simulation of such complex flow remains today a tough challenge even with the increased computing capacities.

In this aspect the two-fluid Euler-Euler can be an interesting approach to avoid having cells smaller than the smallest structure of the flow. The main reason is that while resolving large gas-liquid interfaces, the small scales objects (sub-grid bubbles or droplets) are not resolved but modelled. This equation system for mass, momentum, and energy requires interfacial closure relationships that largely rely on semi-empirical correlations, and which are different according to the nature of the phase and if it is a small or large object.

To carry out simulations without assuming the flow pattern, it is thus necessary to determine which set of closure laws need to be applied at a given time and position depending on the size of the objects within the cells. FullGLIM is a relatively recent modelling method that combines a sub-grid approach based on standard dispersed model and a large interface model to capture large interfaces. Gas and liquid are modelled in two distinct fields that both contain small and large objects of the same physical phase. A criterion characterizing the transitions between bubbly, large interfaces and droplets-laden flow allows to select the suitable closure laws to apply. It is therefore able to simulate a wide range of two-phase flow configurations and have been already validated on several test cases.

The current study is focused on the transition between bubbly and plug flow as it implies that continuous and dispersed structures will be encountered. The transition from dispersed bubbles to continuous pack of vapor occurs through the competing processes of i) agglomeration of bubbles when the bubble density is enough and ii) breakup of larger bubbles when the turbulence of the flow is sufficient.

Experimental studies have suggested that the transition from bubbles to slug flow occurred at a critical value of void fraction around 0.25-0.3. The void fraction is a convenient parameter to play the role of the transition criterion as its value can be correctly calculated. Numerical optimization of the critical void fraction value on different test cases has been found to be around 0.5 with a continuous transition from dispersed to large interface models resulting in a mixing of closure terms.

However, this constant critical value cannot be generalized to all systems as it does not depend on any properties of the fluids such as the surface tension nor on any operating parameters such as the pressure or temperature. Other criteria can be considered to distinguish dispersed from continuous phases. For instance, GEMMA is one based on the interface shape (curvature) in the cell. It is thus related to geometrical aspects of the objects, and high curvature relatively to the grid size are associated to small structures.
Non-dimensional numbers may be a way to improve the applicability range of the transition criterion based on more physical considerations.

The purpose of this study is to test different criteria. The numerical simulations are compared against each other and with the experimental data of the METERO experiment designed to validate numerical codes. In this experimental adiabatic two-phase test loop, regimes obtained for various water and air superficial velocities circulating in a horizontal pipe are investigated. To validate this approach comparisons with both the void and

liquid velocity profiles at given positions and averaged in time are made for different couple of superficial velocities and the expected regimes from METERO flow map around the bubbly-plug transition are compared to the numerically ones.

References

Mer S., Praud O., Neau H., Merigoux N., Magnaudet J., Roig V. The emptying of a bottle as a test case for assessing interfacial momentum exchange models for Euler-Euler simulations of multi-scale gas-liquid flows. Int. J. of Multiphase Flow (2018)

Davy G., Reyssat E., Vincent S., Mimouni S. Euler-Euler simulations of condensing two-phase flows in mini-channel: Combination of a sub-grid approach and an interface capturing approach. Int. J. of Multiphase Flow (2022)

Bottin M., Berlandis J.P., Hervieu E., Lance M., Marchand M., Öztürk O.C., Serre G. Experimental investigation of a developing two-phase bubbly flow in horizontal pipe. Int. J. of Multiphase Flow (2014)

HEATED LIQUID FILM IN VERTICAL FREE FALL AIR-WATER ANNULAR FLOW

Y. Rivera, C. Berna, Y. Córdova, J.L. Muñoz-Cobo, A. Escrivá

Universitat Politècnica de València, Institute for Energy Engineering, Camino de Vera s/n, 46022 València (Spain). Tel: +34 963879245. E-mail: yaridu@upv.es

Extended Abstract

Liquid films appear in multiple applications in the industrial field and have been studied from many points of view. They are especially important in the nuclear field since they can appear in the different types of light water reactors. In particular, annular downward flow is observed in accident scenarios both in the steam generators of a PWR and in the core itself in BWRs. The annular flowing liquid film itself plays an important role in heat transfer, as it is responsible for extracting or transferring heat to the wall. The interaction between the liquid and the gas leads to the appearance of interfacial waves, which directly affect the heat transfer.

To study this phenomenon, experiments have been carried out in the GEPELON facility (GEneración de PElícula ONdulatoria or Wavy Film Generator) of the thermal-hydraulics laboratory of the Institute for Energy Engineering of the Polytechnic University of Valencia. This facility is capable of generating different types of vertical annular flow including upward co-current, downward co-current or free-fall, and counter-current flow. In addition, it has a temperature control system that allows experiments to be carried out at different temperatures. The temperature of the liquid produces a variation in surface tension and viscosity that directly affects the behavior of the interfacial waves.

The experimental range that can be studied varies between 800 and 8000 for the liquid Reynolds number and between 0 and 110,000 for the gas Reynolds number. However, in this paper only the measurements for free-falling film are presented ($Re_{gas}=0$). Film thickness measurements were made using conductance probes built and calibrated in our laboratory. The conductance probe uses an electrical method to obtain the relationship between the current passing between two electrodes and the film thickness.

Experimental results show a decrease in film thickness as water temperature increases. This is due to the fact that the surface tension decreases and therefore the cohesion of the molecules on the interphase. The decrease in cohesion facilitates droplet detachment and therefore the height of the waves is lower. In addition, viscosity decreases with temperature, which causes the velocity between layers to increase and, consequently, the height of the waves decreases.

Experimental measurements obtained in this facility can be used to validate and verify CFD models. The most important phenomena to simulate are the two-phase flow itself and the effect of surface tension and viscosity on it due to the temperature change. As the temperature varies between experiments, it may also be important to consider heat loss from the film although it is not necessary to model the phase change.

Two-phase flow simulations are still a challenge even if they do not include phase change effects. Preliminary CFD results show the ability of these codes to predict film thickness and even the occurrence of surface waves. It is noted the need to carefully refine the mesh around the wall where the film is located. Moreover, turbulence models based on Large Eddy Simulation seem to better predict the behavior and especially the definition of the interface. However, further studies are needed to study the behavior of the film with surface tension and viscosity.

CFD investigation of two-phase flow pressure drop in helical tube steam generator for LWR based SMR application

Doh Hyeon Kim, Seunghwan Oh, Jeong Ik Lee

Department of Nuclear and Quantum Engineering, Korea Advanced Institute of Science and Technology (KAIST)

Extended Abstract

SMRs (Small Modular Reactors) are being actively developed to meet energy demands. To construct SMRs in remote areas, transport by train or truck is an important design requirement. Therefore, SMRs mainly use an integral type reactor to reduce the size of the reactor, and a compact heat exchanger different from the existing U-tube type steam generator to reduce the size of the whole plant. As examples of a compact heat exchanger, there are helical steam generator, printed circuit steam generator, and shell and plate steam generator. However, since in-service inspection of the steam generator is required, most of light water reactor based SMRs soon to be licensed usually adopt a helical type steam generator. It can be seen from the Martinelli-nelson curve that the pressure drop in the case of a two-phase flow is higher than that of a single-phase liquid and gas flow in a straight tube. In addition, the behavior of two-phase flow and corresponding flow regimes in helical tubes significantly differ when compared to two-phase flows in straight tubes due to centrifugal and torsion forces. In the past, the two-phase frictional pressure drop in helical tubes were investigated by many researchers. As a result of investigation, the modified Lockhart and Martinelli model was confirmed to have errors within 50% of the measured data. The pressure drop of helical tube appears differently depending on helical tube design variables such as rotational diameter, pitch, tube diameter, and angle. Moreover, in order to evaluate the two-phase instability within the helical tubes, understanding various loss mechanisms is also important.

In this study, the design value range of helical tube used in SMR is investigated. The target nuclear system to be evaluated for helical pressure drop is SMART (System-Integrated Modular Advanced Reactor) developed by KAERI (Korea Atomic Energy Research Institute) in S. Korea. From the publicly available information, pitch, diameter, angle, and thermal hydraulic design information of SMART helical steam generator are obtained. The geometry and the mesh are prepared in commercial CFD environment, ANSYS. The helical tube has three windings and the boundary effect is minimized by having 10D additional flow length at the inlet and the outlet boundaries, respectively. Water and vapor properties at 5.2MPa and 266.4 °C are used for the fluid flowing in the tube. For the shape of the target helical tube, the designed inlet flow rate was applied by changing the mass fraction of water and vapor. Single phase and two-phase pressure drop with respect to the vapor mass fraction was calculated using the commercial CFD code, CFX, assuming liquid and vapor are at thermal equilibrium. As a result of CFD analysis, it can be confirmed that the secondary flow occurred inside the helical tube, which induces additional viscous energy dissipation resulting in higher pressure drop. CFD calculation results shows that the pressure drop of the helical tube was higher than that of the same length straight tube. Also, it was confirmed that a pressure drop curve according to the vapor mass quality was formed similar to the Martinelli-Nelson curve even in the helical tube.

CFD SIMULATION ON THE TRANSIENT HEAT AND MASS TRANSFER PERFORMANCE OF A WATER-COPPER WICKED HEAT PIPE

Dali Yu[a,*], Jian Liu[a,b], Chongju Hu[a,b]

a Institute of Nuclear Energy Safety Technology, HFIPS, Chinese Academy of Sciences, Hefei, China
b University of Science and Technology of China, Hefei, China

Corresponding author: dlyu@inest.cas.cn

Abstract

The application of heat pipes in space nuclear reactors, radiators, and thermal management has gained an enormous amount of attention nowadays. A 3D transient model is necessary for studying the flow and heat transfer characteristics when considering the complex behaviors and special conditions such as the start-up process, power variation process, non-uniform heating condition, microgravity condition, and so on. However, the current CFD models according to the public records are concentrated on predicting the thermal-hydraulic characteristics under the steady-state conditions. The transient process during the startup is significant in the evaluation of heat pipes' normal startup and transient performance, since there are a lot of heat transfer limits occurring in the process, such as the sonic limit, entrainment limit, and viscous limit. Very few 3D numerical analysis were implemented to demonstrate the inner velocities and temperature profile of annulus wick heat pipes during the startup process.

In this study, a 3D CFD model for water-copper wicked heat pipe was developed to predict the transient characteristic of heat pipes. A novel source terms method was used through user-defined functions (UDFs) to calculate the evaporation and condensation rates on the water-vapor interface. The laminar flow hypothesis was applied to the flow region. The compressibility of liquid and vapor was considered and the ideal gas equation was adopted for the vapor flow. The Darcy flow characteristic of liquid wick flow was considered in the porous wick region.

The simulated outer wall temperature, velocity, pressure, and temperature variation of the wick and vapor during the startup process were obtained and compared with the experimental data. Good prediction results were obtained under the same conditions. The heat flux on the condenser wall will increase quickly due to the quick response-ability of heat pipes. The max vapor velocity shows a minor decrease trend due to the vapor pressure recovery. The distribution of vapor temperature has a significant non-uniformity due to the compression work at the initial time. The beginning of the condensation point will migrate to the condenser section in the start-up process.

This study can provide both knowledge and tool for the design of space thermal radiators.

Pre-Test Design of PANDA Experiments with Steam Injection through a Sparger Pipe by Effective Heat and Momentum Models

Xicheng Wang, Dmitry Grishchenko, Pavel Kudinov

Nuclear Engineering Division, Royal Institute of Technology, KTH, 100 44 Stockholm, Sweden

Extended Abstract

Containment served as the final physical barrier to prevent the release of fission products is of great significance for reactor safety. Depressurization by discharging steam into the Pressure Suppression Pool (PSP) through multi-hole spargers and blowdown pipes is a safety design for Boiling Water Reactors (BWRs) during normal and accident conditions. Competition between heat and momentum sources induced by Direct Contact Condensation (DCC) can result in the development of thermal stratification and therefore affect the performance of PSP. Prediction of such phenomena is computationally expensive if both small-scale condensation and large-scale pool circulation are solved by using Computational Fluid Dynamics (CFD) codes. Therefore, the Effective Heat Source (EHS) and Effective Momentum Source (EMS) models have been proposed to enable the prediction of the thermal behavior of the pool.

The motivation of this work is to use the CFD tool combined with EHS/EMS models to provide a pre-test design of steam injection tests (P1A6) in the framework of OECD/PANDA project. Several tests under P1A6 are arranged to study the effect of interaction between the steam jet issued radially outward from the multi-hole Sparger Head (SH) and perpendicularly downward from the Load Reduction Ring (LRR). Development of thermal stratification and gradual erosion as the steam flow rate increases are expected during the tests. The parameters required to be investigated are (i) elevation of sparger tip above pool bottom, (ii) flow rate and duration in each injection phase, and (iii) configuration of instrumentation, e.g., Particle Image Velocimetry (PIV), ThermoCouples (TCs).

To accomplish these tasks, internal flow simulations of the sparger pipe were conducted to provide flow distribution between SH and LRR holes. EHS/EMS models validated separately against SH and LRR tests were implemented in ANSYS FLUENT. Several simulations were performed including activation of both SH and LRR holes and activation of either SH or LRR holes.

Thermal stratification can be observed during all injection phases with the elevation of the sparger tip lifted to 3.7m. Radial jet from the SH head would deflect the downward flow from LRR and results in lower mixing efficiency compared to activation of only LRR with the same steam flux. Asymmetrical flow with symmetrical injection conditions is observed. Steam flow rates, injection durations, and instrumentations of the shakedown test of the P1A6 series are determined.

Keywords: Steam condensation, pressure suppression pool, EHS/EMS models, multi-hole sparger, CFD, pre-test design.

1 INTRODUCTION

Containment is the last physical barrier that prevents the release of radioactive products into the environment. Direct Contact Condensation (DCC) of steam into a large water pool is applied in Light Water Reactors (LWRs) to avoid rapid pressurization of the reactor pressure vessel and containment. In Boiling Water Reactors (BWRs), this pool is known as Pressure Suppression Pool (PSP), and in advanced Pressurized Water Reactors (PWRs), it is called In-containment Refueling Water Storage Tank (IRWST). In a Nordic BWR design [1], steam can be injected into the PSP through blowdown pipes and sparger pipes. Sparger pipes with relatively small diameter holes connect the primary coolant system and wetwell pool, where the steam can be discharged through multi-hole Sparger Head (SH) and Load Reduction Ring (LRR) holes.

Steam condensation can be regarded as a source of momentum and heat. Competition between these two sources determines whether the pool is thermally stratified or mixed [2]. The former case is a safety concern since it can reduce the active volume for heat storage, leading to a rapid increase of pool surface temperature and thereby the increase of containment pressure compared to a completely mixed pool condition. Therefore, validated code with the sufficient predictive capability to resolve the interplay between these phenomena is necessary.

Modelling of the DCC can be achieved by using the Eulerian-Eulerian two-fluid approach in CFD [3][4]. However, the large-scale and long-term features of our case make computational efficiency a necessity for the codes. To enable such prediction with affordable computational resources, Effective Heat/Momentum Sources (EHS/EMS) models have been proposed [2][5]. [4]. These models assume that the large-scale pool circulation and temperature distribution can be determined by the time-averaged heat and momentum sources. EHS/EMS models can be implemented in any CFD-type code with a single-phase solver. These models have been developed for spargers in [6][7][8][9][10] and validated against large-scale pool tests performed in PPOOLEX [11] and PANDA [12] facilities.

The goal of this paper is to provide pre-test design of the tests in the framework of OECD/PANDA project by using CFD code combined with EHS/EMS models. The PANDA project follows the OECD/NEA HYMERES-1 (HYdrogen Mitigation Experiments for REactor Safety) [12] and HYMERES-2 projects [13], aiming to investigate the nuclear safety related issues concerning containment.

The test to be designed is under the topic of extension of the database on the suppression pool of BWR and IRWST of PWR. Specifically, it is to investigate the development of thermal stratification and erosion of stratified layers induced by steam injection through a sparger pipe. In previous tests, steam was injected either radially outward from the multi-hole SH or vertically downward from the LRR holes. In this test, both of them will be activated to study their interaction with the pool behavior. The parameters required to be determined are (i) elevation of sparger tip above pool bottom, (ii) flow rate and duration in each injection phase, and (iii) configuration of instrumentation, e.g., Particle Image Velocimetry (PIV), ThermoCouple (TCs).

To accomplish these tasks, internal flow simulations of the sparger pipe were conducted to provide flow distribution between SH and LRR holes. EHS/EMS models validated separately against SH and LRR tests were implemented in ANSYS FLUENT and several simulations were conducted.

The remainder of the paper is structured as follows: Section 2 presents the facility of PANDA experiments, Section 3 the numerical schemes for simulations, and Sections 4 and 5 the results of pre-test simulations and conclusions.

2 PANDA EXPERIMENT

PANDA [14] is a multipurpose test facility designed to address containment thermal-hydraulics phenomena and safety issues in Light Water Reactors (LWRs). The facility contains 2 drywells, 2 wetwells, 1 Gravity Driven Cooling System (GDCS) tank, and an RPV vessel with a steam generator of 1.5 MW. All the sparger experiments were performed in one of the wetwell vessels as shown in Figure 1. The pool is filled with water up to 6 m at room temperature 15°C or more in different cases. Interconnecting pipe (IP) is blocked by an iso-thermal lid to reduce the heat loss.

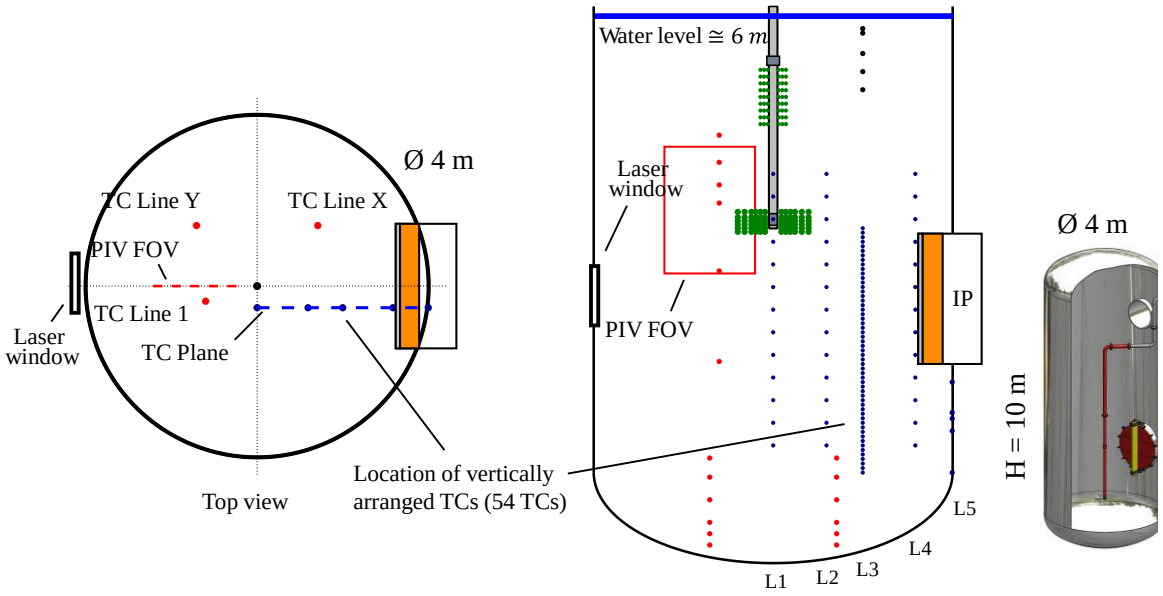

Figure 1. Proposed instrumentation for future PANDA test. Details can refer to Section 4.3.

The geometrical specifications of the sparger placed along the central axis of the pool is illustrated in Figure 2. The multi-hole SH contains 32 holes arranged in 4 rings to inject steam radially outwards, and the LRR contains 8 holes in 1 ring to inject steam vertically downward. LRR is designed in the plant to reduce dynamic loads on the sparger pipe, and it is located at 1.8 m above the SH. Each hole has an inner diameter of 9.5 mm and a conical chamfer. The hole at the tip of the sparger was blocked during the test.

The safety relevant phenomena studied in this work are the development of thermal stratification and the dependence of the erosion rate of thermocline on the steam injection and pool conditions. The regimes that are expected during most of the anticipated scenarios are sub-sonic condensation regimes where the maximum steam flux can reach ~200 kg/(m^{2}s). Therefore, the injection conditions were designed in these regimes (Figure 3). The steam injection usually started with a low flux (minimum flux to avoid internal chugging) to enable the development of thermal stratification in the pool. After reaching a stable thermocline, the mass flow was increased to erode the stratified layer.

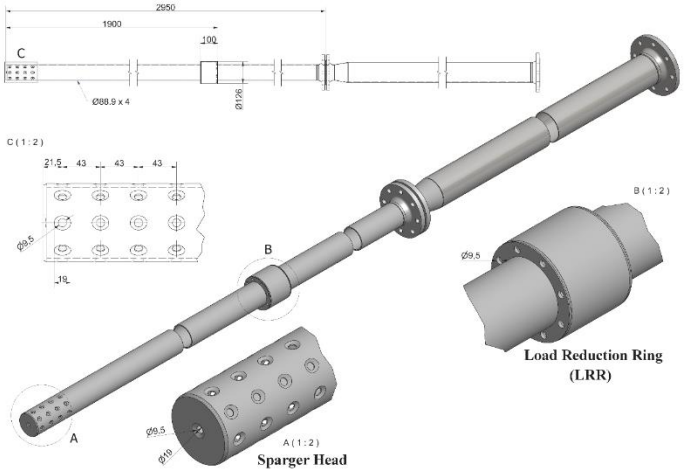

Figure 2. Geometry of the sparger pipe [12].

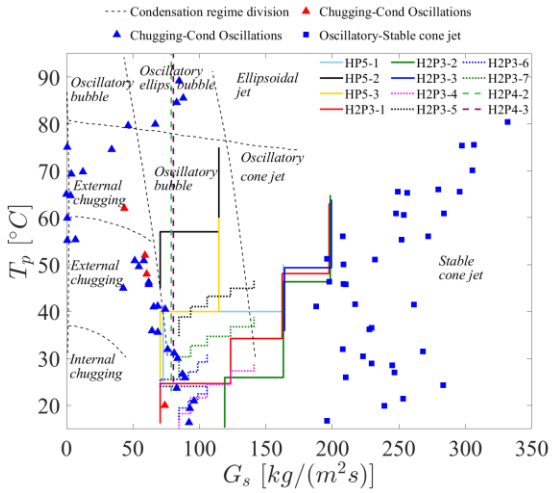

Figure 3. Trajectories of PANDA HP5 [12], H2P3, and H2P4 [13] tests with sparger on condensation regime map, using Chan & Lee [16] and Song et al. [15] data. G_s is the steam flux and T_p is the pool temperature.

3 NUMERICAL SCHEME

EHS/EMS models with "Unit Cell" implementation for modeling of steam injection through a sparger pipe were implemented in ANSYS Fluent 2021 R2 [23] with a single-phase solver. Water properties were determined by piecewise polynomial profiles as functions of temperature. Energy equation was turned on to include the effect of buoyancy and the dynamic mesh was used to enable the motion of the pool surface to accommodate increasing water pool level. All simulations were considered fully converged with the residual below 1e-6 for energy and 1e-4 for the other variables. Details of the modeling setups can be found in [6][22].

3.1 EHS/EMS models

Effective momentum source for subsonic steam flow conditions (steam flux $G \leq 300\ kg/m^2\ s$) has been measured in the Separate Effect Facility (SEF) with respect to a large range of injection conditions of a Nordic BWR sparger [17]. It can be written as:

$$\dot{M}_{eff} = C\dot{M}_{th} = C\rho_s A_0 U_s^2 = \rho_l A_{eff} U_{eff}^2 \quad (1)$$

$$C = 4.28\Delta T^{-0.35} \quad (2)$$

where A_{eff} and U_{eff} are the effective hole area and velocity of the liquid to reproduce the effects induced by the steam injection; ρ_s and ρ_l are the density of steam and liquid; U_s is the velocity of steam and A_0 is the area of the orifice. C is the condensation regime coefficient [17] utilized to evaluate how much momentum is transferred from the steam to mean flow liquid under certain subcooling.

The effective heat source $\dot{q}_s$ is estimated by the EHS model as:

$$\dot{q}_s = \dot{m}_s h_s \quad (3)$$

where h_s and h_l are the enthalpy of the steam and liquid.

3.2 "Unit Cell" implementation

Thermal stratification and mixing in a large pool are determined by a competition between buoyancy and momentum induced by the injected steam. Velocity of the jet in the downstream of steam condensation region develops a self-similarity profile similar to the single-phase turbulent jet [14]. Modeling of individual jets induced by steam injection through multi-hole SH and LRR holes can be achieved by using single-phase liquid with the effective momentum and heat estimated by Eqs. (1)~(3).

This approach is called "Unit Cell" implementation and is illustrated in Figure 4a. EHS/EMS models were introduced by imposing boundary conditions (see Section 3.3) at the sparger surface. By doing this, the interaction among the individual jets from multi-hole SH as well as the interaction between the LRR jets and merged SH jets can be resolved to provide a better understanding of the local phenomena in the vicinity of the sparger.

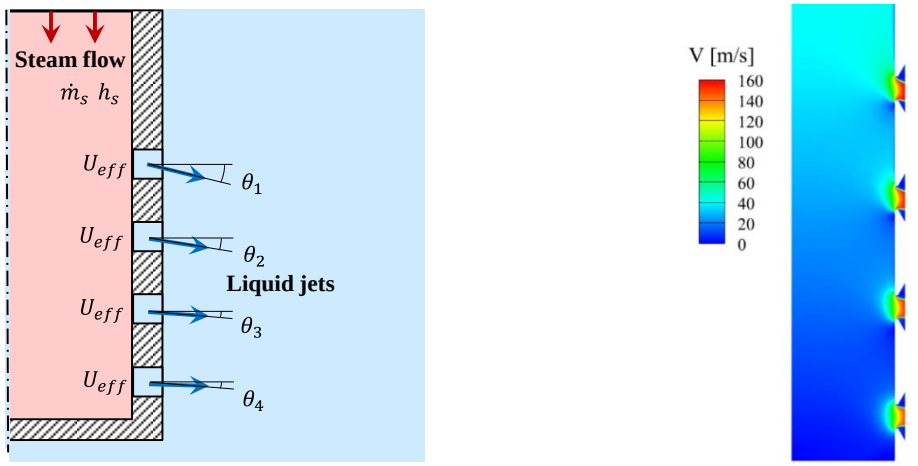

(a) (b)

Figure 4. (a) Schematic of "Unit Cell" implementation for SH and (b) velocity contours obtained by internal flow simulation of PANDA sparger using steam with $\dot{G}_s = 71\ kg/m^2 s$ [22].

The computational domain for the PANDA pool with "Unit Cell" implementation is presented in Figure 5. The height of the water level and sparger tip are 4 m and 3.7 m above the bottom of the pool. Previous study [8] suggests that a $1/16$ sector domain (22.5°) is insufficient to resolve the flow pattern in the pool. Both 180° and 360° domains can provide reasonable results for temperature evolution. Thus, we use the 180° domain in this work to improve computational efficiency.

The pool mesh was created with polyhedral cells on the surface and hexahedral cells inside the fluid region (poly-hexacore meshing in ANSYS [23]). Smooth transition from the sparger tip to the surrounding wall was applied and the mesh below the sparger tip was refined in order to better capture the evolution of thermocline. Mesh sensitivity study of similar geometry can refer to this work [10].

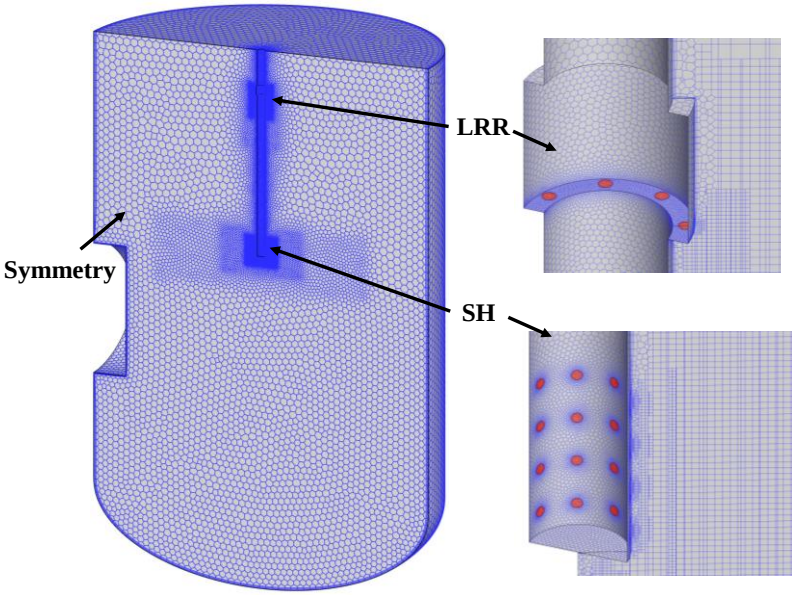

Figure 5. Computation domain of PANDA pool.

3.3 Boundary conditions

For jets discharged from LRR holes, the steam flow rate was assumed evenly distributed and normal to the inlet surface. While for the SH injection, the distribution of the steam flow and its downward angles among different elevations were determined by an internal flow simulation (Figure 4b). The simulation results [22] suggest the variation of these angles toward different steam fluxes (70~160 kg/m^2s) varies little, providing averaged angles of $14°, 12°, 9.5°, 0°$ from up to down. Similarly, the difference in steam flow rates among different holes is within $\pm 2.0\%$ and a uniform distribution was assumed. The flow distribution between LRR and SH holes is obtained from internal flow simulations and summarized in Table **1**

Table 1. Steam distribution through PANDA sparger with different flow rates.

Flow rates [g/s]	**LRR**		**Sparger head**	
	Steam flow [g/s]	Steam flux [kg/(m^{2}s)]	Steam flow [g/s]	Steam flux [kg/(m^{2}s)]
160	62.1	109.6	97.9	43.1
260	72.1	125.1	187.9	82.9
360	85.1	150.2	274.9	121.2
450	100.7	177.6	349.3	154.0

The effective liquid jet was introduced by providing the uniform velocity profile at the injection holes (Figure 4a) with a diameter of 9.5 mm. According to Eqs.(1), (2), the magnitude of velocity can be written as:

$$U_{eff} = \sqrt{\frac{C\rho_s}{\rho_l}} U_s \tag{4}$$

Since the momentum created by steam was modeled by water injection, the respective mass flow rate of water was higher than that of steam injection. To preserve the mass balance, a fraction of injected water should be taken out from the pool with a total mass flow rate given by Eq. (5).

$$\dot{m}_{out} = \dot{m}_{in} - \dot{m}_s \tag{5}$$

where $\dot{m}_{in}$ is the total mass flow rate of the effective liquid and $\dot{m}_s$ the mass flow rate of steam. the water that should be removed $\dot{m}_{out}$ applied on the pool surface.

Heat balance was achieved by the time-averaged heat source provided by the EHS model given by Eq. (3). In these cases, when mass was taken out from the pool, the energy would be removed too. Therefore, to preserve the heat balance, the enthalpy of the injection water h_l^{in} should be defined such that:

$$\dot{q}_{in} = \dot{q}_s + \dot{q}_{out} \tag{6}$$

$$h_l^{in} \cdot \dot{m}_{in} = h_s \cdot \dot{m}_s + h_l^{out} \cdot \dot{m}_{out} \tag{7}$$

The h_l^{in} is implemented by setting the temperature on inlet boundary according to Eq. (8).

$$T^{in} = \frac{h_l^{in}}{C_p} \tag{8}$$

where sub-indexes l and s are indicating liquid and steam respectively, in and out are indicating the input and output, C_p and T are the specific heat capacity and water temperature, respectively.

3.4 Turbulence model

Stable stratification with a significant temperature difference between the cold and hot layers was observed in all PPOOLEX and PANDA experiments. The development of the stratified layer is governed by buoyancy, which is modelled by the temperature-dependent water density. To model the effect of buoyancy on turbulence, source terms for turbulent kinetic energy k and specific dissipation rate ω were modified respectively. Details of the turbulence model implementation can be found in [6].

The turbulence model was $k-\omega$ BSL model with low-Re corrections which provided the best agreement between prediction and experimental temperature evolution in PANDA & PPOOLEX pool tests [6]. Kato-Launder production term and production limiter are turned on to limit the build-up of k in the stagnation regions (i.e. the cold layer below the thermocline).

Extremely high turbulent intensity was observed in PIV measurement in PANDA tests [12] with steam injection in the oscillatory bubble regime. Measurement in SEF tests [24] suggests that with the same amount of effective momentum, the jet induced by steam injection diffuse much

more than the liquid injection. Previous validation against PANDA and PPOOLEX pool tests showed that a good agreement on temperature evolution can be achieved if a high-level turbulence (e.g., turbulence intensity I=70%, and turbulent viscosity ratio μ_t/μ_l = 3000) is introduced at the inlet boundaries [9][10].

However, this high level turbulence introduced by setting large I and μ_t/μ_l on inlet boundaries dissipated rapidly by using RANS turbulence models as those models were calibrated against single phase turbulence flow. In reality, turbulence is not generated at the inlet but in the downstream region where the interface of condensing steam creates rapid motion of the ambient liquid. Therefore, an extra source term S_k that represents the effect of condensation induced turbulence is introduced in the transport equation of k and it can be written as:

$$S_k = \begin{cases} \frac{3}{2}\left(v_m I_{eff}\right)^2 \rho_l \frac{1}{\tau} \ , & v_m \geq U_{eff} C_{limit} \\ 0, & v_m < U_{eff} C_{limit} \end{cases} \quad (9)$$

where v_m and U_{eff} are cell velocity and effective velocity; I_{eff} is introduced to relate the generation of turbulence to local average velocity v_m and is called an "effective turbulent intensity"; τ is a characteristic time scale (assumed to be unity), ρ_l is liquid density. C_{limit} is a global filter based on the local averaged velocity that determines the region where S_k should be imposed (assuming that turbulence is actively generated in the region where local velocity is larger than $U_{eff}C_{limit}$). In this work, $I_{eff} = 2.5$ and $C_{limit} = 0.1$ were applied. Model validation and parameters analysis can be found in [22].

4 RESULTS AND DISCUSSION

The test planned in PANDA project aims to investigate the thermal stratification induced by steam injection through the sparger. The goal is to obtain data on how the development and erosion of the thermocline are affected by (i) activation of both SH and LRR holes (ii) the high temperature gradient across the thermocline. CFD simulations conducted for pre-test analysis are summarized in **Error! Reference source not found.** and the results are used to determine the test conditions of (i) elevation of sparger tip above pool bottom, (ii) flow rate and duration in each injection phase, and (iii) configuration of instrumentation.

Table 2. List of simulations carried out for pre-test analysis.

Case	Holes opened?		Phase 1		Phase 2		Phase 3		Phase 4	
	SH	LRR	Flow rate[1]	Duration	Flow rate	Duration	Flow rate	Duration	Flow rate	Duration
	-	-	g/s	s	g/s	s	g/s	s	g/s	s
C1	Yes	No	97.9	6000	187.9	4000	274.9	4000	349.3	4000
C2	No	Yes	62.1	6000	72.1	4000	85.1	4000	100.7	4000
C3	Yes	Yes	160	6000	260	4000	360	4000	450	4000
C4	Yes	Yes	160	12000	260	6000	360	3000	450	3000
C5	Yes	Yes	160	18000	260	6000	360	4000	450	4000

[1] Total steam flow rate through the pipe. The distribution between LRR and SH holes can refer to Table 1.

Simulation with a sparger placed 2.5 m above the pool and opening of both LRR and SH holes suggests that the thermocline might be completely eroded at the end of the injection phase with $\dot{m}_s = 450 g/s$. Meanwhile, a larger submergence also requires a longer injection time to achieve

a strong stratification. Therefore, the sparger was lifted from 2.5 m to 3.7 m, leaving 0.5 m between LRR holes and the pool surface. All simulations were running with a 6 m water level and 15 ℃ initial pool temperature.

4.1 Interaction between LRR and SH injections

The interaction between LRR and SH injections was studied in Cases C1~C3 in which LRR and SH holes were opened individually and then opened together (**Error! Reference source not found.**). The steam flow rates in C1 and C2 were set to ensure the injected steam creates the identical amount of momentum source at LRR or SH holes compared to C3 (Table 1).

The snapshots of temperature fields among these three cases obtained at end of second injection phase are shown in Figure 6. It can be found that the mixing efficiency was reduced when opening both LRR and SH holes compared to activation of only LRR holes. This is because that the downward flow from the LRR was deflected by the jets from the SH (Figure 7b), reducing the momentum directed toward the cold layer. Meanwhile, the buoyancy-dominant flows from SH where the jets were bending upward by the strong buoyancy can be deflected downward by the jets from LRR and thus enhance the pool mixing compared to activation of only SH holes.

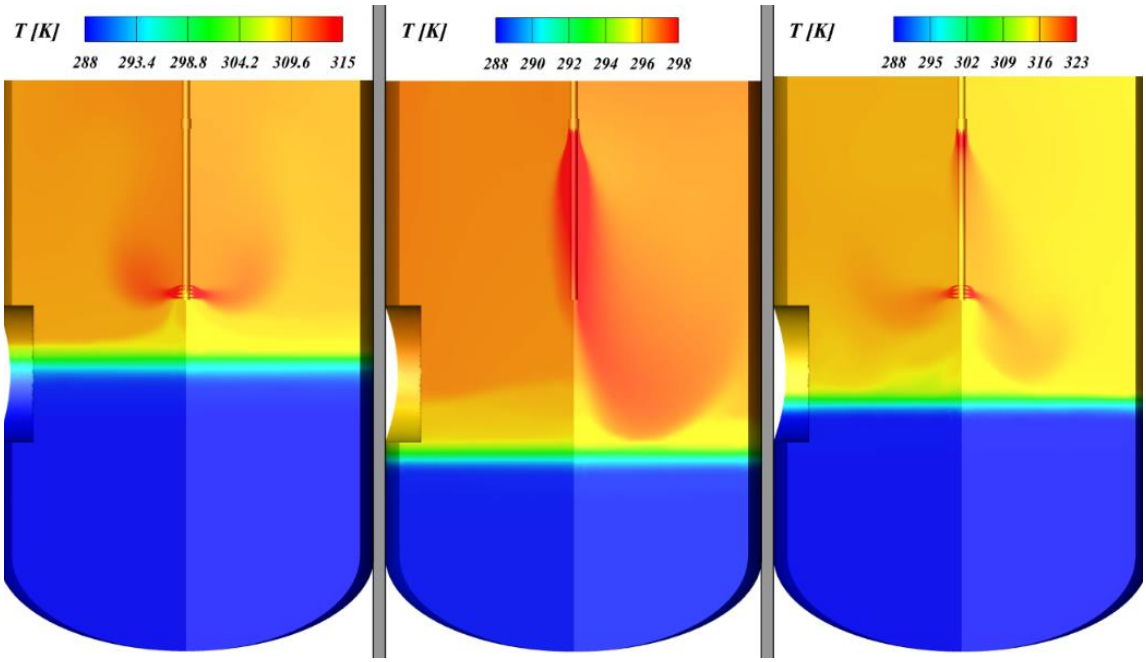

(a) (b) (c)

Figure 6. Temperature contours obtained in cases with opening of (a) SH holes, (b) LRR holes, and (c) SH and LRR holes at $t = 10000s$.

The comparison in Figure 8 indicates that the elevation of thermocline with activation of both SH and LRR is between the cases where only one of them opened during the whole transient. However, exceptions can be found if the distance between LRR and SH increases. Two additional conditions can be expected, i.e., (i) two stratified layers are developed if the momentum created by LRR injection is relatively small, developing a thermocline above the SH whereas jets from SH injection develops another thermocline below the SH, (ii) the elevation of the thermocline of opening both holes is lower than activation of any of them if the jets created by LRR are not sufficient to penetrate further than the jets from SH but just enough to further deflect the SH jets

downward. In the second way, the pool mixing efficiency is enhanced compared to activation of only one of them.

Asymmetry flow pattern and temperature distribution of LRR jets were observed in all injection phases except for phase 1 (Figure 7). It was also reported in previous PANDA LRR tests [25] where the temperature measured from one TC shows higher oscillation and magnitude compared to the one from its mirrored position. These low frequency and high amplitude temperature oscillations were confirmed to be caused by large-scale fluid motions. Later on, CFD simulation provides a good agreement on both temperatures and an asymmetry flow was observed in which the jets induced by LRR injection firstly attached to the sparger pipe and then slightly inclined to the IP side, resulting in an opposite direction compared to the jets in Figure 7b. In current simulations, both inclined directions (either near or far from the IP) are observed and the reason is still unclear. This asymmetry pattern and unpredictable direction will impose difficulty in preparing the PIV plane and possible TCs grid.

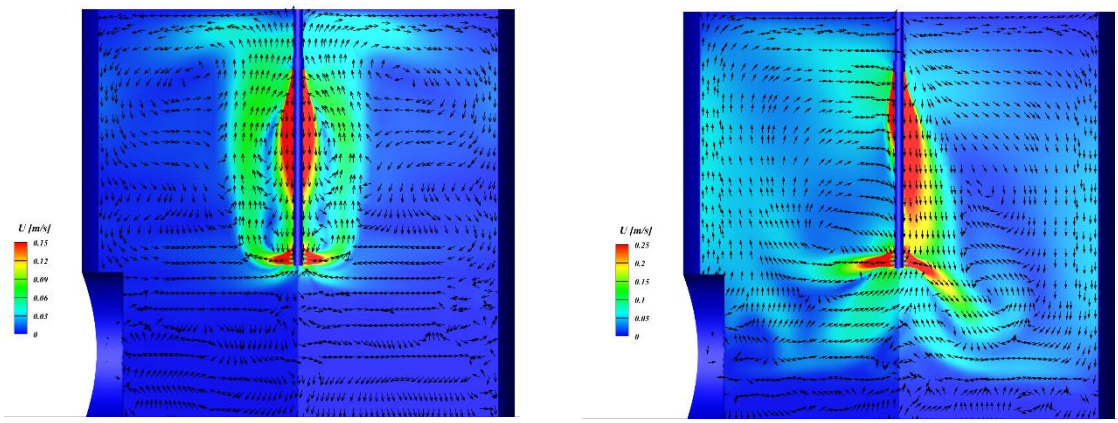

(a) (b)

Figure 7. Velocity contours obtained in case C3 with opening of SH and LRR holes at (a) $t = 6000s$ and (b) $t = 10000s$.

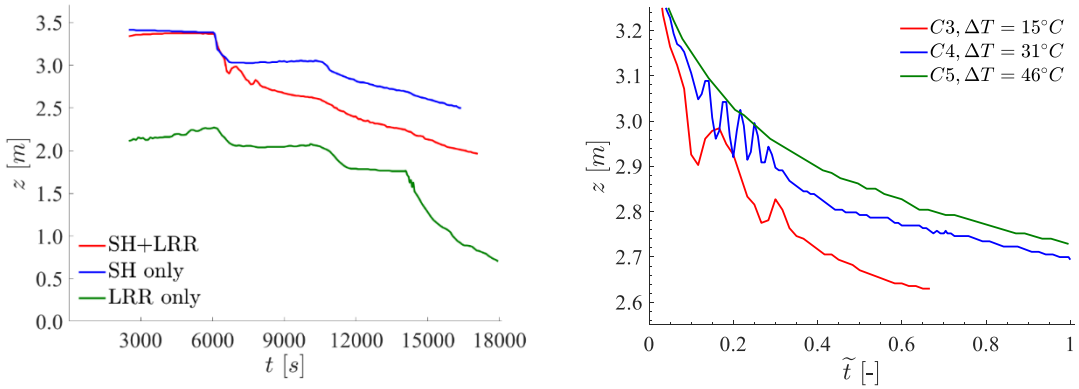

(a) (b)

Figure 8. Comparison of thermocline evolution among cases (a) C1~C3 and (b) C3~C5 at injection phase 2 where $\tilde{t} = (t - t_1)/6000$ (t is the injection time, t_1 the duration in phase 1), ΔT the temperature difference across the thermocline at the end of phase 1 (Figure 9).

4.2 Injection procedures

The 6000s injection period in phase 1 created a stratified layer with a temperature difference of ~15℃ (Figure 9). Given the goal of the test is to study the effect of high temperature gradient on the evolution of thermocline, simulations with a longer injection period in phase 1 were performed, resulting in a difference of 31℃ by 12000s duration and 46℃ by 18000s duration. It can be found from Figure 8b that the erosion velocities are reduced when the temperature difference of the thermocline increases. A stronger stratified layer leads to a larger buoyancy force that can resist the vertical momentum to erode the thermocline.

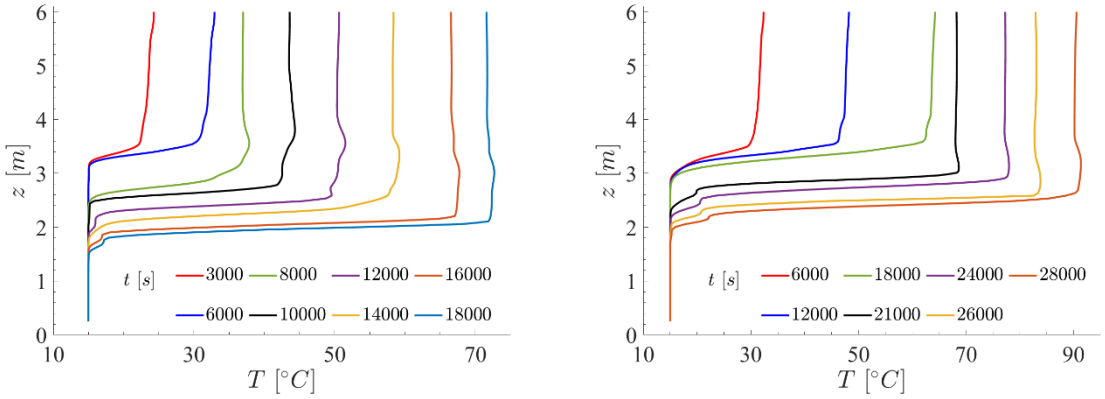

(a) (b)

Figure 9. Vertical temperature profiles in (a) C3 and (b) C5.

The stable or quasi-stable thermocline where the erosion velocity tends to zero was achieved only in the first injection phase (Figure 8a). A 4000~6000s duration seems insufficient for the rest of the phases to develop a stable thermocline. Extending the duration of each phase will lead to a too long overall time and the pool could become saturated. Therefore, we decide to keep 6000s in the first injection phase and increase the duration of the second phase to 12000s. By doing so, we are likely to obtain stable thermal stratification at the end of phase 1&2 and achieve a high temperature gradient at the end of the second phase. The rest of the two phases are set to 4000s to keep the overall time reasonable. The proposed injection procedures are shown in Table 3.

Table 3. Injection procedures proposed for PANDA shakedown test.

Case	Holes opened?		Phase 1		Phase 2		Phase 3		Phase 4	
	SH	LRR	Flow rate[1]	Duration	Flow rate	Duration	Flow rate	Duration	Flow rate	Duration
	-	-	g/s	s	g/s	s	g/s	s	g/s	s
P1A6-1	Yes	Yes	160	6000	260	12000	360	4000	450	4000

4.3 Instrumentation

In previous PPOOLEX sparger tests [19], a 6×7 TC grid with a minimal interval of 36 mm was placed 50 mm from the SH. Temperature measured by this grid provides valuable information for the understanding of jet induced by steam injection and was used for validation of CFD simulations [22]. In this test, similar arrangements are proposed to measure the temperature profiles of the jet discharged from LRR and SH holes.

For LRR jet, the configuration of the TC grid is designed to enable the measurement of the main flow feature as shown in Figure 10b. The space between each column and row of TCs is 40 mm and 75 mm respectively, and the innermost column is 20 mm away from the sparger wall. Placing two grids symmetrically is preferable as it can capture potentially asymmetrical LRR jets.

Figure 11 illustrated the configuration of the TC grid for the SH jet. Two typical flow patterns were observed in previous tests [22], one is buoyancy-dominant flow in the low steam flux phase (Figure 11a) where the downward jets were bending upward by the relatively strong buoyancy and another one is inertial-dominant flow (Figure 11b) in which the buoyancy is insufficient to overcome the inertial, resulting in downward jets. The grid is arranged to capture both flow patterns. The space between each row is 40 mm except for the first two rows which has a space of 60 mm. The innermost column is 50 mm from the sparger wall and it is placed every 50 mm until last three columns with a larger distance of 75 mm.

The comparison of contours between velocity and temperature at the same moment suggests a possibility that the velocity field can be inferred from the temperature measurement. Their relationship can also be observed by looking at the Navier-Stokes (N-S) equations for incompressible buoyant flow. Work done in [26] used Physics-Informed Neural Networks (PINNs) to infer the 3D velocity and pressure fields from 3D temperature fields induced by flow over an espresso cup. The temperature measurement was obtained by Tomographic background-oriented Schlieren (Tomo-BOS) imaging and was trained by PINNs to minimize the loss function derived from N-S equations.

Measurement obtained by TC grids can be regarded to sever a similar function to the results from Tomo-BOS but in an extremely coarse resolution. The mapping from sparse measurement (e.g., TC grid) to full field could be solved by introducing extra information such as simulation results by CFD with similar boundary conditions. Afterward, this complete temperature field can be used to infer the velocity as introduced in [26]. The above discussion on the possibility of using sparse temperature measurement to infer full field velocity will be investigated in future work.

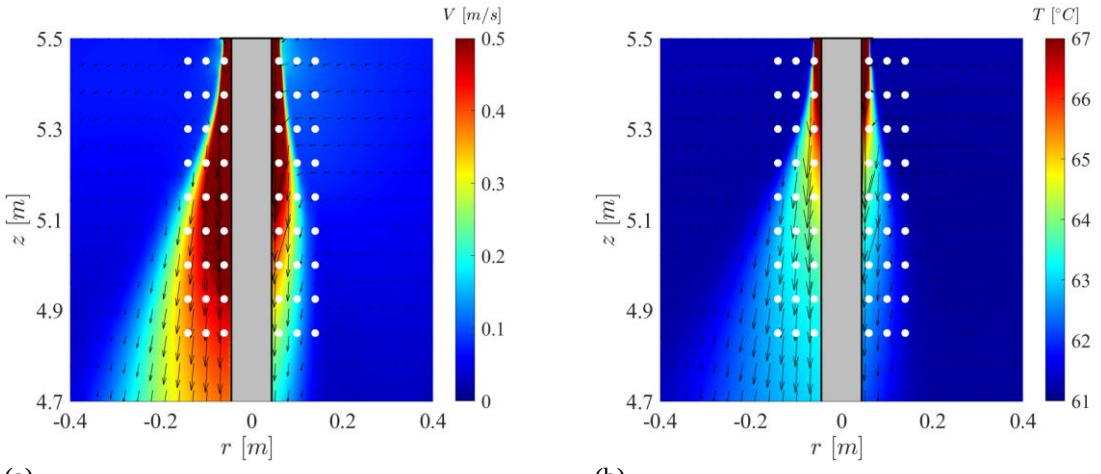

(a) (b)

Figure 10. TC grid arrangement for measuring jets from LRR with (a) velocity and (b) temperature contours at end of second injection phase (18000s) in C4.

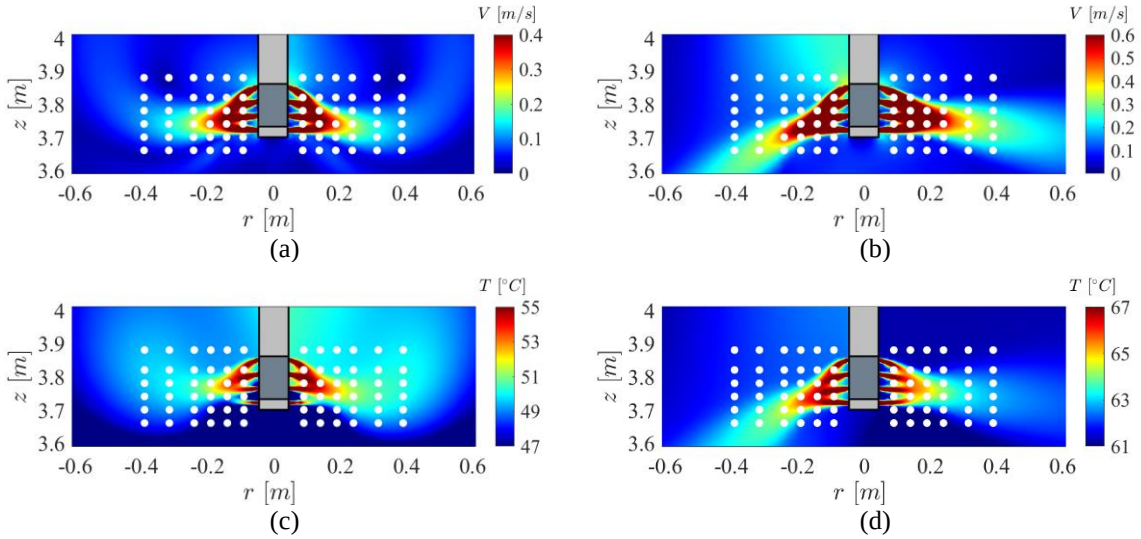

Figure 11. TC grid arrangement for measuring jets from SH with (a)(b) velocity and (c)(d) temperature contours at end of (a)(c) first (12000s) and (b)(d) second (18000s) injection phases in C4.

PIV measurements will also be planned in this work. In PANDA H2P3 experiments [13][25], two PIV planes with each of size $1000 \times 700\ mm$ were combined together to provide a larger Field of View (FOV) and were placed in front of the SH orifice (similar to the one in Figure 1) with a distance of $400\ mm$ to reduce the effect of steam condensation. It provided a reasonable measurement for jets from SH but failed to capture the main flow characteristics of the LRR jet. A small portion of the flow field that closes to the shear boundary of the downward jet was captured by a few snapshots and most of the measurements cover the region in which only secondary upward jets was available (Figure 12a).

In this work, we propose two options that might be considered in future experiments. Option A still combines two planes together but moves closer to the sparger with a distance of $200\ mm$ away from the sparger wall (Figure 12). The near field information of SH jets might be lost caused by strong condensation but the $1000\ mm$ size in radial direction should be enough to measure the downstream flow. To increase the possibility of capturing the downward part of the jet from LRR, the distance from the sparger wall can be even reduced. If possible, option B which separately places these two planes (Figure 13) could provide better results for both jets. Overlapping of the TC grid and PIV plane is recommended to provide cross-validation results for both measurements.

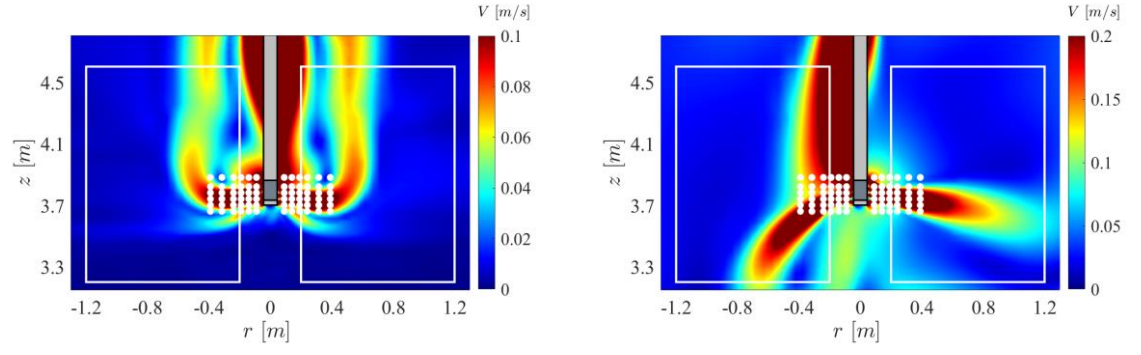

Figure 12. Option A of PIV arrangement for measuring jets from SH and LRR with velocity contours at end of (a) first (12000s) and second (18000s) injection phases in C4.

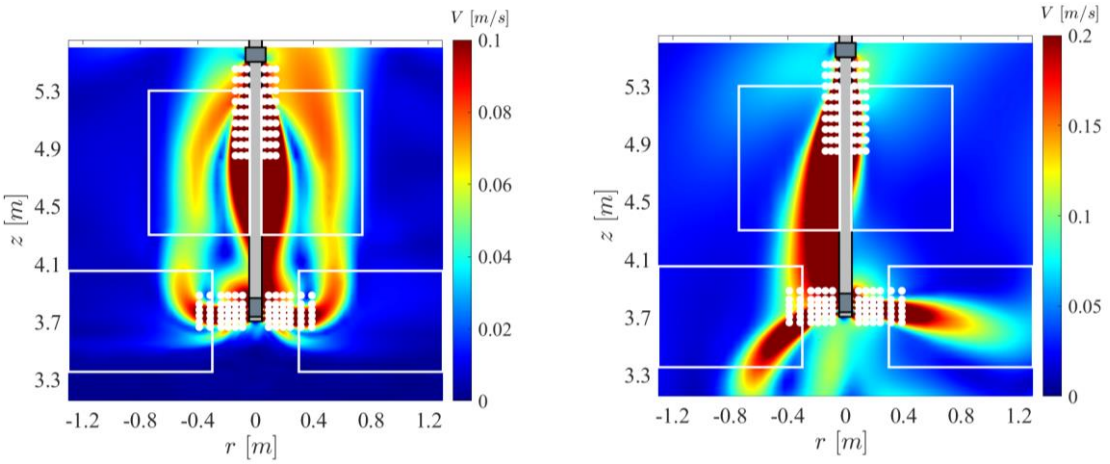

(a) (b)

Figure 13. Option B of PIV arrangement for measuring jets from SH and LRR with velocity contours at end of (a) first (12000s) and second (18000s) injection phases in C4.

The remaining TCs used to measure the global pool behavior is proposed as illustrated in Figure 1. Since the elevation of the thermocline obtained from CFD simulations varies from 3.7 m to 2 m, a TC plane which contains 5 trains of TCs is planned to cover the elevation from $1m$ to $3.7m$. It is important to prepare at least one train of TCs with a fine spatial resolution (50 mm) along vertical direction to provide data on thermocline erosion. This fine resolution TCs should be placed far away from the sparger pipe with at least $1000\ mm$ distance to avoid the effect of local flow circulation. Other trains with coarse resolution could be applied to provide complementary results to resolve the thermal behavior of the pool. One train with a larger interval should be sufficient for measuring uniform temperature above the injection orifice.

5 CONCLUSIONS

Pre-test simulations have been performed to support the definition of the PANDA P1A6 shakedown test. The EHS/EMS models were implemented in ANSYS CFD code to resolve the steam injection into a subcooled pool through a sparger. Scoping calculations are carried out to specify geometrical setup, instrumentation, and injection procedures.

ACKNOWLEDGEMENTS

The authors are thankful to the Swedish Radiation Safety Authority (SSM) for support of the authors participation in the OECD/NEA HYMERES, HYMERES-2, and PANDA projects. The authors are grateful for feedback and discussions with the experts of the PANDA project reference group, and especially to the members of PANDA experimental team led by Dr. Domenico Paladino. The authors are also thankful to support from NKS (Nordic Nuclear Safety Research) for the NKS-THEOS project. The computations were enabled by resources provided by the Swedish National Infrastructure for Computing (SNIC) at SNIC CENTRE, KTH partially funded by the Swedish Research Council through grant agreement no. 2018-05973"

REFERENCES

[1] Pershagen, B., Light Water Reactor Safety. Pergamon Press. 1994.

[2] Li, H., Villanueva, W., Kudinov, P., Approach and Development of Effective Models for Simulation of Thermal Stratification and Mixing Induced by Steam Injection into a Large Pool of Water. *Science and Technology of Nuclear Installations*, Article ID 108782, 2014.
[3] Tanskanen, V., Jordan, A., Puustinen, M., Kyrki-Rajamäki, R., CFD simulation and pattern recognition analysis of the chugging condensation regime. *Annals of Nuclear Energy*, 66, 133-143, 2014.
[4] Patel, G., Tanskanen, V., et al. Direct contact condensation modeling in pressure suppression pool system. *Nuclear Engineering and Design*, 321, pp. 328–342, 2017.
[5] Li, H., Villanueva, W., Puustinen, M., Laine, J., Kudinov, P., Validation of Effective Models for Simulation of Thermal Stratification and Mixing Induced by Steam Injection into a Large Pool of Water. *Science and Technology of Nuclear Installations*, Article ID 752597, 2014.
[6] Gallego-Marcos, I., Kudinov, P., Villanueva, et al., "Pool Stratification and Mixing Induced by Steam Injection through Spargers: CFD modeling of the PPOOLEX and PANDA experiments", *Nucl. Eng. Des*, 347, 67-85, 2019.
[7] Wang, X., Grishchenko, D., Kudinov, P. "Pre-test analysis for definition of steam injection tests through multi-hole sparger in PANDA facility", *Nucl. Eng. Des*, *386*, 111573, 2021.
[8] Wang, X., Grishchenko, D, Kudinov, P. "Development of Effective Momentum Model for Steam Injection Through Multi-Hole Spargers Using a Condensation Region Approach", ICONE-2020. Virtual, Online. August 4–5, 2020.
[9] Wang, X., Grishchenko, D, Kudinov, P. "Development of Effective Momentum Model for Steam Injection Through Multi-Hole Spargers: Unit Cell Model". ICONE-28. Virtual, Online. August 4–6, 2021.
[10] Wang, X., Grishchenko, D., Kudinov, P. "Modeling of large pool response to steam injection through spargers using A "UnitCell" model", NURETH-19, Brussel Belgium, March 6–11, 2022.
[11] Laine, J., et al., "PPOOLEX Experiments with a Sparger," *Nordic Nuclear Safety Research*, NKS-334, 2015.
[12] Gallego-Marcos, I., Villanueva, W., Kudinov, P., et al., Pool Stratification and Mixing Induced by Steam Injection through Spargers: analysis of the PPOOLEX and PANDA experiments. *Nuclear Engineering and Design*, 337, 300-316, 2018.
[13] Paladino D., Kapulla R., Paranjape S., Suter S., Andreani M., PANDA experiments within the OECD/NEA HYMERES-2 project on containment hydrogen distribution, thermal radiation and suppression pool phenomena. Nuclear Engineering and Design, 392, 111777. 2022.
[14] Paladino, D., Dreier, J., PANDA: a multipurpose integral test facility for LWR safety investigations. *Science and Technology of Nuclear Installations*, Article ID 239319, 2012.
[15] Song, C.H., Cho, S., Kang, H.S., Steam Jet Condensation in a Pool: From Fundamental Understanding to Engineering Scale Analysis. *Journal of Heat Transfer*, 134, 031004-1, 2012.
[16] Chan, C.K., Lee, C.K.B., A regime map for direct contact condensation. International Journal of Multiphase Flow, 8 (1), 11-20, 1982.
[17] Gallego-Marcos, I., et al., Effective Momentum Induced by Steam Condensation in the Oscillatory Bubble Regime. *Nuclear Engineering and Design*, 350, 259-274, 2019.
[18] Kang, H.S., Song, C.H., CFD analysis of a turbulent jet behavior induced by a steam jet discharge through a single hole in a subcooled water tank. *Nuclear Engineering and Design*, 240, 2160-2168, 2010.
[19] Laine, J., Puustinen, M., Räsänen, A., PPOOLEX Experiments with a Sparger, *Nordic Nuclear Safety Research*, NKS-334, 2015.
[20] Chan, C.K., Lee, C.K.B., A regime map for direct contact condensation. *International Journal of Multiphase Flow*, 8, 11-20, 1982.

[21] R.J.E. Van Wissen, et al., Particle image velocimetry measurements of a steam-driven confined turbulent water jet. Journal of Fluid Mechanics 530, 353-368. 2005.
[22] Wang, X., Grishchenko, D, Kudinov, P. “Simulation of Jets Induced by Steam Injection through Multi-hole sparger using Effective Heat and Momentum Models”, (Submitted to *Nuclear Engineering and Design*)
[23] ANSYS® Fluent Theory Guide, Release 2021 R2.
[24] Yun, F., Wang, X., Grishcehnko, D., Kudinov, P. Measurement of velocity induced by steam condensation into a water pool by tracking the motion of bubbles”, NUTHOS-13, Hsinchu, Taiwan, September 5-10, 2022.
[25] Kudinov, P., Wang, X., Feng, Yun., et al., Thermal Hydraulic Phenomena of the Suppression Pool. NKS-THEOS Report, NKS-465, 2022.
[26] Cai, S., Wang, Z., Fuest, F., et al., Flow over an espresso cup: inferring 3-D velocity and pressure fields from tomographic background oriented Schlieren via physics-informed neural networks. Journal of Fluid Mechanics, 915, A102, (2021).

U.S.NRC
United States Nuclear Regulatory Commission
Protecting People and the Environment

Center for Advanced Small Modular and Micro Nuclear Reactors
Texas A&M Engineering Experiment Station

NEA
NUCLEAR ENERGY AGENCY

Technical Session 5

Numerical Studies

Feb 20, 15:45-17:15, Room A.

CFD FOR NATURAL CIRCULATION FLOWS: NUMERICAL INVESTIGATIONS WITH TRIOCFD FOR A PITCHFORK BIFURCATION IN THE FRAMEWORK OF SYSTEM SCALING UNCERTAINTY QUANTIFICATION

Haifu HUANG[1, 2], Jorge PEREZ[1], Nicolas ALPY[1], Marc MEDALE[2]

[1] French Alternative Energies and Atomic Energy Commission, DEN, DER, F-13108 Saint Paul lez Durance, France
[2] Aix-Marseille University IUSTI, UMR 7343 CNRS, Technopôle de Château-Gombert, Marseille, France

Extended Abstract

To enhance safety, nuclear power plants under conception rely on passive mechanisms such as natural convection for decay heat removal. Simulations consist in solving a system of equations to model the nonlinear physics that drives flow dynamic start-up and stability. The actual bottleneck in performing CFD computation of such problem at the actual plant scales is that the classical turbulence models (K-eps, wall functions, etc.) are not very suitable in such natural flow configurations, where the presence of thresholds, bends, etc. can induce very specific behaviors. Besides, for different spatial and time discretizations and related resolutions, a classical engineering question arises from a fine balance between the accuracy of a targeted figure of merit (FOM) and CPU costs. Regarding code qualification for nuclear safety, this question should be extended by considering the ability of the numerical approach for system scaling that could indeed jeopardize the reliability of reactor case simulations. Therefore, in this paper we present an approach that enables to objectify the choices of numerical models and algorithms and turbulence models, towards a high fidelity approach. Then, uncertainty and sensitivity analyses could be applied to reveal and quantify the scaled effects with given simulations for natural circulation.

This work focuses on the stability analysis of a natural circulation loop with horizontal heater and horizontal cooler (HHHC) to highlight some numerical challenges. DNS and turbulent models LES/URANS are performed in 2/3D with CEA in-house code TrioCFD, using the Boussinesq's approximation. The spatial discretization is performed by a hybrid-differencing scheme for advective terms along with second order approximation for the diffusion term in both momentum and energy equations. For turbulent models, with poor prediction of eddy motions by standard κ-ε model, the limitations of standard wall functions have led to consideration of fully wall resolved solutions for LES. The HHHC loop configuration has the peculiar potential to define two stability boundaries. A critical Rayleigh number is characterized at the onset of convection, which is a pitchfork bifurcation, so clockwise and anti-clockwise steady-state solutions are indeed obtained by CFD. Interestingly, one can take advantage of the numerical noise arising from the iterative solution algorithm to reduce the CPU costs related to the flow activation time. Going further in this direction, the introduction of a synthetized noise is shown to accelerate the computations of the metastable state without degrading the accuracy for next spatial convergence analysis. The second stability boundary is related to the transition from steady state to unsteadiness, when increasing the Rayleigh number, a linear trend of the corresponding mean cross-sectional velocity squared is firstly captured, where a dynamic instability can be faced. Inline, the HHHC loop is highlighted through CFD results as a promising academic topology in order to couple scaling distortions due to physics (e.g. arising from buoyancy, cross-flow and turbulence developments that could change with the scale) with bias due to numerical modelling.

A point to be investigated regarding flow with stability boundary is to map the possible uncertainty growth - with scales and numerical approaches - of its position that could indeed challenge the confidence in the safe operating distance (as a FOM). Methodological progresses regarding scaling uncertainty evaluation are inline provided for this peculiar point. First, for a given topology, a Grid Convergence Index (GCI) methodology is applied to quantify the discretization uncertainties according to a 2D approach. The critical Rayleigh number is then bounded by propagating the uncertainties from calculated cases through Monte-Carlo sampling. Then, the critical Rayleigh uncertainty bands for different topologies are established and highlight some scaled effects. Complementary analyses of energy spectra are carried out to discuss the numerical results.

Highly Scalable Meshless Multi Grid Solver for simulation of 3D Reactor Vessel Analysis

Seong Ju Do,Han Young Yoon

Korea Atomic Energy Research Institute, 989-111 Daeduk-daero, Daejeon, 305-353 Korea

Extended Abstract

Most CFD (computational fluid dynamics) codes involving incompressible water conduct simulations by using a pressure-based solver. A pressure-based scheme is a numerical technique that corrects the pressure by coupling an intermediate velocity that does not properly reflect the pressure and a conservation equation such as the law of mass conservation.

This pressure correction process is equivalent to solving a sparse linear system with a non-zero pattern proportional to the number of cells. Therefore, in situations where large-scale simulations involving a large number of cells are simulated, this process takes up a large proportion of the total simulation time. In the case of the BCG(Bi-Conjugate Gradient) solver, which is the most popular and well-known method for solving asymmetric matrices, about 90% of the time is spent on solving the pressure correction equation in simulating a problem with about 20 million cells.

With the above background, it is essential to improve the solver of the linear system that solves the pressure correction equation in order to significantly reduce the calculation time of the problem using a large-scale grid system. In this presentation, an introduction and verification of the MMG (Meshless Multi Grid) technique developed to use the classic GMG (Geometric Multi Grid) algorithm in an unstructured grid will be followed.

The GMG technique is an algorithm that requires all grids at each level, and is mainly used in the structured grid. In order to extend this technique so that it can be used in unstructured grids, some algorithm which is capable of automatically generating coarse grids based on the finest grid should be provided. However, since it is not easy to extend the cell merging based technique to 3D, the auto coarsening technique was easily implemented by creating a graph consisting of nodes and edges instead of creating a grid where an edge are a connection relationship between two nodes. In addition, it is well known that the convergence of the GMG technique deteriorates in the case of a stretched grid with a high aspect ratio. In order to effectively perform a thermal hydraulic analysis in a nuclear reactor, it is likely that some parts of the grid have high aspect ratio to minimize the number of grids. In this case, a semi-coarsening technique was introduced to improve convergence rate. The semi-coarsening algorithm is a technique that defines certain conditions during the coarsening process and excludes nodes in a specific direction from coarsening.

Theoretically, when the number of cells in the grid is N, it is known that the computational complexity of BCG is $O(N^{1.5})$ and that of GMG is $O(N^{1})$. That is, in the case of BCG, the calculation time increases exponentially as the number of cells increases, whereas in the case of GMG, it increases linearly. That is, as N is sufficiently large, the performance of the two solvers is significantly different. Through 3D reactor flow analysis such as boiling problem, PWR vessel simulation and OPR1000 full core simulation, the computational complexity of MMG will be evaluated, and it is verified how much advantage the MMG can have over the BCG as the number of cells increases.

ASSESSMENT OF THE CUPID CODE FOR MULTI-DIMENSIONAL ANALYSIS OF INOVATIVE SMALL MODULAR REACTOR

Yun-Je Cho*, Ji-Hyun Sohn, Seong-Jun Lee, Han-Young Yoon

Korea Atomic Energy Research Institute, 111 Daedeok-daero, 989 Beon-gil, Yuseong-gu, Daejeon 305-600
**Corresponding author: yjcho@kaeri.re.kr*

Extended Abstract

With increasing concern about small modular reactors (SMRs), a number of studies have been conducted on the development of analytical tools for the design and safety analysis of SMRs. The one-dimensional thermal-hydraulics system codes have limitations on the prediction of multi-dimensional behaviours such as natural convection in a large vessel or pools, turbulence mixing in completed geometries. Korea Atomic Energy Research Institute (KAERI) has developed CUPID code since 2007 for the high fidelity safety analysis of nuclear reactors, which is based on two-fluid three field models. For the validation of the CUPID code, KAERI has participated in various international benchmark exercises. In the IAEA Coordinated Research Project (CRP) whose title is "Application of CFD Codes for Nuclear Power Plant Design", CUPID showed the best result for predicting the boron dilution behaviour by turbulence mixing when it compared to other submitted results calculated by using commercial and public CFD codes such as STAR-CCM+, CFX, and OpenFOAM [1]. In the HYMERES-2 project organized by OECD/NEA, we participated in the blind benchmark to simulate the helium layer erosion by a steam jet through an obstruction, and showed that CUPID properly predicts the radiative heat transfer and turbulence diffusion in a containment [2]. DEBORA benchmark program is operating by OECD/NEA, and the open benchmark phase is currently ongoing. In the open benchmark phase, the subcooled boiling model, bubble size model, and non-drag bubble force models in CUPID were validated against to the experimental data and compared to other submitted results calculated by commercial CFD codes. Recently, we has participated in the domestic project for the development of innovative small modular reactors (iSMR). Various design issues have been arisen during the design phase for components and safety features, and many of them are closely related to multi-dimensional behaviours. CUPID is currently being used for sensitivity analysis for the design of emergency cooling tank (ECT) in which the passive auxiliary feedwater system (PAFS) and passive containment cooling system (ECCS) were emerged. A size and connected locations of PCCS pipes affect the mixing behaviour in the ECT and consequently, the cooling capability of the PCCS. In addition, CUPID simulates the transient of reactor coolant system (RCS) water level to decide a proper size of pressurizer during the non-LOCA condition where the RCS temperature is continuously decreasing. The precise prediction of the coolant level with considering the boiling and flashing of coolant in the reactor vessel plays an important role since it determines the success of RCS cooling by natural circulation. Other safety issues such as unexpected failure of reactor coolant pumps (RCPs) and local reactivity insertion accident (RIA) were also simulated by CUPID. When one or two RCPs stop, the natural circulation flow rate can be deteriorate more than the expectation due to the reverse flow. On the other hand, RIA results in the local power increase and possibly low DNBR after the reactor trip. Therefore, an assembly or sub-channel scale simulation is required with the multi-physics coupling technique between the reactor physics code and sub-channel scale thermal-hydraulics code. In the future, the multi-scale and multi-physics (MSMP) integral system will be developed and used for the performance and safety analysis for newly developed iSMR.

[1] Y.J. Cho, H.Y. Yoon, Numerical analysis of the ROCOM boron dilution benchmark experiment using the CUPID code, Nuclear Engineering and Design, Vol. 341, pp. 167-175, 2019.

[2] J.H. Sohn, Y.J. Cho, H.Y. Yoon, Analysis on helium stratification erosion by vertical steam jet using the CUPID code, Nuclear Engineering and Design, Vol. 388, 2022.

MULTIPLE FLOW REGIME CFD SIMULATING GENERIC POOL BOILING

T. Höhne, D. Lucas

Helmholtz-Zentrum Dresden-Rossendorf (HZDR) - Institute of Fluid Dynamics

Bautzner Landstraße 400, D-01328 Dresden, Germany

Extended Abstract

Due to latent heat, boiling heat transfer plays a very important role in wide number of applications in many technological and industrial areas including nuclear reactor cooling systems, car cooling and refrigeration systems. Boiling is a process in which heat transfer causes liquid evaporation. When a liquid is in contact with a surface maintained at a temperature above the saturation temperature of the liquid, boiling will eventually occur. Pool boiling is the process in which the heating surface is submerged in a large body of stagnant liquid. The relative motion of the vapor produced and the surrounding liquid near the heating surface is due primarily to the buoyancy effect of the vapor. Much progress has been achieved in establishing models to describe various multiphase boiling flow phenomena using Computational Fluid Dynamics (CFD). The GENTOP-concept [1] enables to consider such processes. The potential of this concept was demonstrated in Hänsch et al. [2,3] for adiabatic flows and in Höhne et al. [1] with heat and mass transfer. In this paper, the GENTOP concept is applied to simulate boiling effects in a pool where transitions from small bubbly flow to larger bubbles and structures are involved. Thus, in order to fully understand and predict the boiling phenomenon, the large gas structures must be taken into account. GENTOP allows the modelling for bubbles smaller than the grid size and tracking the interface of large continuous bubbles (larger than the grid size). Thus, it is like a combination of Euler –Euler two fluid modeling and interface tracking techniques. It has been further advanced and validated for churn turbulent flow regimes (Montoya, [4]). This work presents a simulation of a generic pool boiling phenomenon with the help of the GENTOP concept in ANSYS-CFX. To illustrate the previous described concept a demonstration example of a wall heated pool is given. The pool has a length of 250 mm, a width of 100 mm and a height of 100 mm. Liquid water is considered at a pressure of 1 bar. At this pressure, the saturation temperature amounts to 372 K. The initial temperature was set to a subcooling of 2 K. The temperature of the heated wall is set to a superheat of 38 K. In grid cells where the continuous gas volume fraction stays below the threshold value, the gas is treated as a dispersed phase following the particle model formulations. At the later phase larger structures are created. These structures are rising towards the surface of the pool. Close observation of the dispersed gas- and the continuous gas-liquid interface show that different flow regimes can be found in the simulation. The bubble flow regime occurs at relatively low gas flow rates, for which the gas phase appears in the form of small bubbles in the lower part. Later bubbly–slug flow is characterized by the presence of relatively large cap-shaped bubbles, which occupy nearly the entire pool and flow alongside smaller bubbles. The utilization of the GENTOP concept of boiling in a pool needs constant improvement and validation effort using suitable CFD grade experiments.

References

1. Höhne, T.; Krepper, E.; Lucas, D.; Montoya, G., CFD-Simulation of boiling in a heated pipe including flow pattern transitions using the GENTOP concept, *Nuclear Engineering and Design 322(2017),* 165-176
2. Hänsch, S., et al., A multi-field two-fluid concept for transitions between different scales of interfacial structures. *International Journal of Multiphase Flow, 2012. 47: p. 171-182.*

3. Hänsch, S.; Lucas, D.; Höhne, T.; Krepper, E., Application of a new concept for multi-scale interfacial structures to the dam-break case with an obstacle, *Nuclear Engineering and Design 279(2014), 171-181*.
4. Montoya, G., et al. Analysis and Applications of a Generalized Multi-Field Two-Fluid Approach for Treatment of Multi-Scale Interfacial Structures in High Void Fraction Regimes. *Proc. Int. Congress on Adv. on Nucl. Power Plants. ICAPP2014-14230*, USA. 2014.

Numerical Simulation of Tritium Behavior in tritium confinement system for China Fusion Engineering Test Reactor

Haixia Wang, Xuewei Fu, Jincheng Han, Wenhao Wu, Taosheng Li, Jie Yu

Hefei Institutes of Physical Science, Chinese Academy of Sciences, Hefei 230031, China

Introduction

In future fusion reactors of high safety and acceptability, tritium safety is one of the key issues. Tritium will be handled under multiple barriers served by detritiation system. This concept has been successfully adopted in tritium facilities of the world. It is important to ensure that the design of the containment system is appropriate. China Fusion Engineering Test Reactor (CFETR), a new generation of large-scale fusion engineering experimental reactor, is an important milestone project in the development of nuclear fusion in China and the world. The tritium plant for CFETR is under detailed design, and it is of great important to simulate 3D tritium transport behavior in CFETR tritium safety containment system.

As a member in digital technology of CFETR tritium plant, our tritium technology team is responsible for 3D tritium transport behavior simulation in tritium safety containment systems. The study is mainly focused on, 1) investigate tritium mixing and migration in the 3D space such as glove box and process room; 2) to evaluate the clean up performance of the detritiation systems. In this paper, the first stage results are summarized. Tritium behavior in the glove box after pipeline of TEP leak (initial tritium behavior) and the behavior when tritium is removed by the glove detritiation system (removal tritium behavior) under an incident condition are discussed; tritium behavior in the glove box and process room under a postulated accident condition are also investigated.

1 Typical incident and postulated accident

As one of the most important systems in the inner fuel cycle process, CFETR's TEP is similar to ITER's using three-stage process to treat plasma exhaust gas: front-end processing, impurity processing, and final cleanup processing. The equipment of the front-end processing system is placed in a separate glove box served by Glove box Detritiation System (GDS), and the other two systems share one glove box with GDS. Before released to the environment, the remaining waste gas is temporarily stored in the decay tank.

The postulated initiating event is the instantaneous failure of the tritium process line in the front-end processing system at maximum design flow. Process gas will be released from the higher pressure process line into glove box. The release will cause tritium concentration to increase rapidly in glove box. When the concentration increases to the alarm set point (3.7×10^{7} Bq·m^{-3}), the alarm will be activated simultaneously. After the concentration increases to the isolation set point (1.3×10^{9} Bq·m^{-3}), failed tritium process line will be isolated and tritium will stop leaking, while the GDS purges the contaminated glove box with pure nitrogen gas with the maximum design flow rate of 300 m^{3}·h^{-1}. In particular, tritium release will continue until the isolation operation and GDS activation complete, and it is assumed that the delayed time from tritium release to isolation operation and GDS activation is 15 s.

The postulated accident is the glove box failure superimposed on the above incident, and tritium in glove box sprayed into the process room along the breach in glove box wall resulting in tritium concentration to increasein the process room. Tritium concentration at or above 1 DAC (3×10^{5} Bq/m3) will trigger the alarm. If the concentration exceeds the threshold of 1×10^{8} Bq/m^{3}, failed tritium process line will be isolated, and the DS will isolate the affected sector from the HVAC system and purges the contaminated process room with pure air with the design flow rate of 9000 m^{3}/h. The transport route of tritium is: process line >> glove box >> process room >> DS >> environment. It should also be noted that, there is a time interval between the moment of the exceeded tritium concentration detected and process line isolation as well as DS activation. The time delay of DS actuation is 5 minutes.

2 Methodology

The above accident involves three-level confinement systems: the first one is TEP related pipeline (broken), the second one is the glove box system (failure), and the third one is the process room. The released tritium is assumed in the form of T_2. What concerned about is the behavior of the leaked tritium in the working gas of the second and third confinements, which essentially is the mass transfer issue of the fluid in the flow process. This numerical simulation is conducted by the fluid module of COMSOL Multiphysics software.

During the tritium transport process, there are fluid component transport processes since the leaked tritium is mixed with nitrogen and air. When solving this kind of problem, COMSOL predicts the local mass fraction of each component by solving the component transfer equation. The tritium leaked during the whole accident can be predicted to less 10% of the glove box volume, and this ratio is even smaller for the process room. Therefore, it is reasonable to apply the Transport of Diluted Species module of COMSOL.

3 Geometric Model

According to the design information of CFETR TEP, three dimensional geometrical model is built using the geometric kernel of COMSOL, shown in Figure. 1.

The front-end processing system glove box is an overall 3.82 m×0.667m×1.2m rectangular body (see Fig.1a)), filled with nitrogen and controlled at the negative pressure of 200Pa below atmospheric pressure. There are one buffer tank and four permeators. The assumed leak point is a circle with a 0.02 m radius located at the top of the second permeator. 16 measuring points are set to monitor the changes in tritium concentration in the glove box. 8 measuring points in group M are located on M-plane (PY=0.33 m), and 8 measuring points in group P are located on P-plane (PZ=0.6 m).

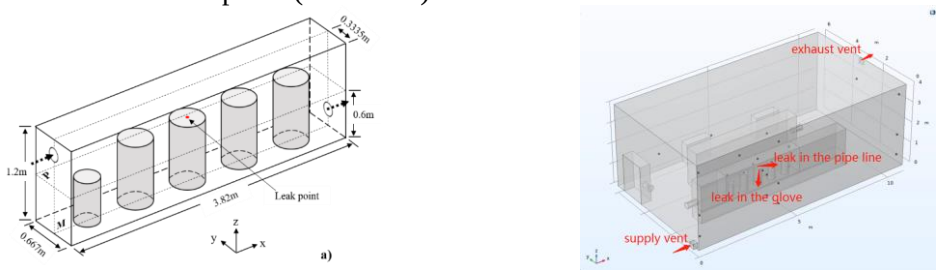

a) glove box b) process room

Fig. 1. Geometry model of glove box and the process room

As shown in Fig.1b), the process room of TEP is a complete rectangular parallelepiped (10.83 m×6 m×4m), filled with air and controlled at the negative pressure of 100Pa below atmospheric pressure. There are three glove boxes serving the front-end processing, impurity processing and final cleanup processing, and gamma decay tank. Besides, two Power Distribution Cabinets stand by a wall. There is a leak hole located where the glove contacts the glove joint plate or sealing ring, and assumed as a circle with a radius of 0.02 m.

4 Results and Discussion

4.1 Tritium behavior in the incident

(1) In the tritium leak stage

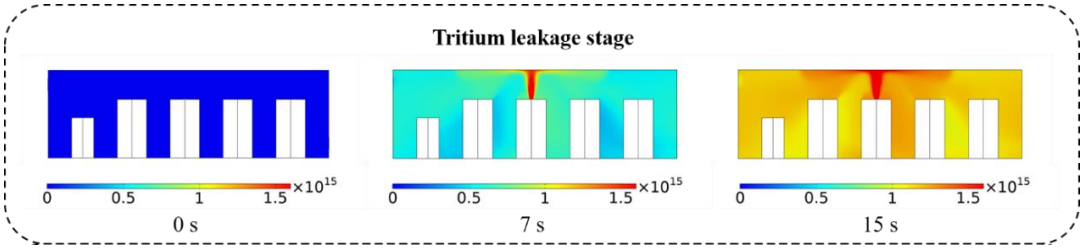

Fig. 2. Tritium concentration distribution on the M plane in the release stage

The distribution of tritium concentration in the glove box at the M-plane is given in Figure 2. During the tritium release stage, tritium is ejected and released from the leak point to the top of the glove box, and then migrates to the left and right sides, forming an umbrella-shaped concentration distribution. As the release time increases, the tritium concentration kept increasing. At the end of the tritium release stage, the tritium concentration level is basically above 1×10^{15} Bq·m^{-3}.

The change of tritium concentration at the measurement points can more accurately capture the time information. Figure 3 shows the monitor near the upper wall of the tritium leakage area should be selected to activate the the alarm and isolation because of the fastest abnormal rise of tritium concentration detected. Since tritium concentration at most of the measurement points has exceeded the alarm and isolation settings within 0.5s, it is at moment of 15s after the leak moment (0s) that the GDS start to purge the contaminated glove box .

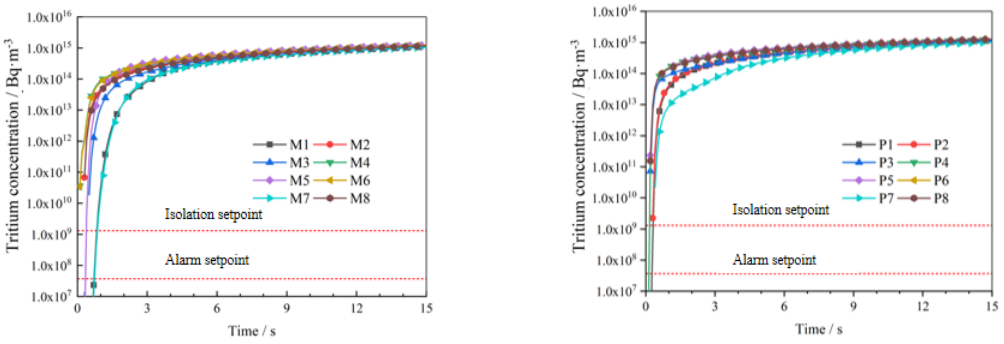

Fig. 3. Tritium concentration change of monitor points during tritium release stage

(2) In the tritium removal stage

When the GDS starts, pure nitrogen gas gradually flows into the glove box and destroys the original distribution law gradually. As shown in Figure 4, the tritium concentration in the area directly opposite the supply vent was the first to decrease, and the tritium concentration in the glove box gradually decreased under the continuous work of GDS; At about 45s, another new tritium concentration distribution law was established. Although the tritium concentration in the glove box decreases over time, this newly established tritium concentration distribution law seems to be maintained in the subsequent tritium removal stage.

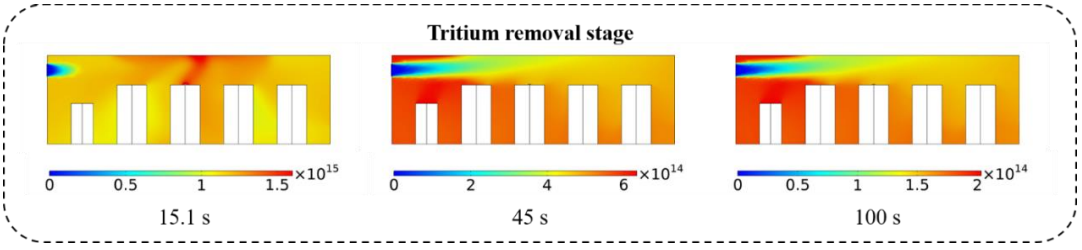

Fig. 4. Tritium concentration distribution on the M plane in the removal stage

A half-exhaustion period $T_{1/2} = Ln2/\phi$ is defined, and its physical meaning characterizes the time needed to remove half of the tritium content. Its value reflects the detritiation efficiency of GDS and the smaller the half-exhaustion period, the faster the tritium is removed.

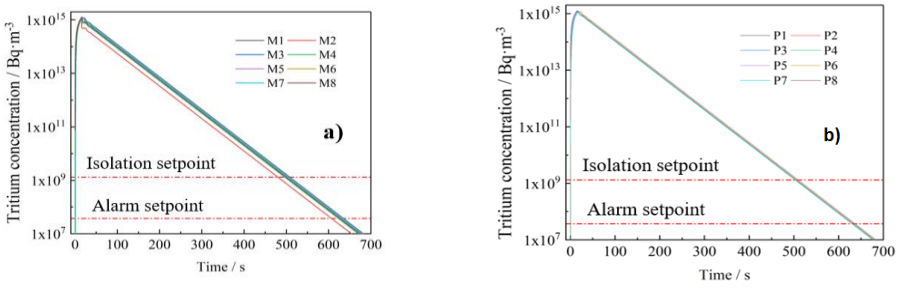

a) M group 0~700 s b) P group 0~700 s

Fig. 5. Tritium concentration at measuring points in the tritium leak stage

To obtain the most effective clean up performance of the detritiation systems, we compared half-exhaustion periods of 26 typical ventilation patterns (combination of different supply vent and exhaust vent location) and find that the scheme (the air outlet and exhaust outlet are located on both sides of the top of the glove box) improves the efficiency of tritium removal by about 58% without increasing the air supply flow.

4.2 Tritium behavior in the accident

(1) In the tritium leak stage

We calculated the transport of tritium in the glove box and process room under the accident condition. The three-dimensional distribution of tritium in the space concentration, the slice of tritium concentration in the representative section, and so on are presented.

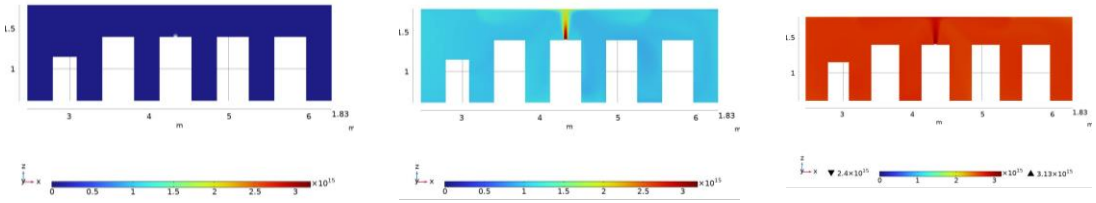

0s 15s 300s

Fig.6. Tritium concentration distribution on the M plane in the release stage in the accident

In Figure 6, tritium transport behavior in the glove box seems to be very similar to that in the incident. Tritium is ejected and released from the leak point to the top of the glove box, and then migrates to the left and right sides, forming an umbrella-shaped concentration distribution. At the end of the tritium release stage (300s), the tritium concentration is (2.4~3.1)×10^{15} Bq/m^3.

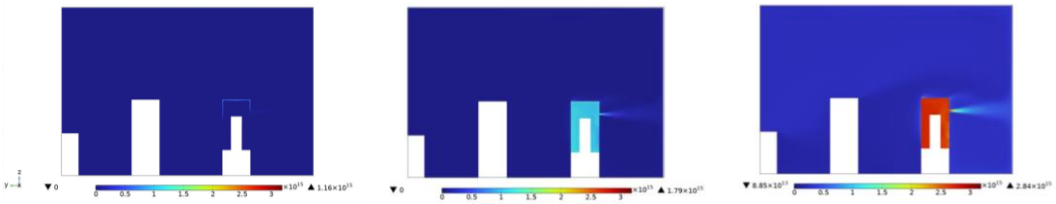

0.1s 15s 300s

Fig.7. Tritium concentration of YZ slice with x=4.18m (the same with the leak in glove-box wall)

In fact, tritium escapes into the process room in a very short time, and it is found from the Figure 7 that tritium mainly moves quickly along the glove box wall and escape into the process room through the leakage in the glove-box wall. Total tritium and tritium concentration at monitor point in the room are also given in Figure 8 and 9 for more clear demonstration.

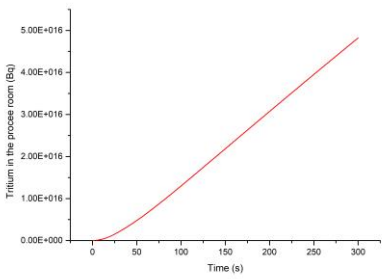

Fig. 8. Total tritium in the room in the accident

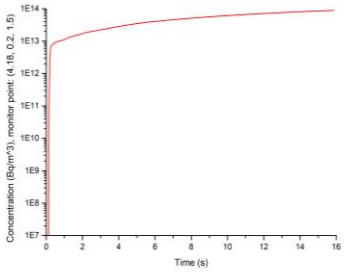

Fig. 9. Tritium concentration at monitor point in the room in the accident

(2) In the tritium removal stage

When the DS of the process room starts, pure air gradually flows into the room, making

tritium concentration in glove box and the process room decrease with the time. Tritium concentration at room monitor point (see Figure 10) gives the quantitative value, and it is about 2000s that are needed to make tritium decreased to the isolation threshold. During this time, total tritium in the glove box and process room is reduced from 5.57×10^{16} Bq to 1.35×10^{10} Bq.

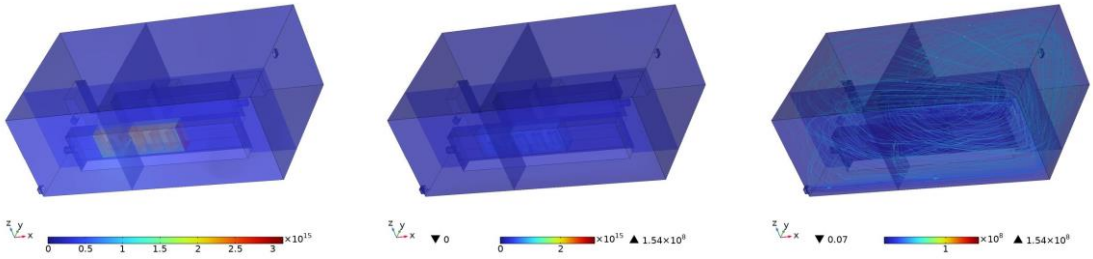

a) 0s b) 150s c) 2000s

Fig. 10. Tritium concentration distribution in glove box and room when purged by pure air

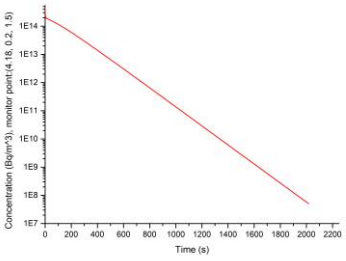

Fig. 11. Tritium concentration at room monitor point in accident tritium removal stage

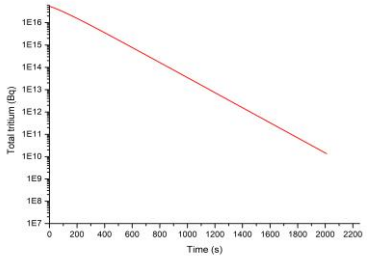

Fig. 12. Total tritium in the room in accident tritium removal stage

We can also see from the streamline in Figure 10c), the direction of primary flow cannot be directed from the supply vent to the exhaust vent due to the obstruction of the internal facilities. it is well known that the flow field characteristics are the decisive factor affecting the tritium transport process. The more effective DS ventilation patterns (combination of different supply vent and exhaust vent location) need to be studied systematically.

5 Summary

In this paper, tritium mixing and migration in the glove-box and process room are investigated for CFETR TEP system based on finite element software COMSOL Multiphysics, as well as the clean up performance of the DS system. To design more effective ventilation pattern for GDS, half-exhaustion periods of 26 ventilation patterns are compared. A most effective pattern is finally obtained, which can significantly reduce the scale of the recirculation area caused by back-mixing and improved the detritiation efficiency by more than 50%. The tritium transport in the room under accident conditions has just begun, and more numerical simulation and further analysis will be conducted.

Acknowledgments

This work is supported by the National Key R&D Program of China-National Magnetic Confinement Fusion Science Program (Grant No. 2017YFE0300305). A special thanks goes to the China Academy of Engineering Physics for providing valuable design information of CFETR.

CFD SIMULATION FOR EVALUATING PRESSURE DROP AND HEAT TRANSFER CORRELATIONS FOR PEBBLE BED REACTOR

Muhammad Sohaib Malik, Jiaqi Chen and C.S. Brooks*

Department of Nuclear, Plasma and Radiological Engineering, University of Illinois, 104 South Wright Street, Urbana, IL 61801, United States
csbrooks@illinois.edu

Extended Abstract

Pebble bed high temperature gas-cooled reactor (PBR) is a promising generation-IV reactor which involves spherical fuel pebbles composing a packed bed with cylindrical and conical sections through which helium gas flows as a coolant from top to bottom, offering advantages like high coolant outlet temperature and intrinsic safety against core melting. The fluid flow passing through the gaps between the pebbles exhibits complex flow features. Pressure drop, heat transfer, as well as flow structure between the gaps of PBR are dependent upon spatial porosity variation through the domain. The flow characteristic affects the forces on pebbles and heat transfer between the particles and fluids, which further affects temperature distribution inside the pebble reactor core. Being able to predict peak temperature in the reactor is important for the reactor safety.

Due to flow complexities in pebble bed reactor, detailed measurement of fluid flow is a challenging task. Although studies have been conducted using Particle Image Velocimetry (PIV) to characterize local fluid flow with water and other liquids. However, for gas flow, such local velocity measurement is still difficult. To understand the fluid flow in gas cooled reactors and for more complex reactor geometry, Computational Fluid Dynamics (CFD) simulation is required. However, simulating the whole pebble bed is difficult. On one hand, the computational cost of modeling the whole domain is fairly high. On the other hand, detailed pebble distribution in the experiment is usually not available. Investigating the flow through regular unit cell of simple cubic (SC), face-centered cubic (FCC), body-centered cubic (BCC) provides useful insights on the flow characteristics in PBR.

As the first step to validate the CFD model, comparisons are made with the global characteristics, the pressure drop coefficient. Previously, empirical or semiempirical pressure drop correlations have been developed based on experiments (Ergun, KTA and VDI correlations). In the study, fluid flow analysis through different standardized structures is performed to predict fluid velocity, temperature, pressure inside PBR domain as well as the pressure drop, drag force and coefficient of drag. Initial simulations have shown that pressure drop increase with increasing Reynolds number for all cell structures (SC, BCC, FCC). The preliminary simulations utilized contact treatment strategy of reduced diameter to artificially create gap between pebbles. For Reynolds number variation, five cases are run with superficial velocity v=0.082m/s, 0.6m/s, 0.826m/s, 1.156m/s, 1.652m/s corresponding to Reynolds number 500, 3630, 5000, 7000, 10000 respectively. For porosity variation, these cases were run for SC (ϵ=0.51392), BCC (ϵ=0.423265), FCC (ϵ=0.359172). FCC structure has lowest porosity and is likely to offer more resistance to flow and pressure drop. This finding agrees well with the Ergun, KTA and VDI correlations. CFD results agree more with the KTA and VDI correlations in high Reynolds number regime. Similarly, pressure coefficient shows the similar behavior for the three cell structures. Furthermore, for evaluation of the local flow prediction, the CFD model is also compared with the PIV experiment by Hassan and Dominguez-Ontiveros (2008).

The most important quantity related to the safety of the pebble bed reactor is the pebble temperature. After verifying the CFD model with hydrodynamic data, simulations are also performed to study the

temperature distribution in the unit cell. Simulation with constant heat flux yields unphysically high surface temperature near the contact region. Studies have shown that surface temperature and heat flux on pebble surface is not uniform. In order to predict the temperature distribution correctly, conjugate heat transfer (CHT) model is required for heat transfer analysis with uniform volumetric heat generation source inside the pebble. With the CHT model enabled, the unphysical temperature in the simulation is eliminated. The results of the simulation are compared with pebble heat transfer correlation from Wakao et al. (1979)

In addition, the result from the simulation shows a big impact from the contact treatment. Point contact between neighboring pebbles in PBR cause numerical difficulties, which signifies the importance of contact treatment in accurately determining flow characteristics. Studies have shown contact treatments like increased diameter, reduced diameter, bridging and capping to help in accurately simulating flow through pebble bed reactor. The influence of these contact treatment is also briefly discussed in this work.

U.S.NRC
United States Nuclear Regulatory Commission
Protecting People and the Environment

Center for Advanced Small Modular and Micro Nuclear Reactors
Texas A&M Engineering Experiment Station

NEA
NUCLEAR ENERGY AGENCY

Technical Session 6

Liquid Metals

Feb 20, 15:45-17:15, Room B.

Understanding the need for proper turbulent heat flux modelling for non-unity Prandtl number fluids

Afaque Shams[a,b]

[a] Mechanical Engineering Department, King Fahd University of Petroleum and Minerals (KFUPM), Dhahran 31261, Saudi Arabia
[b] Interdisciplinary Research Center for Renewable Energy and Power Systems, KFUPM, Saudi Arabia
afaque.shams@kfupm.edu.sa

Abstract

This article reports the need for proper turbulent heat flux modelling in non-unity Prandtl number (Pr) flows, particularly in the liquid metal flows, using the Reynolds-Averaged Navier-Stokes (RANS) approach. The Pr number of liquid metals is of the order of 0.025-0.001, making it very challenging for "off-the-shelf" RANS models to accurately predict the heat transfer phenomena. In this regard, some peculiarities of the "off-the-shelf" RANS models are highlighted in different flow regimes, i.e., natural, mixed, and forced convection. Furthermore, the status and perspectives of the available turbulent heat flux modelling closures within the nuclear community are provided with a special focus on the low-Pr fluids. Lastly, a comparison of a well-calibrated turbulent heat flux model with the classical eddy diffusivity model has been demonstrated for natural, mixed, and forced convection flow regimes.

1. Introduction

Turbulent heat transfer is an extremely complex phenomenon that has challenged turbulence modellers for various decades. Both turbulent momentum and heat transfer are based on the same physical mechanism of cross-streamwise mixing of fluid elements. Therefore, modellers have often assumed that the turbulent heat transfer can be predicted from the knowledge of momentum transfer; this approach is known as the Reynolds analogy. Even though this approach is overly simplistic, it has been successfully adopted for several decades in a large majority of industrial applications of CFD, which are based on Eddy Diffusivity models (EDM). This success is justified because for fluids with a Prandtl number (Pr) close to unity and particularly in wall-bounded forced convection flows, this approach has provided reasonable predictions of global parameters such as Nusselt numbers and mean temperature distributions [1, 2].

Fig. 1 provides an overview of the Pr for different working fluids used in different reactor types [3]. It is clearly noticeable that apart from the gas-cooled reactor, none of the working fluids exhibit equality in the momentum and the thermal boundary layer. Therefore, one should always be careful in applying the Reynolds analogy to non-unity Pr fluids, particularly to low-Pr fluids and must realize its limitations with respect to accuracy. Nevertheless, the obvious limitations of this assumption for natural and mixed convection flow regimes have become more evident and are highlighted in [1, 2]. The limitations of this approach have become evident in non-unity Pr fluids, particularly at low-Pr, and in all flow regimes,

i.e., natural, mixed, and forced convection, as underlined for example in [1-11]. To understand better these issues for liquid metal flows, readers are referred to Shams [1] and Grötzbach [2].

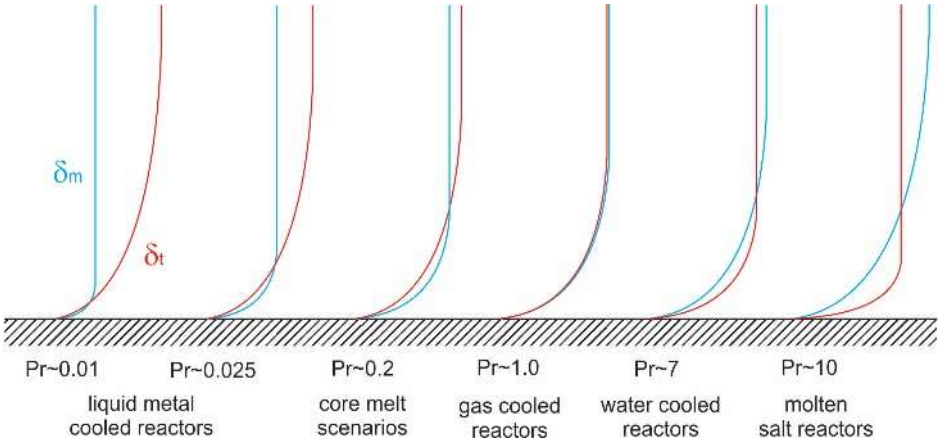

Fig. 1. Comparison of momentum (δ_m) and thermal (δ_t) boundary layers for different working fluids in various reactor applications [3].

In the recent past, the nuclear community has directed its attention towards improving the turbulent heat flux modelling approaches in various CFD codes; particularly, for the application of liquid metal fast reactors. In 2002, in the EU ASCHLIM (Assessment of Computational Fluid Dynamics Codes for Heavy Liquid Metals) project, assessment of different CFD codes was performed for heavy liquid metals [4]. It was concluded that the prediction of turbulent heat transfer by some of the nuclear community CFD (Computational Fluid Dynamics) codes, which were based on sophisticated turbulent heat flux models (THFMs), was superior to the considered commercial softwares (which were based on Reynolds analogy). Subsequently, in 2010, in the framework of the EU project THINS (Thermal-hydraulics of Innovative Nuclear Systems), an effort was put forward to implement more accurate closures of turbulent heat flux (THF) for liquid metals in engineering codes [8]. In that respect, several attempts were made for the assessment and further development / calibration of the available THF modelling approaches. In this regard, one of the main obstacles was the lack of reference data, i.e., experimental or numerical via the use of Direct Numerical Simulations (DNS). In June 2013, European liquid metal modelling experts gathered in Amsterdam to discuss the current status and the future outlook. At that time, the available models and reference data were limited to natural and forced convection liquid metal flows in relatively simple geometric configurations [12]. It was also concluded that more efforts should be devoted to the further validation and, if needed, improvement of these models.

Within the framework of the EU SESAME (Thermal hydraulics Simulations and Experiments for the Safety Assessment of Metal Cooled Reactors) and MYRTE (MYRRHA Research and Transmutation Endeavour) projects, an extensive and collaborative effort has been put forward to generate a wide range of reference data, both experimental and numerical, to fill this gap [12]. In parallel, both these projects have provided a unique platform for the turbulence modellers to use this database for the further validation and/or improvement of the selected THF modelling approaches. Although these efforts are extensively discussed in Shams et al. [3], however, they will also be briefly highlighted in this article.

The main goal of this article is to provide an overview of the THF modelling for low-Pr number fluids and highlight its importance. First, in Section 2, some light has been shed on the limitations and peculiarities of the 'off-the-shelf' RANS models. Section 3 provides a brief overview of the available THF modelling approaches. In Section 4, collaborative efforts put forward by the European liquid metal community are highlighted. This section also provides a comprehensive list of THFMs and their performance in different flow regimes. Accordingly, the assessment of the best THFM [3], in comparison with the 'off-the-shelf' RANS models, is demonstrated in Section 5. This is following by a summary in Section 6.

2. Why do 'off-the-shelf' RANS models fail?

The Reynolds-averaged momentum and energy equations governing turbulent flows are as follows:

$$\frac{DU_i}{Dt} = F_i - \frac{1}{\rho}\frac{\partial P}{\partial x_i} + \frac{\partial}{\partial x_j}\left(\nu\frac{\partial U_i}{\partial x_j} - \overline{u_i u_j}\right) \tag{1}$$

$$\frac{DT}{Dt} = \frac{q}{\rho c_p} + \frac{\partial}{\partial x_j}\left(\frac{\nu}{\sigma_T}\frac{\partial T}{\partial x_j} - \overline{\theta u_i}\right) \tag{2}$$

Where $\frac{D}{Dt} = \frac{\partial}{\partial t} + U_k\frac{\partial}{\partial x_k}$ is the material derivative, F_i is the body force, and q is the internal energy source. A closure is required for $\overline{u_i u_j}$ (turbulent momentum flux (TMF)) and $\overline{\theta u_i}$ (turbulent heat flux) to close these equations. There is a wide range of closures available in the literature for turbulent momentum flux; see, for example [13-16]. There are different levels of approximations involved when closing equation 1, such as algebraic models; one-equation models; two-equation models and Reynolds stress models. The most frequent approach adopted to close equation 1 is the eddy viscosity model (EVM), and is given as:

$$\overline{u_i u_j} = \frac{2}{3}k\delta_{ij} - \nu_t\left(\frac{\partial U_i}{\partial x_j} + \frac{\partial U_j}{\partial x_i}\right) \tag{3}$$

Where k is the turbulent kinetic energy, υ_t is the eddy viscosity (and can be defined as $C_\mu k^2/\varepsilon$), Pr_t is the turbulent Pr, C_μ is the model co-efficient, and ε is the turbulent kinetic energy dissipation rate. The focus of this article is to highlight the importance of the THF modelling. Among different available THF closures, the most frequent approach adopted to close equation 2 is the EDM, and is given as:

$$\overline{\theta u_i} = -\frac{\nu_t}{\mathrm{Pr}_t}\frac{\partial T}{\partial x_i} \tag{4}$$

The EDM uses the concept of Pr_t and is based on the Reynolds analogy. This approach is available in most of the RANS based CFD codes and is also referred, in this article, as an "off-the-shelf" heat flux model. To get a better understanding of why do 'off-the-shelf' THFMs fail, particularly for low-Pr fluids, some of their main peculiarities are summarized in the following sections.

2.1 Improper use of Reynolds Analogy

As depicted in Fig. 1, the statistical features of the turbulent velocity and the thermal fields are similar for the Pr ~ 1. Meaning that the diffusive and conductive wall layers have almost the same thickness; so, their fluctuation fields behave similarly when subjected to heating or cooling. Accordingly, the use of the Reynolds analogy (which is based on the similarity principle, as discussed in the introduction) is justified for such situations. However, liquid metals have relatively large thermal conductivity or diffusivity; hence, the conductive sub-layer in the thermal boundary layer becomes thicker. As a consequence, the thermal boundary layer is thicker than the momentum boundary layer. Accordingly, the similarity assumption breaks down and for liquid metals, and consequently, this approach leads to large errors, see Shams et al. [7].

2.2 Incomplete modelling of turbulent heat flux

It is clearly noticeable from equation 4 that the components of the turbulent heat flux are aligned with the corresponding components of the temperature gradient vector. This makes the EDM intrinsically incomplete and, therefore, not suitable for scenarios where the aforementioned components are not aligned. The Rayleigh-Bénard Convection (RBC) is a classical example of one such scenario. This issue is, in general, related to the accurate prediction of thermal field in natural convection flows, rather than particular to liquid metal flow. Nevertheless, in section V, a liquid metal example is demonstrated to highlight the importance of sophisticated turbulent heat flux modelling.

3. Modelling of turbulent heat flux

Equation 2 has three unknown heat fluxes, containing the complete heat exchange due to the turbulent fluctuations. In that respect, several modelling approaches have been proposed and are briefly discussed in the following sections.

3.1 Simple Gradient Diffusion Hypothesis

The simple gradient diffusion hypothesis (SGDH) is the most commonly used approach to compute the unknown turbulent heat fluxes. This hypothesis is based on the well-known Reynolds analogy, and uses the turbulent Pr (Pr_t) concept, as given in equation 4. This approach is also known as the EDM and is available in almost all the RANS-based CFD codes. Broadly speaking, this approach of Pr_t has been adopted in two different ways: (i) a constant value and (ii) in the form of a correlation; for details, see Shams [1].

3.2 Generalized Gradient Diffusion Hypothesis

To overcome the drawbacks of the SGDH approach, a number of ideas have been proposed in the literature. Namely, the generalized gradient diffusion hypothesis (GGDH) approach, as in Daly and Harlow [17] and Ince and Launder [18]. In terms of complexities, this is the simplest closure in which the temperature gradient perpendicular to gravity results in buoyancy production. Hence, making this model anisotropic and is given as:

$$\overline{\theta u_i} = -C^{\theta} \frac{k}{\varepsilon} \left(\overline{u_i u_j} \frac{\partial T}{\partial x_j} \right) \tag{5}$$

The GGDH approach has provided a reasonable improvement over the SGDH approach close to unity Pr fluids in natural and weakly mixed convection flow regimes, see [19].

3.3 WET Approach

In 1987, Launder [20] proposed another sophisticated approach to determine the thermal field by invoking the WET (Wealth = Earnings × Time) theory. The author applied this approach to compute the turbulent heat flux by "Value of Second Moment = Production Rate of Second Moment × Turbulent Time Scale", and eventually, this model yields:

$$\overline{\theta u_i} = -C^{\theta}\frac{k}{\varepsilon}\left(\overline{u_i u_j}\frac{\partial T}{\partial x_j} + \overline{\theta u_j}\frac{\partial U_i}{\partial x_j}\right) \tag{6}$$

3.4 Second Order Models

The next in the hierarchy of the heat flux modelling is the algebraic heat flux models. However, to understand such modelling approach it is important to understand the second order closures. In second moment closures, the system of the equation can be closed by the transport equations for the turbulent heat fluxes, the temperature variance and its respective dissipation. There are a large number of second moment closure models appear in the literature [6, 21-13]. One such model has also been developed in the nuclear field with a special focus on the liquid metal flows and is known as Turbulence Model for Buoyant Flows (TMBF) [21]. The TMBF is a combination of a linear two-equation k-ε model, as the TMF model, and a second order 5-equation model for the transport of heat: three transport equations for the three turbulent heat fluxes, 1-equation for the transport of the temperature variance, and 1-equation for the transport of its dissipation rate. These five equations form a low-Péclet number formulation, meaning that the simulation mesh has to be fine to resolve the conductive wall layers. In total, the TMBF contains seven transport equations and 17 empirical co-efficients.

3.5 Algebraic Heat Flux Models (AHFM)

The algebraic heat flux models (AHFMs) form a class of heat flux models that are sophisticated enough to provide a good physical representation for the turbulent heat transfer. Broadly speaking, the AHFMs are divided into two main formulations, i.e., explicit and implicit[1].

Explicit Algebraic Heat Flux Models

In an explicit formulation, the turbulent heat flux is calculated using a gradient hypothesis with the eddy diffusivity concept. In the framework of the THINS project, one such model, based on four-equation (κ-ε-κ_θ-ε_θ) was developed for liquid metal flows, for details see [24].

Implicit Algebraic Heat Flux Models

In an implicit AHFM formulation, the turbulent heat flux is computed directly from an algebraic solution of the THF transport equation; that is, by solving a non-linear algebraic equation. In that respect, second-moment closures can serve as a basis for deriving algebraic models. Different forms of the AHFM formulations can be obtained by truncating different terms appearing in the differential equations of a second-moment closure. There have been a number of implicit AHF models (AHFMs) proposed in the literature [1], and these models have shown superior results compared to the SGDH, GGDH and WET modelling approaches for a wide range of natural convection, mixed and forced convection flow regimes, however for the Prandtl number fluids close to unity. Depending on the assumption, an implicit AHFM can be based on one or two transport equations. One approach would be to solve separate transport equations for temperature variance θ^2 and its dissipation ε_θ.

Another approach to close the AHF formulation is to evaluate the ε_θ from the thermal to mechanical time-scale ratio (R). In the framework of the THINS project, one such model, based on three-equation (k-ε-θ^2) was developed for liquid metal flows and is called as the AHFM-NRG formulation, for details see [7]. The algebraic expression for the turbulent heat flux of the AHFM-NRG formulation is given as:

$$\overline{\theta u_i} = -C_{t_0}\frac{k}{\varepsilon}\left(C_{t_1}\overline{u_i u_j}\frac{\partial T}{\partial x_j} + C_{t_2}\overline{\theta u_j}\frac{\partial U_i}{\partial x_j} + C_{t_3}\beta g_i\overline{\theta^2}\right) \tag{7}$$

where g_i is the gravity vector, β is the thermal expansion co-efficient, and C_{t_0} ... C_{t_4} are the co-efficients of the AHFM-NRG formulation. To know about the AHFM-NRG formulations, readers are referred to [7].

4. Collaborative efforts within the liquid metal community

Within the liquid metal community, particularly in Europe, a number of collaborative efforts have been put forward to assess and further improve the available advanced turbulent heat flux models. And, wherever it is needed, extra measures have been taken to develop new THF models for the accurate prediction of heat transfer in liquid metal flows.

In 2002, the EU ASCHLIM project started with the main focus to assess the performance of the available CFD, commercial and research, codes for the application of heavy liquid metals [4]. As an outcome of this project, it was found that the approach used to model the heat transfer in some of the codes from the nuclear community was superior to the commercial softwares. This is mainly because these codes were not relying on the 'off-the-shelf' heat flux models. Namely, a second order THFM, called TMBF, was developed and assessed in this framework of this project. Nevertheless, the need to further validate such sophisticated THF models and to make it easily available for the nuclear community was provoked.

In 2010, within the framework of the EU THINS project, a dedicated effort was put forward to develop advanced THFMs and make them accessible to the nuclear community. Accordingly, several interesting THF modelling approaches were proposed, within the THINS project, and are given below:

- Mixed law-of-the-wall model [25] based on Kays correlation [26]
- Look-up tables [27]
- AHFM-NRG formulation [7]
- κ-ε-κ_Θ-ε_Θ model [24]

The assessment of these models (except the κ-ε-κ_Θ-ε_Θ model), within the THINS project, for various flow configurations was summarized and is given in Fig. 2. As an outcome of this exercise, it was concluded that now the focus should be dedicated to the extension of these approaches for all three flow regimes, like the AHFM-NRG, and their further validation. Consequently, in Europe, a consensus was achieved that the further development of models should be limited. And, now, the efforts should be directed: (i) to validate and calibrate the available THFMs for complex geometric configurations and (ii) to extend these models to natural, mixed and forced convection flow regimes. Accordingly, in the framework of the SESAME and the MYRTE projects, three different THF models were selected to be further validated. These models are:

- AHFM-NRG formulation
- κ-ε-κ_Θ-ε_Θ model
- Turbulence Model for Buoyant Flows (TMBF)

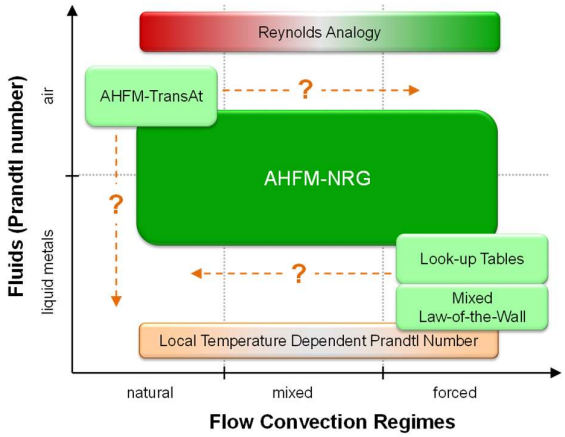

Fig. 2 Liquid metal model developments and their future perspective [8], an outcome of the EU THINS project.

Moreover, as an outcome of this validation study, a few models were calibrated to deal with more complex scenarios and are as follows:

1. The AHFM-NRG was re-calibrated to deal with a wide range of Rayleigh number numbers, i.e. Ra = 1-10^{17}, and the resulting model was called AHFM-NRG+ [28]. It is also worth mentioning that the main development of the AHFM-NRG+ formulation was primarily within the EU IVMR (In-Vessel Melt Retention Severe Accident Management Strategy for Existing and Future Nuclear Power Plants) project for the severe accident scenarios.
2. The AHFM-NRG was extended from the building block linear k-ε model to a non-linear Reynolds Stress Model based on Elliptical blending (RSM-EB). This resulting model is called AHFM-NRG:RSM. Currently, the applicability of this model is only limited to the forced convection flow regimes [29, 30].
3. Following the AHFM-NRG calibration strategy, some of the co-efficients of the TMBF model were re-calibrated and the resulting model is called TMBF-eq-ATHFM [31].

Nevertheless, the EU SESAME and the MYRTE projects provided a unique platform to assess the prediction capabilities of these aforementioned models, and a summary of this assessment is given in Table I. The dark orange colour in the table indicates the intrinsic limitations of a model to perform well for the highlighted flow regimes. Whereas, the light orange colour indicates the room for potential improvements of a model to perform better in the highlighted flow regimes.

It is clearly noticeable that among all these tested models, the AHFM-NRG:k-ε formulation has been well calibrated and tested for all three flow regimes; hence, it is highlighted in dark green colour. It must be noted that all the variants of AHFM-NRG could only perform well if they are used in conjunction with the calibrated correlations for C_{t1} and C_{t3}. Namely, these correlations are called Shams

correlation and as explicitly given in [7, 28-31]. Many researchers have tried to use different variants of this model; however, reportedly, they have failed to utilize the full potential of these AHFM formulations successfully. Therefore, to avoid confusion, hereafter, these formulations are called AHFM-SC (AHFM based on Shams Correlation). It is worth mentioning that, so far, the AHFM-SC formulations are based on linear k-ε and non-linear RSM-EB models.

Table I An overview of the performance of different turbulent heat flux modelling approaches [3], outcome of the EU SESAME and MYRTE projects.

		Natural Convection		Mixed Convection		Forced Convection	
		Prandtl Number (Pr)					
		Pr << 1	Pr ~ 1	Pr <<	Pr ~ 1	Pr <<	Pr ~ 1
	THF Modelling Approaches	Rayleigh Number (Ra)		Richardon Number (Ri)		Peclet Number (Pe)	
SGDH	Pr_t = constant	-	-	-	-	Changing Pr_t	All values
SGDH	Pr_t (Kays Corr.)	-	-	-	-	$Pe_t \leq 10$	$Pe_t \leq 10$
SGDH	Look-up Tables	-	-	-	-	56 - 6400	22000
AHFM	AHFM-NRG:k-ε	$1\text{-}10^{17}$		0 - 4		≥ 180	
AHFM	k-ε-k_θ-ε_θ	-	-	-	-	300 - 2500	
AHFM	AHFM-NRG:RSM	-	-	-	-	≥ 145	
2nd Order	TMBF	24 000 & 100 000	63 0000	-	Ri=1-4	Pe=70	-
2nd Order	TMBF-eq-ATHFM	24 000 & 100 000	Ra=63 0000	-	Ri=1-4	Pe=40-4000	Pe=10000

performs good for the mentioned numbers | performs fairly well, but needs more improvement | model co-efficients need to be calibrated | model has intrinsic limitations

Nevertheless, these correlations are well calibrated and cover a wide range of global parameters to provide better results in all three flow regimes. One of the main limiting factors of this model is that for each flow regime the model co-efficients must be modified. Therefore, there is a need to automate this modelling approach so that it can be applied to real industrial applications, where all three flow regimes could appear simultaneously. The performance of the AHFM-SC formulation is briefly demonstrated, in the next section, to highlight the importance of sophisticated THF modelling.

5. The need of sophisticated turbulent heat flux models

To highlight the need and the importance of sophisticated THF modelling, a comparison of AHFM-SC formulation with the 'off-the-shelf' SGDH modelling approach has been demonstrated for all three flow regimes.

5.1. Natural convection flows

The classical case of RBC has been selected to represent the natural convection flow regime. The RBC simulations have been performed on a slender geometry with a 1:8 aspect ratio, with the Rayleigh number (Ra) = 100000 and the Pr = 0.025. The RANS models assessed for this flow configuration comprise of the AHFM-SC:k-ε and the SGDH:k-ε. The obtained results have been validated against the

reference DNS data [32]. Fig. 3 illustrates the evolution of the mean temperature for this considered test case. The prediction capabilities of the AHFM-SC formulation to identify the effect of large thermal diffusivity (because of low-Pr fluid) are clearly noticeable, and the obtained results are found to be in very good agreement with the reference DNS. On the other hand, the off-the-shelf SGDH approach fails to accurately predict the thermal field.

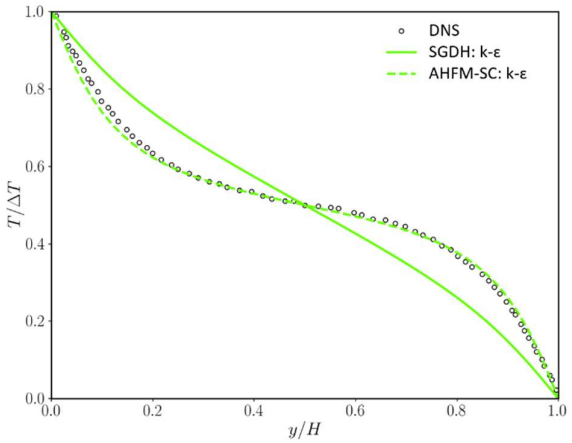

Fig. 3 A comparison of mean temperature profiles corresponding to Ra=100 000 and Pr=0.025.

5.2. Mixed convection flows

A differentially heated turbulent planar channel case has been selected for the mixed convection flow regime, see Fig. 4. The recently published DNS database of Guo at al. [33] is used to assess the performance of the AHFM-SC:k-ε and the SGDH:k-ε models. The steady-state simulations are performed at a fixed bulk Reynolds number Re_b = 4667 (which corresponds to the Re_τ = 151 in the forced convection flow regime) for two different values of the Richardson number (Ri), i.e., 0.25 and 1. By looking at the results in Fig. 5, it can be seen that the used sophisticated THFM shows superior results than the off-the-shelf SGDH approach. For both cases, the Reynolds analogy displays large errors and does not seem to be an appropriate choice for the considered test cases. On the other hand, the AHFM-SC formulation display very good agreement at relatively low Ri, i.e., 0.25. With the increase in the buoyancy influence, a slight mismatch can be observed at Ri=1. Nevertheless, the overall results are very encouraging and highlight the need of a sophisticated THF modelling approach.

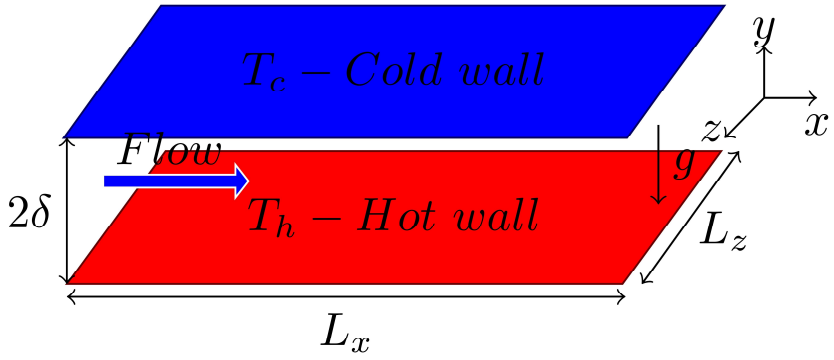

Fig. 4 A 3D sketch of the mixed convection channel flow [33].

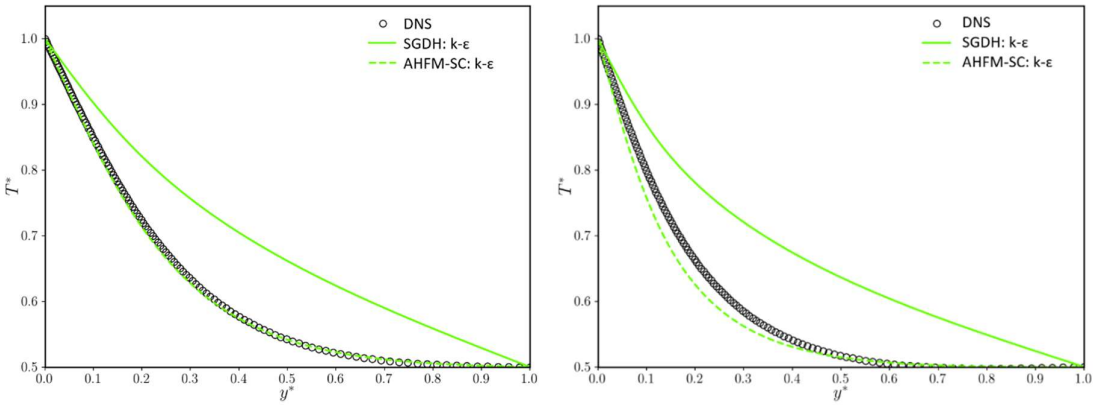

Fig. 5 A comparison of mean temperature profiles for (Left) Ri=0.25 and (Right) Ri=1.0 at Pr=0.025.

5.3. Forced convection flows

In the category of the forced convection flow regime, two test cases are selected to demonstrate the combination of linear and non-linear momentum flux models in combination with the turbulent heat flux models. These test cases include (i) a planer turbulent channel flow and (ii) a loosely spaced triangular bare rod bundle. For both test cases, simulations are performed using the AHFM-SC:k-ε, the AHFM-SC:RSM-EB and the SGDH approach based on both the aforementioned TMF closures.

Fig. 6 shows the obtained non-dimensional temperature for the turbulent channel flow calculated at Re_τ = 395 and Pr = 0.025. It can be seen that regardless of the closure used for the TMF, the limitations of the Reynolds analogy at this low-Pr value are evident. On the other hand, the AHFM-SC formulation shows a good agreement with the reference DNS [34].

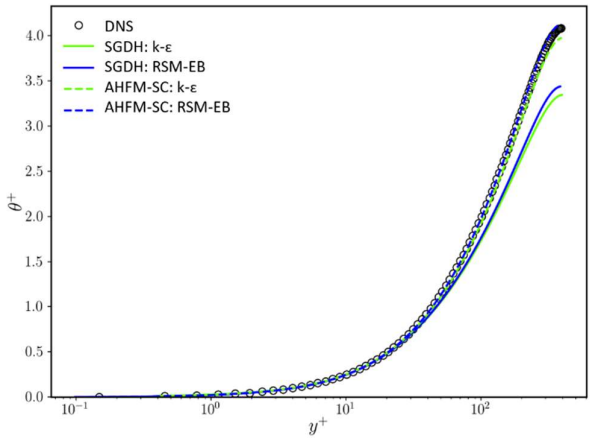

Fig. 6 A comparison of mean temperature profiles corresponding to Re_τ = 395 and Pr=0.025.

Fig. 7 (Left) illustrates the computational domain to study the prediction capabilities of the aforementioned models for the heat transfer in a bare rod bundle. This rod bundle is a representative

of the loosely spaced triangular rod bundle of the ALFRED reactor [35]. It has a pitch to diameter ratio (P/D) = 1.32. The simulations are performed corresponding to the Reynolds number of 54600 and the Pr = 0.016. The face pairs NW-SE and NE-SW represent the periodic boundary conditions in the cross-sectional direction. For more details regarding this case, readers are referred to Shams at al. [36]. The obtained profiles of the mean temperature in the narrow gap region of the rod bundle are shown in Fig. 7 (Right). It is clearly noticeable that the models relying on the SGDH approach tend to significantly underestimate the wall temperature. On the other hand, it is evident that the use of the AHFM-SC formulation results in a noticeable improvement in the accuracy of the results. Particularly, the use of the non-linear TMF model in combination with the AHFM-SC, i.e., AHFM-SC:RSM-EB, yields an excellent agreement with the reference LES data.

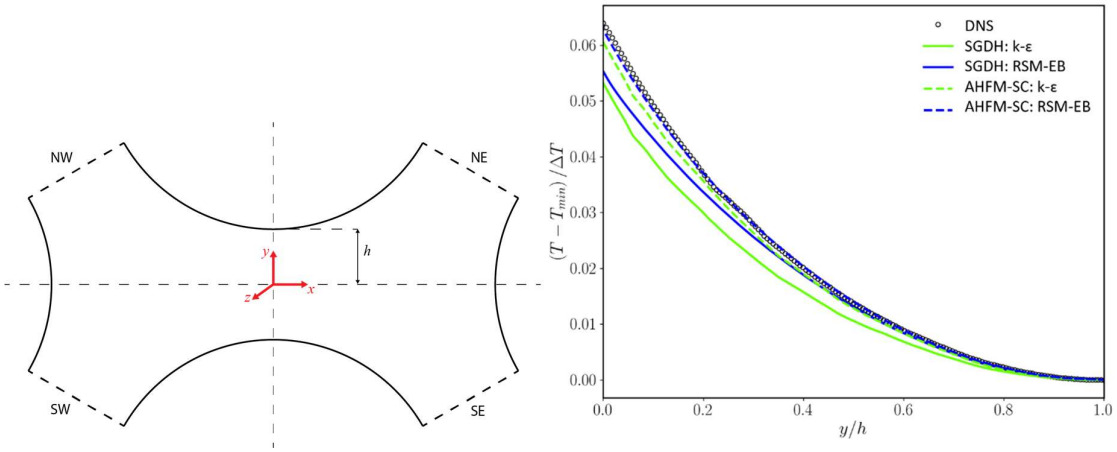

Fig. 7 (Left) Cross-section of the bare rod bundle computational domain [29] (Right) A comparison of mean temperature profiles in the narrow region of the bare rod bundle.

6. Conclusions

In this article, an effort has been put forward to highlight the need for proper turbulent heat flux modelling in non-unity Prandtl number flows, particularly in the liquid metal flows. The main focus of this numerical prediction has been on the use of RANS modelling approach. Because of very low Prandtl number, the prediction of heat transfer phenomena in liquid metals becomes challenging for the "off-the-shelf" RANS models. To understand that, some limitation and peculiarities of the "off-the-shelf" RANS models are highlighted for different flow regimes, i.e. natural, mixed and forced convection. In addition, the status and perspectives of the available turbulent heat flux modelling closures within the nuclear community are provided with an especial focus on the low-Pr fluids. Various collaborative efforts within the European liquid metal community are briefly discussed. These collaborative endeavours have been the corner stones for the development of sophisticated turbulent heat flux models currently available in the market. Among these available models, a well-calibrated and tested THFM, namely AHFM-SC, is selected to show the need and the importance of such sophisticated models in non-unity Prandtl number fluids in natural, mixed, and forced convection flow regimes.

References

1. A. Shams, Turbulent heat transport. In: Thermal Hydraulics Aspects of Liquid Metal Cooled Nuclear Reactors. Elsevier, pp. 273–292 (2019).

2. G. Grötzbach, Anisotropy and buoyancy in nuclear turbulent heat transfer – critical assessment and needs for modelling, Forschungszentrum Karlsruhe, FZKA 7363 (2007).
3. A. Shams, F. Roelofs, I. Tiselj, J. Oder, Y. Bartosiewicz, M. Duponcheel, B. Niceno, W. Guo, E. Stalio, D. Angeli, A. Fregni, S. Buckingham, L. K. Koloszar, A. Villa Ortiz, P. Planquart, C. Narayanan, D. Lakehal, K. van Tichelen, W. Jaeger and T. Schaub, A collaborative effort towards the accurate prediction of turbulent flow and heat transfer in low-Prandtl number fluids, Nuclear Engineering & Design 366, 110750 (2020).
4. B. Arien, et al., Assessment of computational fluid dynamic codes for heavy liquid metals – ASCHLIM. EC-Con. FIKW-CT-2001-80121-Final Report (2004).
5. I. Otic I, and G. Grötzbach, Turbulent heat flux and temperature variance dissipation rate in natural convection in lead-bismuth. Nucl. Sc. Engg. 155: 489-496 (2007).
6. K. Hanjalic, One-point closure models for buoyancy-driven turbulent flows. Annual Review of Fluid Mechanics, 34, 321–347 (2002).
7. A. Shams, F. Roelofs, E. Baglietto, S. Lardeau and S. Kenjeres, Assessment and calibration of an algebraic heat flux model for low-Prandtl fluids. International Journal of Heat and Mass Trans. 79, 589–601 (2014).
8. F. Roelofs, A. Shams, I. Otic, M. Böttcher, M. Duponcheel, Y. Bartosiewicz, D. Lakehal, E. Baglietto, S. Lardeau and X. Cheng, Status and perspective of turbulence heat transfer modelling for the industrial application of liquid metal flows. Nuclear Engineering & Design. Vol. 290, 99-106 (2015).
9. OECD, Best practice guidelines for the use of CFD in nuclear reactor safety applications. NEA/CSNI/R 5, Paris, France (2007).
10. A. Shams, The importance of turbulent heat transfer modelling in low-Prandtl fluids. In: ATH 2018, ANS Winter Meeting Embedded Topical, November, Orlando, Florida (2018).
11. A. Shams, Turbulent heat transport. In: Thermal Hydraulics Aspects of Liquid Metal Cooled Nuclear Reactors. Elsevier, pp. 273–292 (2019).
12. F. Roelofs, A. Shams, J. Pacio, V. Moreau, P. Planquart, K. van Tichelen, I. Di Piazza and M. Tarantino, European Outlook for LMFR Thermal Hydraulics. NURETH-16, Chicago, IL (2015).
13. C.D. Wilcox, Turbulence Modeling for CFD, second ed. DCW Industries, La Canada. ISBN 0963605100 (1998).
14. B. Andersson, R. Andersson, L. Hakansson, M. Mortensen, R. Sudiyo and B. van Wachem, Computational Fluid Dynamics for Engineers. Cambridge University Press, Cambridge, p. 83. ISBN 978-1-107-01895-2 (2012).
15. J. Piquet, Turbulent Flows – Models and Physics. Springer, Berlin (1999).
16. W. Rodi, Turbulence Models and their Application in Hydraulics - a State of the Art Review, third ed. IAHR Publication, Delft, Balkema Rotterdam (1993).
17. B.J. Daly and F.H. Harlow, Transport equations in turbulence. Phys. Fluids 18, 2634–2649 (1970).
18. N. Ince, and B. Launder, On the computation of buoyancy-driven turbulent flow in rectangular enclosures. Int. J. Heat Fluid Flow 10, 110–117 (1989).
19. S. Kenjeres, S.B. Gunarjo and K. Hanjalic, 2005. Contribution to elliptic relaxation modelling of turbulent natural and mixed convection. Int. J. Heat Fluid Flow 26 (4), 569–586 (2005).
20. B. Launder, An introduction to single-point closure methodology, an introduction to the modelling of turbulence, Lecture Series 1986-1987, Von Karman Institute for Fluid Dynamics, Rhode-Saint-Genese, Belgium (1987).
21. L.N. Carteciano, D. Weinberg, U. Meuller, Development and analysis of a turbulence model for buoyant flows. In: 4th World Conference on Experimental Heat Transfer, Fluid Mechanics and Thermodynamics. Brussels, June 2–6, vol. 3. Edition ETS, Pisa, pp. 1339–1347 (1997).

22. C.d.P. Donaldson, Construction of a dynamic model of the production of atmospheric turbulence and the dispersal of atmospheric pollutants. In: Haugen, D.A. (Ed.), Workshop on Micrometeorology. Amer. Met. Society, pp. 313–392 (1973).
23. B.E. Launder, Second-moment closure: Present – and future. Int. J. Heat Fluid Flow 10, 282–300 (1989).
24. S. Manservisi, F. Menghini, Triangular rod bundle simulations of a CFD (κ-ε-κ_Θ-ε_Θ) heat transfer turbulence model for heavy liquid metals. Nuclear Engineering and Design 273: 251–270 (2014).
25. M. Duponcheel, L. Bricteux, M. Manconi, G. Winckelmans and Y. Bartosiewicz, Assessment of RANS and improved near-wall modeling for forced convection at low Prandtl numbers based on LES up to Re_τ=2000, International Journal of Heat and Mass Transfer 75, 470 – 482 (2014).
26. W. M. Kays, Turbulent Prandtl number — where are we?, Journal of Heat Transfer 116 (2) 284 – 295 (1994).
27. M. Böttcher, CFD investigation of LBE rod bundle flow, The Connector, Pointwise, http://www.pointwise.com/theconnector/September-2013/Rod-Bundle-Flows.html (2003).
28. A. Shams, Towards the accurate numerical prediction of thermal hydraulic phenomena in corium pools. Annals of Nuclear Energy, Vol. 117, 234 – 246 (2018).
29. A. Shams and A. De Santis, Towards the accurate prediction of the turbulent flow and heat transfer in low-Prandtl fluids, International Journal of Heat and Mass Transfer 130, 290 – 303 (2018).
30. A. Shams, A. De Santis and F. Roelofs. An overview of the AHFM-NRG formulations for the accurate prediction of turbulent flow and heat transfer in low-Prandtl number flows. Nuclear Engineering and Design 355: 110342 (2019).
31. A. Shams, A. De Santis, L.K. Koloszar, A. V. Ortiz and C. Narayanan. Status and perspectives of turbulent heat transfer modelling in low-Prandtl fluids. Nuclear Engineering and Design 353: 110220 (2019).
32. I. Otic, G. Grötzbach and M. Worner, Analysis and modelling of the temperature variance equation in turbulent natural convection for low-Prandtl-number fluids. Journal of Fluid Mechanics. 525: 237-261 (2005).
33. W. Guo, A. Shams, Y. Sato and B. Niceno, Influence of buoyancy in a mixed convection liquid metal flow for a horizontal channel configuration, International Journal of Heat and Fluid Flow 85, 108630 (2020).
34. H. Kawamura, H. Abe and K. Shingai, DNS of turbulence and heat transport in a channel flow with different Reynolds and Prandtl numbers and boundary conditions. 3rd International Symposium on Turbulence, Heat and Mass Transfer (2000).
35. A. Alemberti and L. Mansani, The Advanced Lead Fast Reactor European Demon- strator (ALFRED), in: 15th International Topical Meeting on Nuclear Reactor Thermal-hydraulics, NURETH-15, Pisa, Italy (2013).
36. A. Shams, B. Mikuz, F. Roelofs, Numerical prediction of flow and heat transfer in a loosely spaced bare rod bundle, International Journal of Heat and Fluid Flow 73, 42 – 62 (2018).

NUMERICAL MODELLING OF ROTATING FLOWS WITH LARGE FREE-SURFACE DEFORMATION

S.D. Amar[1,2], A. Rashkovan[2], G. Ziskind[1]

[1]*Department of Mechanical Engineering, Ben-Gurion University of the Negev, Beer-Sheva, Israel*

[2]*Physics Department, NRCN, P.O.B. 9001, Beer-Sheva 84190, Israel*

Extended Abstract

Rotating flows that involve free-surface vortex with axial liquid flow through an outlet occur in many engineering applications such as rotary equipment (e.g. pumps and turbines), liquid tanks, and in nuclear reactors. With strong circulation or relatively shallow liquid depth, the created gas core can reach the outlet and potentially cause operational problems in the hydraulic intakes due to vibrations, cavitation, etc.

In Sodium Fast Reactors (SFRs) argon is used as a cover gas above the sodium surface in order to isolate it from air. If entrained into the core, argon can cause reactivity fluctuations due to the void reactivity coefficient. Large amounts of accumulated entrained gas can deteriorate the efficiency of the heat exchanger and threaten the fuel elements. The primary pump can also suffer from entrained gas due to cavitation, and measuring instruments can be disturbed by the gas entrained into the core.

In the course of a loss-of-coolant accident (LOCA) in Light Water Reactors (LWR), emergency core cooling systems (ECCS) should provide the necessary cooling for the reactor components by means of centrifugal pumps. However, with relatively shallow coverage of the pump inlet port, a hollow vortex can develop with further gas entrainment into the ECCS pumps. This can potentially lead to substantial pump damage up to its complete malfunction.

The basic theory of vortex flows is well established and numerous basic solutions with some simplifications are available in the literature. However, the numerical studies concerning rotataing flows with highly deformed free-surface are rather limited due to the complexity of the problem. Morover, flows which involves unsteady and highly deformed free-surface flow accompanied with turbulence, are even more challenging to treat numerically.

In this study two cases of liquid flows with highly deformed free-surface have been modelled using ANSYS Fluent -r19.0.0 software as a platform. The first is the so-called bathtub vortex in which a free-surface vortex is created in a rotating cylinder with a drain hole in its bottom. A 2D axisymmetric model was implemented using two-phase flow with the Volume Of Fluid (VOF) method. The simulations were validated with the available measurements from the experiments in the literature. The numerical results allow to elucidate the velocity field in all the flow regions, including those where the experimental measurements are limited. The most interesting region is the vortex region, where high azimuthal velocity is accompanied by axial velocity. These velocities were quantified for a number of the cylinder rotation rates. Existing analytical describing the velocity fields in different flow regions, were compared and tested, in order to judge which is more accurate. In addition, modified analytical model was suggested to better represent the relation between the velocity fields and the free-surface profile.

The second modeled case is a free-surface vortex created in a stationary tank in which the liquid is pumped out through a nozzle at its bottom. A 3D model was implemented using two-phase flow with the VOF method accompanied with the Large Eddy Simulation (LES) to simulate the expected turbulent flow. Several experiments were performed in a dedicated experimental set-up with different flow rates. In each experiment image processing was conducted to establish the accurate time-dependent shape of the free-surface. These observations were compared to the simulated free-surface profiles and good agreement was found.

SIMULATION OF A PARTIALLY BLOCKED WIRE-WRAPPED FUEL ASSEMBLY USING LES WITH WALL FUNCTIONS

Octavio Bovati and Yassin Hassan

Extended Abstract:

One of the most promising nuclear reactor designs is the Liquid-Metal Fast Reactor (LMFR). Its fuel assembly consists of rods containing the fuel material, arranged in a triangular lattice and covered by a hexagonal duct. The rods are separated with wire spacers that are helically wrapped around each fuel pin. Because this geometry is tight and compact, accumulation of debris, cladding deformation or detachment of the wires may generate a partial or total flow blockage of coolant subchannels at different locations. The understanding of the coolant behavior in LMFR fuels under the influence of a partially blocked flow area is required for a thorough safety assessment. A Large Eddy Simulation (LES) with wall functions was executed to simulate the flow on a 61-pin wire-wrapped rod bundle under the presence of a blockage located on the bundle periphery to simulate an abnormal operation condition. The Reynolds number was $Re = 17000$, which is in the turbulent regime. Results of mean velocity and root mean square (rms) fluctuating velocity profiles were compared with PIV experimental data from the Texas A&M Thermal-Hydraulic Research Lab. Both mean and rms velocities were found in reasonable agreement with the experimental data among different locations because the simulation results were within 2σ from the PIV measurements. A pressure form loss coefficient due to the blockage was calculated and found to be $K_{loss} = 1.0455$.

PREDICTION OF TURBULENT HEAT TRANSFER IN BUOYANCY-AFFECTED FLOW REGIME

Andrea Pucciarelli[1], Afaque Shams[2] and Nicolad Forgione[1]

[1]*Università di Pisa - Largo Lucio Lazzarino 2, 56122 Pisa*
[2] *King Fahd University of Petroleum & Minerals - Dhahran, 31261, Saudi Arabia*

andrea.pucciarelli@unipi.it, afaque.shams@kfupm.edu.sa, nicola.forgione@unipi.it

Extended Abstract

Liquid metals thermal-hydraulics represent an interesting topic for several industrial and engineering applications. In the nuclear field, lead and sodium were considered for two plant concepts included by the GIF consortium among the accepted proposals for the fourth generation of the nuclear power plant, namely the LFR (Lead Fast Reactor) and the SFR (Sodium Fast Reactor). Among the advantages of the adoption of such fluids are the extremely large heat capacity, good thermal conductivity and heat transfer capabilities, low scattering, and absorption cross sections. Several EU projects supported (e.g., THINS, SESAME, MYRTE), and presently support (e.g., PATRICIA, ANSELMUS) the development of Liquid Metal Fast Breeder Reactors (LMFBRs), providing room for further liquid metal thermal-hydraulics experimental and numerical investigations. Unlike other fluids adopted in industrial applications, liquid metals exhibit very small Prandtl numbers, in the range of 0.004-0.04. This occurrence strongly impacts heat transfer to liquid metals: thermal boundary layers turn, in fact, to be relevantly larger than the ones experienced by fluids reporting an almost unitary Prandtl number.

The present paper investigates the capabilities of some selected Reynolds-Averaged Navier-Stokes (RANS) turbulence models in reproducing liquid metals thermal hydraulics Direct Numerical Simulation (DNS) data: forced and mixed convection conditions, both addressing buoyancy-aided and buoyancy-opposed flow, are considered. The paper mainly focuses on velocity and temperature field estimates, comparing the RANS and DNS calculations: the turbulence models' capabilities are discussed, trying to highlight the ones providing the best predictions. In particular, attention is paid to the approach adopted for the calculation of the turbulent heat flux contributions. Together with models assuming the commonly adopted Simple Gradient Diffusion Hypothesis (SGDH) approach and the Reynolds analogy, a model including the Algebraic Heat Flux Model (AHFM) approach is considered. While being a practical and robust approach to deal with turbulent heat fluxes, the SGDH approach shows intrinsic limits in dealing with liquid metal thermal hydraulics. The adoption of more advanced AHFM method may instead relevantly improve the quality of the obtained predictions.

The obtained results show that the selected model adopting the AHFM method provides definitively better predictions of the addressed phenomena with respect to the ones considering the SGDH approach. While some discrepancies are still observed for the velocity fields, the temperature fields are captured very well, suggesting a clear superiority of the AHFM model. The present paper thus provides further validation and supports the use of AHFM as a valuable tool to predict turbulent heat fluxes.

Prediction of flow regime boundary and pressure drop for hexagonal wire-wrapped rod bundles using artificial neural networks

Hansol Kim[a*] and Yassin A. Hassan[a,b]

[a] J. Mike Walker '66 Department of Mechanical Engineering, Texas A&M University
[b] Department of Nuclear Engineering, Texas A&M University

Extended Abstract

Fuel rod bundles are typically arranged in a triangular lattice in reactor designs for Generation IV reactors, involving a spirally-wrapped wire around each pin. Among its featured functions, the wrapped wire maintains the gap between the rods, thereby increasing the heat transfer capability and reducing flow-induced vibrations. With the advancement of computational capabilities and the development of algorithms, the accumulated database enabled the use of machine learning for regression or classification tools. In this study, we constructed a surrogate model for the transition-to-turbulence flow regime boundary and friction factor in complex geometry. This study used an artificial neural network (ANN) regression model in wire-wrapped fuel assemblies to estimate the transition-to-turbulence flow regime boundary (RebT) and friction factor. The two layered ANN models were trained and validated using existing experimental datasets. The bundle dataset comprised several design parameters, such as the number of rods, rod diameter, wire diameter, lattice pitch, edge pitch, and wire helical pitch. RebT data was selected using existing 103 bundles experimental data. ANN models for friction factor were trained and validated using previously collected 142 bundles of experimental data. The log-log scale Reynolds number and linearity characteristics of the friction coefficient were used to over-sample the friction factor in the laminar and turbulent regimes for resolving the data imbalance. The ANN design is R_0-R_1-1, where R_0 and R_2 are the number of neurons in the input and output layer, and R_1 is the number of neurons in the hidden layer, which was determined by the minimum validation error principle. Three-quarters of the entire dataset was used for training, while the remainder was used for validation. The Levenberg-Marquardt approach with the Gauss-Newton approximation for the Hessian of the training cost function was used for training the model. The number of hidden layers for RebT was selected based on the minimum validation error. The goodness of ANN model for RebT have 0.03% of mean error and 10.92 % of RMSE. The pin number effect was additionally considered for the friction factor while selecting the number of hidden layers. It was used to compare ANN models trained on existing and oversampled data. The ANN model predicted using the oversampled data set had a 50% reduction in root mean square error (RMSE) than the model predicted using the original data set. The model predicted from the oversampled dataset showed better accuracy than the model built using the existing dataset. When compared to correlations such as REH, NOV, BDD, ZHU, UCTD, ANN, and PCTD in prior research, the prediction of ANN models for friction factor revealed significantly lower errors (0.10% mean error, 7.35% standard deviation of the error, 12.10% of 90% confidence interval, 0.9392 of R^2 and 7.36% of RMSE of 142 bundles data).

U.S.NRC
United States Nuclear Regulatory Commission
Protecting People and the Environment

Center for Advanced Small Modular and Micro Nuclear Reactors
Texas A&M Engineering Experiment Station

NEA
NUCLEAR ENERGY AGENCY

Technical Session 7

Fuel Fluid Interactions.

Feb 20, 10:30-12:00, Room A.

Utilization of 3D Boron Asymmetry information in nuclear reactor generated from CFD for 1D Safety Analysis

Seunghwan Oh, Doh Hyeon Kim, Jeong Ik Lee

Korea Advanced Institute of Science and Technology (KAIST)

Extended Abstract

The pressurized water reactor (PWR) uses borated coolant to control reactivity. A uniform concentration of borated coolant flows through the core under normal operating condition. However, the boron concentration in the core may become disrupted when the coolant is injected with a reduced boron concentration in one leg. This can lead to a temporary asymmetry of boron concentration in the core. If this occurs, it is inevitable that the local reactivity of each fuel assembly becomes different. Finally, this phenomenon can adversely affect the core safety margin. In this study, an extreme situation is assumed in order to conservatively evaluate the safety due to temporary boron concentration asymmetry. It is expected that a power distribution gradient will occur in the core due to the boron concentration asymmetry. Since this will affect the fuel assembly temperature, the departure from nucleate boiling ratio (DNBR) evaluation should be performed to evaluate the safety margin.

In the nuclear engineering field, CFD is widely used as means to replace expensive experiments and as a way to supplement the limitation of one-dimensional analysis codes. Unlike one-dimensional analysis codes such as RELAP5 and MARS-KS, CFD provides qualitative data by analyzing three-dimensional flow, enabling accurate safety evaluation. Moreover, 1D safety analysis code such as MARS-KS cannot accurately reflect the three-dimensional data of CFD because the core is not modeled with each fuel assembly. Therefore, when simulating the assumed situation with MARS-KS, only the overall average boron concentration can be used, and there is a limit to confirming the effect of 3D boron concentration asymmetry.

In this study, for CFD analysis of flow mixing and asymmetry in a large PWR, the internal geometry of the vessel is simulated as realistically as possible. The CFD used is ANSYS-CFX 2020R1. The flow field is calculated using the limited computational resources efficiently by applying the porous medium model to the nuclear fuel assembly region, and the Unsteady Reynolds-Averaged Navier-Stokes Scheme and standard turbulence model are applied. The CFD model consists of about 57,000,000 cells, and a tetrahedral grid is applied to the flow domain, and a prism grid is applied near the wall to increase the accuracy of the wall model. New simulation methods are also proposed and evaluated to utilize CFD data in the 1D safety analysis. The first proposed method simulates fuel assemblies individually without considering cross-flow between fuel assemblies. The second proposed method considers only direct cross-flow. In other words, if one fuel assembly is selected, the modeling range is only the adjacent fuel assemblies. The last proposed method considers both direct and indirect cross-flow, and calculates similarly to the existing 1D model.

The reference reactor selected in this study is APR1400, which has four cold-legs. The event is assuming that water comes from one cold-leg while other three legs have the normal borated water. For the assumed conditions, the 3D boron concentration distribution is analyzed with CFD and the result is transferred to 1D system analysis code MARS-KS to perform the safety evaluation while utilizing 3D data. In summary, the degree of boron concentration asymmetry caused by the injection of pure water from one of the four cold-legs is analyzed with 3D CFD, and this result is reflected in 1D MARS-KS to understand the power distribution and variations in DNBR which leads to the evaluation of safety margin changes during the event.

VALIDATION PRACTICES OF MULTI-LEVEL ANALYSES ON PLANT THERMAL-HYDRAULICS IN AN ADVANCED REACTOR DESIGN STUDY

Masaaki Tanaka, Takero Mori, Kazuo Yoshimura, Erina Hamase, Norihiro Doda, Kentaro Matsushita, Norihiro Kikuchi, Ryuji Yoshikawa, and Toshiki Ezure

Japan Atomic Energy Agency

Extended Abstract

In Japan Atomic Energy Agency (JAEA), an artificial intelligence (AI) aided integrated digital system named ARKADIA (Advanced Reactor Knowledge- and AI aided Design Integration Approach through the whole plant lifecycle) is being developed to offer the best possible solutions for challenges arising during the design process, safety assessment, and operation of a nuclear plant over its life cycle. ARKADIA consists of three inter-connected systems: EAS (Enhanced and AI-aided optimization System) as controller of numerical simulations and evaluations for design study, VLS (Virtual plant Life System) for a numerical simulator, and KMS (Knowledge Management System) with knowledge obtained through the development of sodium-cooled fast reactors (SFRs) including the relevant R&Ds in JAEA. Until 2023, the platform for the basement of the systems and the three partial systems of AKRADIA: ARKADIA-Design for design study, ARKADIA-Safety for safety assessment, and ARKADIA-KMS for knowledge-base, are separately being developed. Until 2028, these systems are going to be unified into one system of ARKADIA. Focusing on the VLS of ARKADIA-Design, this paper describes representative validation practices in the development of the numerical analysis methods to evaluate static and transient thermal-hydraulic phenomena in the reactor vessel (RV) including the core part under normal operating conditions and design basis events for an advanced reactor design study. Numerical analyses in the design study are performed in the virtual plant model formulated with the multi-level (ML) approach using necessary numerical analysis codes equipped in the VLS. In the ML approach, the models at different degrees of resolution in the decomposed domains can be used according to the user's requirements. Therefore, the user can select an analysis method from the following options: the single analysis using a one-dimensional plant dynamics analysis (PDA) code with simplified models, the single analysis using a multi-dimensional analysis (MDA) code with detailed models in a specific region, the coupled analysis using the MDA codes in different regions and physics, and the coupled analysis using the PDA and the MDA codes. A validation matrix is indicated with the performance test data conducted at the SFRs including EBR-II, FFTF, JOYO, and MONJU, the plant dynamics sodium test data obtained at the PLANDTL facility in JAEA, and the small-scaled experimental test data. Typical practices of the validation with these data in the development of the in-house code named Super-COPD for the PDA, the commertial computational fluid dynamics (CFD) code FLUENT for the MDA, and the coupled analysis method with those codes are described, in comparison with the representative physical indexes measured at the test, such as the temperature and flow rate through each component in the heat transfer systems. For the MDA, the development of a numerical analysis method to predict the multi-dimensional thermal-hydraulic phenomena in the RV during decay heat removal (DHR) operation is the main interest. During the DHR operation in a reference SFR design in JAEA, the phenomenon called "core-plenum thermal interaction" involving the penetration flow of the cold sodium into the fuel assemblies (FAs), the inter-wrapper flow, and the radial heat transfer between neighboring FAs, is caused by the flow of the low-temperature coolant from direcrt heat exchanger installed in the upper plenum of the RV. A representative practice to validate the unified model of the inter-wrapper gap between FAs, the flow area inside of the FA, and the upper plenum in the RV is explained in comparisons with the experimental test data at the PLANDTL facility to investigate the interaction phenomena. Moreover, with review of the validation matrix, future works for nessersary validation studies to establish AKADIA-Design are discussed.

EFFECT OF BAFFLE JETTING ON THE HEAT TRANSFER AND FLUID FLOW WITHIN ROD ASSEMBLY

Mohamed Ali[1,2], Ahmed Alkaabi[1,2], Yacine Addad[1,2], Imran Afgan[2,3]

[1]Emirates Nuclear Technology Center, Khalifa University, PO BOX 127788, Abu Dhabi, UAE
[2]College of Engineering, Khalifa University, PO BOX 127788, Abu Dhabi, UAE
[3]Department of MACE, School of Engineering, University of Manchester, M13 9PL, UK

Extended Abstract

In this numerical investigation, the flow and heat transfer properties are studied in the case of the baffle jetting phenomena. Baffle jetting is caused by the horizontal flow at the plate gap of the nuclear reactor rod assembly during the vertical flow of the coolant. The flow impinging on the corner rods leads to vibratory behavior causing wear fretting and, hence, rod failure. Baffle jetting was reported as the cause of some accidents for specific Pressurized Water Reactors (PWR) designs. Therefore, a deep understanding of the mechanisms governing baffle jetting is crucial for the safety of nuclear reactors.

In this investigation, the experimental rig, PANACHET, developed by French Atomic Agency (CEA) in the '90s was numerically mimicked for a detailed analysis. The rig consists of a 6×6 fuel rod assembly subjected to a turbulent jet developed along a channel connected to the assembly's corner. The dimension of the assembly is $80 \times 80 \times 80$ mm^3. The rods are inline arranged with a diameter of 9.5 mm, a pitch-to-diameter ratio of $4/3$, and a gap-to-diameter ratio of 0.38. The channel width is 0.5 mm and its length is 80 mm. Varying the inlet velocity U_{inlet}, three different configurations were considered corresponding to Reynolds numbers $Re = 5{,}010$, $10{,}000$, and $20{,}000$, based on the hydraulic diameter of the channel and the inlet velocity. A periodic boundary condition was used in the span-wise direction (parallel to the rods) while an outlet flow boundary condition was imposed at the outlet. A synthetic eddy method was used to generate a fluctuating velocity field as required by the Large Eddy Simulations (LES). A wall temperature boundary condition was imposed at the rods' surface to assure a temperature difference of 5°C compared to the jet flow.

LES were performed to solve the governing equations of the single-phase flow using the Wall-Adapting Local Eddy-viscosity (WALE) model. The PISO algorithm was used to solve the velocity-pressure coupling. The convective terms were discretized with a second-order bounded central difference scheme. The iterative solvers were performed using a Gauss-Seidel scheme with a Conjugate Gradient acceleration method. The time step was set to keep an average value of the CFL below 1. The LES quality was evaluated based on Pope's index related to the ratio between the resolved turbulent kinetic energy and the total turbulent kinetic energy. For the heat transfer, the temperature was considered as a conserved passive scalar. The numerical results were validated against both the experimental data and previous LES investigations of the PANACHET rig. The novelty of the simulations lies not only in the detailed understanding of the flow physics but also on the heat transfer data which is missing from literature for this configuration. The current simulations were able to predict the recirculation zones as well as the flow structures around the corner rod and near the jet inlet. Results show that the baffle jetting significantly affects the flow and heat transfer properties around the stream-wise rods while its effects are negligible far from the assembly inlet. Furthermore, contrarily to the uniform flow case, the mean pressure coefficient and Nusselt number lose symmetry around the rods. Moreover, increasing the Reynolds number leads to higher mean forces and Nusselt numbers. Considering the mean force coefficients and their fluctuations, it was concluded that the corner rod is subjected to higher loads while the third stream-wise rod is subjected to higher vibrations. Moreover, smaller vertical scales are generated within the assembly for larger Reynolds numbers as the shear layers around the rods breakdown faster.

NUMERICAL PREDICTION OF FLOW AND HEAT TRANSFER IN A BARE ROD BUNDLE WITH SQUARE AND TRIANGULAR LATTICE CONFIGURATION

Tomasz Kwiatkowski[1], Anna Talarowska[1] and Afaque Shams[2]

[1] *National Centre for Nuclear Research, A. Sołtana 7, 05-400 Otwock-Świerk, Poland*
[2] *King Fahd University of Petroleum & Minerals - Dhahran, 31261, Saudi Arabia*

tomasz.kwiatkowski@ncbj.gov.pl, anna.talarowska@ncbj.gov.pl, afaque.shams@kfupm.edu.sa

Extended abstract

The majority of currently operating reactors are water-cooled reactors with fuel arranged in bundles. Two basic bundle types can be distinguished based on the fuel rods' geometrical configuration inside bundles, namely square or triangular arrays. In reality, rod bundles are characterised by very complex geometries with grid spacers. Such geometries are too complicated to investigate in detail different physical phenomena. As a remedy, scientists are using simplified geometries for their research work (both experimental and numerical) to limit the impact of various factors. Thus, in the present study, a wide range of steady-state and Unsteady Reynolds Averaged Navier-Stokes (URANS) computations are performed to reproduce the turbulent flow and heat transfer conditions in different bare rod bundle configurations. As a reference, two well-known experiments have been considered. The first one is based on the Krauss and Mayer experiment, in which turbulent flow in a bundle of heated 37-rods with triangular array at two different pitch-to-diameter ratios (P/D = 1.12 and P/D = 1.06) was investigated. The second experiment is related to a square configuration, and it referred to hydraulic experiment of Hooper. The six-rod array test section with pitch-to-diameter ratio of P/D = 1.107 was built to model the fluid mechanics inside a large symmetrical square-pitch rod array. It is known that the pitch-to-diameter ratio is one of the most important geometrical parameters which could influence the main characteristics of the coolant flow (such as existence of gap vortex street, dominant flow and thermal frequency or wavelength of the pulsations). Therefore, in the present research work, a parametric study of the turbulent flow and thermal quantities is performed in a systematic way. As a first step, the macroscopic flow characteristics of both experiments are numerically reproduced. Secondly, the Reynolds numbers of the reference experimental cases were scaled-down in such a way that the overall phenomenology of the flow field was preserved, by means of existence of gap vortex street. Special attention has been put forward to the possible reproduction of the gap vortex street in the laminar and transient flow regimes. In addition, a parametric study for different passive scalars is performed to take into account the heat transfer analysis within the domain. These passive scalars correspond to the Prandtl numbers of three different working fluids, i.e., liquid metal, air and water. The heat transfer of these three fluids has been studied along with two different boundary conditions on the walls, i.e., a constant temperature on the rod wall and a constant heat flux. As a consequence, the main flow and heat transfer characteristics from two different array configurations have been compared to each other. The performed study has allowed designing a proper set-up for the higher order turbulent modelling approaches by means of Large Eddy Simulations (LES) or even Direct Numerical Simulations (DNS).

Abstract for CFD4NRS-9
February 20-22, 2023
College Station, Texas, USA

USE OF COMPUTATIONAL FLUID DYNAMICS IN WESTINGHOUSE INNOVATION PROJECTS

Michael E. Conner*, Milorad Dzodzo, Emre Tatli, Yiban Xu, Paolo Ferroni, Jorge V. Carvajal
Westinghouse Electric Company

** Corresponding Author*
5801 Bluff Road, Hopkins, SC 29061 USA
connerme@westinghouse.com

Abstract

Computational Fluid Dynamics (CFD) has been used extensively across Westinghouse in analysis of current designs, development of new designs, and investigation into performance issues. This includes use of CFD for fuel (PWR, BWR, VVER), safety analyses, existing plants, new plant design (**AP1000®** [1], Westinghouse Lead Fast Reactor), and a wide range of nuclear services and products. Westinghouse has used numerous commercial CFD software products depending on the analysis of interest. This paper focuses on the use of CFD in the Westinghouse Digital and Innovation department. Specifically, how CFD is being used to enable development of innovative technology and solutions to meet customer needs now while working to deliver new products in the future.

[1] **AP1000** is a trademark or registered trademark of Westinghouse Electric Company LLC, its Affiliates and/or its Subsidiaries in the United States of America and may be registered in other countries throughout the world. All rights reserved. Unauthorized use is strictly prohibited.

Perspectives on the use of Wall-Resolved Large Eddy Simulation for Flow Induced Vibrations

Sofiane Benhamadouche and Thomas Norddine

EDF R&D, Fluid Mechanics, Energy and Environment Dept.,
6 quai Watier, 78401 Chatou, France

Sofiane.benhamadouche@edf.fr

Flow Induced Vibrations may cause severe damages in a Nuclear Power Plant (NPP). The Steam Generator Tube Rupture in the US NPP San Onofre in 2012 is a perfect example; two units have been shut down due to extensive wear, and tube damage was found to be related to FIV [1]. Predicting such complex phenomena is thus a crucial issue and Computational Fluid Dynamics (CFD) may contribute to the physical understanding and to the prediction of structural vibrations.

We start by recalling Large Eddy Simulation (LES) approach and its validation in code_saturne [2], [3]. Then, several examples of industrial needs where LES already brought an added value using either a one-way or a two-way coupling between the CFD and reduced order Computational Solid Mechanics are given: the flow through a whole Control Rod Guide Assemblies (CRGA) and their guide plates [4], the flow through a Fuel Assembly mixing grid [5] and the flow through in-line tube bundles [6]. Finally, perspectives on the use of Wall-Resolved LES with two-way coupling are introduced through two examples of preliminary and future computations in the framework of the recently accepted Euratom European project Go-Viking: (i) the vibrations due to a cross flow through an in-line tube array with a pitch-to-diameter ratio of 1.44, (ii) the vibrations due to an axial flow along a cantilevered rod using the experiment [7].

[1] NRC, 2015, https://www.nrc.gov/docs/ML1501/ ML15015A419.pdf.

[2] Afgan, Y. Kahil, S. Benhamadouche and P. Sagaut. “Large eddy simulation of the flow around single and two side-by-side cylinders at subcritical Reynolds numbers”, *Phys. Fluids,* 23, 075101 (2011)

[3] M-C. Gauffre, S. Benhamadouche & P-B. Badel, Wall-Modeled Large Eddy Simulation of the Flow Through PWR Fuel Assemblies at Re*H* = 66 000 - Validation on CALIFS Experimental Setup, *Nuclear Technology*, 206(2), pp. 255–265, DOI:10.1080/00295450.2019.1642684 (2020)

[4] S. Benhamadouche, M-C. Gauffre, J. Bonnici, V. Fichet, M. Denis, T. Muller. Experimental and Numerical Study of the Turbulent Flow through a Simplified PWR Guide Plate at Re_H=30,000. *The 19th International Topical Meeting on Nuclear Reactor Thermalhydraulics, NURETH-19*, *Virtual Meeting, March 6-11, 2022.*

[5] S. Benhamadouche, P. Moussou, C. Le-Maître. “CFD estimation of the flow-induced vibrations of a fuel rod downstream a mixing grid”, *Proceedings of PVP 2009 ASME Pressure Vessels and Piping 2009 / Creep 8 Conference*, July 22-26, Prague, Czech Republic (2009).

[6] Berland, J., Deri, E., and Adobes, A., 2014*, Large-Eddy Simulation of cross-flow induced vibrations of a single flexible tube in a normal square tube array*. Proceedings of the ASME 2014 Pressure Vessels & Piping Division Conference, July 20-24, 2014, Anaheim, USA.

[7] Cioncolini, A., Silva-Leon, J., Cooper, D., Quinn, M. K., Iacovides, H., 2018, *Axial-flow-induced vibration experiments on cantilever rods for nuclear reactor applications*, Nuclear Engineering and Design, 338, pp. 102-118.

U.S.NRC
United States Nuclear Regulatory Commission
Protecting People and the Environment

Center for Advanced Small Modular and Micro Nuclear Reactors
Texas A&M Engineering Experiment Station

NEA
NUCLEAR ENERGY AGENCY

Technical Session 8

Verification and Validation I.

Feb 21, 10:30-12:00, Room B.

NOVEL MEASUREMENTS OF FLUCTUATING TEMPERATURE IN THE SOLID PIPE WALL FOR VALIDATION OF CFD OF STRATIFICATION AND THERMAL FATIGUE IN CLOSED BRANCH LINE FLOWS

Howard Richard[1], Angele Kristian[2], Veber Pascal[3], Edh Nicolas[2], Olivier Braillard[4], Victor Petrov[5], Annalisa Maneira[5]

[1]*EDF, R&D, France*
[2]*Vattenfall AB, R&D Laboratories, Sweden*
[3]*Ringhals AB & Vattenfall AB, R&D Laboratories, Sweden*
[4]*Commissariat à l'énergie atomique et aux énergies alternatives, France*
[5]*Paul Scherrer Institute, Switzerland*

Extended Abstract

The purpose of the present work is to generate a novel experimental database of the temperature fluctuations inside the solid pipe wall of an isolated branch line in the presence of a stratified layer. The background and practical relevance of the case is thermal fatigue in an isolated branch line with a leaking valve with a small cold flowrate. The cold, almost stagnant, branch line water interacts with flow coming from a hot main line with a large flowrate. This sort of flow can frequently occur in the reactor coolant system and the residual heat removal system of PWRs (e.g. in the ECCS lines connected to the cold leg). This phenomenon has been found to lead to cracks (e.g., Dampierre-2 in 1992 and Dampierre-1 in 1996). The flow is not well understood and hence the thermohydraulic forcing is not well accounted for by current screening methods. The remedy is to develop more accurate tools by means of validating more advanced prediction methods. First experiments are required to reproduce the phenomena. The experiments can then be used to validate CFD, which in turn can be used as a basis to evaluate the phenomena under reactor conditions. A new pressurized experimental set-up has been designed and constructed at Vattenfall where the temperature difference is planned to be relevant for plant conditions (150°C). The thermohydraulic conditions (i.e., flowrates and temperatures) will be controlled and kept stable through feedback loops on the measured conditions using electromagnetic flowmeters (uncertainty 0.5 %) and PT100-sensors (uncertainty 0.1°C). The experiment also includes measurement of the temperature fluctuations inside the solid pipe wall material in the region of the unsteady stratified layer. This experiment will provide data for an NEA/OECD CFD benchmark. The benchmark exercise includes two phases. In the first phase the pipe geometry and data for an initial test case are shared to provide a preliminary assessment of the CFD. In the second phase the experimental conditions are shared but the experimental results are withheld for an initial period. This makes it possible for researchers to carry out CFD before having knowledge of the experimental results. The benchmark exercise is terminated with a comparison between the blind CFD and the newly released experimental data. The information for the first phase will be published in this paper along with the experimental conditions for the second phase. The blind CFD comparison with the experimental results will be the subject of a future publication.

CFD ANALYSIS OF COMPLEX MIXING PHENOMENA IN DEAD-END LINES

C. Riga, D. Dourneau, and P-A. Douxchamps
Tractebel Engineering, CFD & Accidents Competence Center
Boulevard Simón Bolívar 34-36, 1000 Brussels - BELGIUM

P. Planquart
Von Karman Institute, Environmental and Applied Fluid Dynamics Department
Chaussée de Waterloo 72, 1640 Rhode-Saint-Genèse

Extended Abstract

Dead-end lines connected to the primary system of Pressurized Water Reactor (PWR) can be subjected to thermal fatigue (subject of several publications or issue of international guidelines for lines which are vertically oriented). A sharp temperature transition between the turbulent mixing zone close to the main line temperature and the stagnant zone close to the cold source temperature induces a thermal fatigue in these lines.

Horizontally oriented lines are generally excluded from thermal fatigue as the buoyancy forces induce a mixing process thereby reducing the temperature differences across these lines.
Nevertheless, temperature measurements at the external surface of horizontal dead-end lines connected to the reactor pressure vessel of a 2-loops PWR show large temperature fluctuations at a significant distance from the connection point.

Through CFD analyses, the root cause has been identified as a peripheral flow ingress in the line resulting from the complex mechanical assembly at the reactor pressure vessel connection. The peripheral flow ingress induces a counter-current swirling flow structure extending in the dead-end line up to the point where the natural circulation induced by the heat losses prevails. At the transition point between the two flow structures, the temperature field shows a sharp temperature gradient that explains the measured temperature fluctuations.

A Plexiglas mock-up has been developed at VKI, designed to be a simplified layout of the actual PWR dead-end line, yet having the main characteristics of the dead-end lines, i.e. an horizontal 4-inch line, connected to a main pipe (in which the flow velocity is lower than 1m/s) with a hot water peripheral flow ingress and a cold heat sink. This mock-up was instrumented with thermocouples and dye injection to allow visualization of the flow structures.

This experimental set-up confirmed the conclusions drawn in the root cause analysis by mean of CFD computations, i.e:

- The flow structure is composed of three zones (from pipe end to connection with the main line):
  - A natural convection loop with an axial velocity towards the pipe end in the top and towards the pipe connection in the bottom. The temperature field exhibits a top to bottom temperature difference
  - A transition from natural convection to swirling flow. The axial temperature gradient is important in the pipe bottom in this region
  - A swirling flow region, advecting hot water towards the pipe end in the outer pipe section and drawing cold water from the convection loop to the pipe connection in the pipe center. The azimuthal velocity component is important at the flow ingress location and decays towards the pipe end until natural convection prevails.
- The CFD model of the mock-up was able to predict the average position of the transition zone with up to 10% accuracy. The transition zone position correlates with the azimuthal velocity at the connection point.
- Although the operating conditions of the experiment are steady-state by design, the transition zone displays an unstable behavior, with oscillation of its axial position. The consequence is temperature fluctuations on the pipe surface in this region, mostly in the pipe bottom.

As a conclusion, the experimental setup allowed to validate the methodology followed in the root cause analysis, to validate models chosen for the CFD simulations and to confirm the conclusion drawn from onsite measurement and full scale CFD analyses.

CFD VALIDATION : FLOMIX-R ROCOM HETEROGENEOUS BORON CONCENTRATION TRANSIENT – IMPACT OF MODEL SELECTION ON RESULTS

Christophe Riga, Simon Verdebout and Pierre-Alexis Douxchamps

Tractebel Engineering, CFD & Accidents Competence Center
Boulevard Simón Bolívar 34-36, 1000 Brussels - BELGIUM

Extended Abstract

One of the recognized CFD applications for nuclear reactor safety is related to the so-called heterogeneous 'boron dilution' transients for which the determination of local boron concentration must be determined in the Reactor Pressure Vessel (RPV). Such transient analysis requires in particular to capture the variation of boron concentration across the core.

One of the possible approaches to predict the dilution effects on the core transient is to provide the time-dependent radial distribution of boron concentration at core inlet as a boundary condition for 3-D core physics simulation. A CFD model of the primary loop and internals is therefore used to predict the transport of a boron-free coolant slug up to the core inlet.

To evaluate the applicability of current CFD software and models to tackle such application, a validation work is performed based on the experimental measurements realized during the FLOMIX-R European project on the ROssendorf COolant Mixing Model (ROCOM) experimental test facility. In particular, this project considered slug mixing transients for which CFD-grade data have been collected on a 1:5-scale experimental facilities. This work concentrates on reproducing the data obtained on the ROCOM test facility modelling a German KONVOI PWR reactor type (4-loops PWR with 193 fuel channels).

The conducted CFD analyses correspond to uncompressible, isothermal, transient, turbulent (RANS type turbulence model) flow analyses of the 3-D geometry of the ROCOM facility. The tracer is modelled as a scalar being advected by the flow including turbulent diffusion.

As any validation work, it is required to quantify the existing difference between the experimental and calculated results. The aim of quantifying the boron concentration uncertainty is directly related to the foreseen application behind the validation work, i.e. heterogeneous boron dilution transient. For such transient, the time dependent core inlet concentration estimated using CFD calculation is used to perform core calculation. It is therefore important to evaluate the uncertainty associated we the CFD results in order to be able to assess the impact of these uncertainties on the core calculation results.

The validation work performed by Tractebel aims at finding the best balanced modelling approach to ensure both reliable predicted data and reasonable computational time. To reach this balanced approach, several parametric cases from a base case (determined based on internal and international recommendations) are performed to quantify the impact of the different modelling choices on both the deviations with respect of the experimental measurement data and the computational time:

- not considering inlet pipe to obtain a fully developed flow at the vessel inlet;
- not considering the core outlet part including the hot legs;
- considering the Baseline Explicit Algebraic Reynolds Stress Model (BSL EARSM) turbulence model;
- adopting a pure tetrahedron mesh with the same inflation layer;
- Adopting a hybrid mesh with a inflation layer aiming at getting an y+ ~1;
- from non-conform interfaces to conform interfaces (1:1);
- increasing time step from 0.01s (CFL ~ 29.0) to 0.05s (CFL~ 144.0);

- adopting the measured local tracer concentration at the injection location instead of the space averaged value.

For each calculation the impact of the modeling choice on the deviation with respect to the experimental measurement data at the various locations (upper downcomer, lower downcomer and core inlet) is determined and discussed. In addition to time and spatially averaged deviation quantity useful to discriminate between modelling choices, the maximum tracer concentration and its location at the core inlet are compared and discussed.

UNSTABLE FLOWS : ASSESSMENT OF CFD FOR THE PREDICTION OF TEMPERATURE FLUCTUATIONS

Jan-patrice SIMONEAU

EDF (électricité de France) - Nuclear Engineering
19, rue P. Bourdeix, F69007 Lyon, France

Extended Abstract

CFD is now extensively used for various domains of industry, and among them, for design and safety of the nuclear reactors. The acceptation of this tools for addressing safety issues can be obtained only thanks to a rigorous validation process and to a large number of parametric calculations.

Some configurations are known to be difficult and are still highly investigated: e.g. fluid structure interaction, two-phase flows. But unstable single phase flows remain also difficult to calculate and they are potential sources of thermal loadings, which, for example, may lead to thermal fatigue.

The objective of the paper is to assess the EDF in-house software *code-saturne* on unstable flow experiments. The experiments retained here involve a parallelepiped cavity heated from below, leading to oscillatory convection (works of Koster and Müller, published in *J. Fluid Mechanics*, 1984). The experimental device is a thin tall cavity filled with silicon oil and surrounded by either high or low conducting walls. Depending on those walls and on the temperature differences, different unstable oscillating flows are observed: fluctuations with one or several peaks (harmonics), presence of beatings, stabilizing flow. The instrumentation is made of several thermocouples providing instant temperature signals. Moreover, some visualizations via cameras are also available.

Among the large set of experiments, four configurations have been chosen for the CFD comparison, with specific behaviors: two with high conducting walls featuring peak frequencies with harmonics, two with low conducting walls featuring beating and a stabilizing flow.

The *code-saturne* software is a general purpose CFD code, solving Navier-Stokes, energy and turbulence equations, in a time marching process. It is coupled to the (also in-house) *Syrthes* code, dedicated to the solving of conduction in solids. A hybrid grid (hexahedrons / prisms / tetrahedrons) is used with about 5 millions cells (both fluid and solid). The boundary layers are precisely described without any wall function (low Reynolds formulation). The objective being the validation of industrial computations, the standard k-ω-SST turbulence model is preferred to a Large Eddy Simulation.

The Rayleigh numbers vary from about $5.\ 10^8$ to 5.10^9 and the physical times of computations match about 500 s.

The comparisons with experiments extend from global visualization (flow patterns), damping or not of fluctuations, and precise analyses of temperature signals: time histories, amplitudes, fast Fourier transforms (peaks, harmonics, and beatings).

The results show that the instable characteristic is well predicted: the right behavior is predicted on both sides of the threshold triggering the oscillations. The frequency peaks, including harmonics, are found within 10%. In one experiment, the beating frequency, observed experimentally, is also found by the calculation, within 30%. Considering the amplitudes, the comparisons are also within 10%.

From this work, the *code-saturne* tool can be used with industrial models (i.e. affordable CPU times) to predict temperature fluctuations in situations close to cavities heated from below. However, the study itself has to include first the influence of numerical and discretization parameters (e.g. computational grid) and secondly a large set of parametric studies (mainly boundary conditions). Indeed, the later are generally not precisely known on the reactor.

For the definition of this set of different physical conditions, a PIRT (Phenomena Identification Ranking Table) process is highly recommended.

Finally, the paper will draw some general conclusions on the validation processes of CFD.

A NEA/OECD BENCHMARK EXPERIMENT TO EVALUATE CFD IN BRANCH LINE FLOWS

Angele Kristian[1], Howard Richard[2], Veber Pascal[3], Edh Nicolas[1], Olivier Braillard[4], Victor Petrov[5], Annalisa Maneira[5]

[1]Vattenfall AB, R&D Laboratories, Sweden
[2]EDF, R&D, France
[3]Ringhals AB, Sweden
[4]Commissariat à l'énergie atomique et aux énergies alternatives, France
[5]Paul Scherrer Institute, Switzerland

Abstract

The purpose of the present work is to generate a novel experimental database to study dead leg flows in pressurised water reactors (PWR). The background and practical relevance of the case is thermal fatigue in an isolated branch line with a leaking valve with a small cold flowrate. The cold, almost stagnant, branch line water interacts with flow coming from a hot main line with a large flowrate. A flow forms in the stagnant 'dead leg' branch. This can lead to mixing, the formation of a dead leg vortex [1], and stratification in the reactor coolant system and the residual heat removal system of PWRs for example in the emergency core cooling systems (ECCS) lines connected to the cold leg. This phenomenon has been found to lead to cracks in the pipes (in France and the USA [2]). The flow is not well understood and hence the thermohydraulic forcing is not well accounted for by current screening methods. The remedy is to develop more accurate tools by means of validating more advanced prediction methods. The methodology is the following: Once experiments are shown to reproduce the phenomena, they can be used to validate CFD, and CFD in turn can be used as a basis to evaluate the phenomena under reactor conditions. A new pressurized experimental set-up of a T-junction has been designed and constructed at Vattenfall R&D labs where the temperature difference is planned to be relevant for plant conditions (150°C) and the flowrates and temperatures are controlled and kept stable. The experiment includes measurement of the temperature fluctuations inside the solid pipe wall material in the isolated branch line and forward looking infra-red (FLIR) camera measurement of the temperature on the outer pipe surface. Preliminary data with a temperature difference of 20°C shows how the vortex penetration varies with the main line flow rate. Additional cases with temperature differences of 70°C and 140°C will be provided for a future blind CFD benchmark exercise in the framework of an OECD/NEA project.

Introduction

Thermal mixing in a T-junction is a generic flow case where two streams of flow at different temperatures, T_h (hot) and T_c (cold) mix. This leads to temperature fluctuations, often at low frequencies (<1Hz), in the fluid mixing zone. The temperature fluctuations in the fluid are also transferred to the solid pipe wall material, which can lead to thermal fatigue. The temperature difference between the two fluid streams, $\Delta T=T_h-T_c$, determines the maximum magnitude of the temperature fluctuations in the solid material and the risk for thermal fatigue in the material. The heat transfer in the solid acts as a low pass filter. Thus, the solid is rather insensitive to high frequency thermal fluctuations (>5Hz). The low frequency fluctuations (<1Hz) on the other hand can provoke local expansion and contraction in the solid and hence thermal fatigue.

A T-junction with a dead leg or a closed branch line (i.e., with stagnant water) or a small leakage flow is a special case. Here the side branch flow rate is negligible (<1%) compared to the main line flow rate. In all nuclear power plants (NPP), the primary circuit is connected to a large variety of auxiliary circuits with many different functions for the safe operation and control of the reactor. Some of the auxiliary circuits can be several metres long and lead to valves that are closed under normal operating conditions. A typical example is the main reactor coolant system and the residual heat removal line in a Pressurized water reactor (PWR). T-junctions with dead legs are therefore very common in NPPs. It has been found that dead leg flow in NPPs has the potential to lead to high cycle thermal fatigue. For example, through wall cracks have occurred in the past [2]. Similar observations have been made in Boiling water reactors (BWR) for example the system 331 at Forsmark 1, where through wall cracks where observed.

Experimental work [3] has shown the thermohydraulic phenomena that form in a dead leg flow. Near the junction, a sort of cavity flow forms at the joint with the branch line. This eventually transforms into an axial vortex along the branch line if the flow rate is high enough in the main line. The vortex can penetrate several diameters along the branch line. The penetration distance depends principally on the flow rate in the main line. However, detailed analysis shows that the penetration is unsteady and difficult to predict [3], [4]. Since the vortex transports fluid at a different temperature (in NPPs a higher temperature) to the branch line, thermal stratification forms between the vortex and the cold stagnant flow in the rest of the line.

Semi-empirical tools based on experiments conducted at room temperature [5], [6] are used for the screening of potential problems and plant measurements are used to monitor potential risks [7]. The current prediction and screening methods are inaccurate and have at times lead to the wrong conclusions. Monitoring is also uncertain, time consuming and expensive. The incentives to generate more advance models are therefore clear.

A major drawback is that current empirical correlations for prediction methods are based on experiments carried out at room temperature and ambient pressure [3], [8]. Not many experiments have been carried out at temperatures closer to plant conditions. Experiments carried out in Plexiglas pipes at lower temperature differences do not include the heat conduction in the solid metal pipe wall from the hot pipe to the cold branch. Heat loss to the solid has been shown to slow the progression of the dead leg vortex [13]. This also drives a natural circulation flow in a thermal boundary layer along the vertical pipe wall, which is not present in a cold or isothermal test (when the main line is cold and therefore at the same temperature as the branch line).

To be able to predict the phenomena at stake more accurately, more advanced predictive tools are required such as a combination of experiments and numerical simulations (i.e., CFD - Computational Fluid Dynamics). Experimental validation is necessary since numerical simulations contain modelling uncertainties which are difficult to quantify.

A thermohydraulic model intended to feed into a mechanical model to predict the thermal forcing responsible for high cycle thermal fatigue should include the thermal transfer between the fluid and solid pipe wall. Validation of such models requires hot experiments in steel pipes with measurements of the temperature variations in the solid pipe wall material. To our knowledge this sort of experimental data is not available in the literature. In NPPs, thermocouples are used on the outside of the pipe for monitoring reasons, however, through-wall attenuation of temperature fluctuations do

not allow direct prediction of thermal cycling. Inner wall measurement of the temperature is not generally feasible in NPPs however this can be done in laboratory experiments. Ideally such measurements must be conducted inside the pipe wall material and at a distance very close to the inner surface of the pipe wall.

The novelty of the present experiments consists in measuring the temperature fluctuations at a range of different ΔT inside the solid pipe wall material, close to the inner pipe wall for the case with a dead leg and a leaking valve. As mentioned above this type of data does not exist in experimental data for CFD validation. Some experiments make use of density changes due to differences in salinity to represent the density changes due to temperature differences. This sort of approach has the disadvantage that the thermal transfer between the fluid and the wall is neglected.

The proposed research is a complement to, or an extension of, the planned and ongoing ones at the University of Michigan [6]. The CFD-benchmark will be like a previous NEA/OECD benchmark in which a mixing T junction was studied [9].

This paper represents the basis for the NEA/OCDE dead leg flow benchmark. First, the experimental method is discussed followed by a description of the instrumentation. Preliminary results are given for some initial tests along with a test matrix (for cases 1 to 8). The preliminary tests can be used for initial future CFD evaluation. The tests cases B1 and B2 in the test matrix are proposed for the blind CFD benchmark exercise. The data necessary for CFD evaluations is discussed. The paper ends with some conclusions and perspectives.

Method

Experimental test rig

A new experimental setup has been designed and constructed to extend the experimental data currently available for dead leg flows.

The experimental setup consists of a pressurized closed flow loop with a recirculating hot flow, a pressurized injection of a small cold flow (less than 1% of the main line flow rate) and an on-line heating to compensate for the reduction in temperature as the cold flow mixes with the hot flow.

To achieve the high velocities and penetration depths that can occur in NPPs with the available pump capacity in a pressurized system at 10 bar, the pipe dimension is set to DN40.

To avoid fluctuations in the main flowrate from the pump, two large tanks and a flow-straightening and pulsation damping device are utilized.

The test set-up is shown schematically in Figure 1. The small water tank (T1) has a volume of 2.4 m^3 and can be pressurized up to 11 bar and a temperature of up to 180°C can be used. The larger tank (T2) has a volume of about 3 m^3. If the cold flowrate is 0.01 l/s with a temperature 10°C and the hot water has a temperature of 180°C, the required on-line heating capacity becomes 6 kW. The hot parts of the system are insulated.

With the current pump, a flowrate of about 15 l/s can be reached. This renders a maximum velocity in the main pipe of about 11 m/s at 40°C.

The cold flow (from tank T1) in the vertical pipe to the T-junction is provided by a pump with a capacity of 0.5 l/s at 11 bar.

A stable flowrate is assured by rpm-regulation of the pumps using PID-regulation based on the measured flowrate. The same goes for the temperature, which is regulated using the heater and a PID based on the temperature measurement.

A N2 flask 50 l at 200 bar is used to pressurize the system.

Figure 1: Flow chart of the test rig.

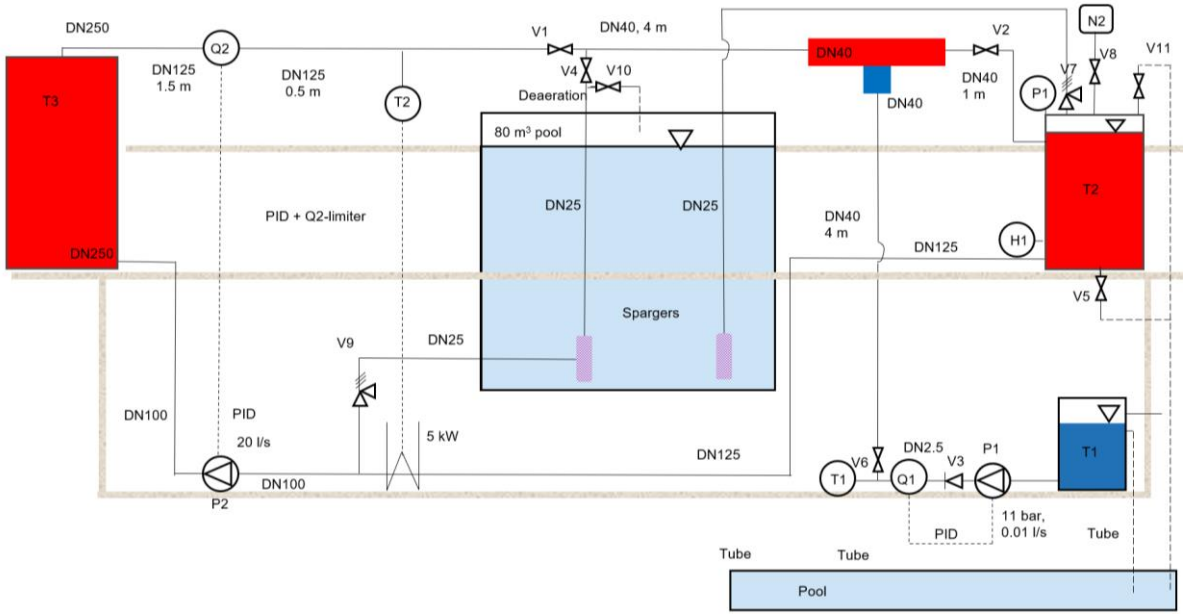

Figure 2: Photo of the test rig.

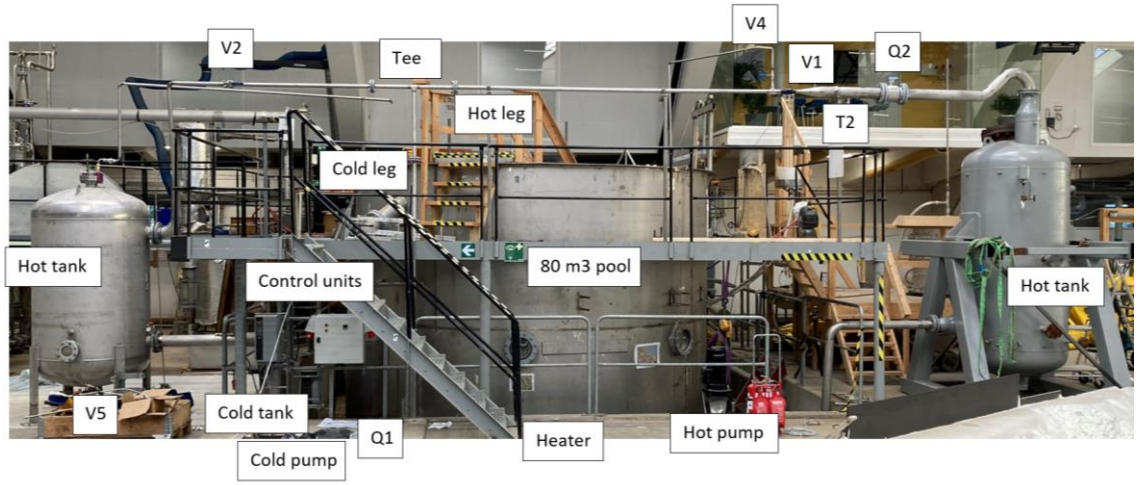

The T-junction has equal diameters in both legs, sharp corners at thee flange connections between the two pipes. Figure 3 and Figure 4 show the dimensions of the T-junction and several measurement positions.

Figure 3: The tee junction dimensions and measurement positions (black and yellow dots), the FLIR camera and a part of the steel pipe.

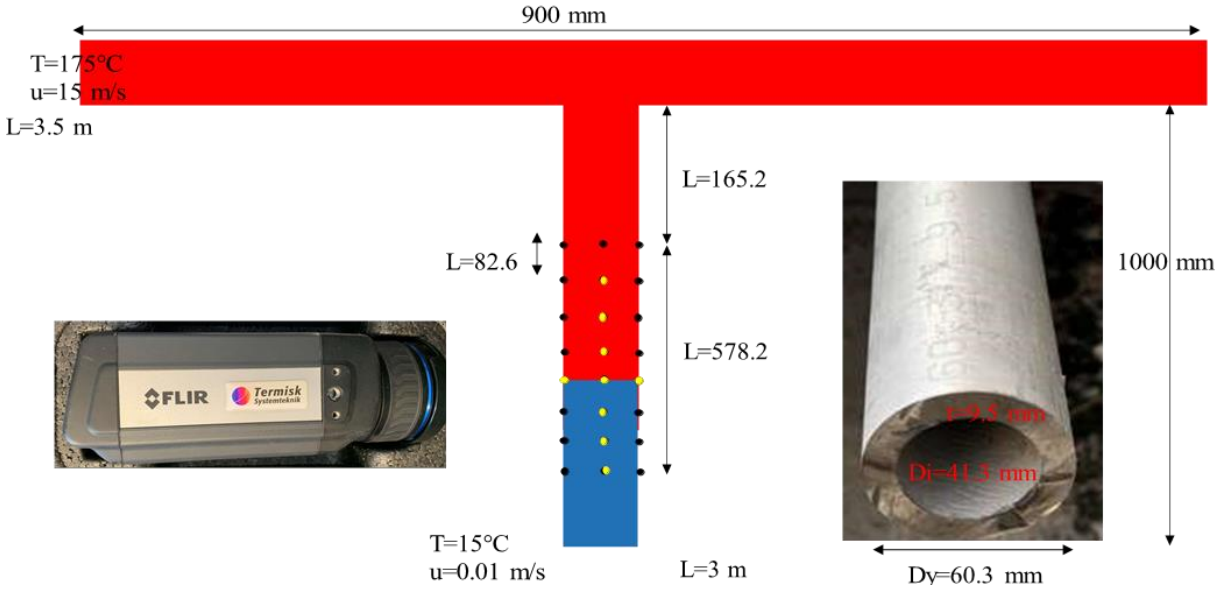

Figure 4: A side view and isometric view of the tee junction and measurement positions.

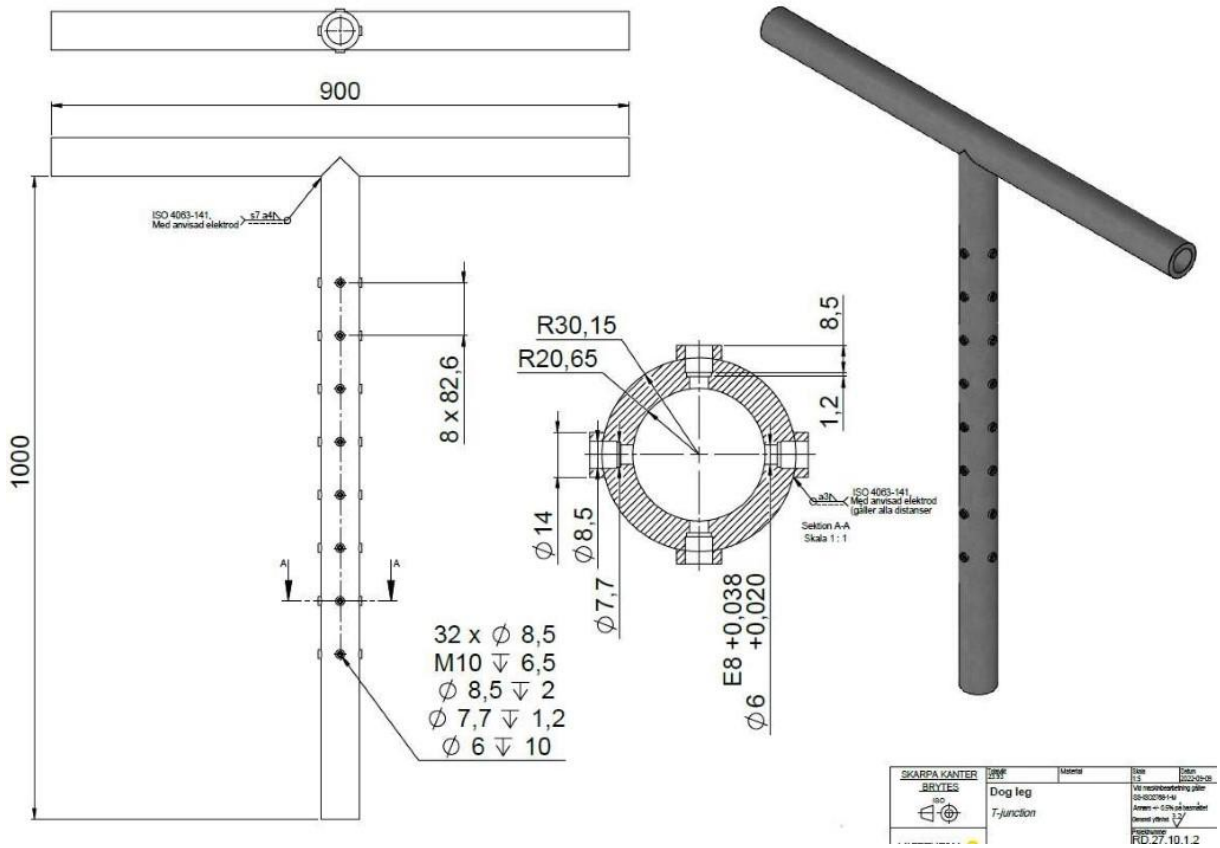

The thermohydraulic conditions in the hot and cold pipes respectively are described in Table 1. Variations can easily be made in the flowrates and temperatures and thereby the velocities, densities, viscosities, and Reynolds numbers.

Table 1: Reference thermohydraulic properties and conditions.

	Cold leg	Hot leg
Q (l/s)	0.01	15
D (m)	0.0416	0.0416
u (m/s)	0.007	11.2
T (°C)	20	160
ρ (kg/m^3)	1000	880
Re (-)	280	$2.3 \cdot 10^6$

Instrumentation

The flow rate is measured with electromagnetic flow meters with an uncertainty of about 0.5 % of the flow range according to calibrations made externally. All installations are made according to the requirements on the length of straight pipe upstream (ten diameters) and downstream (five diameters) of the sensor. To measure the flowrates accurately the velocity through the orifice plate flowmeter must be high enough (1-10 m/s). Therefore, the flowmeter for the low flow rate cold flow in the vertical DN40 pipe will be reduced to a DN2.5 pipe to locally increase the velocity. As shown in Figure 1 the flowmeters are well upstream of the T junction. A flow straightening device is used to remove swirls from upstream bends. The entrance lengths in the pipes are 100 diameters upstream of the T junction to ensure a fully developed velocity profile. This procedure has been shown to give a well-defined boundary condition for CFD-simulations [10].

The temperatures are measured with temperature gauges T1 and T2 of Pt-100 type. The temperature sensors are calibrated in-house and have an uncertainty of about 0.2°C. The temperature control system keeps the temperature constant within about 0.2°C during a test, see instability of the whole stratified layer has a wave motion in the circumferential direction, in line with the spiralling downward vortex flow reported by e.g. [3], [8], [12] and [13].

Figure *8* (a and b).

The system pressure P1 is measured with a pressure gauge with a measurement range of 16 bar calibrated in-house using a Druck calibrator. This sensor type is very linear and the uncertainty of less than 0.5 % (according to the manufacturer) essentially comes from a slow drift (an offset), which is compensated for before each test.

The water level in the pressurized tank is measured using a differential pressure transducer.

A FLIR-camera (see Figure 3) filming the outside wall of the T-junction detects the location of the stratified layer and measures the temperature gradient along the whole mixing region.

Ten special made sensors as in [11] for a Tee with lower ΔT and equal flowrates are used. They are based on thermocouples welded directly to the stainless-steel material at 0.3 mm, 1.3 mm, and

2.6 mm from the inside wall, and are employed to measure the temperature fluctuations inside the pipe wall (see

Figure 5). The uncertainty of the temperature measurement using a K-type of thermocouple is about 0.5°C.

The sensors have already provided relevant data (mean and fluctuating temperature, heat flux and heat transfer coefficient) for qualifying the thermal load for mixing tees in the French program, where they were performed in the French facilities (Father and Fatherino at CEA Cadarache). In this paper, the same sensors are installed in the Vattenfall laboratory.

Figure 5: Thermal sensor and test section.

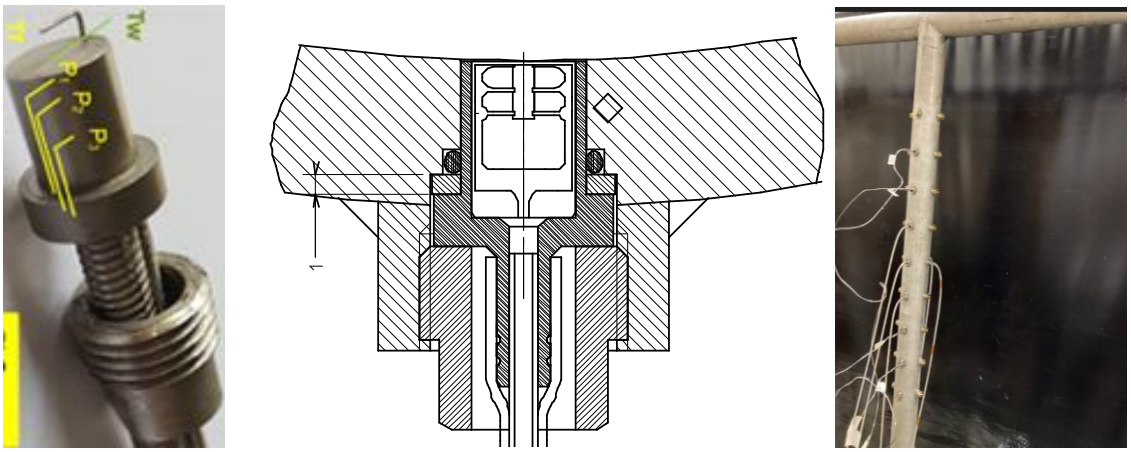

Figure 6: Example temperature response of the thermal sensor.

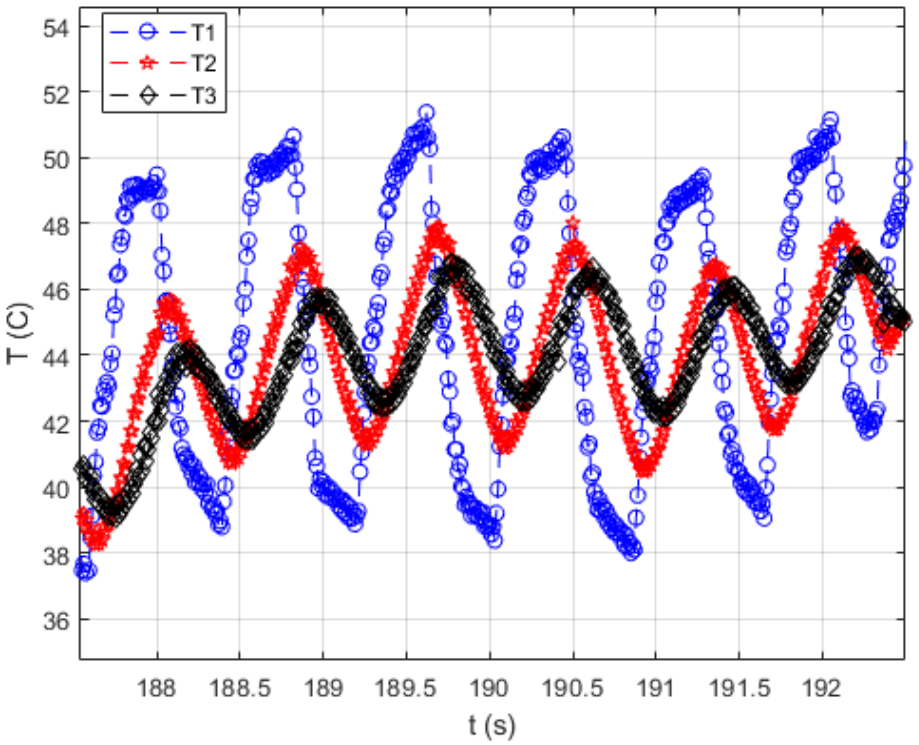

A time response test was carried out with water at 20°C and 90°C. The heat transfer diffusion time depends on the thermocouple depth. There is therefore a time delay for different thermocouples in response. For a periodically varying ΔT, there is a phase shift and a damping visible in Figure 6.

Test Matrix

The proposed test matrix is shown in Table 2. The cases 1-8 are intended to provide preliminary data for CFD evaluation. Examples of this data are given in the results section of this paper. The cases B1 and B2 are intended as a blind CFD benchmark. The data for these cases will be provided within the context of the NEA/OCDE benchmark exercise in 2023 (at a date to be decided).

Table 2: Test matrix

#	Test	ΔT (°C)	T_h (°C)	T_c (°C)	Q_h (l/s)	u_h (m/s)	Q_c (l/s)	P1 (barö)
1	No leakage flow	22	40	18	0.8	0.6	0	1
2	Hot flow rate	22	40	18	1.3	1.0	0	1
3	Hot flow rate	22	40	18	2.2	1.7	0	1
4	Hot flow rate	22	40	18	5.5	4.3	0	1
5	Hot flow rate	22	40	18	8.0	6.2	0	1
6	Hot flow rate	22	40	18	15	11	0	1
7	Temperature variation	42	60	18	15	11	0	1

8	Leakage flow	22	40	18	15	11	0.01	1
B1	Temperature variation	72	90	18	15	11	0	1
B2	Temperature variation	142	160	18	15	11	0	10

Preliminary results

Figure ***7*** shows that the flowrate, system pressure and water tank (T2) level are stable during a test based on the conditions of case 1 in the test matrix.

instability of the whole stratified layer has a wave motion in the circumferential direction, in line with the spiralling downward vortex flow reported by e.g. [3], [8], [12] and [13].

Figure *8* shows that the hot and cold temperatures are stable within their measurement uncertainty but that the temperature in the mixing region is unstable with intermittent peaks of hot water penetrating the cold water during some seconds, like the mixing zone in [10]. Sudden large increases (up to 5°C or about $0.2\Delta T$) in the temperature are observed at irregular intervals. After each instance of high temperature, the temperature drops back down again rapidly to a slightly larger value. The temperature then decays much more slowly (over several 100 seconds) towards the initial value.

Figure *10* also shows that the temperature fluctuations inside the solid are correlated with the ones in the fluid but have a slower response and smaller amplitude.

Figure *9* shows the low frequency nature of the mixing layer in more detail (about τ=10 s or f=0.1 Hz). The intermittent irregular large peaks are accompanied by smaller more regular fluctuations which become progressively damped until a new intermittent large peak occurs.

Figure 7: Stability in the boundary conditions in terms of mass flow rate (a), pressure and water tank height (b) for case 1.

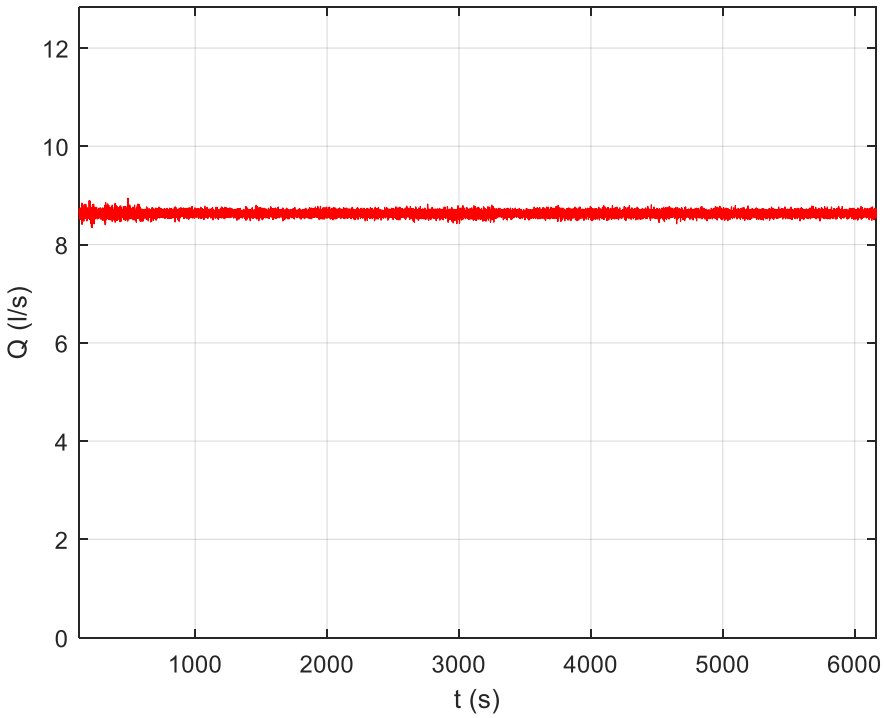

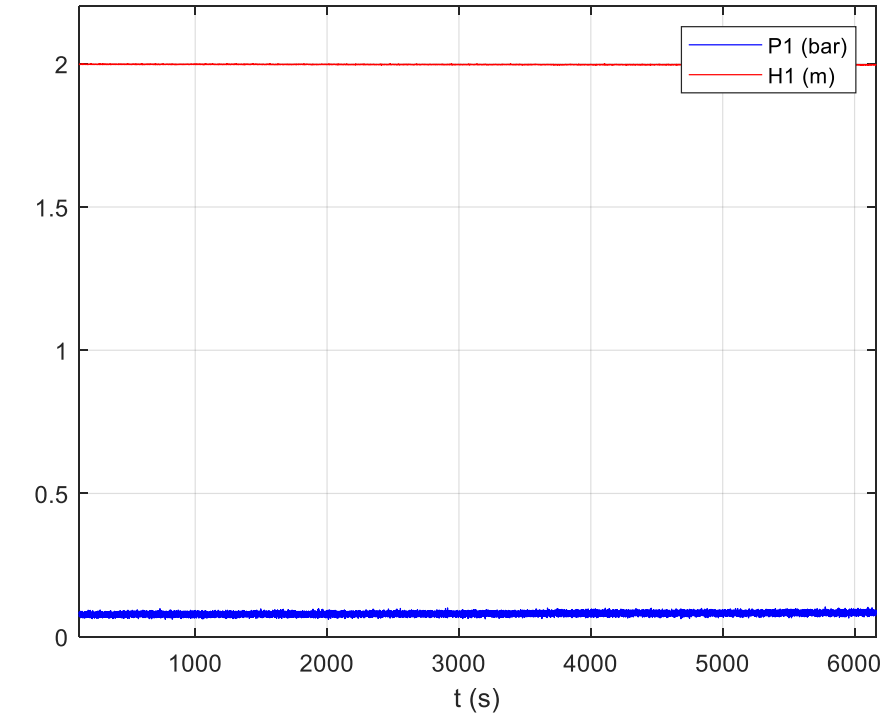

Figure *10* shows that there is a time shift between the signals at different angular positions (180° apart, here 90° and 270°) which is about half a period of the instability, i.e., 5 s. This implies that the instability of the whole stratified layer has a wave motion in the circumferential direction, in line with the spiralling downward vortex flow reported by e.g. [3], [8], [12] and [13].

Figure 8: Fluid temperature variations for cold water, hot water, and mixing region (a) and zoom of temperature for mixing region (b) for case 1.

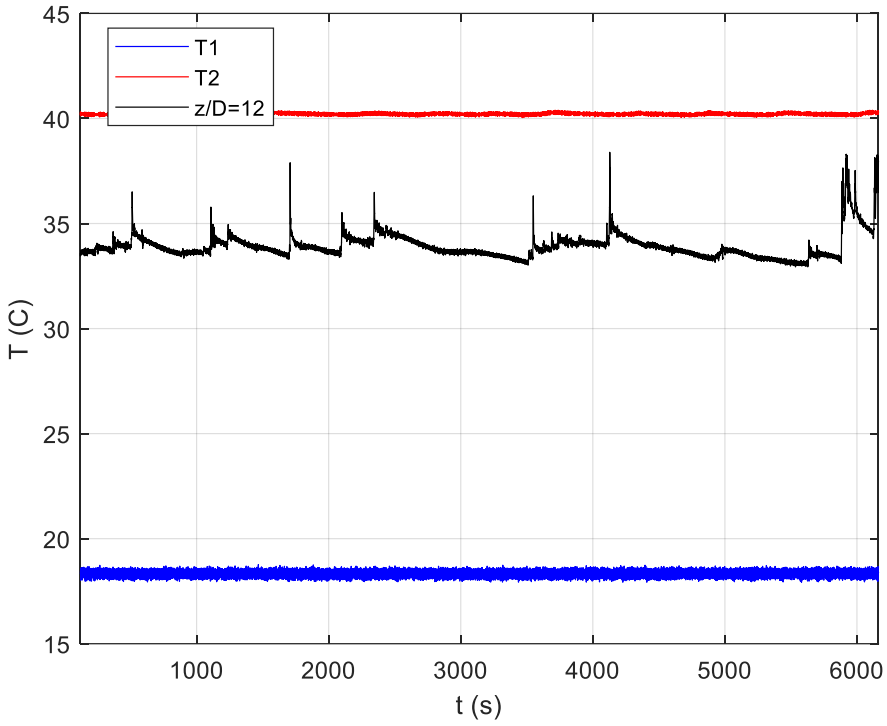

a)

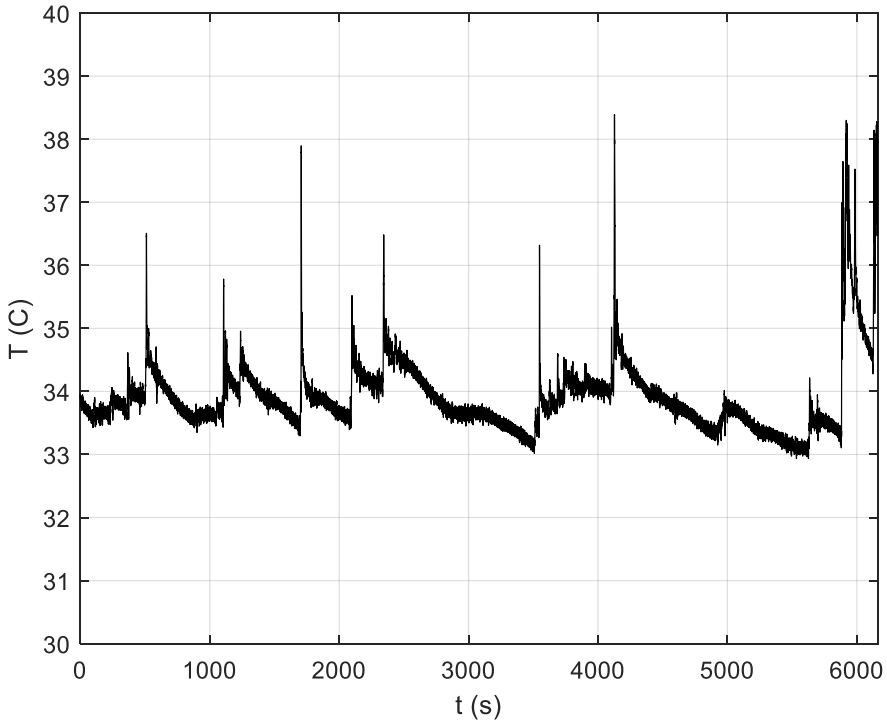

b)

Figure *10* also shows that the temperature fluctuations inside the solid are correlated with the ones in the fluid but have a slower response and smaller amplitude.

Figure 9: Low frequency temperature variations.

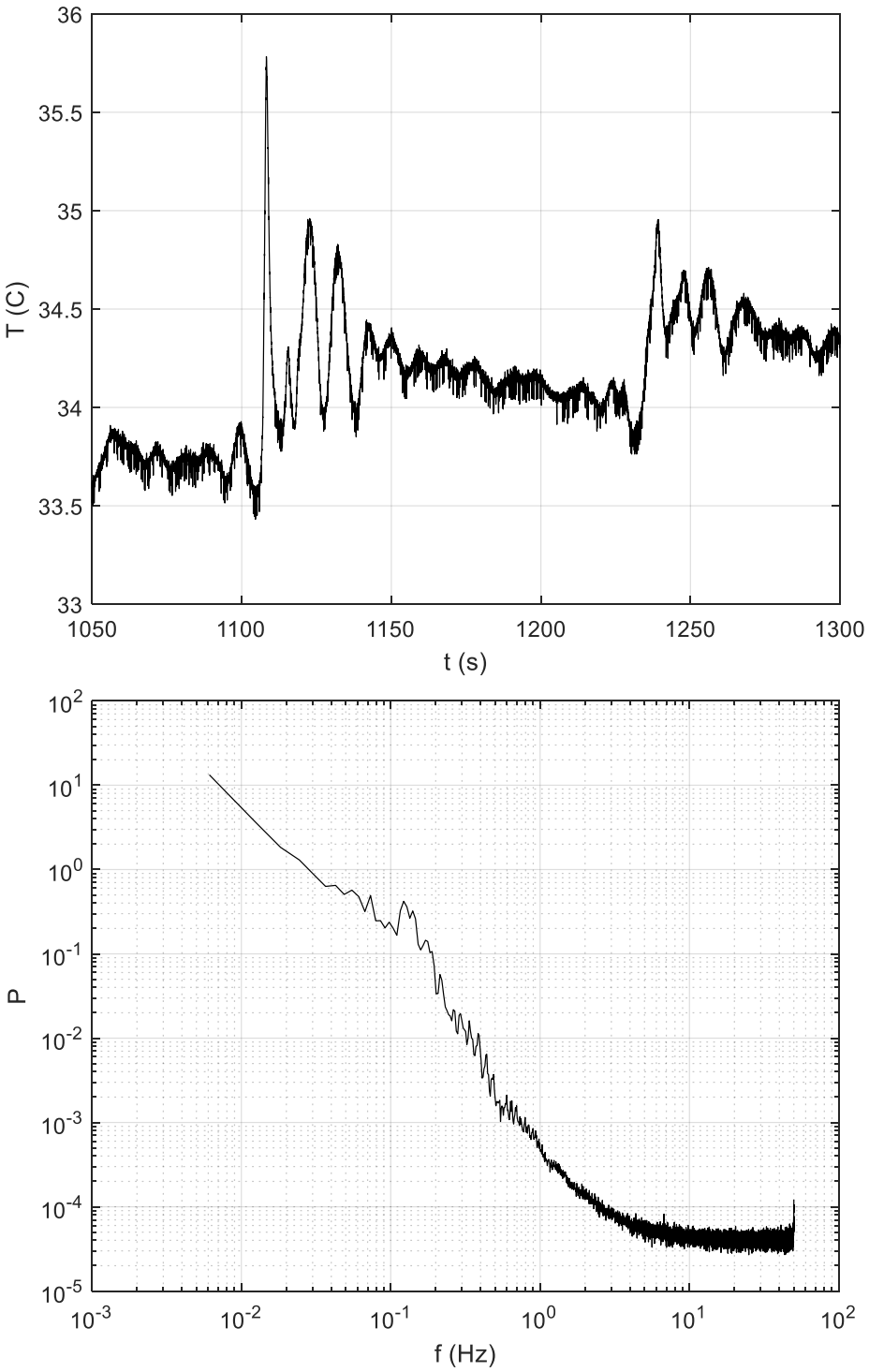

Figure 10: Circumferential differences in temperature (a) and temperatures inside the solid pipe wall at different distances from the inner pipe wall (b) for case 5.

a)

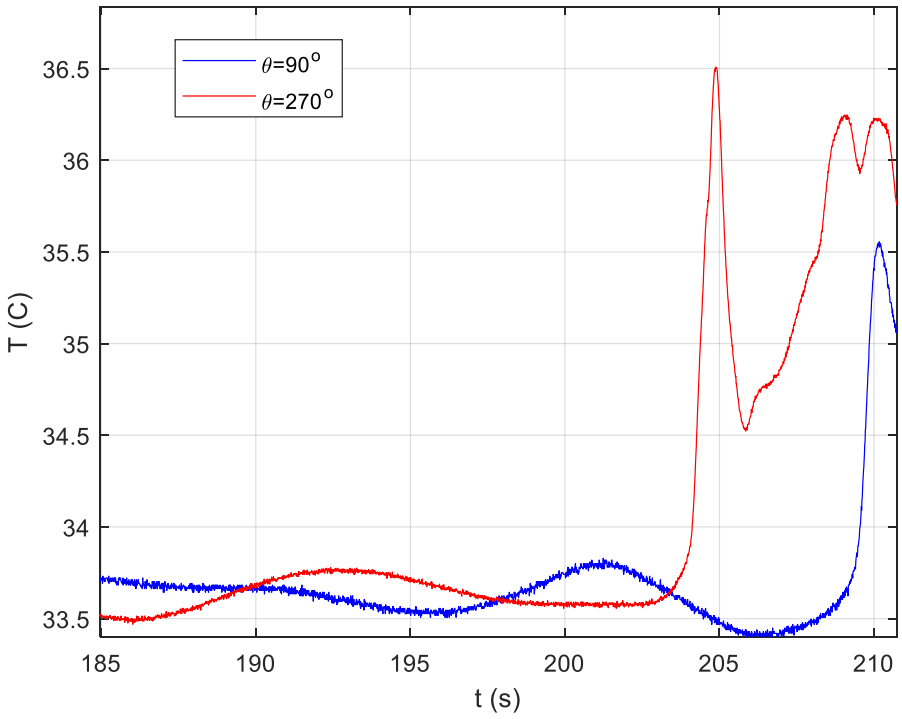

b)

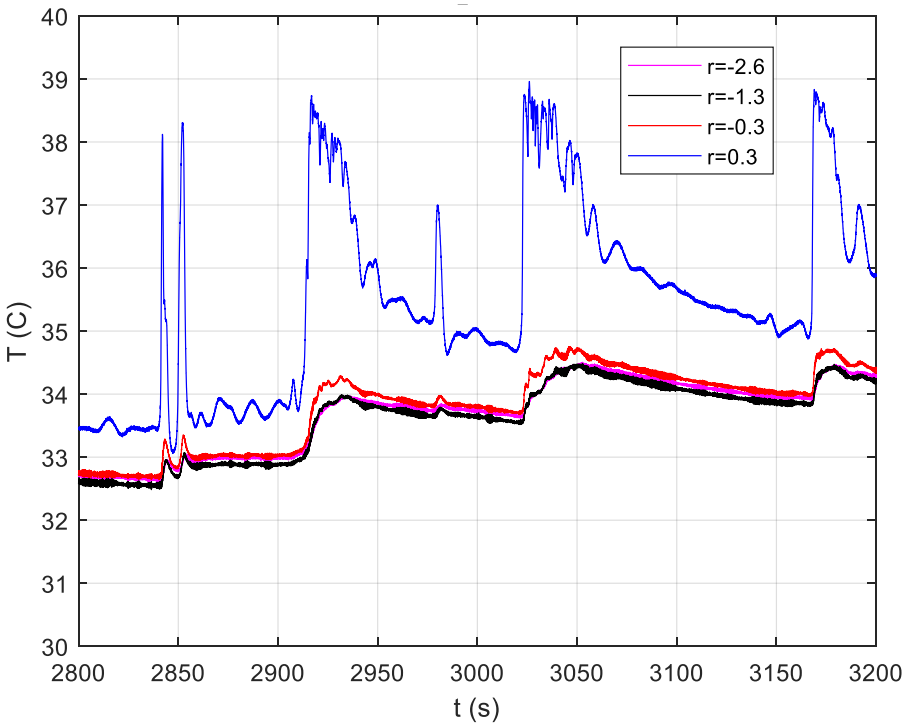

Figure 11 -

Figure *13* show the temperature on the outer surface of the Tee measured with a FLIR camera for cases 1-6. This measurement makes it possible to determine the penetration depth, L, of the hot water into the cold water. Increasing the velocity leads to an increased penetration depth, L, as reported by [12]. The camera measurements show the gradual change in temperature from the hot to the cold regions. The penetration depth is based on the position where the cold-water temperature is reached. Further work is necessary to describe these values in more detail with some estimation of the uncertainty.

Figure 11: Outside wall temperature for case 1 (a) based on FLIR camera measurements.

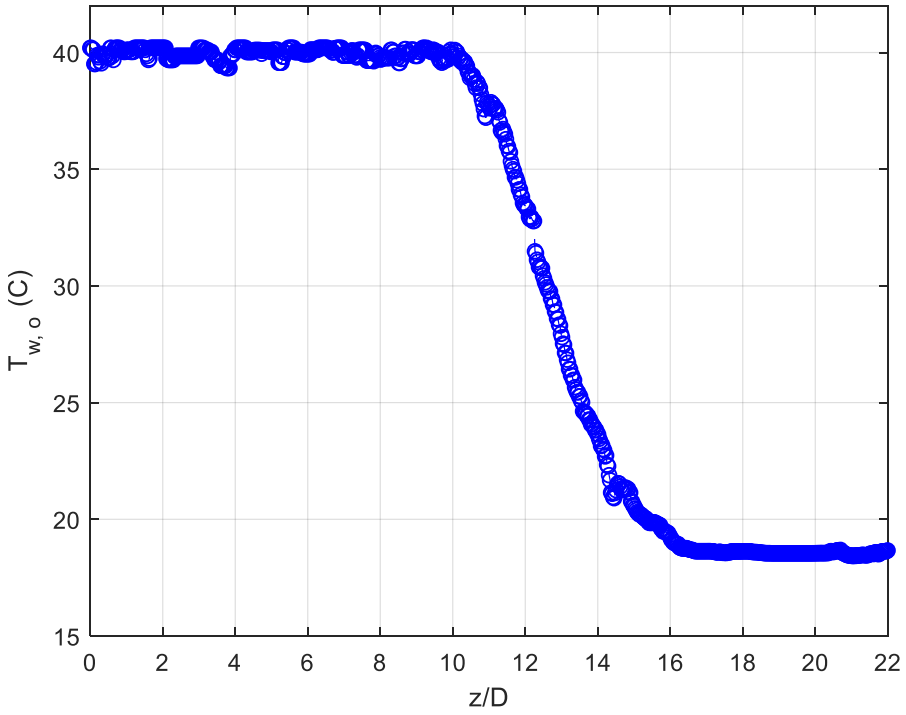

Figure 12: Outside wall temperature for cases 1-3 (and additional flow rates) using the FLIR camera (bright 40°C, dark 20°C).

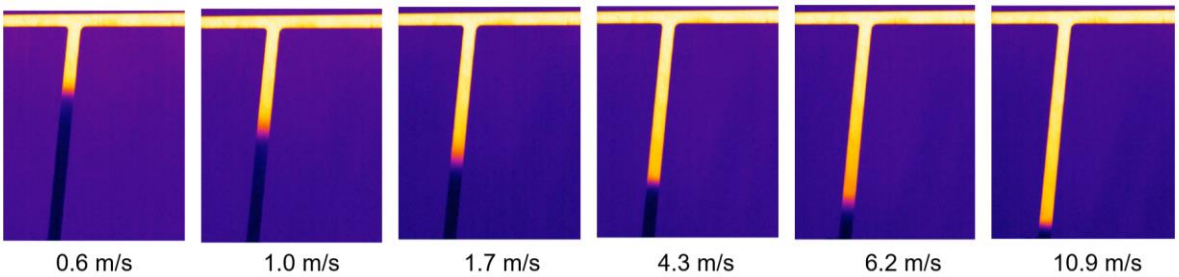

Figure 13: Penetration depths based on FLIR camera measurement for cases 1-8.

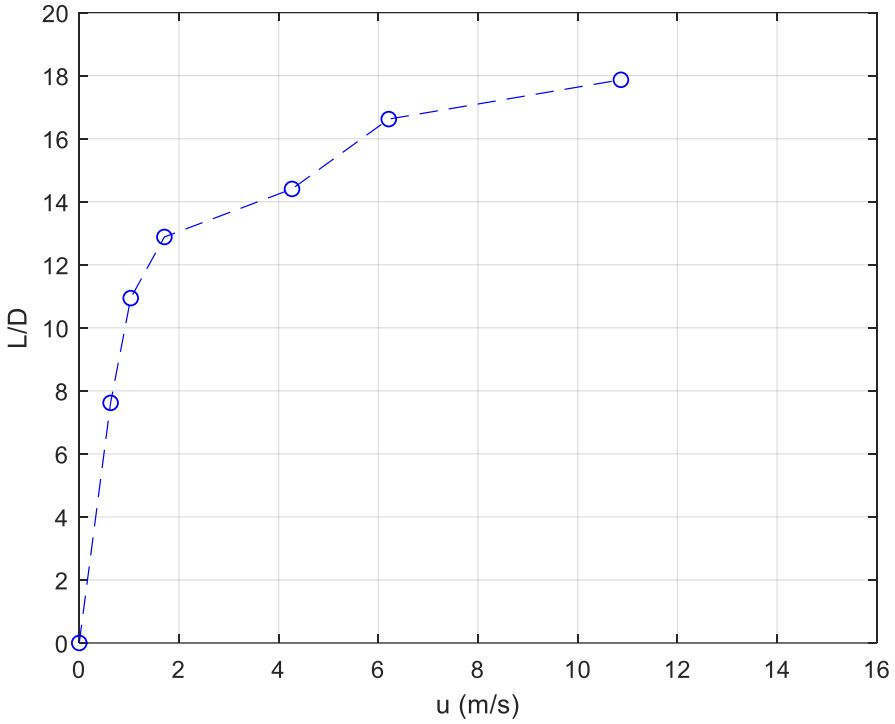

Data for CFD comparison

In the final version there will be a more complete description. At this stage there is just a preliminary description of the type CFD data to be compared.

The temperature should first be made non-dimensional: **$T^* = (T_h - T)/(T_h - T_c)$** with **T*1=0.8**, **T*2=0.5** and **T*3=0.3.** The penetration distance (L/D) is obtained from isolines of T*1, T*2 and T*3. For each isoline the lowest position should be recorded and included in table 3.

Table 3: Example results matrix

#	Test	ΔT (°C)	T_h (°C)	T_c (°C)	Q_h (l/s)	L/D T*1	L/D T*2	L/D T*3
1	No leakage flow	22	40	18	15			
2	Hot flow rate	22	40	18	10			
3	Hot flow rate	22	40	18	5			
4	Hot flow rate	22	40	18	3.8			
5	Hot flow rate	22	40	18	1.3			
6	Hot flow rate	22	40	18	0.8			
7	Hot flow rate	22	40	18	0.4			

Conclusions

The purpose of the present work is to generate a novel experimental database of the temperature fluctuations inside the solid pipe wall of a dead leg flow. In this flow, the branch line flow rate is considered negligible (<1% of the main flow rate) with respect to the main line flow rate. The background and practical relevance of the case is thermal fatigue in an isolated branch line with a leaking valve with a small cold flowrate (<1% of the hot flow rate). The cold, almost stagnant, branch line water interacts with flow coming from a hot main line with a large flowrate. This sort of flow mixing, and stratification situation can occur in the reactor coolant system and the residual heat removal system of PWRs (e.g., in the ECCS lines connected to the cold leg). This phenomenon has already been found to lead to cracks in the pipes (in France and the USA [2]).

The flow is not well understood and hence the thermohydraulic forcing is not well accounted for by current screening methods. The remedy is to develop more accurate tools by means of validating more advanced prediction methods. First, experiments are required to reproduce the phenomena. The experiments can then be used to validate CFD, which in turn can be used as a basis to evaluate the phenomena under reactor conditions.

A new pressurized experimental set-up has been designed and constructed at Vattenfall R&D labs where the temperature difference is planned to be relevant for plant conditions (140°C). The thermohydraulic conditions, such as flowrates and temperatures, are controlled and kept stable through feedback loops on the measured conditions using electromagnetic flowmeters and PT100-sensors. The experiment includes novel measurement of the temperature fluctuations inside the solid pipe wall material in the region of the unsteady stratified layer. There is also FLIR camera measurement of the temperature outer pipe surface.

Results at different flow rates with a temperature difference of approximately 20°C are given in this paper. The vortex penetration shows a non-linear relationship with main line velocity in line with the observations from the literature [12]. This data can be used for preliminary CFD evaluation. The data to be used for comparison is discussed. Two further tests cases with higher temperature differences (70°C and 140°C) are proposed for a blind benchmark exercise, in the framework of an OCDE/NEA CFD benchmark.

Acknowledgements

This work is financed by Forsmark NPP, Ringhals NPP, Oskarshamn NPP, Teollisuuden Voima NPP and Electricité de France.

References

[1] Robert M., 1992, Corkscrew flow pattern in piping system dead legs. NURETH-5, September, Salt Lake City, USA.

[2] EPRI MRP-25, Operating experience regarding thermal fatigue of unisolable piping connected to PWR reactor coolant systems

[3] Nakamura, A., Miyoshi, K. Oumaya, T., Takenaka, N., Hosokawa, S. Hamatani, D. Hase, M. Onojima, D. Yamamoto, Y., Saito, A. Nuclear Engineering and Design 269 (2014) 360– 373. Temperature fluctuation phenomena in a normally stagnant pipe connected downward to a high velocity and high temperature main pipe.

[4] Howard R., "Thermohydraulics of dead legs flows", CFD for Nuclear Reactor Safety, CFD4NRS-8, EDF Lab Paris-Saclay, 25-27 Nov (2020)

[5] EPRI: Materials Reliability Program Thermal cycling screening.

[6] Materials Reliability Program: RCS Stagnant Branch Line Swirl Penetration Test Plan (MRP-447)

[7] Naudin, C., Vidard S., 2013, Evaluation of the stratification loads with the EDF fatigue assessment device, Proceedings of the ASME 2013 Pressure Vessels and Piping Conference, PVP2013-97181, July 14-18, Paris, France.

[8] Iguchi T, Saito A, Takenaka N, Miyoshi K and Nakamura A, 2011, Experimental study on penetration length in a small size branch pipe in a nuclear power plant, The 14th International Topical Meeting on Nuclear Reactor Thermal hydraulics, NURETH-14, Toronto, Ontario, Canada, September 25-30

[9] Smith, B. L., Mahaffy, J. H., Angele, K., Nuclear Engineering and Design, Volume 264, November 2013, p. 80-88. A CFD benchmarking exercise based on flow mixing in a T-junction.

[10] Angele K., Odemark,Y., Cehlin M., Hemström B., Högström C. M., Henriksson M., Tinoco H., Lindqvist H., Flow mixing inside a control-rod guide tube – Experimental tests and CFD simulations Nuclear Engineering and Design 241 (2011) 4803–4812.

[11] Braillard O., Howard R. Angele K., Shams A., Edh N. Nuclear Engineering and Design Volume 330, 15 April 2018, p. 377-390. Thermal mixing in a T-junction: Novel CFD-grade measurements of the fluctuating temperature in the solid wall.

[12] Miyoshi, K., Nakamura, A. INVESTIGATION OF FLOW STRUCTURE TO PREVENT THERMAL FATIGUE IN A DOWNWARD BRANCH PIPE WITH A CLOSED END. Proceedings of the ASME 2017 Pressure Vessels and Piping Conference, PVP2017. July 16-20, 2017, Waikoloa, Hawaii, USA PVP2017-65154.

[13] Ishikawa Y., Okuda, Y., Kasahara, N. NUMERICAL ESTIMATION OF FLOW PENETRATING DEPTH INTO STAGNANT BRANCH PIPES FOR THERMAL FATIGUE PREDICTION. Proceedings of the ASME 2014 Pressure Vessels and Piping Conference, PVP2014. July 20-24, 2014, Anaheim, California, USA PVP2014-28382.

WRONG BUT NOT GUILTY: THE REYNOLDS ANALOGY AND MODEL ERROR IN CFD

Ralph Wiser, Emilio Baglietto

MIT Department of Nuclear Science and Engineering

Extended Abstract

Generations of CFD modelers and practitioners have recognized turbulent heat transfer as a key challenge for CFD model accuracy and uncertainty quantification. The Reynolds analogy, which assumes proportionality between the turbulent momentum flux and turbulent heat flux, has well-known theoretical limitations such as inapplicability to non-unity Prandtl fluids. Indeed, CFD results using the Reynolds analogy often mispredict temperature outputs, especially in complex flows or in the presence of strong buoyancy. Consequently, the CFD community lacks confidence in heat transfer modeling results, which has limited the use of CFD for nuclear reactor safety evaluation.

The traditional view in the thermal hydraulic community blames most CFD temperature errors on model inadequacy coming from the Reynolds analogy. Instead, we see the heat flux model error in context with other types of error in the heat transfer simulation. These include input errors, such as uncertainty in the physical properties and boundary conditions; model errors, including the turbulence model, the Reynolds analogy, and the buoyancy model; and numerical errors such as discretization error. We suggest that when all error sources are quantified, the Reynolds analogy plays a negligible role in the temperature error, even though its physical basis is flawed. Thus, the Reynolds analogy is wrong, but should not be blamed.

To demonstrate our new understanding of turbulent heat flux, we have developed a new framework which accounts for all sources of error in heat transfer simulations. We implement RANS simulations which recreate numerical and real-world experiments across a range of flow conditions including triple jet simulations and buoyancy-effected channel flow. We focus on spanning a wide range of these parameters: Reynolds number, Prandtl number, and Richardson number. We eliminate input errors where possible and quantify numerical errors, so that remaining CFD error comes from three types of model error: the turbulence model, the Reynolds analogy, and the buoyancy treatment. First, we find that the dominant source of error in most cases is the turbulence model, and this can be quantified using a recent physics-based model error propagation technique. Second, the buoyancy treatment in the production and transport of turbulent quantities can introduce significant error, which can be addressed with improved modeling. Finally, the errors due to the Reynolds analogy are measurable, especially in low-Prandtl fluids, but small compared to the other sources of model error.

The new framework for quantifying all sources of error has significant impact in CFD heat transfer calculations for nuclear reactor safety. Now that we can quantify and attribute the CFD error to the correct parts of the model, practitioners can use CFD with more confidence, always including error bars that represent the 95^{th} percentile of the best estimate uncertainty. This gives practitioners the option to either accept the results as accurate enough, or to carry out experiments or higher fidelity CFD to resolve the error. Our framework for complete uncertainty quantification is key for CFD usage in safety evaluation and licensing.

U.S.NRC
United States Nuclear Regulatory Commission
Protecting People and the Environment

Center for Advanced Small Modular and Micro Nuclear Reactors
Texas A&M Engineering Experiment Station

NEA
NUCLEAR ENERGY AGENCY

Technical Session 9 –

Verification and Validation II.

Feb 21, 14:00-15:30, Room A.

Scaling Analysis as a support of CFD Best Practices

Milorad B. Dzodzo
Westinghouse Electric Company, USA

Abstract

Scaling is used in the nuclear industry to support the design of test facilities and provide experimental results that are related to the full-scale prototype (nuclear power plant) during postulated accident scenarios. Test facility sizes and complexity span from basic and separate effect tests to integral effect tests. However, the needed number of control volume cells limits practical CFD domain sizes. Validated CFD models, based on well-instrumented basic and separate effect test results, are currently used only to support the development of small portions of sub-systems (modules) of nuclear power plants. In combination with scaling analysis methods, further development of CFD software compatible with high-performance computing platforms will enable applications of CFD for bigger and more complex domains such as portions, or entire, integral test facilities. The paper addresses the connection between the derivation of dimensionless groups (based on the nondimensionalization of equations used for CFD) and hierarchical and time scaling approaches used to develop test facilities. This helps the validation process and scalability of CFD codes when they are applied to the reactor scale. Several examples related to single-phase flows present how CFD, in combination with experiments and scaling analysis is used to support the extrapolation of distorted test results.

Introduction

Small-scale Basic Tests (BT) and Separate Effect Tests (SET) are used to obtain experimental data needed to study interactions of several local fundamental phenomena (processes) and to validate both: Thermal Hydraulics System (THS) and Computational Fluid Dynamics (CFD) codes developed models.

Mid-scale and more complex SET facilities and Integral Effects Test (IET) facilities are designed to study the transient response of modules and sub-systems of Nuclear Power Plants (NPP). Test results are used to validate THS codes.

To apply developed and validated models based on THS and CFD codes to the prototypical NPP conditions scaling analysis needs to take into consideration distortions due to the use of different length scales and fluids (or different thermophysical properties at lower temperatures if the same fluid is used) in the test facilities.

Scaling analysis for small-scale BT and SET is usually based on the classical Dimensional Analysis (DA) [1] and Scaling of Equations (SE) methods. An overview such as a review of literature, discussion and examples of DA and SE applications, and derived Dimensionless Numbers (DN) for single- and two-phase flows are presented by [2].

The majority of the first generation of mid-scale SET and IET facilities were scaled based on the volumetric scaling by keeping the power-to-volume ratio the same in the model as in the prototype. Later, due to the increased complexity of the Nuclear Power Plant (NPP) systems, increased number of postulated accident scenarios, and complex interactions of multiple passive cooling phenomena the hierarchical and two-tiered (top-down and bottom-up) scaling approach was introduced by [3] and [4].

The scaling analyses such as Hierarchical Two-Tiered Scaling (H2TS) [4, 5] and Fractional Scaling Analysis (FSA) [6, 7], developed later, utilizing the same and consistent time-scaling procedure to derive and quantify all DNs and make them comparable. This provided easier quantification of the distortions and indication of which processes are important.

An overview of scaling analysis approaches applied in the nuclear industry and the new developments in scaling analysis are presented in OECD Report [8].

To illustrate the benefits of combining H2TS and FSA methods and CFD a comparison of dimensionless numbers derived with a time scaling approach for H2TS, and FSA methods and dimensionless numbers usually used for CFD analysis, based on scaling momentum equations for single-phase flows, is performed in [9, 10]. It was concluded that if the convection scaling is used as the last step of scaling equations, then the derived dimensionless numbers for CFD analysis can be compatible with H2TS and FSA methods. Effects of the initial and boundary conditions, changes in the fluid thermophysical properties, flow patterns in the connecting pipes between vessels, inlet and outlet conditions for vessels, reduced vessel heights, and residence times were also considered and discussed.

The purpose of this paper is to present several additional examples of how scaling analysis can support validation and CFD best practices. Also, in some situations validated CFD models (as in [11]) based on the best practices (as in [12]) can support the scaling analysis and help to interpolate or extrapolate the test results from the scaled-down facilities to the prototypical conditions.

Connection of dimensionless numbers used in CFD and HT2S and FSA scaling analyses

The comparison of dimensionless numbers usually used in CFD analysis for single-phase flows and in scaling analyses based on the time scaling as H2TS and FSA is presented in [9, 10]. It was concluded that if the convection scaling is used as the last step of scaling equations, then the derived dimensionless numbers for CFD analysis can be compatible with H2TS and FSA methods.

The dimensionless momentum equation for single-phase flow obtained by dividing with the convection term (in fact, by applying the convection scaling) is

$$\frac{1}{\tau}\frac{L}{\bar{v}} + 1 = \frac{P}{\rho\bar{v}^2} + \frac{\mu}{\rho L\bar{v}} + \frac{gL}{\bar{v}^2}$$

where the terms present (1 - unsteadiness + 2 - convection) = (3 - pressure and hydrostatic pressure) + (4 - viscosity) + (5 -gravity\boyancy). This equation produces four dimensionless numbers: Strouhal number $Sr = \frac{1}{\tau}\frac{L}{\bar{v}}$, Euler number $Eu = \frac{P}{\rho\bar{v}^2}$, Reynolds number $\frac{1}{Re} = \frac{\mu}{\rho L\bar{v}} = \frac{\nu}{L\bar{v}}$, and Froude number $\frac{1}{Fr} = \frac{gL}{\bar{v}^2}$. All dimensionless numbers can be rearranged as the product of corresponding frequency and time (in fact the residence time $\tau = \frac{L}{\bar{v}}$): $Sr = \frac{1}{\tau}\frac{L}{\bar{v}} = \omega_{Sr}\tau$, $Eu = \frac{P}{\rho\bar{v}^2} = \frac{P}{\rho\bar{v}L}\frac{L}{\bar{v}} = \omega_{Eu}\tau$, $Re = \frac{\rho\bar{v}L}{\mu} = \frac{\rho\bar{v}^2}{\mu}\frac{L}{\bar{v}} = \omega_{Re}\tau$ and $\frac{1}{Fr} = \frac{gL}{\bar{v}^2} = \frac{g}{\bar{v}}\frac{L}{\bar{v}} = \omega_{1/Fr}\tau$. Thus, the presented convection scaling is compatible with the convection scaling applied for H2TS for the control volumes of interest and power to volume scaling with full height.

In the case that Boussinesq approximation for density is used in the CFD model the dimensionless momentum equation for single-phase flow obtained by applying the convection scaling is

$$\frac{1}{\tau}\frac{L}{\bar{v}} + 1 = \frac{P}{\rho_0\bar{v}^2} + \frac{1}{Re} + \frac{Gr}{Re^2}$$

where in the last term the Grashoff number $Gr = \frac{g\beta(T-T_0)L^3}{\nu^2}$ represents the ratio of buoyancy and viscous forces. In the case that the heat fluxes, $\dot{q} = \frac{k}{L}\Delta T$, are specified as boundary conditions the modified Grashoff number $Gr^* = \frac{g\beta\dot{q}L^4}{\nu^2 k}$ is used. This dimensionless number, or Rayleigh number $Ra = Gr \cdot Pr$, are almost always used in the CFD models for natural or mixed convection.

The last term is now Richardson number $Ri = \frac{Gr}{Re^2}$ and represents the ratio of buoyancy and convection (in fact $Ri = \frac{1}{Fr} = \frac{g}{\bar{v}}\frac{L}{\bar{v}} = \omega_{Ri} \cdot \tau$). Thus, the evaluation of buoyancy effects with the Richardson number, instead of the Grashoff, or Rayleigh numbers, is more compatible with H2TS and FSA scaling methods. However, in the case of natural convection in enclosures (without inlets and outlets or moving lids) the velocity $\bar{v}$ needs to be calculated based on the experimental or numerical results.

The detailed derivations of mass and momentum dimensionless equations and examples of CFD applications supporting scaling analysis for specific conditions are presented in [9, 10].

The dimensionless energy equation for single-phase flow obtained by dividing with the convection term (in fact, by applying the convection scaling) is

$$\frac{1}{\tau}\frac{L}{\bar{v}} + 1 = \frac{k}{\rho c_p}\frac{1}{L\bar{v}} = \frac{\alpha}{L\bar{v}} = \frac{1}{Pe} = \frac{\alpha}{\nu}\frac{\nu}{L\bar{v}} = \frac{1}{Pr}\frac{1}{Re}$$

This equation produces two dimensionless numbers: Strouhal number $Sr = \frac{1}{\tau}\frac{L}{\bar{v}}$, and Péclet number $\frac{1}{Pe} = \frac{\alpha}{L\bar{v}} = \frac{\alpha}{\nu}\frac{\nu}{L\bar{v}} = \frac{1}{Pr}\frac{1}{Re}$, where Péclet number can be also rearranged as the product of corresponding frequency and time (in fact the residence time $\tau = \frac{L}{\bar{v}}$) as $Pe = \frac{\bar{v}L}{\alpha} = \frac{\bar{v}^2}{\alpha}\frac{L}{\bar{v}} = \omega_{Pe}\tau$.

Péclet number represents the ratio of convection transport and heat diffusion transport $Pe = \frac{L\bar{v}}{\alpha}$ and can be calculated as the product of Prandtl and Reynolds number $Pe = Pr \cdot Re$, where Prandtl number $Pr = \frac{\nu}{\alpha}$ depends on the fluid thermophysical properties as the ratio of kinematic viscosity ν, and thermal diffusivity $\alpha = \frac{k}{\rho c_p}$, or ratio of time scales $Pr = \frac{\nu/L^2}{\alpha/L^2} = \frac{\omega_m}{\omega_e}$ for the momentum ω_m, and thermal energy diffusion transport processes ω_e frequencies.

Table 1 compares and connects the dimensionless numbers used in CFD and scaling analyses.

Table 1: Comparison and connection between the dimensionless numbers used in CFD and H2TS scaling analysis

	CFD	H2TS – Time Scaling	
		Frequency	Time
Unsteadiness	$\boldsymbol{Sr = \frac{1}{\tau}\frac{L}{\bar{v}}}$	$\boldsymbol{\omega_{Sr} = \frac{1}{\tau}}$	$\boldsymbol{\tau = \frac{L}{\bar{v}}}$
Convection (used for normalization)	1		
Pressure	$\boldsymbol{Eu = \frac{P}{\rho\bar{v}^2} = \frac{P}{\rho\bar{v}L}\frac{L}{\bar{v}}}$	$\boldsymbol{\omega_{Eu} = \frac{P}{\rho\bar{v}L}}$	$\boldsymbol{\tau = \frac{L}{\bar{v}}}$
Viscosity	$\boldsymbol{Re = \frac{\rho\bar{v}L}{\mu} = \frac{\rho\bar{v}^2}{\mu}\frac{L}{\bar{v}}}$	$\boldsymbol{\omega_{Re} = \frac{\rho\bar{v}^2}{\mu}}$	$\boldsymbol{\tau = \frac{L}{\bar{v}}}$
Gravity/Boyancy	$\boldsymbol{Ri = \frac{1}{Fr} = \frac{Gr}{Re^2} = \frac{g}{\bar{v}}\frac{L}{\bar{v}}}$	$\boldsymbol{\omega_{Ri} = \frac{g}{\bar{v}}}$	$\boldsymbol{\tau = \frac{L}{\bar{v}}}$
Convection/Heat Diffusion	$\boldsymbol{Pe = \frac{\bar{v}L}{\alpha} = Pr \cdot Re}$	$\boldsymbol{\omega_{Pe} = \frac{\bar{v}^2}{\alpha}}$	$\boldsymbol{\tau = \frac{L}{\bar{v}}}$

The dimensionless numbers in Table 1 apply to all problems where the momentum and energy equations for single-phase flow are used. However, besides the equations, the initial conditions, boundary conditions, different fluid thermophysical properties, flow conditions in connecting piping between the control volumes of interest, inlet, and outlet conditions in the control volumes of interest, adjustment (or not) of the residence times are also important and need to be considered in the scaling analysis. These conditions can produce additional dimensionless numbers. However, these conditions are specific and depend on the geometric configurations, postulated accident scenarios, and considered portion of the plant and cannot be presented in a general form. Some of the conditions and their effects and connections on the scaling analyses are presented and discussed by [9, 10]. Additional conditions will be presented in this paper.

Based on the established connections between the dimensionless numbers the CFD analysis can support the design of the BT and SET facilities similarly as Thermal Hydraulics System (THS) codes support the design of the SET and IET facilities [13]. Also, by using a similar approach, CFD analyses can be used to interpolate test results obtained from the several counterpart test facilities with different scales and extrapolate them to the prototypical conditions. Besides being part of the scaling analyses the CFD models can benefit from the scaling analyses by improving validations and best practices.

The distortion between the model (test facility) experimental results and prototypical (NPP) conditions can be defined as a ratio of dimensionless numbers for the model and prototype $D = \frac{\Pi_m}{\Pi_p}$. The ideally scaled test facility is when the dimensionless numbers are equal, $\Pi_m = \Pi_p$ (in fact $D = 1$).

Sizes of the CFD domains, boundary conditions, and fluid thermophysical properties

CFD cannot be used to model the entire NPP system. Instead, THS codes, or coupled THS and CFD codes, can be applied to model the entire system or sub-systems. CFD codes alone can be applied for lower hierarchical levels such as sub-systems and modules if porous media or Coarse Grid CFD (CG-CFD) space averaging approaches are used for the entire domain, or part of it, in combination with Reynolds Averaged Navier Stokes (RANS) or Unsteady RANS (URANS) turbulence modeling. Depending on the size of the CFD computational domain of interest, various turbulence models [RANS, URANS, Partially Averaged Navier Stokes (PANS), Large Eddy Simulation (LES)] or Direct Numerical Simulation (DNS) can be used for various lower hierarchical levels (presented in Table 2). An overview of possibilities and challenges is presented by [14] and [15].

CFD solutions can be improved by increasing the number of cells and mesh-independent solutions can be achieved. However, the mesh-independent solution alone is not a guarantee that an adequate solution is obtained. Space decomposition and adequate length scales need to be resolved to establish the hierarchy of modeling approaches. Various decompositions of space (including type and distribution of applied mesh) and time (including time steps based on the numerical analysis criteria and frequencies of the present phenomena), the use of discretized equations, and possible numerical analysis approach for various types of problems can improve or limit CFD solutions [16, 17]. The sensitivity of the CFD model results to applied mesh size, mesh quality, meshing approach, applied turbulence models, and boundary conditions need to be tested [18].

Table 2: System decomposition and hierarchy of processes and THS and CFD models

System decomposition	Hierarchy of processes								TH System & Component codes	CFD codes
System (S)	S								TH System Codes	Coupled THS and CG-CFD codes
Sub-system (SS)	SS_1							SS_k		CG-CFD, Combined Porous Media and RANS or URANS
Modules (M)	M_1						M_k		TH Component codes	
Constituents (C)	C_1					C_k				RANS & URANS, PANS, LES, DNS
Phases (P)	g				f	s				
Geometrical Configurations (GC)	G_1			G_k						
Fields (F)	M	MM	E							
Processes			P_1	P_k						

However, the size of the prototypical domain of interest can be limiting for both: the test facility and the CFD model.

For example, in the case of testing fuel assemblies' heat transfer, the prototypical height, fuel rod diameter, pitch, and prototypical coolant pressures and temperatures are specified as the only option to provide correctly scaled SETs facilities [19]. Practically the only parameter left to adjust the size of the SET facility is the number of the fuel rod imitators *N* which will be electrically heated. However, the real PWR fuel assemblies can have for example up to 16 x 16 fuel rods (see Figure 1 – left side presenting one-quarter of the fuel assembly horizontal cross-section). Thus, the available electrical power in the test facility is limiting the number of fuel rod imitators *N* which can be applied.

Heat flux boundary conditions

Depending on the available electrical power in the laboratory only 3 x 3 up to 6 x 6 fuel rod imitators are used (see Figure 1 – right side with 5 x 5 fuel rod imitators which is supposed to represent only part of the fuel assembly inside the dotted square at the left side of Figure 1). Consequently, the fuel rod imitators are positioned in the vertical channel with square cross sections and thermally insulated vertical walls (which are not present in the real fuel assembly). Also, due to the limitations of the available electrical power some fuel rod imitators closer to the channel center are heated with full power, while the surrounding fuel rod imitators closer to the side walls are heated with lower power (see Figure 1 – right side with differently colored fuel rod imitators).

Figure 1: One-quarter of fuel assembly with 16 x 16 fuel rods (left side), Test facility with 5 x 5 fuel rod imitators, and vertical channel side walls (right side)

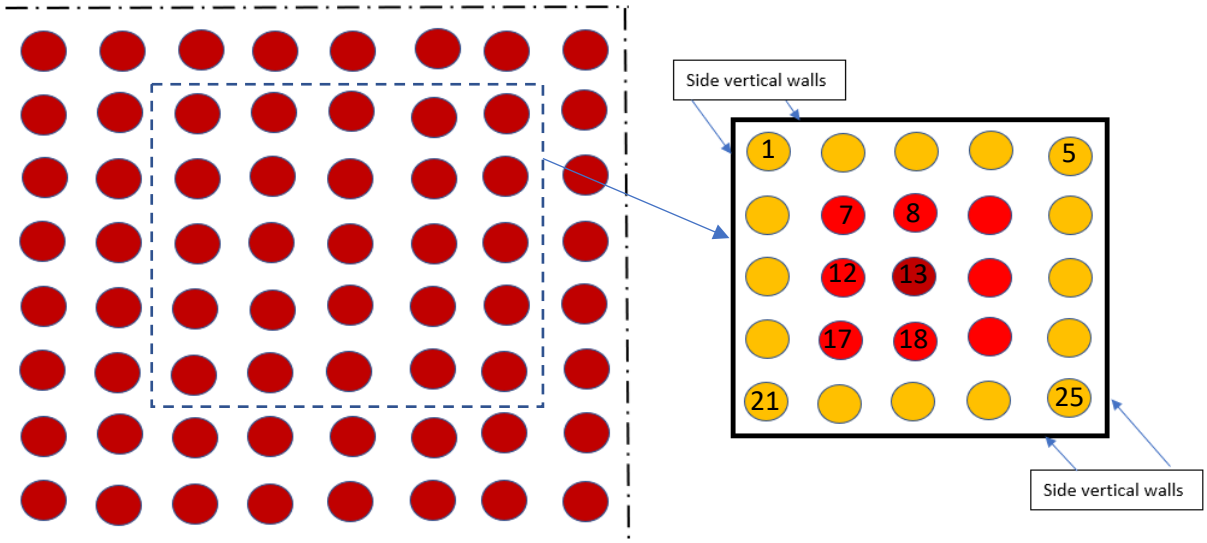

Side walls boundary conditions

The presence of the channel vertical walls causes distortions in the flow and temperature distributions and needs to be considered when test results are used for the full-size fuel assemblies.

The side walls no-slip boundary conditions affecting the velocity field and thermal boundary conditions (either insulated or with various heat fluxes applied) affecting temperature distribution can be introduced in the CFD model which can be validated.

Then, the validated CFD models can be used to model the same domain but with periodic (cyclic) boundary conditions instead the no-slip vertical side walls and prototypical heat fluxes. Considering that the prototypical Reynolds numbers are in the range of $Re = 500{,}000$ and $Pr{\sim}1.0$ the forced convection assumption and Reynolds analogy for velocity and temperature fields are valid and can be applied for CFD modeling.

SETs facilities with prototypical water pressure and temperature cannot be built with transparent walls and cannot provide detailed information on velocity and temperature fields needed for detailed CFD validation. Only local measurements of temperatures (based on the thermocouples) and velocities and pressure drops at specified positions and elevations are available.

Transparent side walls and fluid thermophysical properties

SETs facilities with transparent walls and water at room temperature can provide detailed velocity and temperature fields based on PIV and laser-induced fluorescence, or similar methods. However, the thermophysical properties of water at room temperature are different than at the prototypical conditions resulting in $Pr{\sim}5.0$ and due to the higher viscosity, the achievable velocities are lower, resulting in approximately 10 times lower Reynolds numbers ($Re \sim 50{,}000$). Also, in some cases, to match the refractive index of the transparent walls the other fluids, or mixtures of various fluids, are used and their thermophysical properties need to be measured and used in CFD models used for validation. This results in distortions $D_{Re} = \frac{(Re)_m}{(Re)_p} = \frac{50{,}000}{500{,}000} = 0.1$ and $D_{Pr} = \frac{(Pr)_m}{(Pr)_p} = \frac{5.0}{1.0} = 5$.

Figure 2: Considered CFD domain (left side), Comparison of experimental (PIV) and numerical (CFD) results (based on [22] and [20] - right side)

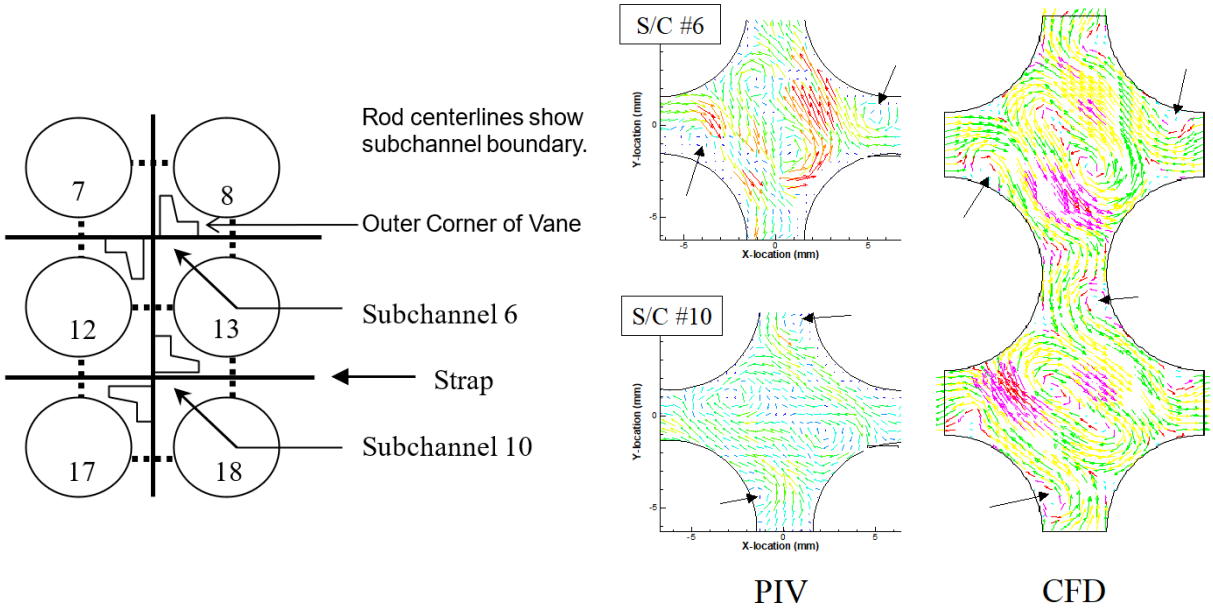

Although high distortions between model (test facility) data and prototype, the CFD model validated based on the model test data can be used for the prototypical conditions after adjusting control volume cells sizes near the walls considering the tinner boundary layers based on the prototypical Re - Reynolds and Pr - Prandtl numbers (as in [20] and [21]).

One example of the comparison of experimental results for velocity field (presented in Figure 2 - right side), obtained with PIV and test facility with 5 x 5 rod imitators and channel with transparent side walls [22], and CFD model results based on the domain of only two subchannels (between six fuel rods – marked with numbers 7, 8, 12, 13, 17 and 18 in Figure 1 – right side) and periodic boundary conditions at open boundaries (dotted lines in Figure 2 – left side) as in [20].

Depending on the available memory of computers various CFD domains and mesh sizes are applicable. The two subchannels and one span were the minimum CFD domain in [20] which can produce results comparable to experiments in [22]. At that time, it was the maximum possible domain based on the available memory of computers and needed mesh size. Later, the whole test section of the 5x5 bundle CFD domain including the effects of the test facility channel side walls was modeled in [21].

Heat transfer tests were performed with a sliding heat transfer probe in [23] and compared with CFD model results in [24]. The distortions for the heat transfer test are lower due to the compensating effects of distortions of Reynolds and Prandtl numbers $D_{Pe} = D_{Re} \cdot D_{Pr} = \frac{50{,}000}{500{,}000} \cdot \frac{5.0}{1.0} = \frac{250{,}000}{500{,}000} = 2.0.$

However, it is more difficult to obtain an agreement between experimental and CFD model results and obtain the validated CFD model for heat transfer. Thus, even do the distortion is formally lower than for the velocity fields the extrapolation of the heat transfer experimental results using the CFD model demands better-organized tests (with measurement of the temperatures of the transparent walls, heating more than one fuel rod, increased applied heat fluxes without increasing fluid temperatures above the

Figure 3: Example of mesh sensitivity tests – cliff effects (based on [25])

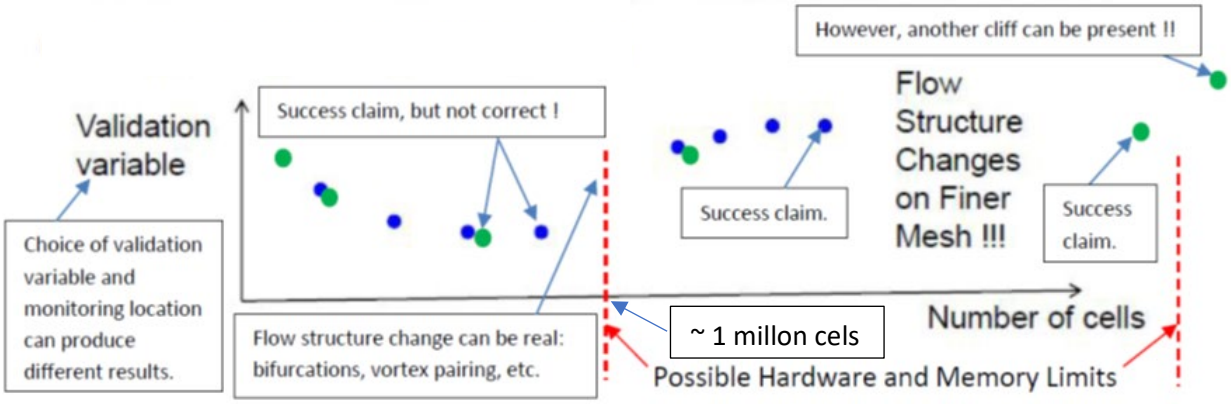

allowable temperatures for transparent wall materials, etc.) and improved CFD models (increased mesh size in the boundary layers, higher fidelity of turbulence models, conjugate heat transfer modeling for fluid rod imitators, etc.).

It could be concluded that good agreement of experimentally and numerically obtained flow patterns can be achieved even with a limited number of applied mesh control volume cells (~1 million per subchannel) and the RANS turbulent modeling approach. However, if less than 1 million cells is applied the numerically obtained flow pattern will have only one eddy in the sub-channel core (instead of two), and without having experimental results the mesh-independent solution might be claimed (see Figure 3 [25]).

It is interesting to note that based on the simple flow visualization techniques (based on the video recording, not PIV which averages results over time) the bifurcations from one eddy pattern to two eddy patterns and vortex pairing (transition back from two to one eddy pattern) were recorded for some type of vanes. This indicates that for regions immediately after the vane in some cases at least URANS, if not LES, turbulence modeling could be more applicable. This could be necessary if complex and Multiphysics phenomena such as Fluid Induced Vibrations (FIV) and Fluid-Structure Interaction (FSI) need to be modeled.

Nowadays, based on the advances in PIV measurements [26], the SET facilities with transparent walls and fluids at room temperature are capable to consider the whole fuel assembles cross-section and several spans. Based on the High-Performance Computing (HPC) platforms CFD models are also capable to consider the entire fuel assemblies' domain (see for example [27]).

Inlet and outlet boundary conditions

The test facility with 5 x 5 rod imitators and a channel with transparent side walls [22] needed three spans to provide inlet and outlet conditions for the middle span where PIV data were obtained.

In the case of the CFD model only, one span and a small extension below the grid where the horizontal inlet plane is defined are necessary. The velocity and temperature fields at the upper elevation at the same distance below the upper grid were mapped and used at the inlet. The temperatures obtained at the upper elevation were decreased based on the fuel rod heat fluxes and water mass flow rates.

Figure 4: Measuring planes (left side), Considered CFD domain (middle), Comparison of experimental and CFD velocities at plane 6 for two designs (based on [28] and [29])

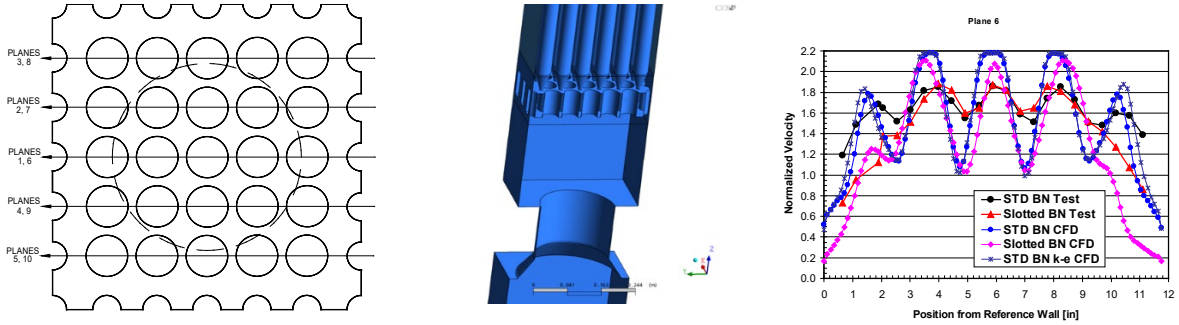

However, in the case that we need to model the entire length of the fuel assembly the inlet velocity and temperature fields need to be provided from the test results, or the bottom nozzle geometry needs to be modeled. For example, CFD models supporting designs of fuel assembly debris filter and bottom nozzle were validated based on the $\frac{L_m}{L_p} = \frac{3.763}{1.000}$ scaled-up air test for inlet nozzle region [28]. Axial velocities were measured in a test section simulating a 6 x 6 rod array of the inlet nozzle region and first grid span. The measurements were taken in multiple planes at 23 positions to map the velocity in both the rod gaps and subchannels (see the left side of Figure 4) to study how each nozzle impacts the dissipation of the lower support flow hole jet velocity downstream of the bottom nozzle. In this case $D_{Pr} = \frac{(Pr)_m}{(Pr)_p} = \frac{1.0}{1.0} = 1$ and D_{Re} can be adjusted to be $D_{Re} = 1$ if air flow rates are adjusted to provide $\frac{\bar{v}_m}{\bar{v}_p} = \frac{L_p}{L_m} \cdot \frac{\nu_m}{\nu_p} = \frac{1}{3.763} \cdot \frac{\nu_m}{\nu_p}$ based on the scaled-up dimensions and ratio of air and water kinematic viscosities.

A comparison of experimental and CFD results for the two designs is presented in [29]. The middle of Figure 4 presents the cross-section of considered CFD for the bottom nozzle with holes. A comparison of experimentally and numerically (based on CFD RANS turbulence models) obtained velocity profiles for the bottom nozzle with holes and slots is presented for plane 6 on the right side of Figure 4. It can be concluded that qualitative agreement exists, but CFD results are underestimating the mixing of parallel jets and producing higher jet velocities and lower values of velocities between jets. Mesh refinements were not able to improve CFD results. Instead, at least URANS turbulence models with adjusted mesh size and time step are needed to get better agreements (as will be presented in the following section).

Real heat transfer boundary conditions – conjugated heat transfer

Heat transfer correlations are usually developed based on experiments with either constant temperature or heat flux surface boundary conditions.

However, with the introduction of passive cooling to remove the heat from the reactor and containment vessels during the postulated accidents the transient heat transfer between the solid structures and surrounding fluids need to be analyzed. Also, due to the oscillatory flows in the portions of NPP during the regular operation, the temperatures of the surrounding solid structures will fluctuate and therefore thermal fatigue of material can occur.

Thus, a more realistic analysis of heat transfer between solid structures and surrounding fluids is necessary as the transient (unsteady) conjugated heat transfer (CHT, or UCHT) CFD models are needed.

However, CHT and UCHT models demand finer meshes in the fluid and solid domains near the interface surface, small time steps, and an adequate number of iterations during each time step, resulting in the increased need for memory and time to obtain solutions. Also, additional effort and time are needed to create conformal meshes at the interface surface and avoid interpolations to provide the surface temperatures (see for example [30]). An indication of needed mesh refinement and adjustments to perform the calculations can be based on the local Biot number, Bi, a dimensionless number that represents the ratio of the heat transfer resistances in the solid body and fluid

$$Bi = \frac{\frac{L_s}{k_s}}{\frac{1}{h}} = \frac{hL_s}{k_s} = \frac{\frac{L_s}{k_s}}{\frac{L_f}{k_f}} = \frac{k_f}{k_s}\frac{L_s}{L_f}$$

where h is the fluid convection heat transfer coefficient and k_s and L_s are solid body conduction heat transfer coefficient and characteristic length, respectively. In the case that the solid body has negligible heat transfer resistance (practically $k_s \to \infty$, $Bi \to 0$) the characteristic length is the ratio of the solid body volume and surface area ($L_s = V_s/A_s$). However, for CFD analysis instead of applying the convection heat transfer coefficient which can be very different at different locations, it is better to use the heat transfer resistance based on the local fluid heat conduction in the boundary layer $\frac{L_f}{k_f}$, where the fluid characteristic length is based on the thickness of velocity or temperature boundary layers (whichever is thinner) defining the thickness of the cells near the solid walls. If the mesh thicknesses near the interface are the same, the L_s is specified to be equal to L_f and Biot number can be estimated as a ratio of the fluid and solid conduction heat transfer coefficients ($Bi \approx \frac{k_f}{k_s}$), resulting in the ratios of the fluid and solid temperature differences from the interface temperature $\frac{\Delta T_f}{\Delta T_s} \approx \frac{k_s}{k_f}$. If the mesh thicknesses near the interface are adjusted to be $\frac{L_s}{L_f} = \frac{k_s}{k_f}$ the Biot number is $Bi \approx 1$ and the differences of the fluid and solid temperature from the interface temperature are the same, $\Delta T_f \approx \Delta T_s$.

For simulating transient accident scenarios, the unsteady conjugated heat transfer (UCHT) is applied and thermal diffusivities of solids $\alpha_s = \frac{k_s}{c_{p_s}\rho_s}$ and fluids $\alpha_f = \frac{k_f}{c_{p_f}\rho_f}$ near the interface needs to be considered. Fourier numbers for solids and fluids, representing the dimensionless time (in fact, the ratios of the diffusion rate and the storage rate) can be adjusted to be the same:

$$Fo_s = \frac{\alpha_s}{L_s^2}\Delta t = Fo_f = \frac{\alpha_f}{L_f^2}\Delta t$$

by adjusting the ratio of cells thicknesses near the interface to be $\frac{L_s}{L_f} = \sqrt{\frac{\alpha_s}{\alpha_f}}$, or, in fact, by adjusting the ratio of thermal energy diffusion transport processes frequencies in fluids and solids to be the same:

$$\omega_s = \frac{\alpha_s}{L_s^2} = \omega_f = \frac{\alpha_f}{L_f^2}$$

In the case that only a fully developed (steady state) solution is necessary, and an underrelaxation based on specifying time steps for the different domains is used, the solution can be obtained by applying the different time steps for different solid and fluid domains based on the thermal diffusivities and cell thicknesses near the interface:

$$\Delta t_s = \frac{\omega_f}{\omega_s}\Delta t_f = \frac{\alpha_f}{L_f^2}\frac{L_s^2}{\alpha_s}\Delta t_f = \frac{\alpha_f}{\alpha_s}\frac{L_s^2}{L_f^2}\Delta t_f \ .$$

A necessary number of total iterations, and iterations per one-time step, will depend on the mesh arrangement near the interface surface and fluid and solid thermophysical properties. Usually, a higher number of iterations is necessary for CHT, or UCHT, problems, and additional convergence criteria, such as checking the energy balance for the entire solids and fluids domains, are necessary to be sure that the converged solution is obtained.

Application of CHT can in some cases provide better validation of CFD codes because it takes into consideration more realistic local temperature distributions. One example is presented in [31] where the better agreement of temperature fields is obtained with the CHT CFD model (see Figure 5).

Also, CHT CFD models can be used to address coolant natural circulation and solid body heat conduction interaction effects. This might be especially important for providing adequate boundary conditions (wall surface temperature distributions) during long-term cooling near the end of transients.

DNS of CHT can be applied for small CFD domains including portions of the side vertical walls to check and eventually improve correlations applied in THS codes and to address the effects of the accumulated heat in the vertical side walls and distortions in time. Some examples of DNS CHT CFD models for laminar and turbulent single-phase flows are available in [32] and [33, 34], respectively.

Figure 5: Considered Domain and Meshing Approach for Modelling Mixed Convection Heat Transfer in Liquid Metal in the Vertical Pipe (left side), Comparison of temperature profiles at the outlet obtained with and without CHT models (right side) (based on [31])

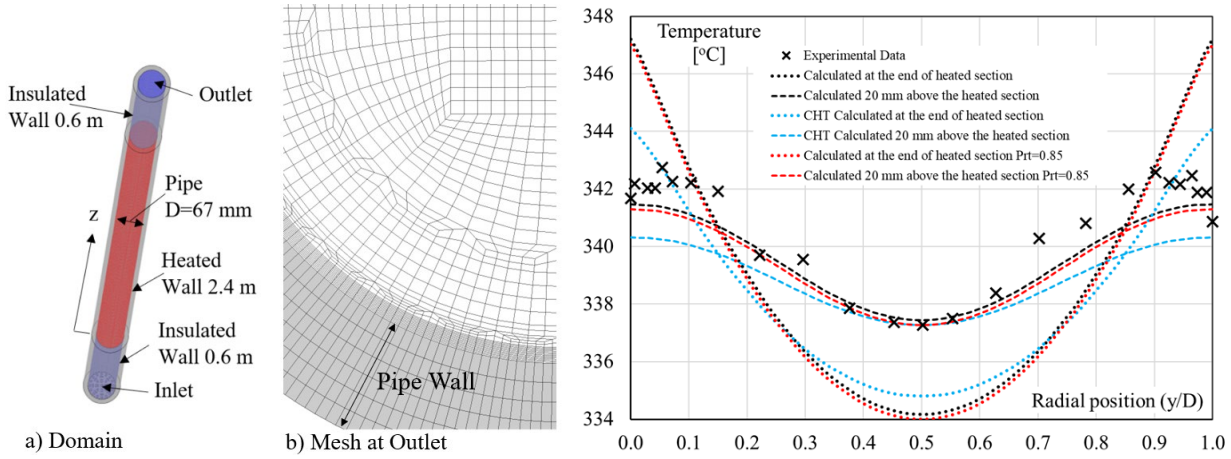

57.6 million hexahedral cells and the mesh refinement in radial and circumferential directions near the pipe walls for fluid domain (red and blue coloured)
11.8 million hexahedral cells and conformal with the fluid cells at the wall's inner surface (grey coloured)

Temperature profiles for descending flow with moderate buoyancy – inlet conditions Re=29800, Gr^*=2.60x10^8, Pe=175, $Ri = Gr^*/Re^2$=0.2928

Unsteady and oscillatory flows - parallel jets mixing

CFD models for mixing parallel jets discharged from multiple steam generators in the Small Modular Reactor (SMR) reactor vessel downcomer were evaluated based on the open literature test data for five [35] and two [36] parallel jets. Figure 6 (lower left side) presents a horizontal cross-section of the SMR reactor vessel and tested configuration in [35].

CFD models were based on different computational domains, meshing approaches, boundary conditions, and turbulence models [37] and [38]. Both, RANS [37] and URANS [38] turbulent modeling approaches were applied. Comparison of jet inlet Reynolds numbers and Strouhal numbers are presented in Figure 6 (upper left side), where Dh/d is the ratio of jet inlet hydraulics diameter Dh and distance between jet inlets d, and Strouhal number $Sr = \omega \cdot L/\bar{v} = \omega \cdot \tau = \omega/\omega_\tau$ is a ratio of phenomena frequency ω (jet lateral fluctuations) and replacement frequency $\omega_\tau = 1/\tau$ (based on the residence time $\tau = L/\bar{v}$).

In Figure 7 momentum decay $(Ujc - Umid)/Ujc$ of parallel jets (based on the jet central velocity Ujc and velocity between jet centers $Umid$) as a function of dimensionless distance from the jet inlet is presented for various models (see lines) and compared with experimental results [35] (see black dots). It can be concluded that RANS based models (see the left side of Figure 6) underestimate jet mixing, while URANS models are capable to provide qualitative agreement with experimental results (see the right side of Figure 7).

Figure 6: Comparison of parallel jets mixing results (based on [35-38])

	$D_{h\text{-}inlet}/d$	Jet Outlet Re	Strouhal Number
Kunz et al., 2001	38.1/38.1= 1	$1.04 \cdot 10^4$	0.13
Bunderson & Smith, 2005	0.112	$2.15 \cdot 10^5$	0.15
SMR	0.89	$8.58 \cdot 10^6$	to be investigated

$Sr = \frac{\omega \cdot L}{\bar{v}}$ - Strouhal number
ω - Jet fluctuation frequency
$L = D_{h-inlet}$
$\bar{v}$ - Jet outlet velocity

jcl – Jet Central Line
mcl – Mid Central Line
jcl – Jet Central Line

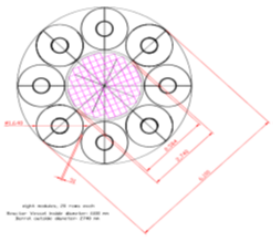

HORIZONTAL CROSS SECTION OF THE SMR REACTOR VESSEL ANNULAR SPACE DOWNCOMER WITH 8 STEAM GENERATOR OUTLETS DISCHARGING 16 PARALLEL JETS

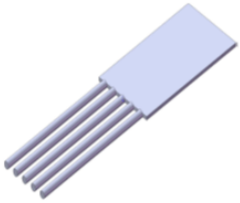

TESTED CONFIGURATION IN (Kunz et al., 2001)

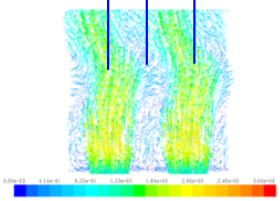

VELOCTY VECTORS OF TWO PARALLEL JETS (Pellegrini at al., 2009)

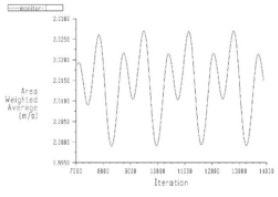

VELOCTY PLOT OF MONITORING POINT ON THE JET AXIS (Pellegrini at al., 2009)

Figure 7: Comparison of parallel jets mixing results (based on [37, 38])

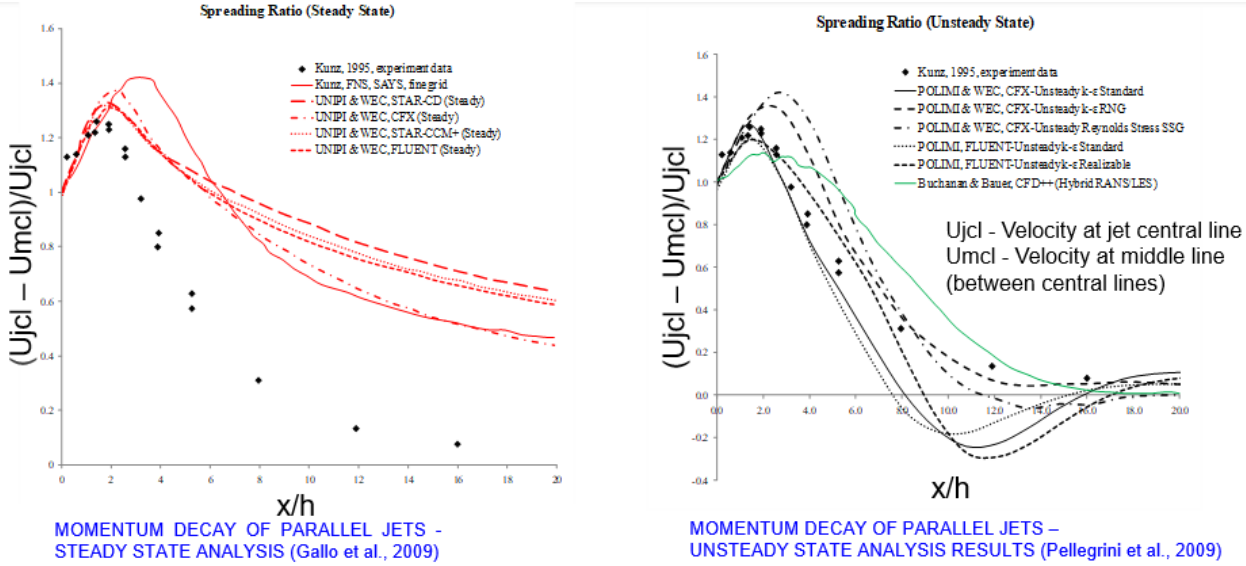

MOMENTUM DECAY OF PARALLEL JETS - STEADY STATE ANALYSIS (Gallo et al., 2009)

MOMENTUM DECAY OF PARALLEL JETS – UNSTEADY STATE ANALYSIS RESULTS (Pellegrini et al., 2009)

Based on the experimental Strouhal numbers, jet average inlet velocity $\bar{v}$, and characteristic length L the frequency of the phenomena ω is available and can be used to evaluate the needed time step for transient CFD simulations needed for validation.

However, for SMR (prototype) Strouhal number is not available and sensitivity studies based on the known parameters ($\bar{v}$ and L) and applied mesh size need to be performed to establish an adequate time step for CFD transient runs.

Depending on the process of interest, or portion of the CFD domain of interest, we can have various time and length scales. The time scales can be based on the frequency of the phenomena (such as the vortex shedding frequency $\tau = 1/\omega$), or in some cases, the time step $\tau = \Delta t \leq \Delta x/v$ which is necessary to provide stable calculations (based on the local mesh size Δx and velocity v). In the last example, the reciprocal value of the Strouhal number is the Courant number and the considered control volume is the volume of the computational cell ($1/Sr = C = \frac{v}{\Delta x}\Delta t \leq 1$). Thus, the time steps for CFD calculations need to be established based on the most demanding process of interest (with the highest frequency) and Courant number criteria (see Figure 8 based on [25]).

Figure 8: Finding the right time step – canyon effect (based on [25])

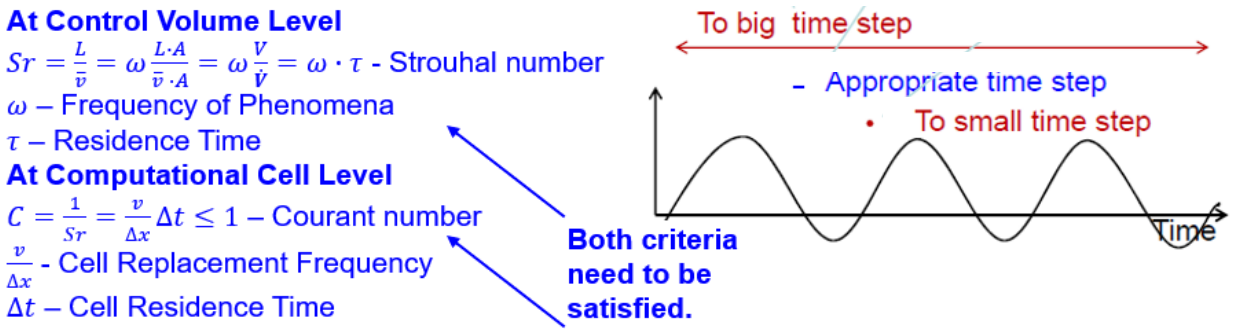

Conclusions

To illustrate the benefits of combining H2TS and FSA scaling analyses methods and CFD comparison of dimensionless numbers derived with a time scaling approach for H2TS, and FSA methods and dimensionless numbers usually used for CFD analysis, based on scaling momentum equations for single-phase flows, is performed in [9, 10].

Some additional dimensional numbers related to the energy equation and boundary conditions are compared in this paper. Also, it presented how scaling analysis can support the choice of CFD domain, mesh size, and distribution and establish needed time steps.

Several additional examples of how scaling analysis can support validation and CFD best practices are presented. Also, it was presented how in some situations validated CFD models, based on the best practices, can support the scaling analysis, and help to interpolate or extrapolate the distorted test results from the scaled facilities to the prototypical conditions.

Acknowledgments

Presented results of validated CFD models include results of multiple years and team efforts of CFD specialists, experimentalists, project managers, and professors at participating universities cited in [20-24], and [37, 38]. Special acknowledgments go to CFD colleagues: Bin Liu for the development of models presented in Figures 1, 2, and 4, Stefano Gallo and Marco Pellegrini, at that time visiting students from the University of Pisa and Politecnico di Milano, respectively, who performed validations presented in Figures 6 and 7. The results presented in Figure 5 are part of the research results funded by DOE NEUP R&D Award CFA17-13179.

References

[1] Buckingham, E., "On physically similar systems; illustrations of the use of dimensional equations," *Phys. Rev.*, Vol. 4, pp.345–376, (1914).

[2] Ruzicka, M.C., "On dimensionless numbers, Chemical Engineering Research and Design," *Chemical Engineering Research and Design*, Vol 86, Issue 8, pp. 835-868, August (2008). https://doi.org/10.1016/j.cherd.2008.03.007

[3] Ishii, M. and Kataoka, I., "Scaling laws for thermal-hydraulic system under single phase and two-phase natural circulation," *Nuclear Engineering and Design*, Vol. 81, pp. 411-425, (1984).

[4] Zuber, N., "Appendix D: A Hierarchical, Two-Tired Scaling Analysis, An Integrated Structure and Scaling Methodology for Severe Accident Technical Issue Resolution," U. S. Nuclear Regulatory Commission, Washington, D.C. 20555, NUREG/CR-5809, November (1991).

[5] Zuber, N., Wilson, G.E., Ishii, M., Wulff, W., Boyack, B.E., Dukler, A.E., Griffith, P., Healzer, J.M., Henry, R.E., Lehner, J.R., Levy, S., Moody, F.J., Pilch, M., Sehgal, B.R., Spencer, B.W., Theofanous, T.G., Valente, J., "An Integrated Structure and Scaling Methodology for Severe Accident Technical Issue Resolution: Development of Methodology," *Nuclear Engineering and Design*, Vol. 186, pp. 1-21, (1998).

[6] Zuber, N., "A general method for scaling and analyzing transport processes," In: Applied Optical Measurements, Eds. Lehner, M., Mewes, D., pp. 421-459, Springer Verlag, New York, USA, (1999).

[7] Zuber, N., Rohatgi, U. S., Wulff, W., Catton, I., "Application of Fractional Scaling Analysis (FSA) to Loss of Coolant Accidents (LOCA) Methodology Development," *Nuclear Engineering and Design*, Vol. 237, pp. 1593 – 1607, (2007). https://doi:10.1016/j.nucengdes.2007.01.017

[8] Bestion, D., D'Auria, F., Lien, P., Nakamura, H., Austregesilo, H., Skorek, T., Bae, B.U., Choi, K.Y., Kim, K.D., Moon, S. K., Martinez-Quiroga, V., Reventos, F., Mascari, F., Schollenberger, S., Umminger, K., Reyes, J.N., Rohatgi, U.S., Wang, W., Zaki, T., "Scaling in system thermal-hydraulics applications to nuclear reactor safety and design: A state-of the-art report," OECD Report NEA/CSNI/R(2016)14, JT03411050, Paris, March (2007).

[9] Dzodzo, M.B., "Scaling and connection with Computational Fluid Dynamics," Specialists Meeting on transient Thermal-Hydraulics in water cooled nuclear reactors (SM-TH), Paper P20, Videoconference hosted by OECD\NEA, March 22-23, (2022).

[10] Dzodzo, M.B., "Scaling and connection with Computational Fluid Dynamics," *Nuclear Engineering and Design*, Vol. 401, 112086, January, (2023). https://doi.org/10.1016/j.nucengdes.2022.112086

[11] Smith, B.L., Andreani, M., Bieder, U., Ducros, F., Graffard, E., Heitsch, M., Henriksson, M., Höhne, T., Houkema, M., Komen, E., Mahaffy, J., Menter, F., Moretti, F., Morii, T., Mühlbauer, P., Rohde, U., Scheuerer, M., Song, C.H., Watanabe, T., Zigh, G., "Assessment of CFD codes for nuclear reactor safety problems – Revision 2," OECD Report NEA/CSNI/R(2014)12, January (2015).

[12] Mahaffy, J., Chung, B., Dubois, F., Ducros, F., Graffard, E., Heitsch, M., Henriksson, M., Komen, E., Moretti, F., Morii, T., Mühlbauer, P., Rohde, U., Scheuerer, M., Smith, B.L., Song, C., Watanabe, T., Zigh, G., "Best practice guidelines for the use of CFD in nuclear reactor safety applications - Revision," OECD Report NEA/CSNI/R(2014)11, February (2015).

[13] D'Auria, F. and Galassi, G.M., "Scaling in nuclear reactor system thermal-hydraulics," *Nuclear Engineering and Design,* Vol. 240, pp. 3267-3293, (2010). https://doi.org/10.1016/j.nucengdes.2010.06.010

[14] Bestion, D., "Multiscale simulation of light water reactor thermalhydraulics," M&C 2017 - International Conference on Mathematics & Computational Methods Applied to Nuclear Science & Engineering, Jeju, Korea, April 16-20, (2017).

[15] Yeoh, G.H., "Thermal hydraulic considerations of nuclear reactor systems: Past, present and future challenges," *Experimental and Computational Multiphase Flow*, Vol. 1, No. 1, pp. 3–27, (2019). https://doi.org/10.1007/s42757-019-0002-5

[16] Date, A.W., "Some Observations on Thermodynamic Basis of Pressure Continuum Condition and Consequences of Its Violation in Discretised CFD," In: Runchal A. (eds) 50 Years of CFD

in Engineering Sciences, Springer, Singapore, (2020). https://doi.org/10.1007/978-981-15-2670-1_2

[17] Dzodzo, M.B., "Examples of Decompositions for Time and Space Domains and Discretization of Equations for General Purpose Computational Fluid Dynamics Programs and Historical Perspective of Some Key Developments," In: Runchal A. (eds) 50 Years of CFD in Engineering Sciences, Springer, Singapore, (2020). https://doi.org/10.1007/978-981-15-2670-1_4

[18] ASME, "ASME V&V 20 – 2009 Standard for verification and validation in computational fluid dynamics and heat transfer," (2009).

[19] Nahavandi, A.N., Castellana, F.S., Moradkhanian, E.A., "Scaling Laws for Modeling Nuclear Reactor Systems," *Nuclear Science and Engineering*, Vol. 72, pp.75-83, (1979). https://doi.org/10.13182/NSE79-A19310

[20] Smith, L.D., Conner, M.E., Liu, B., Dzodzo, M.B., Paramonov, D.V., Beasley, D.E., Langford, H.M., Holloway, M.V., "Benchmarking computational fluid dynamics for application to PWR fuel," 10th International Conference on Nuclear Engineering, vol. 3, Paper No. ICONE10-22475, pp. 823-830, Arlington, VA, USA, April 14-18, (2002). https://doi.org/10.1115/icone10-22475

[21] Conner, M.E, Baglietto, E., Elmahdi, A.E., "CFD methodology and validation for single phase flow in PWR fuel assemblies," *Nuclear Engineering and Design,* Vol. 240, Issue 9, pp. 2088-2095, September (2010). doi.org/10.1016/j.nucengdes.2009.11.031

[22] Langford, H. M., Armfield, M. V., Beasley, D. E., and Conner, M. E., "Particle Image Velocimetry of Swirling Flow in a Subchannel of a Rod Bundle," Proceedings of the 2001 ASME FED Summer Meeting, (2001).

[23] Armfield, M.V., Langford, H.M., Beasley, D.E., and Conner, M.E., "Single-Phase Turbulent Rod Bundle Heat Transfer," Proceedings of 2001 ASME IMECE Meeting, (2001).

[24] Liu, B., Smith, III, L.D., Conner M.E., Dzodzo M.B., Paramonov D.V., Karoutas Z.E., Knott R.P., and Young M.Y., "CFD Approach for Investigating Flow and Heat Transfer in PWR Fuel Assembly," 13th International Conference on Nuclear Engineering, ICONE13-50924, Beijing, China, May 16-20, (2005).

[25] Dzodzo, M.B., "Examples of Computational Fluid Dynamics Models for Nuclear Industry Applications," Invited Presentation on 8th International Symposium on Advances in Computational Heat Transfer – CHT-21, Session in honor of Brian Spalding, Rio De Janeiro, Brazil, Virtual Meeting, August 15, (2021).

[26] Dos Santos, A., Childs, M., Nguyen, T., Hassan, Y., "Convergence study and uncertainty quantification of average and statistical PIV measurements in a matched refractive index 5× 5 rod bundle with mixing vane spacer grid," *Experimental Thermal and Fluid Science*, Vol. 102, pp. 215-231, (2019). doi.org/10.1016/j.expthermflusci.2018.11.009

[27] Merzari, E., Fischer, P., Min, M., Kerkemeier, S., Obabko, A., Shaver, D., Yuan, H., Yu, Y., Martinez, J., Brockmeyer, L., Fick, L., Busco, G., Yildiz, A., & Hassan, Y., "Toward exascale: overview of large eddy simulations and direct numerical simulations of nuclear reactor flows with the spectral element method in Nek5000," *Nuclear Technology*, Vol. 206, no. 9, pp. 1308-1324, (2020). doi.org/10.1080/00295450.2020.1748557

[28] Joffre, P.F., Karoutas, Z.E., "Impact of support plate flow jets on rod vibration for inlet flow region," 14th International Conference on Nuclear Engineering, ICONE14-89325, Miami, Florida, July 17-20, (2006).

[29] Karoutas, Z., Liu, B., Dzodzo, M.B., Joffre P.F., "Comparison of CFD model velocity profiles to test data for inlet nozzle region of nuclear PWR fuel assemblies," Proceedings of ICONE 14, 14th International Conference on Nuclear Engineering, ICONE14-89322, Miami, Florida, July 17-20, (2006).

[30] Dzodzo, M.B., "Examples of Modeling Conjugate Heat Transfer with CFX Commercial CFD Code," Invited Presentation at ASME 2017 IMECE - International Mechanical Engineering Congress & Exposition Tampa, Florida, USA, November 3 – 9, 2017, 9-6-1 Panel: Heat Transfer and Fluid Roundtable: Navigating the code landscape, November 8th, (2017).

[31] Dzodzo, M.B., "Computational fluid dynamics simulation of mixed convection heat transfer to liquid metals in a vertical pipe," 29th International Conference on Nuclear Engineering, Paper No. ICONE 29-94479, August 8-12, Published Online: November 23, (2022). https://doi.org/10.1115/ICONE29-94479

[32] Cuckovic-Dzodzo, D.M., Dzodzo, M.B., Pavlovic, M.D., "Laminar natural convection in a fully partitioned enclosure containing fluid with nonlinear thermophysical properties," *Int. J. of Heat and Fluid Flow*, Vol. 20, pp. 614-623, (1999). doi.org/10.1016/S0142-727X(99)00053-3

[33] Dzodzo, M.B., "Natural and mixed convection in enclosures containing liquid metals and partition walls," In Silva Freire, A.P., Hanjalic, K., Suga, K., Borello, D., Haziabdic, M., Eds., "Turbulence, Heat and Mass Transfer 9," Proceedings of the Ninth International Symposium On Turbulence, Heat and Mass Transfer, pp. 327-330, Rio de Janeiro, Brazil, Begel House Inc., New York, Wallingford, UK., 10-13 July, (2018). http://dx.doi.org/10.1615/TFEC2019.fnd.028098

[34] Dzodzo, M.B., "Natural and mixed convection in rectangular enclosures and channels containing liquid metals and partition walls," 4th Thermal and Fluids Engineering Conference (TFEC), TFEC-2019-28098, pp. 1103-1106, Las Vegas, NV, USA, April 14–17, (2019). http://dx.doi.org/10.1615/TFEC2019.fnd.028098

[35] Kunz, R.F., D'Amico, S.W., Vassallo, P.F., Zaccaria, M.A., "LDV Measurement of Confined Parallel Jet Mixing," *J. of Fluids Engineering*, Vol. 123, pp. 567-573. September, (2001).

[36] Bunderson, N.E., Smith, B.L., "Passive mixing control of plane parallel jets," *Experiments in Fluids*, Vol. 39, pp.66-74 (2005).

[37] Gallo, S., Pasquini, M.E., Simonini, G., Ambrosini, W., Forgione, N., Oriolo, F., Dzodzo, M., "CFD Evaluation of the Parallel Jet Mixing Phenomena in the IRIS Downcomer," NURETH-13, N13P1386, Kanazawa City, Japan, September 27 – October 2, (2009).

[38] Pellegrini, M., Colombo, E., Inzoli, F., Dzodzo, M., "Unsteady CFD Analysis of Parallel Jet Mixing as a Support of the IRIS Steam Generator Outlet Design," NURETH-13, N13P1378, Kanazawa City, Japan, September 27 – October 2, (2009).

LARGE EDDY SIMULATIONS OF FLUID-STRUCTURE INTERACTION OF TWO IN-LINE CYLINDERS IN A TURBULENT FLOW

Pierre-Emmanuel Angeli, Maria Adela Puscas

Service de Thermohydraulique et de Mécanique des Fluides, CEA, Université Paris-Saclay, Gif-sur-Yvette F-91191, France

Extended abstract

This work reports the numerical results obtained by the CEA with the in-house CFD software TrioCFD within the framework of the OECD/NEA Fluid-Structure Interaction benchmark. The experimental facility was operated by OKBM Afrikantov. It consisted of two in-line cylinders with a fixed and a free end placed in a thin channel and subjected to vibrations under the effect of a turbulent flow. The simulations focused on the open-test case corresponding to the lowest flow rate and out of the lock-in mode.

The Large Eddy Simulation approach is used along with the WALE subgrid-scale model with a boundary layer discretization fine enough to exclude the use of wall functions. Three kinds of calculations are considered: first, a simulation with fixed cylinders; second, a primary one-way coupling with imposed displacement on the cylinders; and third, a more realistic two-way coupling.

The first case is used to conduct a sensitivity analysis of the mesh size using two tetrahedral meshes containing respectively 16 and 85 million elements, corresponding to about half the number of degrees of freedom in the numerical method of the finite-volume element employed. The inlet boundary condition is carefully selected in order to conform as much as possible to the experimental conditions. In the test section, the flow goes through a grid downstream the cylinders region, which creates a homogeneous and isotropic turbulent state. Such conditions are numerically reproduced by means of a synthetic turbulence generation method whose parameters, such as the turbulent kinetic energy and turbulent dissipation rate, were preliminarily estimated with a RANS simulation. The average and RMS velocity profiles downstream of the first cylinder are found to be in good agreement with the experiment, confirming the relevance of the inlet boundary condition used, and excluding possible uncertainties associated with the flow structure at the inlet. The coarsest mesh reveals a strong numerical diffusivity, with velocity profiles appearing more flat behind the cylinders compared to the experimental measurements. In contrast, the finest mesh shows a significant improvement with the velocity profiles matching very well to the experimental points, both for the average and the RMS values.

In the one-way coupling, a small harmonic displacement corresponding to a vibration mode of a clamped-free Euler-Bernoulli beam is imposed on the cylinders. TrioCFD employs an Arbitrary Lagrange-Eulerian method to solve fluid-structure interaction problems involving moving boundaries. In the two-way coupling strategy, a reduced Euler-Bernoulli beam model is coupled to the fluid software by using a partitioned time marching algorithm. We use an explicit conventional serial staggered approach for temporal discretization.

The simulations with the one-way and two-way coupling methods are currently underway, and results are still pending at the time of the writing of the present abstract. The average and RMS velocities resulting numerically from these three methods will be compared to each other and to the experiment. Moreover, the spectra of velocity, pressure, and cylinder acceleration pulsations at given points will be compared to that recorded experimentally.

VALIDATION OF MULTI-PHASE-CFD FRAMEWORKS FOR NATURAL CIRCULATION IN ADVANCED REACTORS

Brandon Aranda, Koroush Shirvan, Emilio Baglietto

Massachusetts Institute of Technology, Department of Nuclear Science and Engineering

Abstract

With the development of advanced nuclear reactors, there has been an increasing need for multi-phase CFD to model the two-phase flow interactions that are critical for the safety and performance of the reactors. However, multi-phase CFD has only widely been applied to low void fraction flows in small geometry applications. At higher void fraction multiphase flows present in reactors, complex interactions occur that make their modeling challenging. These interactions can be dependent on the scale of the geometry which introduces uncertainties for large-scale applications. This is especially challenging when a range of flow regimes must be modeled in reactors such as churn-turbulent flow, annular flow, and mist flow as they encompass a wide range of interaction length scales. Hybrid models are attractive for such conditions as they resolve large structures using interface capturing methods (commonly VOF) while modeling dispersed structures with mixture approaches adding slip correlations or the Eulerian framework. Many hybrid models have been developed recently using different techniques such as population balance approaches and flow regime maps to capture the transition from dispersed phase treatment to segregated flow structure treatment. Rigorous validation of the separate models is essential to their advancement and use in hybrid models to extend their application past simple bubbly flows in large nuclear reactor components. In this work, the VOF method and a hybrid mixture-multiphase framework with large-scale interface capturing (MMP-LSI) methods are validated against experiments performed at the TOPFLOW and HUSTLE facilities. These facilities resemble the two-phase conditions of recent Small Modular light water reactor designs. An Eulerian framework was implemented as well to obtain baseline results for comparison as this framework has had a large focus and validation on the models for various applications. This work's objective is to assess the model performance consistently at different mesh resolutions and support future hybrid adoption. The two-phase flow dynamics are analyzed to assess the capability of these models to correctly represent the interactions and determine which models have the largest shortcomings. The results show that, on sufficiently resolved meshes, void fraction profiles are well predicted by the VOF method for the conditions of the TOPFLOW experiment, while also showing good resolution of the shape and distribution of the large gas structures. However, when applied to the mist flow conditions of the HUSTLE facility where the meshes implemented were insufficient to capture many of the fluid structures, the void fraction profiles deviate from the experimental results and do not show sufficient grid convergence, especially in the near wall regions. The MMP-LSI method is still challenged in these applications since its inability to resolve smaller structures leads to larger errors than the VOF method. The Eulerian framework, while able to obtain reasonable estimates for the magnitude of the void fraction, was unable to produce the correct radial distribution of the void fraction obtained in the experiments. This was shown to be due to the lack of interfacial momentum closures that are available to model the interactions that occur at higher void

fractions. Further work is needed to develop models that can model these interactions to allow for their implementation in hybrid models.

VALIDATION OF FUEL ASSEMBLY CFD MODELS USING MAGNETIC RESONANCE VELOCIMETRY AND TURBULENCE MEASUREMENTS FOR 5 X 5 SWIRL TYPE MIXING VANE CONFIGURATION

Martin Bruschewski[1], Kristine John[1], Sven Grundmann[1], Markus Rehm[2], Hidajet Hadžić[2], Peter Pohl[2]

[1]Institute of Fluid Mechanics, University of Rostock, Albert-Einstein-Straße 2, 18059 Rostock, Germany
[2]Framatome GmbH, Paul-Gossen-Str. 100, 91052 Erlangen Germany

The objective of this study is to use Computational Fluid Dynamics (CFD)-grade experimental flow data in models of nuclear fuel assemblies with single-phase isothermal fluid to validate and improve current CFD modelling capabilities. The experiments provide the 3-Dimensional 3-Components (3D3C) mean velocity field for a full span of a fuel bundle with mixing grid in the entire flow domain for the full-field validation of CFD, especially for nuclear reactor safety studies. Furthermore, 2D6C Reynolds stress tensor measurements were also performed at different distances to the spacer grid.

The measurement technique used in the validation data is Magnetic Resonance Velocimetry (MRV), which is based on the medical imaging modality Magnetic Resonance Imaging (MRI). Since MRV requires no optical access, the entire flow structure, including all boundary layers, can be captured within the discretization limits of the measurement resolution. MRV is suitable for measurements in extremely complex flow geometries, such as models of densely packed fuel assemblies. Because optical quality is not required, MRV-compatible models are comparatively inexpensive and quickly built.

The investigated fuel bundle corresponds to the OECD/NEA–KAERI CFD benchmark exercise 5x5 test configuration with swirling vane type[1]. A significant improvement in terms of reaching reactor-realistic Reynolds number in MRV-compatible fuel bundle replicas has been achieved at the Institute of Fluid Mechanics at the University of Rostock. A state-of-the-art MRI scanner is integrated into a unique laboratory, specifically designed for fluid mechanics experiments with high volumetric flow rates. The replica was made of MRI-compatible materials Polyamide (PA) and Polyoxymethylene (POM). The Reynolds number in this test is around 50k based on the average axial velocity and the hydraulic diameter within the bundle. The 3D mean velocity field was measured at an isotropic resolution of 0.8 mm.

In a first step the MRV data is compared against Laser Doppler Anemometry (LDA) measurement data. The agreement between both measurement results demonstrates that MRV is capable of acquiring accurate mean velocity data. In a second step CFD results of the MRV compatible fuel assembly are presented and discussed. The 3D MRV measurements allows for a direct comparison of the two data sets, enabling a full-field validation of the numerical solution. The results of this studies show, that MRV measurements can greatly contribute to improve CFD validation for nuclear safety analysis and fuel assembly design optimization.

[1] https://doi.org/10.1016/j.nucengdes.2014.05.013

MODELLING JOULE HEATING FOR CFD VALIDATION OF SUPERCRITICAL HEAT TRANSFER

Kwun Ting Lau, Song Ni, Jiyun Zhao

Department of Mechanical Engineering, City University of Hong Kong, Hong Kong SAR

Extended abstract

As greenhouse gas emissions continue to increase, governments have collaborated to reduce the emissions despite the escalating energy demand. In this climate, there are six new types of Generation IV nuclear reactors undergoing extensive research. For Supercritical Water Reactor, supercritical water is used directly as the coolant. Regrettably, the Deteriorated Heat Transfer (DHT) phenomenon was discovered for supercritical heat transfer. When DHT is present, the wall temperature peaks may exceed the safety limit of the nuclear core and pipe's material, thereby posing a grave threat to the safety of nuclear powerplants. The mechanism of DHT is generally categorized into buoyancy-induced laminarization and acceleration-induced laminarization. In this study, however, we hypothesize that in addition to the laminarization phenomenon, the DHT observed in the experiment may also be affected by the Joule heating effect.

Joule heating effect is commonly utilized in thermal hydraulics experiments. Joule's law is proposed to quantitatively describe the relationship between the power of heat generation (P), the current (I) and wire resistance (R).

$$P = I^2 \times R$$

However, the electrical resistivity of the electric conductor materials, which are typically metal, is temperature-dependent. That means the local power generated is dependent on both the electrical resistivity of the material and the local wall temperature. When DHT occurs, a temperature spike can be observed on the wall, ranging from a few °C to over 100 °C. Local temperature variations coupled with temperature-dependent electrical resistivity can result in large local heat flux variations. Unfortunately, the majority of boundary conditions for CFD validation are set to the simplified constant heat flux.

The originality of this work resides in the replication of the heat flux profile in experiments for CFD validation. To mimic the experimental heat flux profile, a new approach is suggested, with the use of resistivity-temperature correlation, Piecewise Cubic Hermite Interpolating Polynomial (PCHIP) functions and Joule's Law. By using the resistivity-temperature correlation and wall temperature profile, the electrical resistivity profile is estimated. The electrical resistivity profile is modelled by PCHIP functions, and by numerical integration, the total resistance of the tube is approximated. On the other hand, with the known experiment power supply, Joule's Law is used to calculate the root means square current through the annular tube. With the resistivity equation, discrete local heat flux can be calculated. The heat flux profile along the heated surface is consequently modelled by PCHIP functions.

Joule heating heat flux profile of upward supercritical water heat transfer in the annular tube is therefore modelled and applied as the boundary condition. Wall temperature profile is calculated with FLUENT 21 using the Shear Stress Transport k-ω turbulence model and compared to the Razumovskiy et al. (2015) experiment dataset. The calculated 3D wall temperature contour is reduced to a 2D wall temperature profile by cross-sectional arithmetic, area-weighted, volume-weighted and mass-weighted averaging methods respectively.

It is discovered that by using the PCHIP-modelled Joule heating profiles with the volume-weighted averaging method, the estimated wall temperature for both the Normal Heat Transfer (NHT) and DHT regimes is comparable to the experiment in terms of trend and magnitude, falling within the experimental error margin of ± 3.2%. However, by using the conventional constant heat flux profiles with the volume-weighted averaging method, the upstream and downstream wall temperatures are overestimated and underestimated respectively. Although the predicted temperature is still within the error limit of ± 3.2% in the NHT regime, it exceeds the error margin under the DHT regime. This study demonstrated that the experimental heat flux conditions can be adequately replicated and applied, hence improving CFD estimates of supercritical heat transfer, particularly for the DHT, which has a substantial heat flux variation.

USE OF HOLISITC CFD MODEL EVALUATION TO DEMONSTRATE CONFIDENCE IN INDUSTRY APPLICATIONS OF CFD

Joe Hegarty, Sophie Brown, Heather Davies, Ryan Tunstall

Rolls-Royce, Kings Place, 90 York Way, London, N1 9FX, United Kingdom

Extended Abstract

High quality CFD assessments have an increasingly important role in engineering substantiation, as they are able to provide detailed physical insights and levels of realism beyond the capabilities of lower fidelity methods. Here, effective use of CFD provides opportunities to realise a wide range of industrial benefits including increased plant and component lifetimes, improvements in passive safety, and the implementation of manufacturing efficiencies.

The key challenge in using CFD analyses to support safety claims and design decisions is demonstrating sufficient confidence that the predictions are adequately representative of reality for their intended purpose. Emphasis is often focused on comparisons of CFD predictions against physical measurements and testing. Typical operating conditions are at high temperatures and pressures making them challenging from a measurement perspective, and this issue is amplified for complex geometries. CFD is often employed because it is impractical or even impossible to directly obtain the required information using physical measurements. Good CFD validation requires high-resolution, high-accuracy reference data, ideally with well-quantified uncertainties. The data requirements for good CFD validation using physical experiments and the prototypic conditions of interest are often antithetical to each other in practice. Overall, in many cases it will be impractical if not impossible to demonstrate confidence in CFD predictions by direct comparisons to physical measurements in prototypic geometries at prototypic conditions.

An alternative approach is to focus on validating key physical phenomena and effects, with geometries and flow conditions being non-prototypic but exhibiting physics of interest and being amenable to the collection of CFD validation data. The different levels of validation used to support a CFD study can be placed into a hierarchy or pyramid, as shown in Figure 1. The categories from base upwards are as follows:

Validation of physical phenomena: This may come from academic experiments and test case comparisons; specifically designed to demonstrate that a model can adequately represent a specific physical phenomenon in a flow.

Generic validation: This is where test cases with particular geometries, flow, or heat transfer regimes of engineering interest are modelled. Each of the cases are independent from one another, they are used to model individual effects and phenomena. These test cases are not used to estimate uncertainty, and as such can involve very different geometries and flow conditions to those found in prototypic applications of interest.

Component level validation: Comparing CFD predictions of a specific parameter to component or experimental data. By using component data the need for bespoke rigs can be sidestepped. Overall, this validation type can be used to explicitly determine the uncertainty in model predictions.

Subsystem validation: Used where experiments of the entire complex system may be impossible. This will often require the design of a bespoke rig with flow parameters being as close as possible to those of interest.

System validation: Due to the inherent complexities at the level of systems (such as multiple flow and heat transfer regimes, multiple sources of error) this often requires the use of several pieces of validation evidence from lower levels of the pyramid.

Figure 1: Validation Pyramid for CFD Models

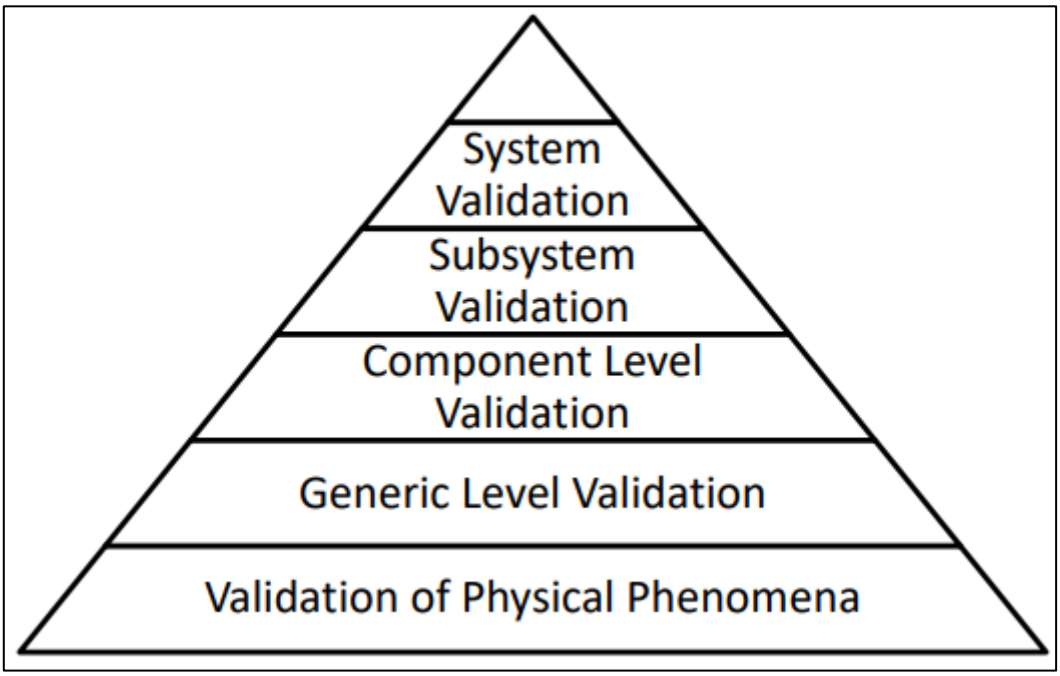

Not every application will require validation at the system level. It is dependent on the case and what the CFD assessment is required to prove or demonstrate. Assessments at higher levels of the pyramid will use validation cases from lower levels.

By generating a library of such validation cases, confidence in CFD modelling can be built up in stages. However, there will then be inevitable differences between applications and their supporting validation cases, and thus a more holistic approach to robustly substantiate CFD is required.

Holistic CFD model evaluation (Reference 1) is a framework that has been adopted and continuously improved by Rolls-Royce to demonstrate and justify that there is sufficient confidence a particular CFD model for its intended purpose. It is not a precise or exhaustive framework given the high range of potential applications and uses of CFD results, but at a high level can be simplified into four broad steps:

Physical Description: Justifying that the geometry, boundary conditions, initial conditions, and material and fluid properties have been considered and chosen appropriately within the context of the problem.

Model Selection: Ensuring the CFD model is configured in such a way that it has the theoretical capabilities needed to predict the physics involved in a problem to sufficient detail and resolution.

Solution Procedure: Ensuring convergence, correct extraction of required information, and that the solution appears physically credible through inspection and expert elicitation.

Sensitivity Studies and Validation: Sensitivity studies are used to understand and, where possible and appropriate, quantify the impact of key modelling decisions or uncertainties in model inputs on predictions. Validation typically involves separate effects tests to demonstrate that the modelling approach can adequately represent key phenomena, supported by other tests where appropriate. This

step provides confidence that modelling choices and assumptions are appropriate, and demonstrates that there is no evidence to undermine the credibility of the approach.

This framework can be applied to a wide range of cases. For example, the following demonstrates some of the salient points (in addition to the general point covered above) relevant to the specific example of modelling a thermal transient passing through a hypothetical valve:

Physical Description: One aspect here is how will any approximations of the geometry impact the results? Depending on the internals and inlet conditions can the geometry be modelled with symmetry planes, or does it need to be modelled entirely? It could for example be possible that due to the complexity of the internals of a valve's body, the flow would be asymmetric and thus symmetry planes can't be used. It might be unlikely that flow paths would interact with certain external surfaces of the valve body and as such these might be more justifiable as being simplified to save computational cost.

What are the initial and inlet conditions to be applied, if they are from an external source are they likely to be conservative? If there are unknowns, then initial and inlet condition sensitivity studies would be required later.

What other physics will be relevant at the model boundaries? For example, will the model's external surfaces be adiabatic or do heat losses need to be accounted for? A further point is whether fluid inlets and outlets have been located sufficiently far from the region of interest so as to not unphysically affect results.

Through answering these and other questions, the CFD model can be set up in a way that has the potential to reflect the physical reality without introducing any significant optimisms.

Model Selection: What kind of turbulence modelling is required, are higher-fidelity models such as Large Eddy Simulation (LES) needed or is a lower-fidelity approach suitable? If lower-fidelity approaches such as Unsteady Reynolds Averaged Navier Stokes (URANS) are used what turbulence modelling is most suitable? In this example the temperature of the fluid will change over time, thus internal heat transfer must be modelled, and the effects of buoyancy should be considered; appropriate models must be used that account for this. A library of more than thirty validation cases has been generated to support holistic CFD model evaluation, the findings of which and other previous experience are useful in informing model selection decisions.

A more specific point in this example would relate to the inlet conditions changing over time, including the flow switching directions. The model must therefore be capable of modelling this direction change by changing boundary condition types mid-simulation.

As a result of the above and consideration of further points within this step, the CFD model should have the theoretical capabilities to predict the inherent physics to sufficient detail and resolution.

Solution Procedure: One important aspect of this is ensuring a code that meets industry standard requirements, such as the ASME Nuclear Quality Assurance Certification Program, is used and that its installation has been properly verified. Key imposed parameters such as the inlet conditions, other boundary conditions and time step size should be monitored at multiple locations, and compared to expected values. This helps verify that key inputs to the model are set as intended. It is also necessary to assess numerical convergence, which typically involves monitoring residuals and the evolution of predicted quantities at key locations.

For each run results should be reviewed and technically checked. Credibility can be ensured through visualisation, checking of the results compared to previous cases, and spot-checks across the model. At Rolls-Royce we have developed a specific model review process that we apply to each simulation, this will be outlined briefly in the presentation.

Proper evaluation of this step ensures that the solutions are converged and that the results are judged to be credible.

Sensitivity Studies and Validation: Some of the key sensitivity studies to be completed for this example would include mesh resolution, inlet conditions such as the velocity profile and assumed turbulence levels, and the time step size. These would demonstrate the impact of key modelling decisions and assumptions, and quantify the associated uncertainties. It can also be useful to perform sensitivity studies which verify that simulation results respond to changes in inputs in a way that is consistent with physical understanding.

Validation would firstly involve reviewing previous validation cases and using their findings to construct support arguments. Consideration should then be given as to whether previous validation cases have shown that the employed modelling approach is able to suitably predict the relevant inherent and underlying physics, and whether further validation cases need to be completed to have sufficient confidence in the results for their intended use.

The sensitivity studies and validation cases combine to provide confidence in the results and demonstrate that there is no evidence to undermine the credibility of the approach.

The framework outlined above has been used to justify the use of CFD models which have supported safety cases, informed design justifications, and reduced pessimisms in other analyses. The success of using this framework has led to greater confidence and usage of CFD within the company.

The presentation will further describe the challenges of taking credit for CFD and the practicalities of using holistic CFD model evaluation in this context. It will discuss the above scenario in more detail, going through each step of the model's holistic evaluation and demonstrating how confidence is provided at each stage.

References

1. C. Boyd, "Computational Fluid Dynamics for Nuclear Systems", Office of Nuclear Regulatory Research, U.S. Nuclear Regulatory Commission. Available online: https://www.nrc.gov/docs/ML1125/ML112570022.pdf, last accessed 22/01/2021.

U.S.NRC
United States Nuclear Regulatory Commission
Protecting People and the Environment

Center for Advanced Small Modular and Micro Nuclear Reactors
Texas A&M Engineering Experiment Station

NEA
NUCLEAR ENERGY AGENCY

Technical Session 10 –

Severe Accident

Feb 21, 14:00-15:30, Room B.

VERIFICATION & VALIDATION OF MULTI-PHYSICAL BEHAVIOR IN HIGH-TEMPERATURE GAS-COOLED REACTOR

Avadhesh Kumar Sharma[a], Wataru Sagawa[a], Yosuke Nishimura[b], Koji Okamoto[a,b]

[a]*Nuclear Professional School, The University of Tokyo, 2-22 Shirakata, Tokai-mura, Naka-gun, Ibaraki, 319-1188, Japan*

[b]*Department of Nuclear Engineering and Management, The University of Tokyo, 7-3-1 Hongo, Bunkyo, Tokyo, Japan*

Extended Abstract

High-temperature gas-cooled reactors (HTGR) have inherent safety features for nuclear accidents. These reactors use graphite as moderator and structure material, and helium gas as a coolant. These can operate at very high temperatures without reacting or deteriorating. It has been accepted by the scientific community that HTGR reactors are not susceptible to core melting accidents, therefore do not require complex emergency core cooling systems to ensure plant safety. At present, the most critical accident for HTGR design is air ingress, which is caused by the guillotine-type break of the main coolant pipe [1-2]. This air reacts with hot graphite at elevated temperatures and results in several types of exothermic and endothermic reactions that cause mechanical degradation of graphite structures and accumulation of explosive CO and CO_2 gases in the reactor. SiC has good resistive properties against oxidation compared to graphite, and graphite compact can be replaced with the SiC compact. However, based on temperature and partial oxygen pressure, SiC may also have passive and active oxidation. Since SiC also reacts with oxygen, it is essential to confirm the safety in the event of an air intrusion accident, which should be considered in a high-temperature gas reactor.

The preliminary experiments are performed at different oxygen concentrations. The objective of these experiments is to understand the thermal and oxidation behavior of SiC and use this data to develop a numerical model. The sealed chamber is filled with argon for providing an inert atmosphere. The IG-110 graphite specimen (denoted as inner graphite) is machined into a cylindrical shape. To install the electrodes, cone-shaped holes are drilled on both the top side and bottom sides of the inner graphite. A SiC tube is placed outside the inner graphite. Furthermore, a graphite tube (denoted as outer graphite) of the same length is placed outside the SiC tube to estimate the thermal energy radiated from the SiC surface and provide a stable gas flow boundary during the oxidation experiment. The inner graphite, SiC tube, and outer graphite are sandwiched between two ceramic isolation plates. The weight and dimension of the SiC test specimen are measured before and after the experiments.

The CFD simulation of thermal balance analysis of inner graphite, SiC tube, and outer graphite during Argon gas injection is performed using STAR-CCM+ commercial software. Two simulation cases are performed; one at 950 ˚C and the other at 1100 ˚C. The Argon gas flow in the annulus region is assumed steady and laminar. The laminar model, segregated flow, and segregated fluid temperature were used for the gas phase. For the solid domain, segregated solid energy and S2S (surface-to-surface) radiation models were used. A comparison between the numerically simulated temperatures and experimentally measured temperatures is carried out. We could also predict the temperature of the SiC surface which couldn't measure during the experiments due to the machining limitations of the SiC surface.

References

1. Hishida M., Fumizawa M., Takeda T., Ogawa M., Takenaka S., Researches on air ingress accidents of the HTTR, Nuclear engineering and design, 1993, 144(2): 317-325.

2. Ogawa M., Mass transfer with graphite oxidation in gas mixture laminar flow through circular tube, Nippon Genshiryoku Gakkai-Shi, 1993, 35(3): 245-252.

FLOW PHYSICS OF SINGLE AND TWO VIBRATING HEATED CYLINDERS

Muhammad Ansab Ali[1], Imran Afgan[2,1], Yacine Addad[2,3], Dominique Laurence[1]

[1]Department of MACE, School of Engineering, University of Manchester, Manchester, M13 9Pl, UK
[2]College of Engineering, Khalifa Univeristy, P.O. Box 127788, UAE
[3]Emirates Nuclear Technology Center, Khalifa University, PO BOX 127788, Abu Dhabi, UAE

Extended Abstract

Coherent structures generally exist in the wake of the flow past bluff bodies. The fluid structure interaction (FSI) of these coherent structures exhibits promising effects such as enhanced flow mixing along with undesirable features like oscillating drag forces. In the literature, these conflicting effects have been explicitly analyzed based on applications, for instance, enhanced flow mixing for heat transfer augmentation and reduction of vibrations in civil engineering applications. Yet, fewer studies in the literature have investigated the interaction of vibrations with heat transfer despite the fact that such scenarios are quite common in many thermal engineering equipment for example power plants tubes, heat exchangers and nuclear fuel rods.

The present study aims to systematically analyze in detail the flow characteristics of freely vibrating single and two cylinders in cross flow that mimic the actual FSI in the aforementioned applications. Both transverse and inline degree of freedom vortex induced vibrations (VIV) are investigated in this study for a rigid heated cylinder for a range of reduced velocities and mass ratios at laminar and subcritical Reynolds number. The FSI is modelled using partitioned approach in an arbitrary Lagrangian-Eulerian (ALE) description whereas the VIV response of the system is modelled using spring damper system. Unsteady Reynolds-Averaged Navier–Stokes (URANS) simulations are performed using two eddy-viscosity URANS models (k-ω-SST and φ-model) and Reynolds-stress model (LRR). Validation and comparisons are drawn against experimental measurement in terms of non-dimensional parameters namely Nusselt number, vibration response, coefficient of pressure, skin friction coefficient, lift and drag coefficient. Moreover, flow physics past the cylinders is analyzed to elucidate the variations in amplitude responses. The best practice guidelines for the numerical simulation are adopted to minimize the validation uncertainty in the simulations. The numerical methodology is corroborated with the benchmark cases in the literature and all presented results for both the stationery and VIV cases are grid independent solutions.

In case of a single cylinder, in laminar regime, the results indicate that two single vortex shedding pattern and figure-eight sort of motion trajectories are exhibited in the range of reduced velocities analyzed. The highest enhancement in heat transfer is observed in the post lock in region yielding up to 5% increase in Nusselt number compared to stationary cylinder. However, for the sub-critical range for the single cylinder, at Re=3900, the eddy viscosity models due to their inherit limitations, lag in capturing the peak amplitude response compared to Reynolds-stress model. The heat transfer enhancement ranging from (3% to 7%) is observed in different amplitude branches compared to the stationary cylinder. On the other hand, for the two-cylinder cases, simulations are performed for a gap ratio between in the range 2.0–5.0. Based on preliminary results, for small gap ratios (<2.4), the proximity interference significantly affects the fluid forces, heat transfer and vibrations amplitudes. However, for higher gap ratio (>3.5), the response seemed to be similar to isolated cylinder. However, for the intermediate gap ratio (2.4-3.5), an asymmetric vibration response is observed.

SIMULATION OF HYDROGEN RISK ANALYSIS DURING SEVERE ACCIDENT IN A NUCLEAR POWER PLANT USING CFD CODE

Amponsah Joseph[1]

[1]Mechanical Engineering Department & Nuclear Scientist at Cape Coast Technical University

Abstract

In light-water nuclear reactors, hydrogen is susceptible to large quantity release during zirconium-water interaction after a serious accident resulting in a potential compromise of the containment process integrity. A direct consequence of this is the combustion hazards posed by the nuclear facility which could potentially lead to the failure of infrastructure nearby. To mitigate this, several European countries have adopted the use of passive autocatalytic recombiners to reduce the risk of gas explosions (PARs). Investigation of failure scenarios demonstrates that it is challenging to always avoid the production of a flammable combination that may otherwise result in a local flame explosion, even when PARs are installed. In this paper, hydrogen generation and distribution concentration in a 1000MWe nuclear power plant was numerically investigated using the commercial CFD code, ANSYS CFX. The effect of using passive autocatalytic recombiners (PARs) as a mitigation system, was evaluated by comparing the results with and without the installation of thirty-nine PARs. The expected outcome of this research work was to ensure the volume concentration of hydrogen generated with 100% fuel clad-coolant reaction was distributed in the containment uniformly and that it should not exceed 10% during or after a severe accident. Results indicate that the final hydrogen concentration percentage for the model was 17.85% (mass of 1600 kg) and 9.72% (mass of 440 kg), with and without PARs respectively. Practically, this meets the targets set and this work could inform the evaluation of hydrogen risk and recommendation of mitigation strategies to prevent future accidents.

Keywords: Hydrogen; Risk; Distribution; Combustion; Mitigation; CFD

Using CFD for U-tube Steam-Generator vibrations

Vivaldi, D.[1], Ruyer, P[1].[1]
[1]Institut de Radioprotection et de Sûreté Nucléaire (IRSN), PSN-RES/SEMIA/LSMA, BP3, St Paul-Lez-Durance 13115, France

Abstract

Evaluation of the risk of steam-generator (SG) tube failure induced by high-cycle fatigue resulting from flow-induced vibrations is a safety issue for several nuclear power plant designs. Fluid-elastic instability can be triggered by sufficiently large velocity of the secondary loop water while vaporizing outside of the U-tube bundle. To this concern, the french Institut de Radioprotection et de Sûreté Nucléaire (IRSN) has developed several research activities including CFD approaches. This paper provides an overview of the scientific issues, of the corresponding ongoing works and provides some perspectives.

Component scale numerical simulation tools are currently used for the determination of the tube failure risk in the safety demonstration. The secondary loop fluid flow is modelled as a homogeneous mixture of steam and liquid water across a porous media considering the local inclination of the flow with respect to the bundle. The most critical region can be identified at the top of the U-shape bundle, on the hot-side of the SG, where the steam-liquid water mixture quality is high, leading to large velocities, and where the SG tubes are bended, leading to a predominant cross-flow configuration. The risk of tube failure is then analysed through an uncoupled mechanical analysis, that verifies if the calculated steam-liquid mixture velocity is acceptable, with respect to a criterion specifying the threshold velocity inducing the instability.

The corresponding research program developed at IRSN focuses on several knowledge gaps that lead to the main remaining uncertainties on this issue.

- First, the knowledge of high-quality two-phase flow patterns across a tube bundle in the conditions of interest is still partial. Some data are missing but there are also some inconsistencies between different flow regime maps. The knowledge of the two-phase flow structures and more particularly the frequency of the tube excitation by large bubbles or vapor pockets determines part of the coupling between fluid and structure. To gain in accuracy with respect to the actual component scale approach, CFD should allow for a more precise simulation of the flow structure, including

[1] Corresponding author and workshop attendee : pierre.ruyer@irsn.fr

prediction of the two-phase flow structures of interest. This issue determined different research activities:

o the clear definition of the regimes and of their boundaries is an experimental challenge in terms of flow conditions as well as in terms of flow instrumentation and data analysis. In collaboration with French partners, IRSN develops an experimental program on the topic that will provide CFD-grade data.

o According to the state of the art of two-phase flow CFD tools capabilities, the approach corresponds to the Euler-Euler six equations averaged two-phase flow model, to which interface-resolving-like capabilities are introduced. IRSN is considering the assessment of the validation of such tools with respect to both experimental data, with a dedicated experimental device, and numerical simulation data inherited from Volume of Fluid simulation results in simplified configurations.

- It must be recalled that, in the current numerical approach retained for the safety evaluation, the homogenous mixture assumption prevents from considering the influence of the two-phase regime configuration on the tube vibrational response. The ability to correctly predict the flow-induced vibrations is assessed thanks to the comparison of coupled CFD-CSD computations against experimental data (that include both fluid and solid measurements) allowing to study the impact of some simplified models for both the fluid (turbulence) and the structure (high-fidelity or reduced-order approach). This includes some single-phase flow cases (within the VIKING UE program, the FSI-OKBM NEA activity) as well as some dedicated two-phase flow experiments on an experimental device built at IRSN.

- The tube bundle is modelled in a porous approach, local pressure drop being function of the inclination of the flow with respect to the tube axis. Considering the subsequent flow deviation is complex for bended tubes. The current formulations are head loss correlations that include the effect of inclination and are inherited from dedicated experimental results of either aligned or purely crossflow. IRSN benched those formulations against RANS single phase flows CFD data with an explicit representation of the bundle geometry.

- The coupling between the primary and secondary loop must be considered in the analysis of the steam generator secondary side flow in order to predict the correct void fraction distribution across the tube bundle. IRSN developed a simplified model for the primary side to be solved within the CFD model for the secondary side.

All those works are illustrated by some studies to provide an overview of the actual R&D on the topic.

Development of Combustion Models for non-homogeneous Hydrogen-Air Mixtures

D. Dovizio, J. De Palma, E.M.J. Komen

Nuclear Research and Consultancy Group

Abstract

In the context of severe accident scenarios in a nuclear power plant, the control of hydrogen in the containment is an important safety issue, since the generation of large quantities of hydrogen in the containment may occur and hence should be addressed. In particular, if the concentration of hydrogen reaches flammability limits, the dynamic pressure loads from hydrogen combustion can be detrimental to the structural integrity of the reactor safety systems and the reactor containment.

CFD codes can serve as a numerical tool for the assessment of the risks associated to hydrogen combustion during severe accidents, by providing detailed transient predictions when compared to one-dimensional system codes.

In the past, we validated CFD based methods to determine the pressure loads from a fast deflagration as well as a slow deflagration with and without the presence of steam. More specifically, the effects of a new correlation for the flame speed were addressed to validate our in-house CFD code based on the open-source software OpenFOAM.

In the present work, the extension of these methods to non-uniform hydrogen–air mixtures is presented. In particular, a dependence of model parameters on mixture fraction is introduced, following previous work. In order to validate the implementation, first the model is applied to an externally piloted industrial gas turbine burner from the open literature. Then, the extended formulation is validated against non-uniform hydrogen–air experiments in the ENACCEF facility.

Numerical results are presented and analyzed in terms of flame front development and propagation, as well as temporal evolution of the pressure for different combustion models, showing the benefits of the extended formulation against the original one.

Future efforts will focus on the inclusion of carbon monoxide, in order to predict the combustion behavior of stratified H2-CO-Air-mixtures.